Luminescent Manganese in Nanocrystals

Liam R. Bradshaw

A dissertation
submitted in partial fulfillment of the
requirements for the degree of

Doctor of Philosophy

University of Washington
2015

Reading Committee:
Daniel R. Gamelin, Chair
Xiaosong Li
David S. Ginger Jr

Program Authorized to Offer Degree:
Chemistry

University of Washington

Abstract

Luminescent Manganese in Nanocrystals

Liam R. Bradshaw

Chair of the Supervisory Committee:
Prof. Daniel R. Gamelin
Chemistry

Manganese doped semiconductors such as ZnSe are classic phosphor materials that have been in wide use for many decades, and a great deal of research has been done on their optical, physical and magnetic properties. Recent developments in nanocrystal synthesis have enabled colloidal, nanometer scale analogs of these classic phosphors, giving the semiconductor new size-dependent physical properties and allowing for applications of these materials that require solution processability. Through investigation of the photoluminescent and magneto-photoluminescent properties of Mn^{2+} in nanocrystals, this thesis both demonstrates that the old understanding of the physical description of Mn^{2+} still holds regardless of crystal size, and demonstrates several properties not noticed in the classic bulk materials. Further, application of these new materials to solar energy collection and optical thermometry is discussed.

Table of Contents

Chapter 1. Introduction

Abstract. Mn^{2+}-doped semiconductors are classic phosphor materials. Shrinking the size of the semiconductor crystal to the nanometer scale allows electronic tunability, solution processability, and increased brightness. Despite the onset of quantum confinement, almost no new physics is needed to describe the properties of Mn^{2+} in these new, doped nanocrystalline materials. Quantum confinement *does* affect the properties of the nanocrystal host, and the coupling of the two systems leads to several new properties of doped nanocrystals. These new properties make them not only ideally suited to a range of novel applications, but also allow contributions to the already exhaustive understanding of these materials' physical properties.

1.1 Overview.

Luminescent Mn^{2+} doped semiconductors were first developed in the 1950s, and rapidly gained widespread use in display technologies due to their efficiency and robustness,[1-3] and are still in use today. When the crystallite size of semiconductor materials reaches the nanometer scale, the interaction of the edges of the crystal with delocalized charge carriers in the semiconductor means that not only the material, but the size of the crystal determines the physical properties. Although these nanocrystal (NC) phosphors have a much shorter history, they have already found new applications from their bulk analogs due to their size-tunability and solution processability.

Only within the last two decades have synthetic advances made Mn^{2+} doped NCs a reality.[4-6] In these new materials, it is clear that the size of the NC affects the electronic properties of the semiconductor, but it was not immediately obvious to what extent NC size affects the properties of the Mn^{2+}. For example, early reports on Mn^{2+} doped ZnS NCs claimed a significant shortening of the Mn^{2+} radiative photoluminescence (PL) lifetime upon quantum confinement,[4] but this effect was soon shown to arise from luminescent surface defects with a similar PL spectrum.[7] Even though Mn^{2+} has been demonstrated to behave largely the same in bulk and quantum confined semiconductors, various studies still claim observations of novel Mn^{2+} in NCs including "ultra-narrow" PL linewidths,[8] broad tunability of the PL,[9] excited state $Mn^{2+/3+}$ oxidation,[10] and size-dependent "giant" Zeeman splittings of the Mn^{2+} PL.[11] Over the course of this thesis, many of these effects will be demonstrated to be the results of experimental artifacts, and possibly symptoms of an over-eagerness to invoke new physics.

Even though the properties of the Mn^{2+} itself do not change substantially when in quantum-confined crystals, these phosphors do not behave identically to their bulk counterparts. Most noticeably, size dependent splittings of the exciton fine structure lead to longer exciton lifetimes,[12] which in turn results in higher efficiency for the sensitization of the Mn^{2+} emission. These splittings are additionally responsible for retained sensitization of the Mn^{2+} emission in a magnetic field, in contrast to bulk behavior where a magnetic field suppresses sensitization. although the average coupling strength of the Mn^{2+} is not dramatically effected by quantum confinement (except in very small nanocrystals),[13] the increased exciton density near the center of the nanocrystal means that dopants located in this region will experience substantially stronger coupling. Furthermore, the small crystal size limits the extent to which energy can migrate, mitigating the effects of trapping and amplifying magnetic coupling and cross-relaxation.

Not only do the new properties of Mn^{2+} doped NCs give them new applications ranging from solar energy converters to microscopy, but the increased brightness and magnetic field-independent PL allows study of these materials to contribute fundamental understanding to an already extensive knowledge base. Investigating the novel properties of these nanocrystalline materials will undoubtedly open further doors for application of these materials at the interfaces of energy, magnetism, photonics, and quantum processing.

1.2 Properties of Luminescent Manganese in II-VI semiconductors.

Mn^{2+} doped semiconductors can be divided, for the purposes of this study, into two distinct categories: those with band-gap energies (E_g) above and below ~2.2 eV. The reason for this distinction is the position of the lowest-lying $^4T_1$ ligand field excited state of Mn^{2+}. If the band-gap energy is below that of this ligand-field state (*e.g.* in large/dilute CdSe and CdTe), the luminescent properties of the material are determined predominantly by the semiconductor. Although doped "narrow-gap" materials are still of significant interest due to the magnetic properties given by the Mn^{2+} to the semiconductor, their discussion is out of the scope of this review, and thorough discussion of these materials can be found elsewhere.[14, 15] In "wide-gap" semiconductors containing Mn^{2+}, exchange coupling of the semiconductor orbitals with the Mn^{2+} *d*-orbitals yields efficient sensitization of luminescence from the Mn^{2+} ion. It should be noted that in ZnO, a low-lying $Mn^{2+/3+}$ charge transfer precludes sensitization of the ligand field states.[16]

Figure 1.1 shows a Tanabe-Sugano diagram for the lowest ligand-field states of Mn^{2+}. For weak-field ligands (such as S or Se) in a tetrahedral environment, the ground state is the high-spin, fully symmetric $^6A_1$ state characterized by half-occupancy of the 5 *d*-orbitals. The lowest-lying excited state is the $^4T_1$ term, generated by moving one electron from the t_2 set to an *e* orbital. The spin-forbidden transition between the $^4T_1$ excited state and the $^6A_1$ ground state is responsible for the strong orange luminescence band, characteristic of these materials. Consistent with the spin-forbidden nature of this transition, the $^6A_1 \rightarrow {}^4T_1$ absorption is notoriously weak ($\varepsilon \sim 1\text{-}10\ M^{-1}cm^{-1}$) and the corresponding $^4T_1 \rightarrow {}^6A_1$ luminescence is long-lived with a lifetime on the order of ms.[17, 18]

Even though the absorption to the ligand-field bands in Mn^{2+} is weak, the $^4T_1$ state can be efficiently sensitized through excitation of the semiconductor. In the case of sensitized PL, a photon is absorbed by the semiconductor, making an electron-hole pair. This exciton can transfer its energy to a higher-energy Mn^{2+} *d-d* state (to conserve energy), and then thermalize to the $^4T_1$. Even though the delocalized carriers of the semiconductor do not have substantial overlap with the very localized Mn^{2+} *d*-orbitals, the fact that the semiconductor bands posses some Mn^{2+} *d* or *s* character (and vice-versa) gives rise to exchange coupling of these two systems,[13] and thus efficient transfer between them. Similarly, electroluminescent excitation through "impact ionization" relies on the same exchange coupling and involves injecting high-energy electrons (> 2.2 eV) into the semiconductor conduction band, which can transfer their energy to the Mn^{2+} *d-d* excited state ladder.[19, 20] Incidentally, exchange coupling additionally mediates the inverse of these processes in "Auger"-type recombination between Mn^{2+} and conduction band electrons,[21] or excitons,[22] as discussed in Chapter 4.

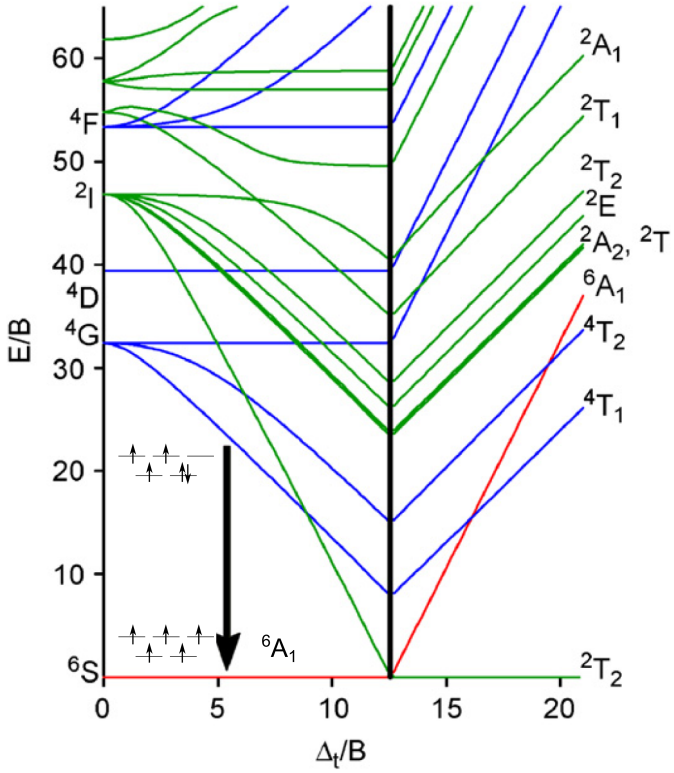

Figure 1.1 A Tanabe-Sugano diagram for the ligand-field levels of Mn^{2+} in a tetrahedral (or octahedral) environment. The luminescent transition in marked at its approximate position for Mn^{2+} in tetrahedral sulfide or selenide lattices. Orbital configurations of the ground- and luminescent excited-state are also shown. Adapted from ref. 23.

In bulk semiconductors and epitaxial quantum dots, even exchange-mediated energy transfer is not quite fast enough to fully outcompete electron-hole recombination, and thus the PL branching ratio is substantially less than unity.[11, 24] In colloidal NCs, however, nearly 100% of emission from doped dots (not from an undoped subset due to poissonian doping statistics)[22] is from Mn^{2+}. This is commensurate with a comparison of the measurement of the energy transfer rate constant (~5 ns^{-1} per Mn^{2+} in both bulk[25] and NC systems[26, 27]) to the excitonic relaxation rate constant (~0.1 ns^{-1}), which is much slower than in bulk or epitaxial NCs (~10 ns^{-1})[28] due to confinement induced dark-bright exciton splitting.[12, 29] Although the energy transfer time in bulk and NCs is similar, the distribution of the sensitized nanocrystals within the exciton volume is undoubtedly different. In a quantum confined crystal, the carrier wavefunctions are well approximated by spherical Bessel functions, which put a substantial amount of carrier density near the center of the NC.[12] Even though the volume (and thereby number of potential

dopant sites) outpaces the die-off of the carrier density at increasing distance from the NC center, the probability of exciting a Mn^{2+} near the center of the wavefunction is still higher in NCs than in bulk. This difference in spatial distribution of excited dopants, combined with the reproducibility of confined carrier wavefunctions as well as their inability to migrate may slightly increase the rates of dopant-carrier Auger recombination processes such as that discussed in Chapter 5, but direct comparison is difficult.[21]

It is somewhat remarkable that energy transfer and Auger recombination between the very localized Mn^{2+} *d* orbital states and delocalized carriers occurs so rapidly (on the picosecond timescale). Unlike the Coulomb-mediated biexciton or trion Auger processes that occur on a similar or slower timescale despite near perfect wavefunction overlap,[30] the coupling between the Mn^{2+} *d*-*d* states and free carriers proceeds through an exchange mechanism. Figure 1.2 shows an example of an orbital exchange pathway responsible for the coupling of the Mn^{2+} to an exciton. Here, electrons from the Mn^{2+} can fill empty orbitals in the valence band, and vice-versa. This type of interaction is mediated mostly by the overlap of the orbitals in question, but also by the energy differences between them.[31-33] The requirement for good overlap favors coupling of Mn^{2+} *d*- orbitals with valence band holes (predominantly *p*-character), which is nearly four times stronger than with conduction band electrons (predominantly *s*- character) due to symmetry restriction on *s*-*d* interactions and lattice iconicity concerns.[13, 32] In quantum confined semiconductors, the confinement of the exciton increases the overall overlap integral due to a small amount of the wavefunction tunneling out of the NC, although the effect is generally understood to be small except for in the smallest nanocrystals.[13] Even so, interactions with Mn^{2+} near the center of the exciton wavefunction are significantly enhanced, and magnetic effects of confinement are non-trivial as evidenced by the size dependence of excitonic magnetic polaron fields.[12, 34] More complete discussions of microscopic exchange mechanisms and their role in defining the properties of narrow gap NCs can be found elsewhere.[12, 13, 15, 32, 35-37]

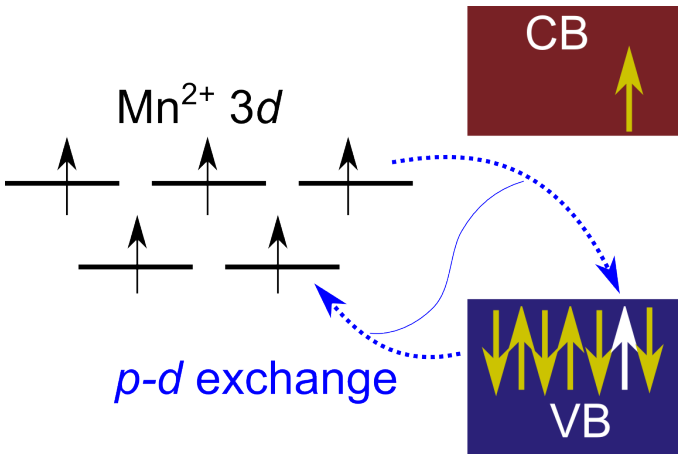

Figure 1.2 A schematic example of kinetic *p-d* exchange between the half-filled Mn^{2+} *d*-orbitals and an electron-hole pair in the semiconductor. Although there are other exchange pathways available, this motif is dominant.[13, 32] Energy spacings and alignment are not to scale.

One of the few examples of a difference in the properties of luminescent Mn^{2+} in NCs from their bulk analogs is the lack of magnetic field-induced energy transfer quenching.[11, 38] In bulk semiconductors and epitaxial quantum dots, application of a magnetic field at low temperature turns off energy transfer to Mn^{2+}, resulting in recovery of excitonic emission.[24, 39, 40] This effect is explained by a lack of spin conservation in the energy transfer process when the $^6A_1$ Mn^{2+} is frozen out in its m_s=-5/2 Zeeman level. In the $|^6A_1(m_s=-5/2),\text{Exciton}\rangle \rightarrow |^4T_1\rangle$ energy transfer, at least one unit of spin must be supplied by the exciton, which is not possible if it has S=0.[39] In colloidal quantum dots, however, this effect is not observed, and the branching ratio for energy transfer remains effectively unity up to fields as high as 55 T (Ref. [11] and Chapter 2). This dramatic difference between the bulk and nanocrystalline materials is likely a result of the splittings, kinetic considerations, and slight differences in overlap and migration discussed above, but no systematic investigation has yet been conducted.[11] Incidentally, however, the fact that magnetic fields do not turn off energy transfer in NCs allows us to study the magneto-luminescent properties of Mn^{2+} without the need for direct excitation of the weak *d-d* transitions. This likely explains how studies such as that presented in Chapters 2 and 3 are able to contribute to the decades-old body of literature on magneto-optical properties of Mn^{2+} in semiconductors.

In Chapter 2, the bright sensitized PL at magnetic fields as high as 55 T reveals new signatures of the Jahn-Teller effect in the Mn^{2+} $^4T_1$ excited state: At fields greater than 6 T (where previous measurements had stopped), the circular polarization of luminescence in the

Faraday geometry *decreases* as a function of applied magnetic field. Modeling these experiments based on a static Jahn-Teller distortion that essentially quenches all first-order spin orbit coupling reveals that this turnover in the circularly polarized luminescence is a direct result of the small remaining second-order spin-orbit coupling. This model used only parameters derived from measurements on bulk single crystals, not only confirming the understanding of Mn^{2+} fine structure developed over decades of investigation,[41-45] but additionally demonstrating that the electronic structure of Mn^{2+} is identical to that of bulk NCs, in contrast to other recent claims.[8, 11] The modeling of these results in the static Jahn-Teller limit additionally demonstrates that any remaining effects of unquenched first-order spin-orbit coupling do not appreciably affect the magneto-luminescent properties of these materials, either bulk or nanocrystalline.

A significant issue for the luminescent and magnetic properties of Mn^{2+} doped semiconductors is the formation of coupled Mn^{2+}-Mn^{2+} dimers in appreciable numbers at concentrations as low as only a couple percent.[46] In their ground state, Mn^{2+} dimers are coupled antiferromagnetically, causing a reduction in overall sample magnetization.[47] Further, the PL properties of dimers are different from monomers, hallmarked by a significantly reduced radiative lifetime due to the Tanabe effect, wherein the coupling of spins lends allowedness to otherwise spin-forbidden transitions.[48, 49] Aided by the magnetic-field independent sensitization of $^4T_1$ Mn^{2+}, Chapter 3 presents the results of time resolved magnetophotoluminescence over a range of concentrations demonstrating that Mn^{2+} dimers are in fact *ferro*-magnetically coupled in their excited state. DFT modeling of this excited state demonstrates that it is the Jahn-Teller distortion of Chapter 2 that allows this ferromagnetic coupling through preferential orientation of the empty *d* orbital of the $^4T_1$ state towards the bridging Se^{2-}. These results answer a debate over the sign of excited state exchange coupling that began in 1963, yet was never settled due to the difficulty in assigning single crystal zero-phonon lines in these materials.[18, 50-52]

1.3 Synthetic Advances.

Nanocrystal analogs of classic semiconductor materials give them new properties based on the size and shape of the crystal, and thus growth of nanocrystalline materials has been a burgeoning frontier of materials science for the last several decades. Even though luminescent Mn^{2+} doped semiconductor phosphors have been in use since the 1960s and nanocrystalline analogs of the same (undoped) semiconductors have been studied for several decades, high

quality doped nanocrystals are a relatively recent development. For example, it was proposed as recently as 2005 that doping of CdSe NCs was impossible, due to kinetic competition during the growth of the nanocrystal.[53] In the race to develop synthetic routes that circumvent this difficulty with doping NCs, several strategies have developed, although the field is rife with false-positives of successful doping.[15]

For the sulfide lattices (e.g. CdS or ZnS), doping with Mn^{2+} is not terribly difficult. In a normal CdS hot-injection synthesis, simply adding $Mn(oAc)_2$ results in high-quality doped NCs with predominantly Mn^{2+} emission.[21, 54] Similarly, Mn^{2+}:ZnS NCs have been made by various low-temperature methods.[4, 7, 55] Although Mn^{2+} doped CdS and ZnS are classic phosphor materials, they have the significant drawbacks of toxicity and instability (CdS)[56] and far-UV semiconductor absorbance (ZnS). Moving to ZnSe solves many of these problems, but doping the selenide lattices proves much more difficult, due predominantly to softness of the selenide.[6] Methods to circumvent this difficulty include use of the extremely reactive Mn^{2+} precursor dimethyl-manganese,[5] growing ZnSe shells around pre-formed MnSe cores,[57] or decreasing zinc reactivity by thermolysis of $NMe_4Zn_4SePh_{10}$.[6] Recently, the "diffusion doping" strategy of depositing a thin MnSe shell followed by diffusion of the Mn^{2+} into the lattice has proved to be a promising general doping strategy,[58] but optimization for ZnSe has yet to be done. Already these synthetic methods enabled the creation of entirely new materials, such as dilute Mn^{2+}:CdSe NCs that show Mn^{2+} emission when confinement increases their bandgap above 2.2 eV.[36]

Nanocrystal synthesis additionally allows for designer growth of heterostructures from different materials, without analogy in bulk materials. These structures can be as simple as core/shell structures, or can be more exotic as in rods, dots within rods, or tetrapods.[59, 60] Even the relatively simple core/shell architecture is an immensely powerful tool to the design of novel materials, as the interface can become the dominant property of the material, such as in "type-II" particles, where the electron and hole become spatially separated because of band offsets between the core and shell materials.[61, 62] Elaborate shell structures can additionally be used for very precise tuning of the NC bandgap.[63] In terms of doped nanocrystals, this type of core/shell architecture has even been used to vary the radial position of Mn^{2+} dopants within a CdS/ZnS NCs to demonstrate position-dependent effects on the energy transfer time.[26] More simply, growth of a shell of equal or larger bandgap material serves to isolate the core of the NC (and therefore frequently the dopant) from surface defects or high-frequency vibrational modes,

usually leading to much higher PL quantum yields. Over the course of the last several years, development of shell growth techniques has allowed these NC phosphors to achieve near-unity quantum yields from Mn^{2+} (e.g. Chapter 5). Sometimes, however, the lattice strain at the core/shell interface or the reduction in symmetry from alloying can break the tetrahedral symmetry around a Mn^{2+} dopant, resulting in shifts of the PL spectrum from what is usually seen in bulk materials.[64, 65]

1.4 New applications of luminescent Mn^{2+} in nanocrystals.

Even though the physical properties of bulk and NC Mn^{2+} doped wide-gap NCs are quite similar, the processability, synthetic tunability, and exciton confinement of NCs give them new potential applications from their bulk counterparts. Most basically, the ability to grow core/shell structures allows demonstration in Chapter 5 that room-temperature quantum yields for Mn^{2+} $Zn_{1-x-y}Cd_xMn_ySe/ZnS$ can reach at least 0.88. In this system, not only is the energy transfer fast enough to be very competitive with trapping, but the alloying of Cd into the predominantly ZnSe core excludes some of the potential trap states by lowering the conduction band. Already, solution processable phosphors with near unity quantum yield could have myriad potential applications such as for fluorescence microscopy, printed displays, or lighting.

For fluorescence microscopy, the bright, stable, and soluble Mn^{2+} doped ZnSe NCs are already being used,[66, 67] but the saturation properties discussed in Chapter 4 make them ideal for new methods in sub-diffraction limit microscopy. So-called "super-resolution" microscopy purposefully saturates parts of an image using structured illumination in order to circumvent the diffraction limit. Using this kind of technique, the theoretical limit for resolution is the size of the luminophore.[68] Currently, most techniques use either luminescent proteins or organic dyes, but these suffer from relatively rapid degradation under intense illumination. Previous reports have used Mn^{2+} doped ZnSe quantum dots for super-resolution imaging, but used sub-gap excitation to quench the Mn^{2+} emission through excited-state absorption.[69] Taking advantage of the efficient PL saturation by the exchange-mediated Auger recombination demonstrated in Chapter 4 could theoretically yield very similar results without the need for high-power irradiation.

In NCs with the correct energy gap, the strong coupling of the fully-allowed excitonic transition to the long-lived Mn^{2+} $^4T_1$ excited state results in the novel property of "exciton

storage."[70, 71] Here, the ~10^4 difference in radiative recombination rates between the exciton and the Mn^{2+} $^4T_1$ state means that a small amount of thermal repopulation of the exciton results in recovered excitonic emission. Recovery of excitonic emission is thus extremely temperature dependent, but the temperature range over which it occurs can be tuned through changing the energy gap between the Mn^{2+} $^4T_1$ state and the exciton. Strong exchange coupling mediates rapid thermal cycling between the states, implying full thermal equilibration on the timescale of luminescence. This "strongly coupled dual emission" therefore implies that the ratio is only dependent on temperature and not affected by quenching processes that might affect one state over the other. For applications in optical temperature sensing, this property implies much more reliable measurement in a broad range of conditions such as in biological environments where pH or oxygen concentration might vary within a sample. Furthermore, the novel properties of these materials motivated development of new metrics of sensitivity for ratiometric optical temperature sensors, as discussed in Chapter 7.

Although the temperature dependent dual emission from Mn^{2+} doped NCs has been demonstrated to be general across different methods of tuning the energy difference between the $^4T_1$ and excitonic states,[63, 65, 70-72] it is informative to consider why this effect was never observed in bulk semiconductors despite decades of experimentation with alloying. The most significant difference between the confined nanocrystals used in these studies and bulk materials with the same band gap is the lifetime of the exciton, which is several orders of magnitude longer in NC materials. This means that, for the same bandgap material, much lower Boltzmann populations would have been necessary to repopulate excitonic states enough to achieve equal Mn^{2+} and excitonic emission. Thus, the difference in excitonic lifetime would merely change the temperature (for a given band-gap energy) at which dual emission occurs, but would not preclude its observation. More likely, however, is that migration of excitons to trap centers in bulk materials leads to non-radiative recombination wen carrier lifetimes are extended by several orders of magnitude due to dual emission. Since energy transfer to Mn^{2+} must compete with trapping each time the energy is cycled through the exciton, thermal repopulation of excitonic states in bulk crystals was most likely ignored as a thermally activated non-radiative process and not noticed for its true potential. A similar mechanism of thermally assisted trapping during cycles from the Mn^{2+} state is undoubtedly present in NCs, but the ability to isolate the exciton from such trap states by core/shell architectures means that particles are able to have very few or

even zero competitive trap states available to the exciton, and thus continue to thermally cycle through Mn^{2+} ions until radiative emission. This implies, however, that the conditions on crystal quality for high quantum yields are much more stringent on dual emitting NCs than other doped or undoped NCs. Luckily, lowering the gap of the semiconductor also excludes many potential traps, mitigating some of these requirements.

A seemingly trivial but nonetheless significant result of the coupling of the strong absorbance of the exciton with the spin-forbidden $^4T_1 \leftrightarrow {}^6A_1$ transition is that Mn^{2+} emission will not be reabsorbed due to the weak oscillator strength of the $^6A_1 \rightarrow {}^4T_1$ absorbance. Further, a large Stokes shift due to strong vibronic coupling implies that overlap of the Mn^{2+} absorbance and PL spectra are minimal. This lack or reabsorption combined with the advantages of NC solution processability make wide-gap Mn^{2+}-doped NCs ideal for applications in luminescent solar concentrators (LSCs). In these devices, sunlight is absorbed by a dye embedded in a waveguide, which carries most of the emitted light to photovoltaics at the edge. Although many potential loss mechanisms exist, reabsorption is the current limiting factor to implementation of this technology since some photons are lost at each reabsorption event either due to less than unity quantum yield or by emission into the "escape cone."[73-75]

Chapters 5 and 6 discuss application of Mn^{2+} doped ZnSe and $Zn_{1-x}Cd_xSe$ to LSCs. Although several other NCs have recently been proposed for use in LSCs, they have been predominantly based on heterostructures that use absorption from a large shell followed by emission from a small core to reduce reabsorption.[76-79] Unfortunately, the small core always has some overlap with the emitted light due to its fully allowed absorption and near-zero stokes shift. Although this may be mitigated to some extent by growing a larger shell, Rayleigh scattering becomes significant before reabsorption is sufficiently suppressed, leading to increased losses. Only doped semiconductors promise to essentially eliminate reasbsorption since they not only couple strong NCs absorption to weak dopant absorbances, but also take advantage of the dopant emission's inherent Stoke's shift. By this mechanism, reabsorption losses from Mn^{2+} doped ZnSe NCs in LSCs has been demonstrated to be essentially zero, with device efficiency limited instead by polymer waveguide transparency.[80] Unfortunately, however, the condition that the band-gap energy must be greater than 2.2 eV in order to sensitize Mn^{2+} emission significantly limits the amount of sunlight that these phosphors are able to absorb, even when Cd-alloying is used to lower the gap near the 2.2 eV limit. To solve this, the experiments in Chapter 5

demonstrate that Cu^{+} doped CdSe gives similar reabsorption performance while increasing solar absorption by nearly a factor of 4. One large advantage of an LSC, however, is that it need not be opaque, and thus can find applications where transmitted photons could be repurposed (e.g. windows or electronic displays). For such applications, Mn^{2+} doped NCs are undoubtedly the best choice.

1.5 The future of luminescent Mn^{2+} in nanocrystals.

It is informative at this point to look at areas for future development of these materials and their applications. First, broad application of the already established Mn^{2+} doped ZnSe or $Zn_{1-x}Cd_xSe$ NCs will rely on movement away from the "cluster decomposition" method due to the expense of precursors, synthetic complexity, and polydispersity of the resulting nanocrystals. Other current syntheses using dimethyl manganese may be more facile, but the danger and difficulty of handling this precursor, as well as the low Mn^{2+} incorporation make this route less than ideal. Progress has already been made in this respect through the "diffusion doping" strategy reported by Vlaskin *et al.*,[58] but the parameters for doping ZnSe have not yet been optimized. Additionally, growth of the high quality shells necessary for stability and quantum yield currently involves several days of slow addition reactions. Recently developed high-temperature shell growths are much more facile,[79, 81] but these conditions often lead to exclusion of dopants.

Doping Mn^{2+} into different nanocrystalline lattices will undoubtedly lead to exciting new applications. Some work has already been done in this respect for doping Mn^{2+} into PbS,[82] InAs,[83] and InP NCs,[84] but the number of studies is relatively small. In octahedral lattices, the strength of the ligand-field interaction goes up by a factor of 9/4, which would result in Mn^{2+} emission at roughly 1.5 eV based on the Tanabe Sugano diagram of Figure 1.1. In bulk GaP (a tetrahedral lattice), Mn^{2+} emission is observed at ~1.3 eV (likely due to increased ligand field strength or lattice density), and shows a strong Jahn-Teller coupling similar to that discussed in Chapter 2.[85] With the correct lattice, the utility of Mn^{2+} for LSCs could therefore be extended to applications requiring absorption of more of the visible spectrum. Furthermore, GaP consists of only earth abundant, non-toxic elements. To the best of our knowledge, NIR emission from Mn^{2+} due to either of these mechanisms has not been observed in nanocrystals.

The magnetic properties of materials such as Mn^{2+} doped ZnSe have already found applications such as in the spin injection layer for spin-LEDs.[86] These devices, however, did not take advantage of the luminescent properties of Mn^{2+} and instead used the giant-Zeeman splitting effects on the bands of the ZnSe. It is interesting, therefore, to examine how the magnetic and luminescent properties of Mn^{2+} might be combined. First, the demonstration of pure circularly polarized emission from Mn^{2+} dimers in Chapter 3 might prove applicable to spin photonic devices similar to the spin-LED. Of course, this would require making materials containing predominantly dimers, a nearly impossible task in bulk materials. However, synthetic routes such as cluster seeded growth[87] may allow for realization of very non-statistical doping in nanocrystals. Additionally, the exciton storage effect may prove to have interesting magnetic applications, but systematic investigation of the magnetic properties of these systems has not been done, mostly due to the high temperatures required for most samples demonstrating exciton storage to date.

1.6 Summary

Over the course of this work, we demonstrate that Mn^{2+} doped nanocrystals can both teach us about the fundamental behavior of Mn^{2+} in these classic phosphor materials and demonstrate completely novel behavior due to their small size. Understanding of the fundamentals of Jahn-Teller distortion and dimer exchange coupling combined with detailed study of exchange-mediated energy transfer and Auger recombination give a complete picture of classic and uniquely nanocrystalline phenpomena. The new nanocrystal-specific properties of these classic phosphor materials open new doors for exciting applications of these materials ranging from solar energy to magnetism and temperature sensing.

1.7 References.

1. Fundamentals of Phosphors. CRC Press: Boca Raton, 2006.
2. Ronda, C., Luminescence: From Theory to Applications. Wiley-VCH: Weinheim, Germany, 2008.
3. Vlasenko, N. A.; Popkov, Y. A., STUDY OF ELECTROLUMINESCENCE OF A SUBLIMATED ZNS-MN PHOSPHOR. *Opt. Spektrosk.* 1960, **8** (1), 81-88.
4. Bhargava, R. N.; Gallagher, D.; Hong, X.; Nurmikko, A., Optical properties of manganese-doped nanocrystals of ZnS. *Phys. Rev. Lett.* 1994, **72** (3), 416-419.
5. Norris, D. J.; Yao, N.; Charnock, F. T.; Kennedy, T. A., High-Quality Manganese-Doped ZnSe Nanocrystals. *Nano Lett.* 2000, **1** (1), 3-7.

6. Archer, P. I.; Santangelo, S. A.; Gamelin, D. R., Inorganic Cluster Syntheses of TM^{2+}-Doped Quantum Dots (CdSe, CdS, CdSe/CdS): Physical Property Dependence on Dopant Locale. *J. Am. Chem. Soc.* 2007, **129**, 9808-9818.
7. Bol, A. A.; Meijerink, A., Long-lived Mn2+ emission in nanocrystalline ZnS:Mn2+. *Phys. Rev. B* 1998, **58** (24), R15997-R16000.
8. Hazarika, A.; Layek, A.; De, S.; Nag, A.; Debnath, S.; Mahadevan, P.; Chowdhury, A.; Sarma, D. D., Ultranarrow and widely tunable Mn2+-Induced photoluminescence from single Mn-doped nanocrystals of ZnS-CdS alloys. *Phys. Rev. Lett.* 2013, **110** (26), 267401.
9. Hazarika, A.; Pandey, A.; Sarma, D. D., Rainbow Emission from an Atomic Transition in Doped Quantum Dots. *J. Phys. Chem. Lett.* 2014, **5** (13), 2208-2213.
10. Chen, H.-Y.; Chen, T.-Y.; Berdugo, E.; Park, Y.; Lovering, K.; Son, D. H., Hot Electrons from Consecutive Exciton-Mn Energy Transfer in Mn-Doped Semiconductor Nanocrystals. *J. Phys. Chem. C.* 2011, **115**, 11407-11412.
11. Viswanatha, R.; Pietryga, J. M.; Klimov, V. I.; Crooker, S. A., Spin-Polarized Mn^{2+} Emission from Mn-Doped Colloidal Nanocrystals. *Phys. Rev. Lett.* 2011, **107** (6), 067402.
12. Efros, A. L.; Rosen, M., The electronic structure of semiconductor nanocrystals. *Annu. Rev. Mater. Sci.* 2000, **30**, 475-521.
13. Beaulac, R.; Feng, Y.; May, J.; Badaeva, E.; Gamelin, D.; Li, X., Orbital pathways for Mn2+-carrier sp-d exchange in diluted magnetic semiconductor quantum dots. *Phys. Rev. B* 2011, **84** (19), 195324.
14. Furdyna, J. K.; Kossut, J., Diluted Magnetic Semiconductors. Academic: N.Y., 1988; Vol. 25.
15. Beaulac, R.; Ochsenbein, S. T.; Gamelin, D. R., Colloidal Transition-Metal-Doped Quantum Dots. In Semiconductor Quantum Dots, 2nd ed.; Klimov, V. I., Ed. CRC Press: 2010; pp 397-453.
16. Norberg, N. S.; Kittilstved, K. R.; Amonette, J. E.; Kukkadapu, R. K.; Schwartz, D. A.; Gamelin, D. R., Synthesis of Colloidal Mn2+:ZnO Quantum Dots and High-TC Ferromagnetic Nanocrystalline Thin Films. *J. Am. Chem. Soc.* 2004, **126** (30), 9387-9398.
17. Dreyhsig, J.; Allen, J. W., Absorption from the Excited State in ZnS:Mn. *J. Phys.: Condens. Matter* 1989, **1**, 1087-1099.
18. McClure, D. S., Optical Spectra of Exchange Coupled Mn++ Ion Pairs in ZnS:MnS. *J. Chem. Phys.* 1963, **39** (11), 2850.
19. Benalloul, P.; Benoit, J.; Duran, J.; Evesque, P.; Geoffroy, A., Diffusion and Trapping in ZnS-Mn Electroluminescent Thin Films. *Solid State Commun.* 1984, **51** (6), 389-392.
20. Törnqvist, R., Manganese concentration dependent saturation in ZnS:Mn thin film electroluminescent devices. *J. Appl. Phys.* 1983, **54**, 4110-4117.
21. White, M. A.; Weaver, A. L.; Beaulac, R.; Gamelin, D. R., Electrochemically Controlled Auger Quenching of Mn2+ Photoluminescence in Doped Semiconductor Nanocrystals. *ACS Nano* 2011, **5**, 4158–4168.
22. Bradshaw, L. R.; Hauser, A.; McLaurin, E. J.; Gamelin, D. R., Luminescence Saturation via Mn2+-Exciton Cross Relaxation in Colloidal Doped Semiconductor Nanocrystals. *Journal of Physical Chemistry C* 2012, **116** (16), 9300-9310.
23. Beaulac, R.; Archer, P. I.; Gamelin, D. R., Luminescence in colloidal Mn2+-doped semiconductor nanocrystals. *Journal of Solid State Chemistry* 2008, **181** (7), 1582-1589.
24. Chernenko, A.; Dorozhkin, P.; Kulakovskii, V.; Brichkin, A.; Ivanov, S.; Toropov, A., Auger recombination of excitons in semimagnetic quantum dot structure in a magnetic field. *Phys. Rev. B* 2005, **72** (4).

25. Hefetz, Y.; Goltsos, W. C.; Nurmikko, A. V.; Kolodziejski, L. A.; Gunshor, R. L., Exciton formation and energy exchange with d,Äêelectron states in ZnSe/(Zn,Mn)Se multiple quantum wells. *Appl. Phys. Lett.* 1986, **48** (5), 372-374.
26. Chen, H.-Y.; Maiti, S.; Son, D. H., Doping Location-Dependent Energy Transfer Dynamics in Mn-Doped CdS/ZnS Nanocrystals. *ACS Nano* 2011, **6** (1), 583-591.
27. Chen, H.-Y.; Chen, T.-Y.; Son, D. H., Measurement of Energy Transfer Time in Colloidal Mn-Doped Semiconductor Nanocrystals. *J. Phys. Chem. C* 2010, **114**, 4418–4423.
28. Oh, E.; Choi, D. G.; Kim, S.; Lee, T. K.; Park, J. H.; Lee, S.; Furdyna, J. K., Time-resolved photoluminescence in CdSe/CdZnSe and CdSe/CdMnSe coupled quantum dot structures. *Anglais* 2006, **49** (2), 5.
29. Efros, A. L.; Rosen, M.; Kuno, M.; Nirmal, M.; Norris, D. J.; Bawendi, M., Band-edge exciton in quantum dots of semiconductors with a degenerate valence band: Dark and bright exciton states. *Phys. Rev. B* 1996, **54** (7), 4843-4856.
30. Cohn, A. W.; Rinehart, J. D.; Schimpf, A. M.; Weaver, A. L.; Gamelin, D. R., Size Dependence of Negative Trion Auger Recombination in Photodoped CdSe Nanocrystals. *Nano Lett.* 2013, **14** (1), 353-358.
31. Weihe, H.; Güdel, H. U., Quantitative Interpretation of the Goodenough-Kanamori Rules: A Critical Analysis. *Inorg. Chem.* 1997, **36** (17), 3632-3639.
32. Beaulac, R.; Gamelin, D. R., Two-center formulation of Mn^{2+}-electron s-d exchange coupling in bulk and quantum-confined diluted magnetic semiconductors. *Phys. Rev. B* 2010, **82**, 224401.
33. Larson, B. E.; Hass, K. C.; Ehrenreich, H.; Carlsson, A. E., Theory of exchange interactions and chemical trends in diluted magnetic semiconductors. *Phys. Rev. B* 1988, **37** (8), 4137-4154.
34. Beaulac, R.; Schneider, L.; Archer, P. I.; Bacher, G.; Gamelin, D. R., Light-Induced Spontaneous Magnetization in Colloidal Doped Quantum Dots. *Science* 2009, **325**, 973–976.
35. Beaulac, R.; Archer, P. I.; Ochsenbein, S. T.; Gamelin, D. R., Mn^{2+}-Doped CdSe Quantum Dots: New Inorganic Materials for Spin-Electronics and Spin-Photonics. *Adv. Funct. Mater.* 2008, **18**, 3873-3891.
36. Beaulac, R.; Archer, P. I.; Liu, X.; Lee, S.; Mackay Salley, G.; Dobrowolska, M.; Furdyna, J. K.; Gamelin, D. R., Spin-Polarizable Excitonic Luminescence in Colloidal Mn2+-Doped CdSe Quantum Dots. *Nano Lett.* 2008, **8** (4), 1197-1201.
37. Archer, P. I.; Santangelo, S. A.; Gamelin, D. R., Direct observation of sp-d exchange interactions in colloidal Mn2+- and Co2+-doped CdSe quantum dots. *Nano Lett.* 2007, **7** (4), 1037-1043.
38. Bradshaw, L. R.; May, J. W.; Dempsey, J. L.; Li, X.; Gamelin, D. R., Ferromagnetic excited-state Mn2+ dimers in Zn1-xMnxSe quantum dots observed by time-resolved magnetophotoluminescence. *Phys. Rev. B* 2014, **89** (11), 115312.
39. Chernenko, A. V.; Brichkin, A. S.; Sobolev, N. A.; Carmo, M. C., Mechanisms of manganese-assisted non-radiative recombination in Cd(Mn)Se/Zn(Mn)Se quantum dots. *Journal of Physics: Condensed Matter* 2010, **22** (35), 355306.
40. Lee, S.; Dobrowolska, M.; Furdyna, J. K., Enhancement of spin polarization in asymmetrically coupled CdSe and CdZnMnSe quantum dots in ZnSe matrix. *Physica E* 2006, **32** (1-2), 367-370.
41. Parrot, R.; Naud, C.; Porte, C.; Fournier, D.; Boccara, A. C.; Rivoal, J. C., Jahn-Teller Effect in Fluorescent Level of Mn++ in Znse and Zns. *Phys. Rev. B* 1978, **17** (3), 1057-1066.

42. Fournier, D.; Boccara, A. C.; Rivoal, J. C., Magneto-Optical Study of the 4T1 State of Mn2+ in ZnS. *J. Phys. C Solid State* 1977, **10** (1), 113-121.
43. Boulanger, D.; Parrot, R.; Cherfi, Z., Cluster model for radiative transition probabilities of d^{5} ions in tetrahedralsymmetry: Case of Mn^{2+} in the common cation series ZnS, ZnSe, and ZnTe. *Phys. Rev. B* 2004, **70** (7), 075209.
44. Boulanger, D.; Parrot, R.; Pohl, U. W.; Litzenburger, B.; Gumlich, H.-E., Magnetic Field Effect and Dynamical Jahn-Teller Effect on a 4T1 Level of a d5 Ion Coupled to ε-Vibrational Modes. *Phys. Stat. Sol. B* 1999, **213** (1), 79-91.
45. Boulanger, D.; Curie, D.; Parrot, R., Strong and Very Strong Covalency Effects on the Lifetime of Mn-2+ in Ii-Vi Compounds. *J. Lumines.* 1991, **48-9**, 680-684.
46. Behringer, R. E., Number of Single, Double, and Triple Clusters in a System Containing Two Types of Atoms. *J. Chem. Phys.* 1958, **29** (3), 537.
47. Brumage, W. H.; Yarger, C. R.; Lin, C. C., Effect of the Exchange Coupling of Mn^{++} Ions on the Magnetic Susceptibilities of ZnS: MnS Crystals. *Phys Rev* 1964, **133** (3A), A765-A767.
48. Busse, W.; Gumlich, H.-E.; Meissner, B.; Theis, D., Time resolved spectroscopy of ZnS : Mn by dye laser technique. *J. Lumin.* 1976, **12**, 693-700.
49. Ferguson, J.; Guggenheim, H. J.; Tanabe, Y., Exchange Effects in the Electronic Absorption Spectrum of Mn(II) in Perovskite Fluorides. *J. Appl. Phys.* 1965, **36** (3), 1046.
50. Benecke, C.; Busse, W.; Gumlich, H.-E.; Pohl, U. W., Systems of Zero-Phonon Lines Due to Mn2+ Pairs in ZnS. *Phys. Stat. Sol. B* 1985, **128** (2), 701-707.
51. Pohl, U. W.; Gumlich, H.-E., Long-Range Mn-Ion Pairs and Other Mn Related Centers in ZnS Detected by Site-Selected Spectroscopy. *J. Cryst. Growth* 1990, **101** (1-4), 521-524.
52. Pohl, U. W.; Gumlich, H.-E., Optical Transitions of Different Mn-Ion Pairs in ZnS. *Phys. Rev. B* 1989, **40** (2), 1194-1201.
53. Erwin, S. C.; Zu, L.; Haftel, M. I.; Efros, A. L.; Kennedy, T. A.; Norris, D. J., Doping semiconductor nanocrystals. *Nature* 2005, **436** (7047), 91-94.
54. Nag, A.; Chakraborty, S.; Sarma, D. D., To Dope Mn^{2+} in a Semiconducting Nanocrystal. *J. Am. Chem. Soc.* 2008, **130**, 10605–10611.
55. Bryan, J. D.; Gamelin, D. R., Doped Semiconductor Nanocrystals: Synthesis, Characterization, Physical Properties, and Applications. In Progress in Inorganic Chemistry, John Wiley & Sons, Inc.: 2005; pp 47-126.
56. Levy, L.; Ingert, D.; Feltin, N.; Pileni, M.-P., Effect of Aging on Luminescence from Isolated Mn2+ Confined in Cd0.95Mn0.05S Clusters. *Advanced Materials* 1998, **10** (1), 53-57.
57. Pradhan, N.; Goorskey, D.; Thessing, J.; Peng, X., An Alternative of CdSe Nanocrystal Emitters:‚Äâ Pure and Tunable Impurity Emissions in ZnSe Nanocrystals. *J. Am. Chem. Soc.* 2005, **127** (50), 17586-17587.
58. Vlaskin, V. A.; Barrows, C. J.; Erickson, C. S.; Gamelin, D. R., Nanocrystal Diffusion Doping. *J. Am. Chem. Soc.* 2013, **135** (38), 14380-14389.
59. Yin, Y.; Alivisatos, A. P., Colloidal nanocrystal synthesis and the organic-inorganic interface. *Nature* 2005, **437** (7059), 664-670.
60. Choi, C. L.; Alivisatos, A. P., From Artificial Atoms to Nanocrystal Molecules: Preparation and Properties of More Complex Nanostructures. *Annual Review of Physical Chemistry* 2010, **61** (1), 369-389.

61. Balet, L. P.; Ivanov, S. A.; Piryatinski, A.; Achermann, M.; Klimov, V. I., Inverted Core/Shell Nanocrystals Continuously Tunable between Type-I and Type-II Localization Regimes. *Nano Lett.* 2004, **4**, 1485-1488.
62. Ivanov, S. A.; Piryatinski, A.; Nanda, J.; Tretiak, S.; Zavadil, K. R.; Wallace, W. O.; Werder, D.; Klimov, V. I., Type-II Core/Shell CdS/ZnSe Nanocrystals:‚Äâ Synthesis, Electronic Structures, and Spectroscopic Properties. *J. Am. Chem. Soc.* 2007, **129** (38), 11708-11719.
63. McLaurin, E. J.; Vlaskin, V. A.; Gamelin, D. R., Water-Soluble Dual-Emitting Nanocrystals for Ratiometric Optical Thermometry. *J. Am. Chem. Soc.* 2011, **133**, 14978-14980.
64. Ithurria, S.; Guyot-Sionnest, P.; Mahler, B.; Dubertret, B., Mn2+ as a Radial Pressure Gauge in Colloidal Core/Shell Nanocrystals. *Phys. Rev. Lett.* 2007, **99** (26), 265501.
65. McLaurin, E. J.; Fataftah, M. S.; Gamelin, D. R., One-step synthesis of alloyed dual-emitting semiconductor nanocrystals. *Chem. Comm.* 2013, **49** (1), 39-41.
66. Wang, S.; Jarrett, B. R.; Kauzlarich, S. M.; Louie, A. Y., Core/Shell Quantum Dots with High Relaxivity and Photoluminescence for Multimodality Imaging. *J. Am. Chem. Soc.* 2007, **129**, 3848-3856.
67. Pradhan, N.; Battaglia, D. M.; Liu, Y.; Peng, X., Efficient, Stable, Small, and Water-Soluble Doped ZnSe Nanocrystal Emitters as Non-Cadmium Biomedical Labels. *Nano Lett.* 2007, **7**, 312-317.
68. Gustafsson, M. G. L., Nonlinear structured-illumination microscopy: Wide-field fluorescence imaging with theoretically unlimited resolution. *Proc. Nat. Acad. Sci.* 2005, **102** (37), 13081-13086.
69. Irvine, S. E.; Staudt, T.; Rittweger, E.; Engelhardt, J.; Hell, S. W., Direct light-driven modulation of luminescence from Mn-doped ZnSe quantum dots. *Angew. Chem.* 2008, **47**, 2685-2688.
70. Beaulac, R.; Archer, P. I.; van Rijssel, J.; Meijerink, A.; Gamelin, D. R., Exciton Storage by Mn^{2+} in Colloidal Mn^{2+}-Doped CdSe Quantum Dots. *Nano Lett.* 2008, **8**, 2949-2953.
71. Vlaskin, V. A.; Janßen, N.; van Rijssel, J.; Beaulac, R.; Gamelin, D. R., Tunable Dual Emission in Doped Semiconductor Nanocrystals. *Nano Lett.* 2010, **10**, 3670–3674.
72. Hsia, C.-H.; Wuttig, A.; Yang, H., An Accessible Approach to Preparing Water-Soluble Mn2+-Doped (CdSSe)ZnS (Core)Shell Nanocrystals for Ratiometric Temperature Sensing. *ACS Nano* 2011, **5** (12), 9511-9522.
73. de Boer, D. K. G.; Broer, D. J.; Debije, M. G.; Keur, W.; Meijerink, A.; Ronda, C. R.; Verbunt, P. P. C., Progress in phosphors and filters for luminescent solar concentrators. *Opt. Express* 2012, **20** (S3), A395-A405.
74. Debije, M. G.; Verbunt, P. P. C., Thirty Years of Luminescent Solar Concentrator Research: Solar Energy for the Built Environment. *Adv. Energy Mat.* 2012, **2** (1), 12-35.
75. Batchelder, J. S.; Zewai, A. H.; Cole, T., Luminescent solar concentrators. 1: Theory of operation and techniques for performance evaluation. *Appl. Opt.* 1979, **18** (18), 3090-3110.
76. Krumer, Z.; Pera, S. J.; van Dijk-Moes, R. J. A.; Zhao, Y.; de Brouwer, A. F. P.; Groeneveld, E.; van Sark, W. G. J. H. M.; Schropp, R. E. I.; de Mello Donega, C., Tackling self-absorption in luminescent solar concentrators with type-II colloidal quantum dots. *Sol. Energ. Mat. Sol. C.* 2013, **111** (0), 57-65.
77. Bronstein, N. D.; Li, L.; Xu, L.; Yao, Y.; Ferry, V. E.; Alivisatos, A. P.; Nuzzo, R. G., Luminescent Solar Concentration with Semiconductor Nanorods and Transfer-Printed Micro-Silicon Solar Cells. *ACS Nano* 2013, **8** (1), 44-53.

78. Meinardi, F.; Colombo, A.; Velizhanin, K. A.; Simonutti, R.; Lorenzon, M.; Beverina, L.; Viswanatha, R.; Klimov, V. I.; Brovelli, S., Large-area luminescent solar concentrators based on "Stokes-shift-engineered" nanocrystals in a mass-polymerized PMMA matrix. *Nat Photon* 2014, **8** (5), 392-399.
79. Coropceanu, I.; Bawendi, M. G., Core/Shell Quantum Dot Based Luminescent Solar Concentrators with Reduced Reabsorption and Enhanced Efficiency. *Nano Lett.* 2014.
80. Erickson, C. S.; Bradshaw, L. R.; McDowall, S.; Gilbertson, J. D.; Gamelin, D. R.; Patrick, D. L., Zero-Reabsorption Doped-Nanocrystal Luminescent Solar Concentrators. *ACS Nano* 2014, **8** (4), 3461-3467.
81. Chen, O., et al., Compact high-quality CdSe,ÄìCdS core,Äìshell nanocrystals with narrow emission linewidths¬†and¬†suppressed blinking. *Nat Mater* 2013, **12** (5), 445-451.
82. Long, G.; Barman, B.; Delikanli, S.; Tsung Tsai, Y.; Zhang, P.; Petrou, A.; Zeng, H., Carrier-dopant exchange interactions in Mn-doped PbS colloidal quantum dots. *Appl. Phys. Lett.* 2012, **101** (6), -.
83. Stowell, C. A.; Wiacek, R. J.; Saunders, A. E.; Korgel, B. A., Synthesis and Characterization of Dilute Magnetic Semiconductor Manganese-Doped Indium Arsenide Nanocrystals. *Nano Lett.* 2003, **3** (10), 1441-1447.
84. Somaskandan, K.; Tsoi, G. M.; Wenger, L. E.; Brock, S. L., Isovalent Doping Strategy for Manganese Introduction into III-V Diluted Magnetic Semiconductor Nanoparticles:‚Äâ InP:Mn. *Chem. Mater.* 2005, **17** (5), 1190-1198.
85. Hofmann, G.; Anderson, F. G.; Weber, J., Jahn-Teller effect in the 4T1 state of Mn2+ in GaP. *Phys. Rev. B* 1991, **43** (12), 9711-9719.
86. Jonker, B. T.; Park, Y. D.; Bennett, B. R.; Cheong, H. D.; Kioseoglou, G.; Petrou, A., Robust Electrical Spin Injection into a Semiconductor Heterostructure. *Phys. Rev. B* 2000, **62**, 8180-8183.
87. Jawaid, A. M.; Chattopadhyay, S.; Wink, D. J.; Page, L. E.; Snee, P. T., Cluster-Seeded Synthesis of Doped CdSe:Cu4 Quantum Dots. *ACS Nano* 2013, **7** (4), 3190-3197.

Chapter 2. Static Jahn-Teller Effect in the Luminescent Mn^{2+} Excited State of Doped Quantum Dots, Probed by Magneto-Photoluminescence

Abstract. The circularly polarized *d-d* magneto-photoluminescence of Mn^{2+} dopant ions in ZnSe-based core/shell quantum dots has been measured at low temperatures and in high magnetic fields up to 55 T. The data are explained well by ligand-field theory using a model that invokes a static (strong) excited-state Jahn-Teller distortion and parameters taken from Mn^{2+}-doped ZnSe single crystals. These results provide new insights into the excited states of Mn^{2+} ions in II-VI semiconductor quantum dots. In preparation for submission in conjunction with Jillian L. Dempsey, Victor Z. Polinger, Remi Beaulac, Alina M. Schimpf, Emily J. McLaurin, Vladimir A. Vlaskin, Scott A. Crooker, and Daniel R. Gamelin.

2.1 Introduction

Mn^{2+}-doped semiconductors have been used as phosphors for decades.[1, 2] As an example, the first thin-film electroluminescent (TFEL) device structures were fabricated from Mn^{2+}-doped II-VI semiconductors in the late 1950s.[3] In these phosphors, Mn^{2+} acts as a luminescence activator, harvesting energy from the surrounding matrix and converting it to a localized *d-d* excitation, which then relaxes with a high radiative quantum yield. In addition to acting as a luminescence activator, Mn^{2+} also imparts unusual magnetic properties to semiconductors, most dramatically the so-called "giant Zeeman splittings" of band-edge and excitonic states that arise from Mn^{2+}-carrier *sp-d* exchange.[4, 5] These giant Zeeman splittings can readily exceed the available thermal free energy at moderate temperatures, leading to large carrier or exciton spin polarization.[6] The remarkable magneto-optical properties of these materials, often referred to as diluted magnetic semiconductors (DMSs), are also attractive for spin-photonics applications, in which electron spin information can be generated, manipulated, and detected using light.[4] In recent years, Mn^{2+}-doped semiconductors have been used in pioneering demonstrations of spin-based LEDs,[7] spin-valves,[6] and various fundamental effects such as tunneling anomalous magnetoresistance[8] that could impact future information processing technologies.

Advances in nanoscience have introduced new opportunities to manipulate the electronic properties of DMSs on unprecedentedly small length scales.[9] Epitaxial quantum dots (QDs)

containing single Mn^{2+} ions[10-14] have demonstrated attractive features for quantum information processing[15] and may portend the emergence of new technologies based on solitary dopant optoelectronics ("solotronics").[16] Advances in direct chemical syntheses of colloidal doped semiconductor nanocrystals (NCs) have stimulated broad interest in these materials,[17-22] in part because colloidal QDs provide even stronger quantum confinement than their epitaxial analogs and in part because of the chemical and processing flexibility offered by colloidal nanostructures. As phosphors, colloidal Mn^{2+}-doped ZnSe and related nanocrystals have been applied as luminescent probes for super-resolution imaging,[23] in ratiometric optical thermometry, [24-26] and as zero-reabsorption spectral converters in luminescent solar concentrators.[27, 28] As DMS nanostructures, colloidal Mn^{2+}-doped QDs have revealed giant excitonic Zeeman splittings,[21, 29-32] spontaneous photomagnetization,[33] and charge-controlled magnetization,[34] among other phenomena, all arising from strong *sp-d* exchange coupling between delocalized band-like charge carriers and localized Mn^{2+} dopant spins.

Although the *d* states of Mn^{2+} ions in II-VI semiconductors are generally considered highly localized, a recent study[35] reported an unexpectedly large Zeeman splitting (ΔE) in the Mn^{2+} $^4T_1 \rightarrow {}^6A_1$ PL of $Zn_{1-x}Mn_xSe/CdSe$ 'inverted' core/shell nanocrystals that is tunable *via* the nanocrystal's quantum confinement. From this result, it was suggested that quantum confinement can strongly influence the emission mechanism of Mn^{2+} ions in DMS nanomaterials. The possibility that the electronic structure of Mn^{2+} in II-VI QDs may be different from that in bulk Mn^{2+}-doped II-VI materials is intriguing and warrants further investigation.

Here, we report magneto-photoluminescence (magneto-PL) data for $Zn_{1-x}Mn_xSe/ZnS/CdS/ZnS$ QDs collected at magnetic fields up to 55 Tesla (T) and temperatures down to 1.65 K. Between 0 and ~6 T, the PL circular polarization increases with increasing magnetic field, and decreases with increasing temperature, and shows apparently simple saturation magnetization consistent with a spin-only description of the Mn^{2+} electronic structure. The data in this temperature and field window appear indistinguishable from those of bulk $Zn_{1-x}Mn_xS$,[36] quantum-confined $Zn_{1-x}Mn_xSe/CdSe$ core/shell nanocrystals,[35] and quantum-confined $Zn_{1-x}Mn_xSe$ nanocrystals,[37] all also measured in this same field and temperature range. The new measurements at higher magnetic fields presented here, however, reveal that the PL circular polarization actually reaches a maximum at around ~5 T (at ~1.65 K) before slowly decreasing again up to 55 T. This maximum in the circular polarization of Mn^{2+}-based PL has not

previously been observed in either bulk or nanocrystalline DMSs and is indicative of a departure from a simple spin-only description of the luminescent Mn^{2+} $^4T_1$ excited state. Detailed analysis shows that these magneto-PL data are consistent with the existence of a strong (static) Jahn-Teller splitting of the luminescent Mn^{2+} $^4T_1$ excited state. A microscopic model based on bulk electronic-structure parameters of Mn^{2+} successfully reproduces the essential features of the experimental Mn^{2+} magneto-PL temperature and magnetic-field dependence. This analysis provides new insights into the electronic structures of Mn^{2+} ions in both bulk and quantum-confined semiconductors.

2.2 Experimental

Colloidal $Zn_{1-x}Mn_xSe$/ZnS/CdS/ZnS NCs were synthesized as described previously.[25] Briefly, $Zn_{1-x}Mn_xSe$ nanocrystals were prepared via the thermal decomposition of $(Me_4N)_2[Zn_4(SePh)_{10}]$ in the presence of $MnCl_2 \cdot 4H_2O$.[30] ZnS and CdS shells were grown by sequential slow additions of zinc- or cadmium oleate and trioctylphosphine sulfide.[38, 39] The nanocrystals were characterized by electronic absorption spectroscopy, photoluminescence, TEM, EPR, MCD, and ICP-AES. Electronic absorption spectra are provided in the Supporting Information (Fig. S1). The sample discussed in the main text has a composition of $Zn_{0.9845}Mn_{0.0145}Se$/ZnS/CdS/ZnS, a core diameter $d \sim 3$ nm, an overall $d = 6$ nm, with $E_g = 2.8$ eV and an average of 4.5 Mn^{2+}/QD.

Magnetic circularly polarized luminescence (MCPL) measurements at fields up to 6 T were carried out in a superconducting magneto-optical cryostat (Cryo-Industries SMC–1659 OVT) with a variable-temperature sample compartment and detection in the Faraday configuration. Samples were prepared by drop-coating thin films of nanocrystals onto quartz substrates. Samples were checked for depolarization (a decrease in the retention of polarization purity of transmitted light due to strain or scattering, for example) by collecting the circular dichroism signal of a chiral reference solution (Ni^{2+} tartrate) placed before and after the sample. Approximately 10% depolarization was observed at all experimental temperatures (1.8 – 80 K). Photoluminescence excitation was provided by the linearly polarized 457.9 nm line of an Ar^+ ion laser (Spectra-Physics). Emitted light was passed through a quarter wave plate and linear polarizer to separate left and right circular polarizations, dispersed through a 0.5 m single monochromator (Acton), and detected using a liquid nitrogen cooled CCD (Princeton

Instruments). Polarization ratios are reported as $\Delta I/I = (I_L - I_R)/(I_L + I_R)$, where I_L and I_R are the intensities of left- and right-circularly polarized light following the sign convention of Peipho and Schatz,[40] as described in ref. [31].

High-magnetic-field MCPL measurements were performed at the National High Magnetic Field Laboratory using the 60 T Long Pulse magnet which is powered by a 1.4 GVA motor-generator.[41] The pulse duration is approximately 2.3 seconds, during which the field is swept up to peak field (55 T in these studies) as described by the pulse profile shown in Fig. S2. Approximately 1000 luminescence spectra are recorded during each pulse, and the corresponding instantaneous fields are measured by a dB/dt pick-up coil. Samples were prepared by drop-coating thin films of nanocrystals onto GaAs substrates. Samples were immersed directly into superfluid liquid helium for studies below 2K, or were mounted in a vacuum jacket filled with helium exchange gas for higher temperatures. Excitation was provided by a 405 nm diode laser (Coherent), and photons were coupled to and from the sample through a 600 μm diameter optical fiber. Polarization sensitivity was provided by a thin-film circular polarizer (optimized at 560 nm) sandwiched between the fiber and the sample. The collected PL was dispersed by a 0.3m spectrometer (Acton), and detected with a liquid nitrogen cooled CCD camera (Princeton Instruments).

2.3 Results and Analysis

2.3.A Experimental results. Figure 2.1A shows the magnetoluminescence spectra of colloidal $Zn_{0.9845}Mn_{0.0145}Se/ZnS/CdS/ZnS$ NCs measured at 1.8 K, resolved into left and right circular polarizations (I_L and I_R, respectively). The PL spectra are dominated by the Mn^{2+} $^4T_1 \rightarrow {}^6A_1$ internal transition at ~2.1 eV.[42] In an applied magnetic field, the PL is circularly polarized, consistent with previous measurements on bulk Mn^{2+}-doped ZnS and ZnSe single crystals,[36, 43] colloidal Mn^{2+}-doped ZnSe/CdSe nanocrystals,[35] and colloidal Mn^{2+}-doped ZnSe/ZnS NCs.[37] Although some studies have reported only minimally (≤ 6%) polarized emission from Mn^{2+} in nanowires[44, 45] and epitaxial $Zn_{1-x}Mn_xSe$ films,[35, 46] these experiments were all conducted on samples with Mn^{2+} concentrations greater than 6%, where reduction of observed MCPL due to dimers or larger clusters could be appreciable.[35, 37] The inset to Fig. 2.1A plots the magnetic field and temperature dependence of the MCPL polarization ratio [$\Delta I/I = (I_L - I_R)/(I_L + I_R)$] over the 0 – 6 T range. These data appear to saturate at a maximum of $(\Delta I/I)_{max} = -0.28$. Previous

investigations have found $|(\Delta I/I)_{max}|$ of approximately 0.4 (at 1.8 K, 4 T) for monomeric Mn^{2+} in ZnSe/CdSe[35] and ZnSe[37] nanocrystals, or 0.35 for dilute Mn^{2+} in bulk ZnS single crystals oriented with B||[111],[36] but $|(\Delta I/I)_{max}|$ is reduced by the presence of Mn^{2+}-Mn^{2+} dimers[35, 37] and by depolarization effects. As in ref. [35], the Mn^{2+} PL is not noticeably suppressed by the applied magnetic field, in contrast to the behavior observed in bulk crystals, nanowires, self-assembled QDs, and thin films.[43, 44, 47-49]

Figure 2.1B shows the intensities of left- and right-circularly polarized PL for these NCs at 1.65 K and plotted as a function of magnetic field up to 55 T. The difference in intensity between the two polarizations increases rapidly at fields up to 5 T and then decreases slightly as the field is increased to 55 T. Similar results were obtained for $Zn_{1-x}Mn_xSe$/ZnS/CdS/ZnS nanocrystals with a higher Mn^{2+} concentration (see Supporting Information).

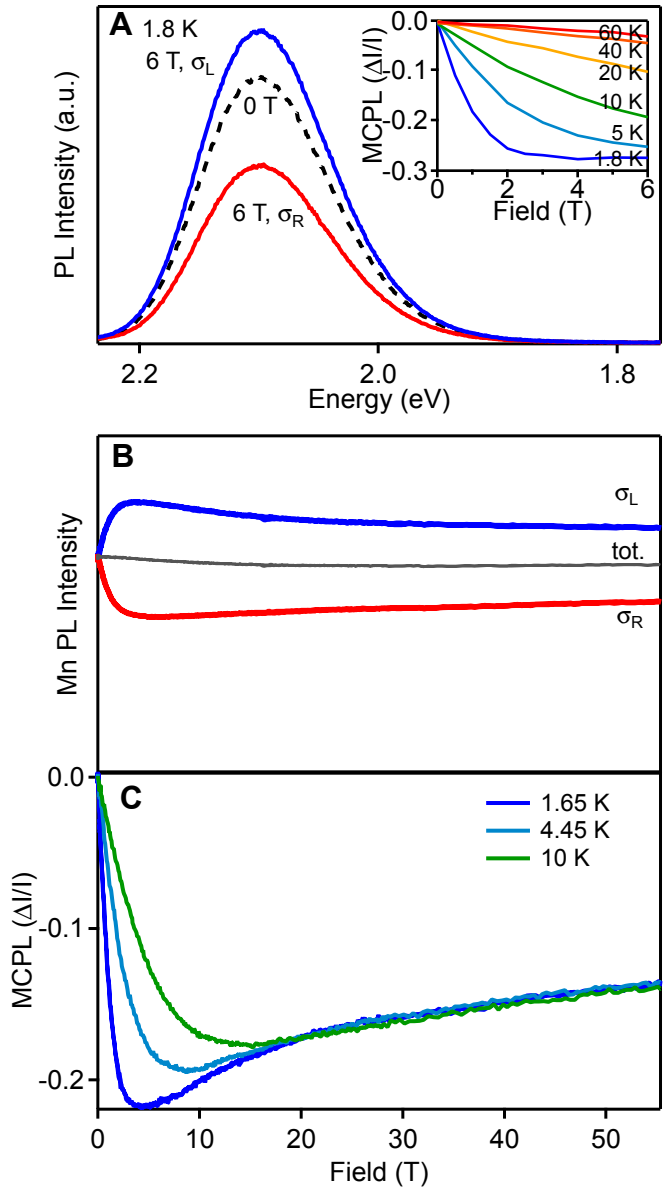

Figure 2.1. (A) Magnetic circularly polarized photoluminescence (MCPL) spectra of colloidal $Zn_{1-x}Mn_xSe/ZnS/CdS/ZnS$ quantum dots measured at 1.8 K. Inset: MCPL ratios ($\Delta I/I$) measured from 1.8 to 60 K and 0 to 6 T. **(B)** Intensities of circularly polarized Mn^{2+} PL and (**C**) the MCPL ratio ($\Delta I/I = (I_L - I_R)/(I_L + I_R)$) as a function of magnetic field, measured at 1.65 K. ($Zn_{0.9845}Mn_{0.0145}Se/ZnS/CdS/ZnS$ QDs, avg. 4.5 Mn^{2+}/QD, core d = 3 nm, d = 6 nm, E_g = 2.8 eV)

Figure 2.1C plots $\Delta I/I$ for these $Zn_{0.9845}Mn_{0.0145}Se/ZnS/CdS/ZnS$ nanocrystals as isotherms measured as a function of magnetic field up to 55 T. At 1.65 K, the $\Delta I/I$ reaches a

maximum of –0.22 at 4.5 T, before decreasing in magnitude gradually to -0.14 at 55 T. The quantitative discrepancy in MCPL polarization magnitudes between Figures 1A(inset) and 1C is attributable to depolarization effects. Depolarization does not affect the field dependence, and consequently these data are superimposable when scaled separately (see Supplementary Information). At 4.45 and 10 K, the MCPL polarization ratios plateau at ~9 T and ~15 T, respectively, and similarly decrease in magnitude with increasing fields. All three isotherms converge at ~18 T, indicating identical Boltzmann population distributions for all three temperatures at this field and above. The turnover in $\Delta I/I$ is inconsistent with a simple spin-only electronic structure of Mn^{2+} and implicates a splitting of the luminescent $^4T_1$ state even at zero magnetic field (see below).

Figure 2.2 plots the energies of the left (σ_L) and right (σ_R) circularly polarized luminescence maxima measured independently at 1.65 K vs magnetic field up to 55 T. The two components split rapidly between 0 and 10 T, and then more slowly at fields above 10 T. Over this entire range, the splitting never exceeds 1.2 meV, which it only reaches at 55 T. This value is much smaller than the splitting reported in ref. [35] for Mn-doped 'inverted' ZnSe/CdSe core/shell nanocrystals (6 meV at 6 T). In fact, the splittings that we observe in these $Zn_{1-x}Mn_xSe$/ZnS/CdS/ZnS nanocrystals are also smaller than expected from a simple cubic spin-only Zeeman splitting of the Mn^{2+} ground and excited states. In the simple model, the Zeeman splitting would increase linearly to 5.8 meV at 50 T (assuming $g = 2$ for both the ground and excited state with σ_R emission arising from a $|^4T_1,-3/2\rangle \rightarrow |^6A_1,-1/2\rangle$ transition and σ_L emission arising from a $|^4T_1,-3/2\rangle \rightarrow |^6A_1,-5/2\rangle$ transition). These magneto-PL results therefore merit a more detailed analysis.

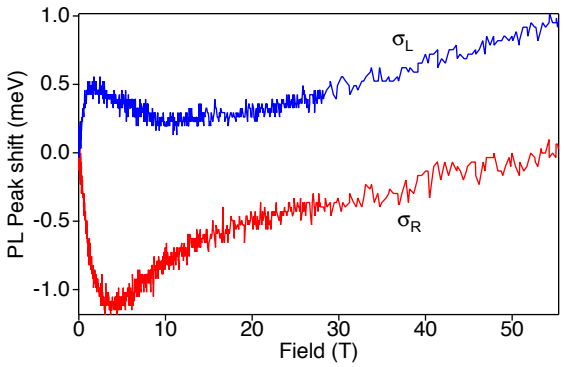

Figure 2.2. Magnetic field dependence of the energies of the left and right circularly polarized components of the Mn^{2+} photoluminescence from colloidal $Zn_{1-x}Mn_xSe/ZnS/CdS/ZnS$ nanocrystals, collected at 1.65 K. ($Zn_{0.9845}Mn_{0.0145}Se/ZnS/CdS/ZnS$ QDs, avg. 4.5 Mn^{2+}/QD, d = 6 nm, E_g = 2.8 eV)

2.3.B. A microscopic model. From ligand-field-theory, Mn^{2+} has a totally symmetric $^6A_1$ ground state and a $^4T_1$ term as the lowest-energy *d-d* excited state in cubic II-VI semiconductor lattices that provide weak tetrahedral fields, like ZnSe. The $^6A_1$ ground-state magnetization is quite well understood: Application of a magnetic field splits this state into six Zeeman components that can be readily probed, for example, by EPR spectroscopy. The EPR spectra of many $Zn_{1-x}Mn_xSe$ and related semiconductor nanocrystals have been reported, and all show $g \sim 2.00$, consistent with bulk $Zn_{1-x}Mn_xSe$.[50] Mn^{2+} EPR spectra are typically dominated by electron-nuclear hyperfine coupling involving the $I = 5/2$ Mn^{2+} nuclear spin, but additional fine structure can reveal very small second-order spin-orbit ("zero-field") splittings in axial lattices on the order of 10^{-5} meV.[51] The zero-field splitting of the $^6A_1$ ground state is thus small enough to be neglected in our model.

In contrast with the $^6A_1$ ground state, a thorough description of the Mn^{2+} $^4T_1$ ligand-field excited state requires explicit consideration of orbital angular momentum. Because this term possesses both spin and orbital angular momenta, it may be subject to strong first-order spin-orbit coupling. It also has a Jahn-Teller-active configuration ($d_e^3 d_{t2}^2$), and may therefore spontaneously distort the Mn^{2+} coordination geometry, thereby reducing the effects of spin-orbit coupling (the Ham effect).[52] Analysis of zero-phonon lines in absorption, luminescence, and PL excitation experiments on $Zn_{1-x}Mn_xSe$ single crystals indicates that first-order spin-orbit coupling is effectively quenched by strong Jahn-Teller coupling.[53, 54] Uniaxial stress experiments on the same crystals demonstrate that this quenching involves strong coupling to an *e* mode (and

relatively weak t_2 coupling).[54, 55] The splitting from the Jahn-Teller distortion and remaining second-order spin-orbit coupling will ultimately determine the characteristics of the Mn^{2+} magneto-PL.

Figure 2.3 illustrates the various splittings that define the luminescent excited state of Mn^{2+} in II-VI semiconductors. The ^4G free-ion term is split by the tetrahedral field to yield a $^4T_1$ term lowest in energy above the ground $^6A_1$ state. The *e*-mode Jahn-Teller distortion described above splits the $^4T_1$ state into ^4E and $^4A_2$ components separated by $3E_{JT}$. E_{JT} has been estimated for Mn^{2+} in ZnSe to be at least 18.6 meV,[56] but has not been definitively measured, and covalency effects have not been quantitatively accounted for.[57] In this strongly distorted excited state, first-order spin-orbit coupling is negligible. Second-order spin-orbit coupling (H_{SO}) further splits the $^4A_2$ term into two Kramers doublets ($m_s = \pm 1/2, \pm 3/2$), separated by $2D = -1.43$ meV as determined by high-resolution photoluminescence excitation scans on $Zn_{1-x}Mn_xSe$ single crystals.[56] The sign of D was determined from analysis of the Zeeman splittings of zero-phonon lines in very high quality $Zn_{1-x}Mn_xS$ single crystals.[57] Finally, application of a magnetic field lifts the Kramers degeneracies of these doublets. These spin-orbit and Zeeman splittings are described by equation 2.1.

$$H_{eff} = H_{SO} + H_{Zeeman} = D(\hat{S}_z^2 - \tfrac{1}{3}S(S+1)) + \mu_B g B(\hat{S}_z \cos\theta + \tfrac{1}{2}(\hat{S}_+ + \hat{S}_-)\sin\theta) \qquad [2.1]$$

The first term of this Hamiltonian accounts for the zero-field splitting of the $^4A_2$ term, and the second term describes the effects of the magnetic field (Zeeman splitting). $\hat{S}_z$, $\hat{S}_+$, and $\hat{S}_-$ are spin operators, $S = 3/2$ is the spin of Mn^{2+} in its quartet excited state, μ_B is the Bohr magneton, B is the applied magnetic field, and θ is the angle between the magnetic field and Jahn-Teller distortion axes. For initial calculations, the excited-state g value for Mn^{2+} is assumed to be 2.00 (see below).

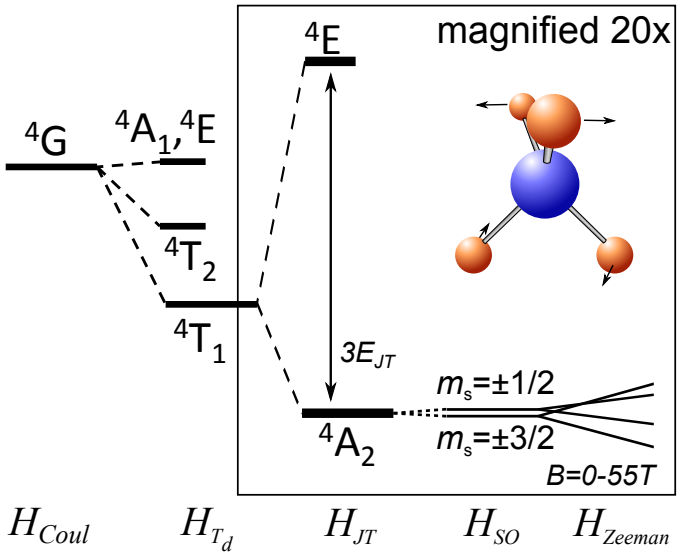

Figure 2.3. Splitting of the lowest excited Mn^{2+} free-ion term (^4G) by the actions of a tetrahedral ligand field (H_{Td}), a strong D_{2d} Jahn-Teller distortion (H_{JT}), second-order spin-orbit coupling (H_{SO}), and a Zeeman interaction with a magnetic field along the z-axis (H_{Zeeman}). Splittings are drawn to scale, with E_{JT} = 18.6 meV and the spin-orbit splitting of $2D$ = –1.43 meV taken from ref. [56]. One potential e-type distortion from T_d to D_{2d} is illustrated in the inset.

The splitting $3E_{JT}$ is sufficiently large to use just the two doublets of the $^4A_2$ state as our basis set for implementation of eq 2.1. In this case, the spin-orbit interaction is simply described by a diagonal matrix with values of H_{SO} along the diagonal, and H_{Zeeman} takes the form of a constant multiplied by the J = 3/2 spin matrices. Solving eq 2.1 as a function of B and θ produces eigenfunctions that are linear combinations of the four $^4A_2$ Zeeman components. For the diagonal eigenvectors, transition probabilities for emission of left- and right-circularly polarized light ($\Delta m_s = \pm 1$) in the $^4A_2 \rightarrow {}^6A_1$ transition are described by the squares of the matrix elements of Table 2.1. These matrix elements were calculated following the procedure outlined in ref. [58], and give the same relative intensities as those calculated by Clebsch-Gordan decomposition and those reported in ref. [36]. These coefficients can then be used to construct the transition probabilities for any mixed excited-state wavefunction.

Table 2.1. Matrix elements describing the relative transition probabilities for transitions between Zeeman sublevels of the $^4A_2$ excited state and $^6A_1$ ground state of Jahn-Teller distorted Mn^{2+} as illustrated in Fig. 2.3. In the sign convention used here, σ_R luminescence arises from $\Delta m_s = +1$ components of the $^4A_2 \rightarrow {}^6A_1$ transition.

m_s $^4A_2$ \ m_s $^6A_1$	5/2	3/2	1/2	–1/2	–3/2	–5/2
3/2	$-\sqrt{1/3}$		$\sqrt{1/30}$			
1/2		$-\sqrt{1/5}$		$\sqrt{1/10}$		
–1/2			$-\sqrt{1/10}$		$\sqrt{1/5}$	
–3/2				$-\sqrt{1/30}$		$\sqrt{1/3}$
					$\nwarrow \sigma_R$	$\nwarrow \sigma_L$

The Boltzmann population of each excited state was calculated under the assumption that the excited-state lifetime (τ_{Lum} = 379 μs, 7.5 K) is significantly longer than the spin-lattice relaxation time; an assumption supported by time-resolved MCPL measurements on $Zn_{1-x}Mn_xSe$ NCs.[37] Finally, detection of the polarized luminescence in a coordinate frame rotated from the crystal axes requires application of the Wigner D matrix, which effectively mixes the spin basis functions.[59, 60] Because all experimental observations were performed in the Faraday configuration (with the field axis parallel to the observation axis), the same angles describe both the Zeeman and detection rotations. To simulate the experimental observations on an ensemble of randomly oriented QDs, transition probabilities for each excited-state eigenfunction were multiplied by the corresponding Boltzmann populations at a given temperature, polarization ratios were calculated, and the results were averaged over all relative orientations of the Jahn-Teller and observation axes. More detailed descriptions of the calculations are provided as Supplementary Information.

2.3.C Calculated results. Figure 2.4A shows eigenvalues of equation 2.1 calculated as a function of magnetic field from 0 to 20 T relative to the zero-field energy of the $m_s = \pm 3/2$ doublet. For $\theta = 0$, the application of a magnetic field does not mix the states, and the Zeeman

sublevels split linearly with field. At $\theta = \pi/2$ (B||[110]) or 0.955 (B||[111]), fields at which the θ = 0 Zeeman levels crossed become avoided crossings because of mixing of the original basis functions. By 20 T, the eigenfunctions are nearly re-diagonalized and the field-induced energy changes are approximately linear again. Even after this re-diagonalization, the zero-field splitting energy influences the energies of the Zeeman levels, resulting in angle-dependent energies even at high fields.

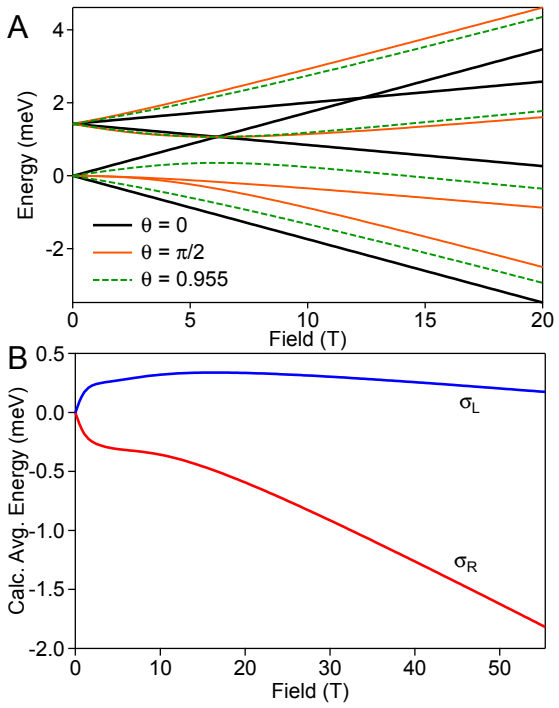

Figure 2.4. (A) Calculated Zeeman splittings of the zero-field-split $^4A_2(^4T_1)$ term, plotted as a function of magnetic field up to 20 T for three representative angles between the field and Jahn-Teller axes: $\theta = 0$, $\pi/2$, and 0.955. **(B)** Calculated σ_R and σ_L emission energies at 1.65 K plotted as a function of magnetic field up to 55 T. See text for details.

Figure 2.4B plots σ_R and σ_L emission energies calculated from the microscopic model described above, relative to the zero-field emission energy. These curves represent average energies of the pure electronic transitions from the various $^4A_2$ Zeeman components (*e.g.*, Fig. 2.4A), weighted by their relative transition probabilities (Table 2.1) and Boltzmann populations and averaged over all orientations. The calculated field dependence of the emission energies reproduces many of the key features of the experimental data in Fig. 2.2: At low field, the energies split rapidly until approximately 1.5 T, at which point they plateau until ~10 T, where

there is a change in curvature until the field dependence becomes approximately linear again at B > ~20 T. These changes in curvature are associated with the avoided crossings of Fig. 2.4A. At the maximum experimental field of 55 T, an energy difference of 1.9 meV is calculated, closely reproducing the experimental splitting of 1.2 meV. The relatively minor differences between experimental and calculated curves are attributed to higher-order effects neglected in this model.

Figure 2.5 shows the MCPL polarization ratios predicted by the model, superimposed upon the experimental MCPL data up to 55 T. The model reproduces the key features of the data very well, accurately predicting both the curvature of each isotherm and the temperature dependence of the entire data set. This excellent agreement with no floating parameters validates the electronic structure description illustrated in Fig. 2.3. Although the calculations appear to overestimate the MCPL magnitude by a factor of ~2, this quantitative discrepancy likely arises from a combination of sample depolarization (suggested by the polarization discrepancies between Figs. 1A (inset) and 1C) and concentration effects in this particular measurement, as discussed above. The model also agrees well with other measurements of related bulk[36] and QD[35, 37] samples, which show a maximum MCPL magnitude of $|(\Delta I/I)_{max}| \sim 0.4$ in the low-Mn^{2+}-concentration limit. We note that the sign of the MCPL ratio predicted from the relative dipole strengths given in Table 2.1 is the opposite of that observed experimentally. This discrepancy is not understood, but is not believed to be trivial in origin. For example, experimental sign conventions may at times be inverted, but previous MCPL measurements on bulk $Zn_{1-x}Mn_xS$ single crystals[36] and bulk-like $Zn_{1-x}Mn_xSe$ nanocrystals (in our laboratories, not shown) also show more intense σ_R emission, ruling out an influence of quantum confinement.

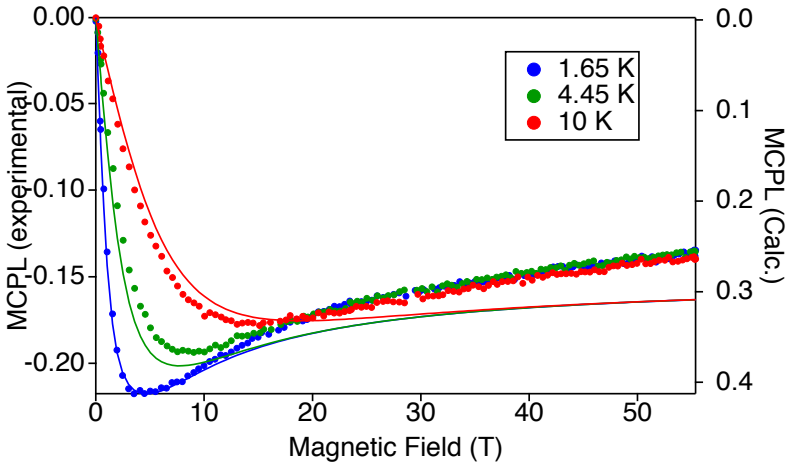

Figure 2.5. Experimental (points, left axis) and calculated (curves, right axis) MCPL polarization ratios ($\Delta I/I$) up to 55 T at 1.65, 4.45, and 10 K.

A striking feature of the MCPL data is that the magnitude of $\Delta I/I$ decreases after reaching its maximum value, wheras a simple spin-only paramagnet would show saturation. This decrease in polarization has not been previously noted, likely because no MCPL experiments on similar systems have been reported at sufficiently high magnetic fields. Furthermore, MCPL experiments on bulk crystals and epitaxial QDs are made more difficult by field-induced suppression of Mn^{2+} sensitization.[35, 43, 44, 47-49] The model successfully predicts this decrease in polarization ratio at high fields. Inspection of the calculated results shows that this decrease originates from the off-diagonal terms in the Zeeman matrix, *i.e.*, the evolution of the excited-state wavefunctions with applied magnetic field, illustrated in Fig. 2.4A. Moreover, the very existence of this MCPL turnover derives from the existence of a zero-field splitting within the emissive $^4A_2(^4T_1)$ term. Specifically, it stems from the energetic proximity of the $m_s = \pm 1/2$ and $m_s = \pm 3/2$ doublets ($2D$ = -1.43 meV). Our simulations show that increasing D isolates the $m_s = \pm 3/2$ doublet and suppresses the downturn in $\Delta I/I$ vs B. The field at which the maximum polarization is initially reached is only minimally sensitive to D (see Supplementary Information).

The static Jahn-Teller model used here predicts a slightly smaller decrease of $\Delta I/I$ at high fields than is observed experimentally. This discrepancy comes from restriction of this model to just Zeeman interactions within the $^4A_2$ term. This approximation is adequate at relatively small fields (0 - 6 T) because the $^4A_2$ term is reasonably well isolated from the nearest other state ($^4E(^4T_1)$, Fig. 2.3). At very large magnetic fields, however, second-order Zeeman contributions

from the ^4E term (and possibly even higher states) become more evident in the data. Similar interactions with higher-energy terms have been addressed explicitly in other related cases, for example in determination of g values within the $^4T_2$ ground term of octahedral Co^{2+} ions.[61] Expansion of the model to explicitly include all 12 sub-states of the parent $^4T_1$ would undoubtedly improve the simulations at very large magnetic fields but it would not significantly improve our understanding of the data and is challenging due to the difficulty of calculating the relative dipole strengths; such calculations were therefore not pursued.

Overall, the four-state static Jahn-Teller distortion model used here accurately predicts the excited-state magnetization of $Zn_{1-x}Mn_xSe$/ZnS/CdS/ZnS nanocrystals, and hence accurately accounts for the zero-field fine structure and the Zeeman splittings of the luminescent excited state. The model successfully predicts the occurrence of a polarization maximum at ~5 T in the low-temperature MCPL data. In particular, the field at which this maximum occurs is very sensitive to the excited-state g value, and confirms an excited-state g value of 2.0. Somewhat unexpectedly, our calculations additionally demonstrate that the data are adequately modeled by an isotropic g value, despite the axial distortion of the Mn^{2+} (see Supplementary Information). Consistent with the modeling of zero-phonon lines in bulk $Zn_{1-x}Mn_xS$ single crystals,[57] this result suggests that second-order Zeeman energies are negligibly small under these experimental conditions. Further, this simple model neglects the effects of random strain in the crystal. Random strain may influence the orientation of the Jahn-Teller distortion axes, but it does so randomly over the ensemble of luminescent Mn^{2+} ions and hence is accounted for in the orientation averaging of the model. Minor discrepancies occur between the predictions of this model and the experimental results at very large magnetic fields that can be attributed to the breakdown of our assumption that the emissive $^4A_2(^4T_1)$ state is electronically isolated from other nearby *d-d* excited states of Mn^{2+}. A more complex analysis of these high-field data may possibly lead to refinement of the estimate of E_{JT} in these systems.

2.4 Discussion

The data and analysis presented here demonstrate that the excited-state Zeeman splittings of Mn^{2+} ions doped into quantum-confined semiconductor nanocrystals are described well using the mechanics of ligand field theory. Whereas the Mn^{2+} ground state possesses the full cubic symmetry of the Zn^{2+} cation site in ZnSe, the luminescent excited state of Mn^{2+} in ZnSe is

characterized by a strong axial Jahn-Teller distortion that quenches the first-order spin-orbit coupling of the parent $^4T_1$ term and places a zero-field-split $^4A_2$ term lowest in energy. The low-temperature luminescence comes from this excited state. Early measurements used a static Jahn-Teller distortion model to analyze the zero-phonon lines of Mn^{2+} luminescence in ZnS[62] and GaP[63] and achieved good quantitative agreement. Subsequent analyses invoked intermediate Jahn-Teller coupling strengths to explain small sub-wavenumber splittings within the two main zero phonon lines of the Mn^{2+} PL in high-quality ZnS crystals,[57] but the complexity of this model necessitated iterative fitting of several parameters. The high-magnetic-field experiments presented here provide qualitatively new data that allow testing of the static Jahn-Teller distortion model. The essential characteristics of the data that relate to the excited-state energy splittings are predicted well by this model, and hence are consistent with a static Jahn-Teller distortion in the luminescent Mn^{2+} excited state. Furthermore, these data provide evidence that the assumption of electronic isolation of the luminescent $^4A_2(^4T_1)$ term in the four-state model begins to break down at very high magnetic fields.

One outcome of these experiments is the observation that the MCPL data from these $Zn_{1-x}Mn_xSe$/ZnS/CdS/ZnS nanocrystals can be very well modeled using an excited-state *g* value of ~2.0 and the corresponding excited-state Zeeman energies. Indeed, the nanocrystal MCPL data reported here are very similar to those reported for bulk $Zn_{0.9999}Mn_{0.0001}S$,[36] which possesses no quantum confinement. This result indicates that quantum confinement does not impact the luminescence of Mn^{2+} in these doped quantum dots in a significant way.

At this stage, it is interesting to ask how, if at all, quantum confinement *might* influence the electronic structures of transition metal ions in semiconductor nanocrystals. On one hand, there is compelling evidence in the literature that the ligand-field excited state energies of 3*d* transition metal dopants are not strongly influenced by nanocrystal quantum confinement. For example, the $^4A_2 \rightarrow {}^4T_1(P)$ energies and band shapes in the MCD spectra of Co^{2+}-doped ZnSe quantum dots at various degrees of quantum confinement are indistinguishable.[64-66] On the other hand, quantum confinement alters the band-edge potentials of the host lattice, and hence the energies of donor- and acceptor-type charge-transfer transitions involving the transition-metal impurity ions. Quantum-confinement-dependent charge-transfer energies have been observed experimentally in $Zn_{1-x}Co_xSe$ and $Zn_{1-x}Co_xSe$/CdSe quantum dots.[65, 66] Charge-transfer excited-state energies relate to the covalencies of the 3*d* wavefunctions, which in turn play critical roles

in determining the intensities of *d-d* transitions[67] and the types and strengths of inter-center (dopant-carrier or dopant-dopant) magnetic exchange interactions.[68, 69] The fact that charge-transfer energies do shift with quantum confinement thus indicates that each of these electronic-structure characteristics must also change with quantum confinement to some extent, *via* the small admixture of charge-transfer configurations into the ligand-field states. Overall, the high similarity of Co^{2+} *d-d* spectra in QDs and bulk semiconductors argues against a dramatic impact of quantum confinement on the electronic structures of 3*d* impurity ions in QDs, supporting the conclusions drawn above from the analysis of quantum dot Mn^{2+} magneto-PL data.

2.5 Conclusion

The temperature and magnetic-field dependence of the Mn^{2+}-centered $^4T_1 \rightarrow {}^6A_1$ photoluminescence of $Zn_{1-x}Mn_xSe$/ZnS/CdS/ZnS QDs has been studied at cryogenic temperatures and in high magnetic fields up to 55 T. A microscopic model of the Mn^{2+} excited-state Zeeman splittings is presented that includes the effects of a static excited-state Jahn-Teller distortion. The data are modeled in terms of a strong excited-state Jahn-Teller coupling with an axial (*e* mode) distortion coordinate to yield an isolated zero-field-split $^4A_2(^4T_1)$ state as the luminescent excited state. Using only literature parameters from previous analyses of zero-phonon lines in bulk Mn^{2+}-doped II-VI semiconductors and no floating parameters, this model successfully reproduces the temperature and magnetic-field dependence of the Mn^{2+} magneto-PL from these QDs. Only at very high magnetic fields are there small deviations from the predictions of the static Jahn-Teller distortion model, and these can be attributed to field-induced mixing with nearby higher-energy Mn^{2+} excited states not included in the model. The success of this bulk static Jahn-Teller model in predicting the MCPL data reported here indicates that quantum confinement does not have a significant impact on the $Mn^{2\,4}T_1 \rightarrow {}^6A_1$ luminescence in these QDs.

2.6 References

1. Fundamentals of Phosphors. CRC Press: Boca Raton, 2006.
2. Ronda, C.; (Ed.), Luminescence: From Theory to Applications. Wiley-VCH: Weinheim, 2008.
3. Vlasenko, N. A.; Popkov, Y. A., Study Of Electroluminescence Of A Sublimated ZnS-Mn Phosphor. *Opt. Spektrosk.* 1960, **8**, 81-88.

4. Furdyna, J. K.; Kossut, J., Diluted Magnetic Semiconductors. Academic: N.Y., 1988; Vol. 25.
5. Kacman, P., Spin Interactions in Diluted Magnetic Semiconductors and Magnetic Semiconductor Structures. *Semicond. Sci. Technol.* 2001, **16**, R25-R39.
6. Awschalom, D. D.; (Ed.), Spin Electronics. Kluwer Academic Publishing: Boston, 2004.
7. Jonker, B. T.; Park, Y. D.; Bennett, B. R.; Cheong, H. D.; Kioseoglou, G.; Petrou, A., Robust Electrical Spin Injection into a Semiconductor Heterostructure. *Phys. Rev. B* 2000, **62**, 8180-8183.
8. Rüster, C.; Borzenko, T.; Gould, C.; Schmidt, G.; Molenkamp, L. W.; Liu, X.; Wojtowicz, T. H.; Furdyna, J. K.; Yu, Z. G.; Flatté, M. E., Very Large Magnetoresistance in Lateral Ferromagnetic (Ga,Mn)As Wires with Nanoconstrictions. *Phys. Rev. Lett.* 2003, **91**, 216602.
9. Bacher, G.; Schömig, H.; Scheibner, M.; Forchel, A.; Maksimov, A. A.; Chernenko, A. V.; Dorozhkin, P. S.; Kulakovskii, V. D.; Kennedy, T.; Reinecke, T. L., Spin–spin interaction in magnetic semiconductor quantum dots (review). *Physica E* 2005, **26**, 37–44.
10. Besombes, L.; Léger, Y.; Maingault, L.; Ferrand, D.; Mariette, H.; Cibert, J., Probing the Spin State of a Single Magnetic Ion in an Individual Quantum Dot. *Phys. Rev. Lett.* 2004, **93**, 207403.
11. Besombes, L.; Léger, Y.; Maingault, L.; Mariette, H., Spin properties of charged Mn-doped quantum dot. *J. Appl. Phys.* 2007, **101**, 081713.
12. Léger, Y.; Besombes, L.; Fernández-Rossier, J.; Maingault, L.; Mariette, H., Electrical Control of a Single Mn Atom in a Quantum Dot. *Phys. Rev. Lett.* 2006, **97**, 107401.
13. Léger, Y.; Besombes, L.; Maingault, L.; Ferrand, D.; Mariette, H., Geometrical Effects on the Optical Properties of Quantum Dots Doped with a Single Magnetic Atom. *Phys. Rev. Lett.* 2005, **95**, 047403.
14. Maingault, L.; Besombes, L.; Léger, Y.; Bougerol, C.; Mariette, H., Inserting one single Mn ion into a quantum dot. *Appl. Phys. Lett.* 2006, **89**, 193109.
15. Cerletti, V.; Coish, W. A.; Gywat, O.; Loss, D., Recipes for spin-based quantum computing. *Nanotechnology* 2005, **16**, R27-R49.
16. Koenraad, P. M.; Flatte, M. E., Single dopants in semiconductors. *Nat. Mater.* 2011, **10**, 91-100.
17. Beaulac, R.; Archer, P. I.; Ochsenbein, S. T.; Gamelin, D. R., Mn^{2+}-Doped CdSe Quantum Dots: New Inorganic Materials for Spin-Electronics and Spin-Photonics. *Adv. Funct. Mater.* 2008, **18**, 3873-3891.
18. Beaulac, R.; Ochsenbein, S. T.; Gamelin, D. R., Colloidal Transition-Metal-Doped Quantum Dots. In Semiconductor Quantum Dots, 2nd ed.; Klimov, V. I., Ed. CRC Press: 2010; pp 397-453.
19. Suyver, J. F.; Wuister, S. F.; Kelly, J. J.; Meijerink, A., Luminescence of nanocrystalline ZnSe:Mn2+. *Phys. Chem. Chem. Phys.* 2000, **2**, 5445-5448.
20. Pradhan, N.; Goorskey, D.; Thessing, J.; Peng, X., An Alternative of CdSe Nanocrystal Emitters: Pure and Tunable Impurity Emissions in ZnSe Nanocrystals. *J. Am. Chem. Soc.* 2005, **127**, 17586-17587.
21. Norris, D. J.; Yao, N.; Charnock, F. T.; Kennedy, T. A., High-Quality Manganese-Doped ZnSe Nanocrystals. *Nano Lett.* 2000, **1**, 3-7.

22. Bussian, D. A.; Crooker, S. A.; Yin, M.; Brynda, M.; Efros, A. L.; Klimov, V. I., Tunable magnetic exchange interactions in manganese-doped inverted core-shell ZnSe-CdSe nanocrystals. *Nat Mater* 2009, **8**, 35-40.
23. Irvine, S. E.; Staudt, T.; Rittweger, E.; Engelhardt, J.; Hell, S. W., Direct light-driven modulation of luminescence from Mn-doped ZnSe quantum dots. *Angew. Chem.* 2008, **47**, 2685-2688.
24. Vlaskin, V. A.; Janßen, N.; van Rijssel, J.; Beaulac, R.; Gamelin, D. R., Tunable Dual Emission in Doped Semiconductor Nanocrystals. *Nano Lett.* 2010, **10**, 3670–3674.
25. McLaurin, E. J.; Vlaskin, V. A.; Gamelin, D. R., Water-Soluble Dual-Emitting Nanocrystals for Ratiometric Optical Thermometry. *J Am Chem Soc* 2011, **133**, 14978-14980.
26. McLaurin, E. J.; Bradshaw, L. R.; Gamelin, D. R., Dual-Emitting Nanoscale Temperature Sensors. *Chem. Mater.* 2013, **25**, 1283-1292.
27. Erickson, C. S.; Bradshaw, L. R.; McDowall, S.; Gilbertson, J. D.; Gamelin, D. R.; Patrick, D. L., Zero-Reabsorption Doped-Nanocrystal Solar Concentrators. *ACS Nano* 2014, **8**, 3461-3467.
28. Bradshaw, L. R.; Knowles, K. E.; McDowall, S.; Gamelin, D. R., Nanocrystals for Luminescent Solar Concentrators. *Nano Lett.* 2015, In press (DOI: 10.1021/nl504510t).
29. Hoffman, D. M.; Meyer, B. K.; Ekimov, A. I.; Merkulov, I. A.; Efros, A. L.; Rosen, M.; Counio, G.; Gacoin, T.; Boilot, J.-P., Giant Internal Magnetic Fields in Mn Doped Nanocrystal Quantum Dots. *Sol. State Comm.* 2000, **114**, 547-550.
30. Archer, P. I.; Santangelo, S. A.; Gamelin, D. R., Direct observation of sp-d exchange interactions in colloidal Mn2+- and Co2+-doped CdSe quantum dots. *Nano Lett.* 2007, **7**, 1037-1043.
31. Beaulac, R.; Archer, P. I.; Liu, X.; Lee, S.; Mackay Salley, G.; Dobrowolska, M.; Furdyna, J. K.; Gamelin, D. R., Spin-Polarizable Excitonic Luminescence in Colloidal Mn2+-Doped CdSe Quantum Dots. *Nano Lett.* 2008, **8**, 1197-1201.
32. Fainblat, R.; Muckel, F.; Barrows, C. J.; Vlaskin, V. A.; Gamelin, D. R.; Bacher, G., Valence-Band Mixing Effects in the Upper-Excited-State Magneto-Optical Responses of Colloidal Mn2+-Doped CdSe Quantum Dots. *ACS Nano* 2014, **8**, 12669−12675.
33. Beaulac, R.; Schneider, L.; Archer, P. I.; Bacher, G.; Gamelin, D. R., Light-Induced Spontaneous Magnetization in Colloidal Doped Quantum Dots. *Science* 2009, **325**, 973–976.
34. Ochsenbein, S. T.; Feng, Y.; Whitaker, K. M.; Badaeva, E.; Liu, W. K.; Li, X.; Gamelin, D. R., Charge-Controlled Magnetism in Colloidal Doped Semiconductor Nanocrystals. *Nature Nanotechnology* 2009, **4**, 681–687.
35. Viswanatha, R.; Pietryga, J. M.; Klimov, V. I.; Crooker, S. A., Spin-Polarized Mn2+ Emission from Mn-Doped Colloidal Nanocrystals. *Phys. Rev. Lett.* 2011, **107**, 067402.
36. Fournier, D.; Boccara, A. C.; Rivoal, J. C., Magneto-Optical Study of the 4T1 State of Mn2+ in ZnS. *J. Phys. C Solid State* 1977, **10**, 113-121.
37. Bradshaw, L. R.; May, J. W.; Dempsey, J. L.; Li, X.; Gamelin, D. R., Ferromagnetic excited-state Mn2+ dimers in Zn1-xMnxSe quantum dots observed by time-resolved magnetophotoluminescence. *Phys. Rev. B* 2014, **89**, 115312.
38. Li, J. J.; Wang, Y. A.; Guo, W.; Keay, J. C.; Mishima, T. D.; Johnson, M. B.; Peng, X., Large-Scale Synthesis of Nearly Monodisperse CdSe/CdS Core/Shell Nanocrystals Using Air-Stable Reagents via Successive Ion Layer Adsorption and Reaction. *J. Am. Chem. Soc.* 2003, **125**, 12567-12575.

39. Chen, H. S.; Lo, B.; Hwang, J. Y.; Chang, G. Y.; Chen, C. M.; Tasi, S. J.; Wang, S. J. J., Colloidal ZnSe, ZnSe/ZnS, and ZnSe/ZnSeS quantum dots synthesized from ZnO. *J Phys Chem B* 2004, **108**, 17119-17123.
40. Piepho, S. B.; Schatz, P. N., Group Theory in Spectroscopy with Applications to Magnetic Circular Dichroism. Wiley-Interscience: New York, 1983.
41. Crooker, S.; Rickel, D.; Lyo, S.; Samarth, N.; Awschalom, D., Magnetic semiconductor quantum wells in high fields to 60 Tesla: Photoluminescence linewidth annealing at magnetization steps. *Phys. Rev. B* 1999, **60**, R2173.
42. Beaulac, R.; Archer, P. I.; Ochsenbein, S. T.; Gamelin, D. R., Mn2+-doped CdSe quantum dots: new inorganic materials for spin-electronics and spin-photonics. *Adv. Funct. Mater.* 2008, **18**, 3873-3891.
43. Abramishvili, V. G.; Komarov, A. V.; Ryabchenko, S. M.; Semenov, Y. G., Magnetic-Field Affected Luminescence of Mn2+ Ions in Zn(1-x)Mn(x)Se Compounds Under Resonance Excitation of Excitons. *Solid State Commun.* 1991, **78**, 1069-1072.
44. Cooley, B. J.; Clark, T. E.; Liu, B. Z.; Eichfeld, C. M.; Dickey, E. C.; Mohney, S. E.; Crooker, S. A.; Samarth, N., Growth of Magneto-optically Active (Zn,Mn)Se Nanowires. *Nano Lett.* 2009, **9**, 3142-3146.
45. Oh, E.; Choi, J. H.; Oh, D. K.; Park, J., Magnetophotoluminescence and energy-dependent circular polarization from CdMnS nanowires. *Appl. Phys. Lett.* 2008, **93**, 041911.
46. Lee, S.; Dobrowolska, M.; Furdyna, J. K., Effect of spin-dependent Mn2+ internal transitions in CdSe/Zn1-xMnxSe magnetic semiconductor quantum dot systems. *Phys. Rev. B* 2005, **72**, 075320.
47. Chernenko, A. V.; Brichkin, A. S.; Sobolev, N. A.; Carmo, M. C., Mechanisms of manganese-assisted non-radiative recombination in Cd(Mn)Se/Zn(Mn)Se quantum dots. *Journal of Physics: Condensed Matter* 2010, **22**, 355306.
48. Chernenko, A.; Dorozhkin, P.; Kulakovskii, V.; Brichkin, A.; Ivanov, S.; Toropov, A., Auger recombination of excitons in semimagnetic quantum dot structure in a magnetic field. *Phys. Rev. B* 2005, **72**.
49. Nawrocki, M.; Rubo, Y.; Lascaray, J.; Coquillat, D., Suppression of the Auger recombination due to spin polarization of excess carriers and Mn2+ ions in the semimagnetic semiconductor Cd0.95Mn0.05S. *Phys. Rev. B* 1995, **52**, R2241-R2244.
50. Beaulac, R.; Ochsenbein, S. T.; Gamelin, D. R., Colloidal Transition-Metal-Doped Quantum Dots. In Nanocrystal Quantum Dots, 2 ed.; Klimov, V. I., Ed. CRC Press: Boca Raton, FL, 2010; pp 397-453.
51. Kreissl, J.; Gehlhoff, W., EPR Investigations of ZnS:Mn and ZnSe:Mn) Single Crystals, Powders, Thin-Film Structures. *Phys. Stat. Sol. A* 1984, **81**, 701-707.
52. Ham, F. S., Dyanmical Jahn-Teller Effect in Paramagnetic Resonance Spectra - Orbital Reduction Factors and Partial Quenching of Spin-Orbit Interaction. *Phys Rev* 1965, **138**, 1727-&.
53. Parrot, R.; Naud, C.; Gendron, F., Structure of a ^{4}T_{2} level of Mn^{++} in tetrahedral symmetry, dynamical Jahn-Teller effect and selective intensity transfer. *Physical Review B* 1976, **13**, 3748-3763.
54. Parrot, R.; Blanchard, C., Effect of Uniaxial Stresses on the 4E Level of a 3d5 Ion in Tetrahedral Symmetry: Study of Mn2+ in ZnS. *Phys. Rev. B* 1972, **6**, 3992-4004.
55. Parrot, R.; Naud, C.; Gendron, F., Structure of a 4T2 level of Mn++ in tetrahedral symmetry, dynamical Jahn-Teller effect and selective intensity transfer. *Phys. Rev. B* 1976, **13**, 3748-3763.

56. Parrot, R.; Naud, C.; Porte, C.; Fournier, D.; Boccara, A. C.; Rivoal, J. C., Jahn-Teller Effect in Fluorescent Level of Mn++ in Znse and Zns. *Phys. Rev. B* 1978, **17**, 1057-1066.
57. Boulanger, D.; Parrot, R.; Pohl, U. W.; Litzenburger, B.; Gumlich, H.-E., Magnetic Field Effect and Dynamical Jahn-Teller Effect on a 4T1 Level of a d5 Ion Coupled to ε-Vibrational Modes. *Phys. Stat. Sol. B* 1999, **213**, 79-91.
58. L. Lohr Jr, L., Spin-forbidden electronic excitations in transition metal complexes. *Coordination Chemistry Reviews* 1972, **8**, 241-259.
59. Feynman, R. P.; Leighton, R. B.; Sands, M. L., The Feynman lectures on physics, Vol III. Addison-Wesley Pub. Co.: Reading, Mass., 1963.
60. Morrison, M. A.; Parker, G. A., A Guide to Rotations in Quantum Mechanics. *Aust. J. Phys* 1987, **40**, 465-497.
61. Abragam, A.; Pryce, M. H. L., The Theory of Paramagnetic Resonance in Hydrated Cobalt Salts. *Proc. R. Soc. Lond. A. Mat.* 1951, **206**, 173-191.
62. Koidl, P., Jahn-Teller Effect in 4t1(1) and 4t2(1) States of Tetrahedrally Coordinated Mn-2+. *Phys. Stat. Sol. B* 1976, **74**, 477-484.
63. Hofmann, G.; Anderson, F. G.; Weber, J., Jahn-Teller effect in the 4T1 state of Mn2+ in GaP. *Physical Review B* 1991, **43**, 9711-9719.
64. Norberg, N. S.; Gamelin, D. R., Giant Zeeman Effects in Colloidal Diluted Magnetic Semiconductor Quantum Dots with Homogeneous Dopant Speciation. *J. Appl. Phys.* 2005, **99**, 08M104.
65. Norberg, N. S.; Dalpian, G. M.; Chelikowsky, J. R.; Gamelin, D. R., Energetic Pinning of Magnetic Impurity Levels in Quantum Confined Semiconductor Nanocrystals. *Nano Lett.* 2006, **6**, 2887-2892.
66. Vlaskin, V. A.; Beaulac, R.; Gamelin, D. R., Dopant-Carrier Magnetic Exchange Coupling in Inverted Core/Shell Nanocrystals. *Nano Lett.* 2009, **9**, 4376-4382.
67. Ballhausen, C. J., Introduction to Ligand Field Theory. McGraw-Hill Book Company, Inc.: New York, 1962.
68. Weihe, H.; Güdel, H. U., Quantitative Interpretation of the Goodenough-Kanamori Rules: A Critical Analysis. *Inorg. Chem.* 1997, **36**, 3632-3639.
69. Beaulac, R.; Gamelin, D. R., Two-center formulation of Mn^{2+}-electron s-d exchange coupling in bulk and quantum-confined diluted magnetic semiconductors. *Phys. Rev. B* 2010, **82**, 224401.

Chapter 3. Ferromagnetic Excited-State Mn^{2+} Dimers in $Zn_{1-x}Mn_xSe$ Quantum Dots Observed by Time-Resolved Magneto-Photoluminescence

Abstract. Colloidal Mn^{2+}-doped semiconductor nanocrystals are solution processable analogs of classic phosphor and diluted magnetic semiconductor (DMS) materials with promising applications ranging from fluorescence microscopy to spintronic information processing. At doping levels of only a few cation mole percent, Mn^{2+} dimers form in appreciable concentration and cause shortened photoluminescence decay times and reduced luminescence circular polarization under applied magnetic fields. Here, we show that these differences allow the use of time-resolved magneto-photoluminescence measurements to investigate the magnetic properties of the luminescent dimer excited state in $Zn_{1-x}Mn_xSe$ nanocrystals. These measurements reveal that Mn^{2+}-Mn^{2+} dimers are coupled *ferromagnetically* in their luminescent excited state, in contrast with the *antiferromagnetic* coupling of their ground state. We find that Mn^{2+}-Mn^{2+} dimers also luminesce with much purer circular polarization than Mn^{2+} monomers under applied magnetic fields. These results are explained well by perturbation theory and density functional theory analyses of the microscopic orbital exchange interactions within the photoexcited Mn^{2+}-Mn^{2+} dimers. This discovery of photoswitchable dimer magnetism (from $S = 0$ to $S = 4$) with strong associated circularly polarized luminescence raises intriguing possibilities for optical spin manipulation in doped semiconductors. Reprinted with permission from: Bradshaw, L. R.; May, J. W.; Dempsey, J. L.; Li, X.; Gamelin, D. R., *Physical Review B* 2014, **89** (11), 115312.

3.1. Introduction

Mn^{2+}-doped semiconductors such as ZnSe or ZnS have been used as commercial phosphors for decades.[1-3] Doping Mn^{2+} into such semiconductors allows efficient sensitization of Mn^{2+}-centered $^4T_1 \rightarrow {}^6A_1$ *d-d* luminescence either through impact excitation of Mn^{2+} (electroluminescence) or via photoexcitation of the semiconductor followed by rapid energy localization at Mn^{2+}.[2, 4, 5] This localized *d-d* transition is formally spin forbidden, and is consequently characterized by radiative decay times of milliseconds to microseconds (depending on the lattice anion). Because of the small absorption oscillator strengths of this and the other *d-d* transitions of Mn^{2+}, these doped semiconductors are also largely transparent at sub-bandgap energies. Colloidal nanocrystals (NCs) of the same compositions enable unique applications of these classic phosphor materials in solution-processed light-emitting devices,[6-8] luminescent

solar concentrators,[9] or optical imaging experiments,[10] and have furthermore revealed entirely new luminescence phenomena including intrinsic exciton/Mn^{2+} dual emission not yet realized in other forms of these phosphors.[11] Finally, the magnetism of Mn^{2+} also imparts exceptional magneto-optical and magneto-electronic properties to the semiconductor, ultimately stemming from Mn^{2+}-carrier *sp-d* exchange interactions. These include giant Zeeman splittings of the semiconductor band edges and strong circularly polarized magneto-luminescence,[12, 13] motivating the development of photonic device structures that exploit the interplay between light and magnetism, such as spin-LEDs and spin-photonic transducers.[14-17]

In their ground states, nearest-neighbor Mn^{2+}-Mn^{2+} dimers in II-VI and III-V semiconductors are antiferromagnetically coupled and hence magnetically silent ($|^6A_1,^6A_1\rangle$, S = 0), reducing the magnetization[18, 19] and consequently the effective Mn^{2+} concentrations available for exchange interactions with free carriers.[19] Dimer formation is therefore generally detrimental to the desired magneto-electronics or magneto-optical materials performance. Recently, a decrease in circular polarization of Mn^{2+} *d-d* magneto-luminescence was reported at elevated Mn^{2+} concentrations in doped semiconductor nanocrystals, from which it was hypothesized that circularly polarized PL arises primarily from isolated Mn^{2+} ions.[12]

Essentially nothing is known about the excited-state magnetic properties of Mn^{2+}-Mn^{2+} dimers in II-VI semiconductors, even though the ground-state magnetic exchange coupling of such dimers has been studied extensively.[20-33] An understanding of dimer excited states is essential for evaluating how Mn^{2+} concentrations influence magneto-luminescence in this important class of materials, but the few relevant experimental results are either debated or inconclusive. In 1963, for example, McClure analyzed the energies of sharp absorption lines in the zero-phonon region of the monomer $^6A_1 \rightarrow {}^4E$ absorption of $Zn_{1-x}Mn_xS$ at high Mn^{2+} concentrations in terms of a dimer spin ladder ($|^6A_1,^6A_1\rangle \rightarrow |^4E,^6A_1\rangle$) and concluded a net ferromagnetic $|^4E,^6A_1\rangle$ excited-state exchange coupling,[20] but Langer and Ibuki later interpreted these sharp transitions as arising from phonon coupling, not magnetic exchange.[26] Subsequent time-gated PL measurements showed that some of these lines originate from dimers (with faster PL decay), and the transitions were assigned assuming the same antiferromagnetic coupling in this excited state as in the $|^6A_1,^6A_1\rangle$ ground state.[25]

Dimer formation can also affect intra-ion absorption and luminescence transition probabilities: The spin ladders generated by exchange coupling within transition-metal dimers

introduce new formally spin-allowed pair transitions that have increased absorption oscillator strengths and radiative decay rate constants. This intensity-gaining mechanism has been investigated widely among exchange-coupled ion pairs and is referred to as the Tanabe mechanism.[20, 34-37]

Here, we describe the use of time-resolved magneto-photoluminescence spectroscopy to study Mn^{2+} spins in colloidal $Zn_{1-x}Mn_xSe$ nanocrystals. We show that this technique allows Mn^{2+}-Mn^{2+} dimers to be resolved from Mn^{2+} monomers, based on their shorter dimer luminescence decay times arising from the Tanabe mechanism. This experiment thus allows dimer excited-state magneto-optical properties to be analyzed separately from those of Mn^{2+} monomers. Time-resolved measurements show that the magnetic circularly polarized photoluminescence (MCPL) of Mn^{2+}-Mn^{2+} dimers saturates at lower magnetic fields than that of monomers, in a manner only consistent with a high-spin, *i.e.*, *ferromagnetically* coupled ($S = 4$) dimer configuration. Additionally, these data reveal essentially complete (~100%) circular polarization in the dimer luminescence at magnetic saturation, in contrast with only ~40% polarization in Mn^{2+} monomer MCPL. This result is interpreted as resulting from a difference in the specific $\Delta m_s = \pm 1$ luminescence transitions available to the monomer and dimer excited states. Perturbation theory and DFT calculations suggest that this dimer ferromagnetic excited-state exchange coupling originates from the dominance of a single orbital superexchange pathway in the luminescent $|^4T_1, {}^6A_1\rangle$ excited state. These results resolve the 50-year-old question of Mn^{2+}-Mn^{2+} dimer excited-state exchange coupling in doped semiconductors, and point to new possibilities for optical spin manipulation in semiconductors of technological interest.

3.2. Experimental

3.2A. Nanocrystal synthesis and characterization.

$Zn_{1-x}Mn_xSe$ nanocrystals were synthesized by lyothermal degradation of the tetramer $[Zn_4(SePh)_{10}](Me_4N)_2$ in the presence of $MnCl_2$ and Se similar to previously published methods.[38] ZnS shells were grown on these cores by successive additions of zinc oleate and trioctylphosphine sulfide at 225 °C.[39, 40] All $Zn_{1-x}Mn_xSe$ core NCs had diameters of $d = 2.9$ - 3.1 nm, and the $Zn_{1-x}Mn_xSe$/ZnS core/shell NCs had $d = 3.7$ - 4.0 nm. Mn^{2+} concentrations were determined by inductively coupled plasma atomic emission spectroscopy. All of the core/shell nanocrystals made following these procedures showed similar absorption and PL spectra to those

reported here, and all had room-temperature PL quantum yields of ~40%. Additional synthesis and characterization details are provided as Supplemental Material.[41]

3.2.B. Spectroscopic measurements.

PL experiments were performed on partially evaporated films of NCs sandwiched between quartz plates. For magneto-optical measurements, samples were mounted in a superconducting magneto-optical cryostat with a variable-temperature sample compartment (Cryo-Industries SMC–1659 OVT or Oxford SM-2). Excitation was provided by a nitrogen-pumped dye laser operating at 360nm, 20Hz, with an 800ps pulse width. The laser output was coupled into a multimode fiber and then refocused onto the sample at an incident angle of ~10° relative to the magnetic field axis. PL was collected along the field axis and passed through a liquid crystal variable retardation plate (Meadowlark) set to $\lambda/4$ at the emission maximum followed by a linear polarizer to separate left and right circularly polarized components. The PL was then coupled into a fiber and passed to a monochromator equipped with a LN_2 cooled CCD and PMT detectors. PL decay kinetics were measured using a multi-channel scalar, averaging over several thousand laser pulses. Polarization ratios are reported in terms of left- and right-circularly polarized light intensities defined with the sign convention of Piepho and Schatz.[13] Because significant reductions in the MCPL ratios were noted for samples that depolarized or scattered light, all samples were checked for depolarization by measuring the circular dichroism signal from a chiral molecule placed before and after the sample prior to collection of MCPL data. All samples reported here showed depolarization of less than 10%. Nevertheless, we estimate uncertainties in absolute polarization ratios ($\Delta I/I$) of ~±0.07.

3.2.C. Computational methods.

Quasi-spherical $Zn_{86-n}Mn_nSe_{86}$ quantum dots were constructed using the bulk ZnSe zinc blende crystal structure with lattice parameter a = 5.6676 Å.[42] The effective diameters of the QDs are d ~ 2.2 nm, and in the absence of Mn^{2+} the QDs have C_{3v} symmetry. Pseudo-hydrogen atoms with nuclear charges of +1.5 and +0.5 were used to passivate uncompensated surface Zn^{2+} and Se^{2-} ions (dangling bonds) by formation of fully optimized Zn–H and Se–H bonds, according to the scheme described in recent literature,[43-45] leading to a well-defined bandgap and stable QD geometry. Dopants were introduced by substituting either one or two Zn^{2+} ions near the center of the QD with Mn^{2+} to form a monomer or a bridged Mn^{2+}–Se^{2-}–Mn^{2+} dimer, respectively.

Density functional theory (DFT) calculations were performed with the development version of the Gaussian program.[46] Full geometry optimizations of the doped QDs were performed in the ground and excited states for both the antiferromagnetic (AFM) and ferromagnetic (FM) dimer configurations. Energies and electronic structures were obtained by solving the Kohn-Sham equations self-consistently using the PBE1PBE hybrid functional potential[47-49] with the LANL2DZ basis set,[50, 51] in which core electrons are replaced by an effective core and only Zn^{2+} (4*s*, 3*d*, 4*p*), Se^{2-} (4*s*, 4*p*), Mn^{2+} (3*s*, 3*p*, 4*s*, 3*d*), and H (1*s*) atomic obitals are described with explicit basis functions. This computational scheme has been successful in describing the electronic structures of $Zn_{1-x}TM_xO$ (where TM = Co^{2+}, Mn^{2+}),[43, 52, 53] $Cd_{1-x}Mn_xS$,[54] and $Cd_{1-x}Mn_xSe$[55] nanocrystals. Convergence to the correct spin configuration was determined by analysis of the Mulliken spin density on each of the Mn^{2+} dopants. All molecular orbital plots were generated with an isosurface value of 0.035.

3.3. Results and Analysis

3.3.A. TR-MCPL data and simulations.

Figure 3.1A shows room-temperature electronic absorption and 1.7 K magneto-luminescence spectra of 1.5% (x = 0.015) $Zn_{1-x}Mn_xSe$/ZnS NCs (core d ~ 3 nm, shell thickness ~ 0.5 nm). The absorption spectrum is dominated by the ZnSe core, with a first excitonic absorption maximum at ~400 nm. Luminescence spectra of the same sample show only the sensitized Mn^{2+} $^4T_1 \rightarrow {}^6A_1$ *d-d* band centered at ~590 nm. At low temperatures and in the presence of a magnetic field, this Mn^{2+} PL is partially circularly polarized, with greater σ^- intensity than σ^+ intensity. There was no detectable Zeeman splitting of the $^4T_1$ band (<~1 meV at 1.7 K and 6 T, see Supplemental Materials[56]), and we were thus unable to confirm the recent report[12] of quantum-confinement-induced giant (5–10 meV) Zeeman splittings within the $^4T_1$ excited states of Mn^{2+} ions in quantum dots. $^4T_1$ Zeeman splittings of the magnitude proposed in ref 12 are not easily reconciled with the otherwise normal spectroscopic properties of Mn^{2+} ions in ZnSe QDs (PL decay time and energy, EPR g value, etc.) and with the notion that this luminescent excited state is highly localized at the Mn^{2+} center. The inset to Fig. 3.1A plots the MCPL polarization ratio ($\Delta I/I$, as defined in eq 1) vs applied magnetic field, measured at 1.7 K. $\Delta I/I$ increases rapidly with applied field before leveling off between ~3 and 6 T at a value of $\Delta I/I$

~ -0.30. This value of $\Delta I/I$ is essentially identical to that measured for the same luminescence in bulk $Zn_{1-x}Mn_xS$ single crystals.[57]

$$\Delta I/I = (I_+ - I_-)/(I_+ + I_-) \quad (3.1)$$

Figure 3.1B shows room-temperature PL decay traces measured for similar $Zn_{1-x}Mn_xSe/ZnS$ NCs containing various Mn^{2+} concentrations. At 0.1% Mn^{2+}, the PL decay is mono-exponential with a lifetime of τ = 790 µs. As the Mn^{2+} concentration increases to 3.5%, the decay accelerates and becomes multi-exponential. At 3.5% Mn^{2+}, the time required to decay to $1/e$ of the initial intensity is 240 µs.

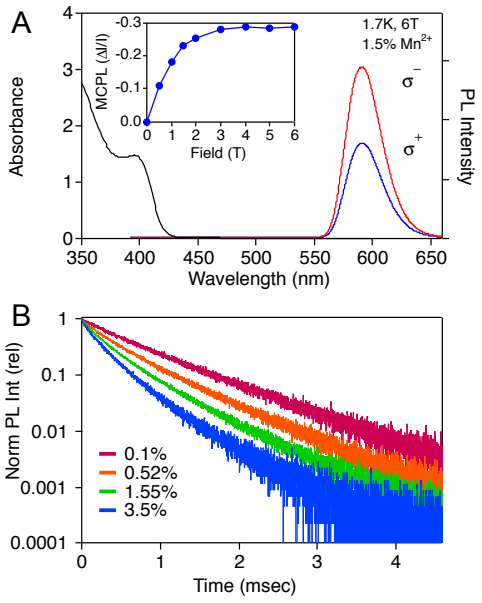

FIG 3.1. (A) Room-temperature absorption (left axis, black) and 1.7 K, 6 T magnetic circularly polarized luminescence spectra of 1.5% $Zn_{1-x}Mn_xSe/ZnS$ nanocrystals. Inset: Magnetic-field dependence of the MCPL ratio, $\Delta I/I$. **(B)** Room-temperature time-resolved PL traces for $Zn_{1-x}Mn_xSe/ZnS$ NCs with Mn^{2+} concentrations from 0.1 to 3.5% as indicated. All nanocrystals have core d ~ 3 nm and shell thickness ~ 0.5 nm.

Figure 3.2A plots decay traces for the 590 nm PL of 0.46% $Zn_{1-x}Mn_xSe/ZnS$ NCs, measured at 1.7 K in a 6 T magnetic field (Faraday geometry) and resolved into σ^+ and σ^- components. Both circular polarizations show mono-exponential decay with τ = 720 µs. Figure 3.2B shows PL decay traces measured for 3.5% $Zn_{1-x}Mn_xSe/ZnS$ NCs under the same conditions.

These decay traces are multi-exponential, but are both fit reasonably well to two exponentials with time constants of 750 μs and 160 μs. Unlike the traces in Fig. 3.2A, the σ^+ and σ^- decay traces of the 3.5% $Zn_{1-x}Mn_xSe/ZnS$ NCs do not overlay one another when normalized, a difference highlighted by plotting $\Delta I/I$ vs time as shown in Fig. 3.2C. For the 0.46% Mn^{2+} sample, $\Delta I/I$ is nearly constant at about -0.31. In contrast, the 3.5% Mn^{2+} NCs show a pronounced evolution of $\Delta I/I$ from ~-0.15 at short times to ~-0.31 at times longer than ~2 ms. The smaller $\Delta I/I$ at short times implicates a subset of luminescent Mn^{2+} ions that emit on a faster timescale with a less negative (or possibly even positive) polarization ratio. As detailed below, this subset can be identified as luminescent exchange-coupled Mn^{2+}-Mn^{2+} dimers. For quantitative analysis, we define the magnitude of the time-independent MCPL polarization (P_{TI}) as the long-time asymptote of $\Delta I/I$ (t > 2.5 ms, experimentally), and the magnitude of the time-dependent MCPL polarization (P_{TD}) as the difference between $\Delta I/I$ at t = 0 and P_{TI}, as described by eqs 2a and 2b. For the 3.5% Mn^{2+} sample of Fig. 3.2, P_{TI} = -0.30, P_{TD} = +0.15, and P_{TD}/P_{TI} = -0.50.

$$P_{TI} = \left(\frac{\Delta I}{I}\right)_{t\to\infty} \tag{3.2a}$$

$$P_{TD} = \left(\frac{\Delta I}{I}\right)_{t=0} - P_{TI} \tag{3.2b}$$

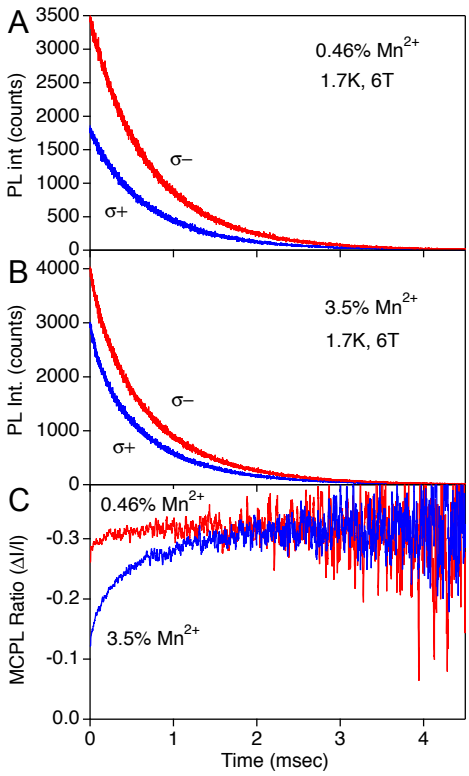

FIG 3.2. (color online) Time-resolved σ^+ and σ^- PL decay traces from **(A)** 0.46% and **(B)** 3.5% $Zn_{1-x}Mn_xSe/ZnS$ NCs (core d = 3nm, respectively), both measured at 1.7K, 6T in the Faraday geometry. **(C)** Time-resolved MCPL ($\Delta I/I$ vs t) traces for the same samples measured under the same conditions.

Figure 3.3 plots P_{TD}/P_{TI} vs Mn^{2+} concentration for a series of $Zn_{1-x}Mn_xSe/ZnS$ NCs. Increasing from the low-Mn^{2+} limit up to 3.5% Mn^{2+}, P_{TD}/P_{TI} grows sub-linearly from zero to ~-0.50. Figure 3.3 also plots CW (time-integrated) 1.7 K, 6 T MCPL ratios vs Mn^{2+} concentration for the same samples. $\Delta I/I$ decreases from about -0.30 at <1% Mn^{2+} to -0.20 at >3% Mn^{2+} (note the negative scale) roughly in proportion to P_{TD}/P_{TI}, but with substantially greater scatter among the data points. These trends are interpreted as reflecting dimer formation as Mn^{2+} concentrations increase. If Mn^{2+} were distributed statistically over the available ZnSe cation sites, the probability, D, of a given Mn^{2+} ion being part of an isolated nearest-neighbor Mn^{2+}-Mn^{2+} dimer would be roughly $D = 12x(1 - x)$[18].[58] Between 0 and 3.5% Mn^{2+}, D increases sub-linearly from zero to ~0.22. The solid line in Fig. 3.3 plots D vs Mn^{2+} concentration, scaled vertically to approximate the MCPL data. The curvature of D reproduces the experimental data well, supporting the conclusion that Mn^{2+}-Mn^{2+} dimer formation is responsible for these changes in time-dependent and CW MCPL signals with increasing Mn^{2+} concentration. As a corollary, the

agreement found in Fig. 3.3 suggests that the individual monomer and dimer MCPL polarization ratios are not significantly concentration dependent.

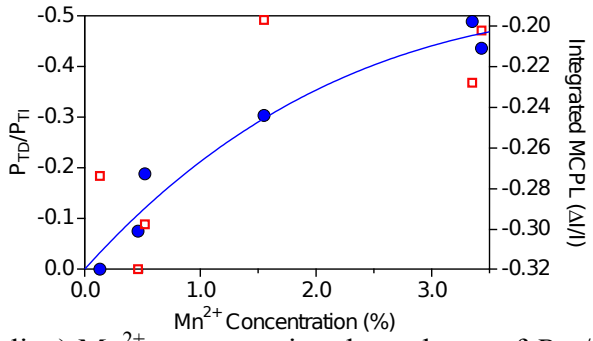

FIG 3.3. (color online) Mn^{2+} concentration dependence of P_{TD}/P_{TI} (left axis, blue circles) and time-integrated $\Delta I/I$ (right axis, red squares), measured at 1.7K and 6T. Note the negative axes. The solid curve plots the calculated probability that a Mn^{2+} ion is part of a nearest-neighbor dimer, scaled arbitrarily to overlay the data. The solid curve runs from zero at 0% Mn^{2+} to 0.22 at 3.5% Mn^{2+}.

To analyze the MCPL time dependence, we describe the time-dependence of $\Delta I/I$ as arising from a superposition of time-dependent monomer and dimer emission with static polarizations, as in eq 3.

$$\frac{\Delta I}{I}(t) = \frac{I_m(t)\cdot\left(\frac{\Delta I}{I}\right)_m + I_d(t)\cdot\left(\frac{\Delta I}{I}\right)_d}{I_m(t) + I_d(t)} \tag{3.3}$$

Here, $I_m(t)$ and $I_d(t)$ denote decaying luminescence intensities of monomers (m) and dimers (d), respectively, and $(\Delta I/I)_m$ and $(\Delta I/I)_d$ refer to the individual time-independent MCPL polarization ratios of each. Because photoexcited dimers decay faster than photoexcited monomers, $\Delta I/I(t)$ converges to $(\Delta I/I)_m$ at long times. Normalizing the total intensity at $t = 0$ and assuming crudely that all luminescence comes from either monomers or dimers ($I_m(0) + I_d(0) = 1$), eq 3 simplifies to eq 4 at $t = 0$.

$$\frac{\Delta I}{I}(0) = \left(1 - I_d(0)\right)\cdot\left(\frac{\Delta I}{I}\right)_m + I_d(0)\cdot\left(\frac{\Delta I}{I}\right)_d \tag{3.4}$$

The experimental quantities P_{TD} and P_{TI} can now be expressed in terms of these same parameters, as shown in eqs 5a and 5b.

$$P_{TI} = \left(\frac{\Delta I}{I}\right)_{t\to\infty} = \left(\frac{\Delta I}{I}\right)_m \tag{3.5a}$$

$$P_{TD} = \left(\frac{\Delta I}{I}\right)_{t=0} - P_{TI} = I_d(0)\left(\left(\frac{\Delta I}{I}\right)_d - \left(\frac{\Delta I}{I}\right)_m\right) \tag{3.5b}$$

P_{TD} (as well as P_{TD}/P_{TI}) is therefore directly proportional to $I_d(0)$ (the intensity of dimer emission at t = 0). Under the assumption that monomer and dimer MCPL ratios and relative quantum yields are concentration independent over this limited range of concentrations, $I_d(0)$ is proportional to D. Note also that $\left(\frac{\Delta I}{I}\right)_d - \left(\frac{\Delta I}{I}\right)_m$ is the only magnetic-field-dependent term in eq 5b. These equations now allow a quantitative analysis of the experimental TR-MCPL results.

Figure 3.4A plots the magnetic-field dependence of the TR-MCPL measured for the 0.52% Mn^{2+} sample from 0 to 4.5 T at 1.7 K. At zero magnetic field, $\Delta I/I(t) = 0$ at all times. As the field is applied, P_{TI} becomes progressively larger, eventually leveling off at ~ -0.38. This result is similar to that observed in the CW MCPL at small x and confirms assignment of the long-time MCPL to Mn^{2+} monomers. P_{TD} also becomes more pronounced with increasing magnetic field. Samples with 1.5% and 3.5% Mn^{2+} show similar trends. Figure 3.4B plots the magnetic-field dependence of P_{TD} and P_{TI} for the 0.52% Mn^{2+} sample, both normalized in the linear (Curie) region of the saturation magnetization. The dashed curves in Fig. 3.4B show 1.7 K, g = 2 Brillouin magnetization curves calculated using eq 6 for various hypothetical spin states, assuming g = 2.0. Here, μ_B is the Bohr magneton, k is the Boltzmann constant, and N is a scaling factor.

$$M(H) = \frac{1}{2} N g \mu_B \left[(2S+1)\cdot \coth\left((2S+1)\cdot \frac{g\mu_B H}{2kT} \right) - \coth\left(\frac{g\mu_B H}{2kT} \right) \right] \tag{3.6}$$

For comparison with the experimental data in Fig. 3.4B, these Brillouin curves have also been normalized at 0.25 T. Such normalization emphasizes the different curvatures of the saturation magnetization of different spin states, with the highest spin states saturating at the lowest magnetic fields and normalized magnetization magnitudes. When plotted in this way, the saturation value of P_{TI} is significantly greater than that for P_{TD}, suggesting that P_{TD} arises from a luminescent state with a greater net spin.[59] Specifically, the P_{TI} data resemble an S = 3/2 state,

consistent with this luminescence coming from the Mn^{2+} $^4T_1$ excited state, but the P_{TD} data most closely resemble the S = 4 Brillouin function. This analysis strongly suggests that dimers luminesce from a high-spin excited state.

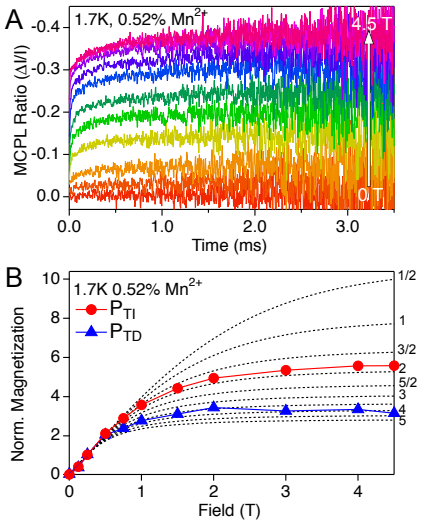

FIG 3.4. (color online) **(A)** Time-resolved MCPL of 0.52% $Zn_{1-x}Mn_xSe$/ZnS NCs, measured from 0 to 4.5 T at 1.7 K. **(B)** P_{TD} (blue triangle) and P_{TI} (red circle) values from the traces in (A) plotted vs applied magnetic field and normalized at 0.25 T. The dashed lines plot Brillouin magnetization functions calculated for S = 1/2 to 5 (g = 2, 1.7 K), also normalized at 0.25 T.

Equations 3-5 were used to simulate both the TR-MCPL and saturation magnetization data and the results are summarized in Fig. 3.5. Simulations of the 3.5% Mn^{2+} TR-MCPL data of Fig. 3.2B,C are described here because P_{TD} is most prominent in these data. Although the PL decay curves in Figs. 1 and 2 are non-exponential for this sample, the simulations were performed using the simplifying assumptions that (a) all monomers decay with the same exponential lifetime as measured in the lowest concentration sample (τ_m = 800 μs) and show the same MCPL ratio ($(\Delta I/I)_m$ = -0.32 at saturation, with S = 3/2 magnetization), and (b) all dimers also decay with the same single exponential lifetime. Thus, the model's variable parameters are dimer PL lifetime, the fraction of photons emitted from dimers, the dimer spin state (which was assumed to be ≤ 4), and $(\Delta I/I)_d$. As detailed below, the individual TR-MCPL decay curves alone could be simulated by many combinations of those four parameters, but their magnetic field dependence could only be reproduced with S = 4 and $(\Delta I/I)_d \sim +1.0$ at 4.5 T, *i.e.*, essentially

complete circular polarization, providing a unique set of viable simulation parameters for both experiments. With these parameters, photoexcited dimers account for ~5% of the total integrated PL for this sample and decay with τ_d = 300 μs.

The inset to Figure 3.5A plots σ^+- and σ^--polarized PL decay traces simulated using the above parameters, overlaid with the experimental data from Fig. 3.2B. The simulated σ^+ and σ^- PL decay traces reproduce the experimental data well. For illustration of the various monomer and dimer contributions, the main panel of Fig. 3.5A plots the four individual σ^+- and σ^--polarized PL decay traces calculated from these simulation parameters. Figure 3.5B plots the simulated TR-MCPL trace ($\Delta I/I(t)$ vs t) along with the experimental TR-MCPL data from Fig. 3.2C. The simulated TR-MCPL curve also agrees well with the experimental data. A noteworthy observation from this analysis is that the apparent decay time of P_{TD} (~600 μs) does not match the dimer decay time (τ_d = 300 μs), but rather is the weighted average of this and the monomer decay time, as described by eq 3.

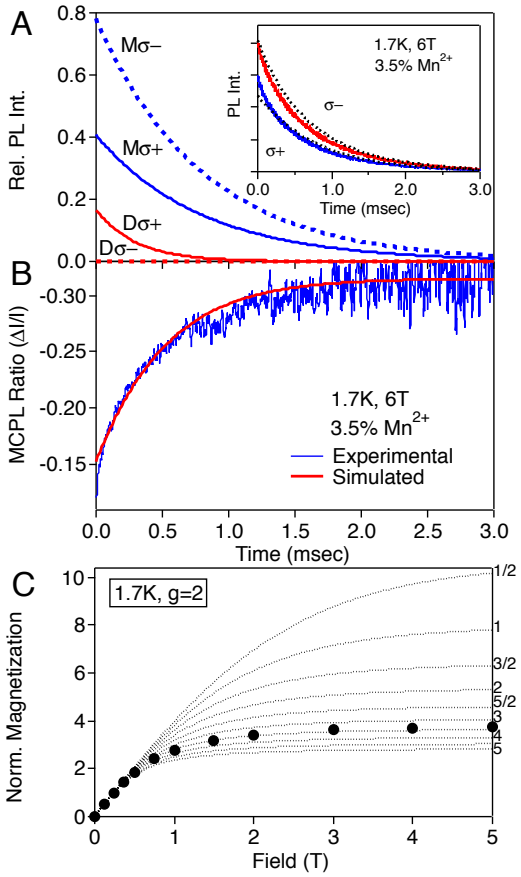

FIG 3.5. (color online) **(A)** Simulated circularly polarized PL decay curves for monomers (blue, τ_m = 800 µs, $(\Delta I/I)_m$ = -0.32) and dimers (red, τ_d = 300 µs, $(\Delta I/I)_d$ = +1.00). σ^- and σ^+ components are shown as dashed and solid lines, respectively. The integrated dimer PL accounts for 5% of the overall PL in this simulation. Inset: The simulated summed σ^- and σ^+ PL intensities overlaid with the experimental data from Fig. 3.2B. **(B)** The simulated MCPL ratio from (A) as a function of time (solid red line), overlaid with the experimental data from Fig. 3.2C. **(C)** Simulated magnetic field dependence of P_{TD} obtained by scaling the monomer and dimer MCPL polarization ratios by the S = 3/2 and S = 4 Brillouin functions, respectively.

Figure 3.5C plots the simulated magnetic field dependence of P_{TD}, for comparison with the experimental data in Fig. 3.4B. As noted in the discussion of eq 5b, the field dependence of P_{TD} is only sensitive to the values of S and $(\Delta I/I)$, and not to emission intensities or lifetimes. Because S_m and $(\Delta I/I)_m$ are known from the low-concentration limit, S_d and $(\Delta I/I)_d$ are the only unknown parameters. To simulate the TR-MCPL magnetic field dependence, 1.7 K monomer and dimer TR-MCPL traces were calculated for each magnetic field by scaling $(\Delta I/I)_m$ and $(\Delta I/I)_d$

at each field by their respective Brillouin magnetization functions (eq 6, S_m = 3/2 and $S_d \leq 4$). From these simulated traces, P_{TD} was then determined at each field by the same methods used to analyze the experimental TR-MCPL data, and the resulting curve was normalized at 0.25 T as in Fig. 3.4. The experimental data could only be reproduced with S_d = 4 and $(\Delta I/I)_d \sim +1.0$. This dimer MCPL ratio in turn defines a unique set of simulation parameters for the full model, necessitating that dimers account for ~5% of the total integrated PL. This fraction is smaller than $D \sim 22\%$ based on Mn^{2+} concentration, a difference that could have many origins including poorer sensitization or smaller PL quantum yields for the dimers.

3.3.B. Interpretation of the sign and purity of the dimer MCPL.

From the simulations summarized in Fig. 3.5, the magnetic-field dependence of P_{TD} implies that dimer MCPL is ~100% circularly polarized, with the opposite sign of the monomer MCPL. Figure 3.6 illustrates the proposed origin of this purely σ^+ polarization schematically. Assuming a cubic spin-only picture for illustrative purposes, magnetized monomers at low temperatures luminesce from only the m_s = -3/2 Zeeman component of the $^4T_1$ excited state. In the Faraday geometry, only transitions with $\Delta m_s = \pm 1$ are allowed, yielding right (σ^+) and left (σ^-) circularly polarized luminescence respectively. The monomer MCPL ratio is therefore defined by the relative probabilities of the m_s = -3/2 → -5/2 (σ^-) and m_s = -3/2 → -1/2 (σ^+) transitions, which are different for non-trivial reasons.[57] In exchange-coupled Mn^{2+}-Mn^{2+} dimers, however, the total luminescence is dominated by spin-allowed (ΔS = 0) components of the dimer spin ladder, as per the Tanabe mechanism. As illustrated in Fig. 3.6, luminescence from a ferromagnetically coupled (S = 4) dimer excited state is thus dominated by transitions to the S = 4 dimer ground state. From Fig. 3.6, MCPL from the fully magnetized S = 4 dimer excited state originates from the m_s = -4 Zeeman sublevel and can only occur with Δm_s = +1, because no Δm_s = -1 transition to the S = 4 ground state is available (*i.e.*, no m_s = -5 component of this state exists). Therefore, to the extent that the overall PL is dominated by the ΔS = 0 dimer transition, the MCPL from coupled Mn^{2+}-Mn^{2+} dimers is purely σ^+ circularly polarized. Although Jahn-Teller distortions and spin-orbit coupling undoubtedly make the actual luminescent excited states of both monomers and dimers more complicated than illustrated in Fig. 3.6, these spin-only pictures capture the essence of the experimental observations.

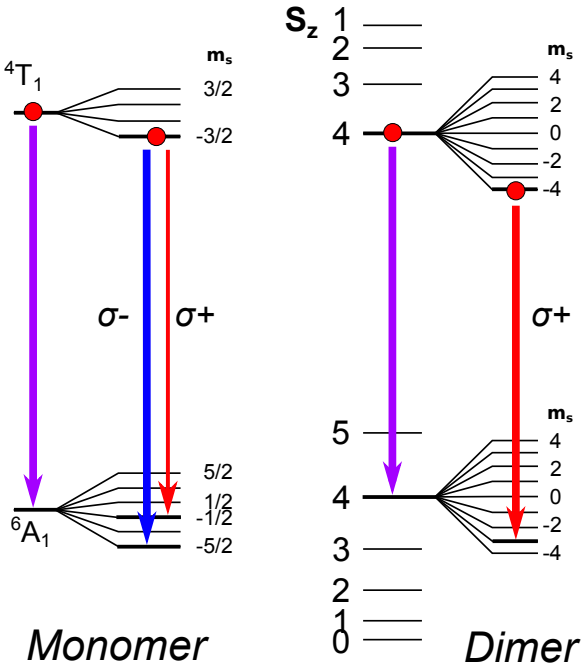

FIG 3.6. (color online) Schematic depictions of the transitions defining MCPL ratios for monomers and dimers in $Zn_{1-x}Mn_xSe$ and related systems in the spin-only limit. In monomers (left), MCPL is determined by the relative transition moment probabilities of $\Delta m_s = -1$(σ-, blue arrow) and $\Delta m_s = +1$(σ+, red arrow). In dimers (right), the ground-state is antiferromagnetically coupled and the luminescent excited state is ferromagnetically coupled. The dimer luminescence intensity is dominated by the spin-allowed $\Delta S = 0$ transition. In the dimer MCPL, only the $\Delta m_s = +1$(σ+) component of this transition conserves angular momentum, leading to 100% circular polarization with the opposite sign as in the monomers. Splittings are not to scale.

3.3.C. Interpretation of the sign of Mn^{2+}-Mn^{2+} excited-state superexchange coupling.

The change in sign of the Mn^{2+}-Mn^{2+} dimer magnetic-exchange coupling constant upon photoexcitation can be understood by evaluating the available microscopic superexchange pathways in the dimer ground and excited states. Figure 3.7A illustrates the *d* electrons of two coupled tetrahedral Mn^{2+} ions schematically. When both Mn^{2+} ions are in their $^6A_1$ ground states ($|^6A_1,^6A_1\rangle$), all five *d* orbitals of each ion are singly occupied. In this configuration, Pauli exclusion dictates that partial spin transfer from one Mn^{2+} to the other can only occur if the electrons on each Mn^{2+} have the opposite spin, *i.e.*, only antiferromagnetic superexchange pathways exist. In the luminescent $|^4T_1,^6A_1\rangle$ excited state of the dimer, however, one of the Mn^{2+} ions has an $e^3t_2^2$ configuration involving an unoccupied t_2 orbital and a doubly occupied *e* orbital. Spin transfer from a half-full to an empty t_2 orbital favors net parallel (ferromagnetic) alignment of the Mn^{2+} spins, as illustrated by the thick blue arrow in Figure 3.7A for the $|^4T_1,^6A_1\rangle$ dimer

excited state. Similarly, spin transfer from the doubly occupied *e* orbital to a half occupied orbital on the other Mn^{2+} (thin blue arrow in Figure 3.7A) also favors parallel spin alignment, but at this stage, *e*-based pathways are neglected for simplicity under the assumption that their interactions are much weaker. At the same time, other antiferromagnetic pathways similar to those of the dimer ground state may still exist (dashed arrows in Fig. 3.7A). Because ferromagnetic and antiferromagnetic pathways are both available in the $|^4T_1,^6A_1\rangle$ dimer excited state, the sign of the overall exchange coupling constant depends on the relative strengths of the active exchange pathways, which in turn primarily reflect overlap of the pertinent *d* orbitals with the valence orbitals of the bridging selenide. From the observation of net ferromagnetic Mn^{2+}-Mn^{2+} coupling in the luminescent dimer excited state, we conclude that the empty t_2 orbital must have substantial overlap with the bridging Se^{2-} mediating the superexchange.

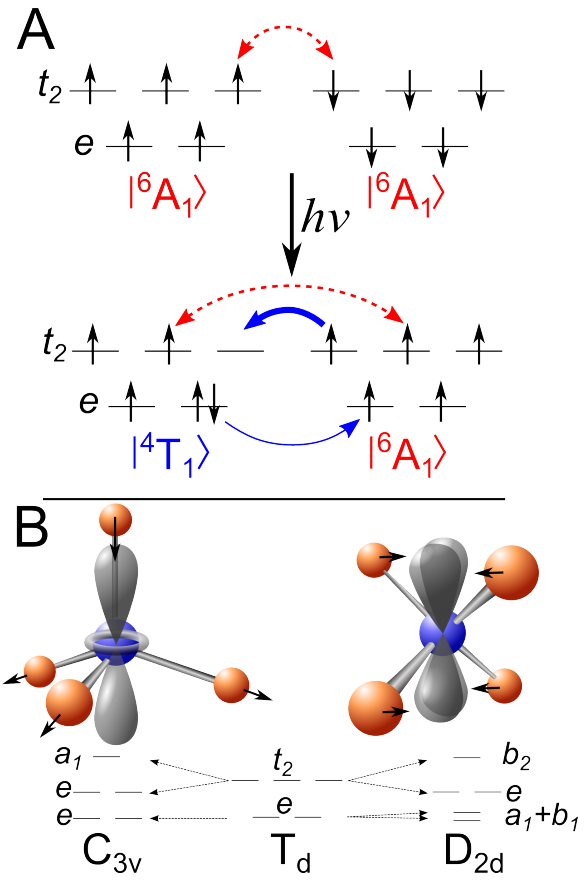

FIG 3.7. (color online) **(A)** Schematic summary of spin-transfer processes responsible for ground- and excited-state magnetic exchange coupling of Mn^{2+}-Mn^{2+} dimers in ZnSe. The dashed red arrows denote spin-transfer processes favoring antiferromagnetic Mn^{2+}-Mn^{2+} coupling, and the solid blue arrows denote spin-transfer processes favoring ferromagnetic coupling. **(B)** Two possible Jahn-Teller distortions of the Mn^{2+} $^4T_1$ excited state (C_{3v} and D_{2d}), and the corresponding *d*-orbital splitting patterns.

Dimer exchange interactions can be assessed more quantitatively using perturbation methods. The exchange interaction between two ions A and B is formulated in terms of the Heisenberg-Dirac-van Vleck effective Hamiltonian shown in eq 7.

$$H = -2J_{dd}\hat{S}_A \bullet \hat{S}_B \tag{7}$$

Here, J_{dd} is the exchange coupling constant and $\hat{S}_A$, $\hat{S}_B$ represent the Mn^{2+} spins. Experimentally, the ground-state coupling constant of Mn^{2+}-Mn^{2+} dimers in ZnSe is $J_{dd} \approx$ -1.0 meV, *i.e.*, antiferromagnetic.[33, 60] This coupling constant can be described with reasonable accuracy using 4th order perturbation theory.[61] Interestingly, similar perturbation calculations performed for

Cr^{2+}-Cr^{2+} dimers in ZnSe predict that *ferro*magnetic coupling may be possible in these dimers under certain circumstances.[62] Cr^{2+} has an $e^2t_2^2$ electronic configuration, and hence has ferromagnetic superexchange pathways analogous to the t_2-t_2 ferromagnetic pathway of the Mn^{2+} $^4T_1$ excited state illustrated in Fig. 3.7A. Notably, the magnitude and even the sign of the Cr^{2+}-Cr^{2+} dimer exchange coupling was predicted to be sensitive to the Cr^{2+} Jahn-Teller distortion.[62]

To assess the superexchange coupling in the $|^4T_1,^6A_1\rangle$ Mn^{2+}-Mn^{2+} dimer excited state, we take a similar 4th-order perturbation approach, based on the formalism developed by Weihe and Güdel for molecular transition-metal dimers.[63-65] Details of these calculations are provided as Supplemental Materials.[66] From the perturbation formalism, the most sensitive parameter determining the strength of an individual superexchange pathway is the overlap of the relevant *d*-orbital with the bridging ligand valence orbitals, which determines that pathway's transfer integral. Calculation of the pathway-specific transfer integrals for the Mn^{2+}-Mn^{2+} excited state is exceedingly difficult because of the Jahn-Teller distortion of this excited state. We therefore calculate two extreme scenarios for illustrative purposes: (*i*) the nine individual t_2-t_2 transfer integrals are all equal to the average transfer integral, and (*ii*) superexchange proceeds solely through a single dominant t_2-t_2 pathway whose transfer integral is therefore nine times the average. For simplicity, we neglect pathways involving the *e* orbitals, and we estimate the excited-state transfer integrals from the ground-state exchange coupling strength, neglecting changes due to overall bond-length contraction upon photoexcitation. Because the transfer integral is the only unknown parameter in these calculations, it can be fixed to reproduce the experimental ground-state coupling constant, and then used to predict the excited-state coupling.

In the limit where ground-state superexchange proceeds through nine equivalent t_2-t_2 pathways, the experimental ground-state $J_{dd} \approx$ -1.0 meV implies an average transfer integral of 0.6 eV. Applying this transfer integral to the dimer excited state, the six remaining antiferromagnetic pathways contribute -0.4 meV each and the three ferromagnetic pathways contribute +0.05 meV each, to yield an overall coupling constant of J_{dd}(ES) ~ -2.5 meV (antiferromagnetic). This scenario is thus inconsistent with the experimental observation of ferromagnetic excited-state coupling, from which we conclude that ferromagnetic superexchange pathways must play a greater-than-average role.

In the limit of just one active superexchange pathway, the experimental ground-state J_{dd} implies a transfer integral of 1.0 eV. If upon photoexcitation, the empty orbital does not

participate in the dominant superexchange pathway, then the excited-state superexchange remains antiferromagnetic, and the reduced charge-transfer energy increases the magnitude of J_{dd}(ES) to ~-3.6 meV. On the other hand, if photoexcitation removes an electron from the *d* orbital involved in the principal superexchange pathway, then the excited-state superexchange is ferromagnetic with J_{dd}(ES) ~ +0.4 meV. This result qualitatively supports the conclusion that the empty t_2 orbital of the photoexcited Mn^{2+} ion must be directed at the bridging selenide such that it dominates the excited-state Mn^{2+}-Mn^{2+} superexchange.

We hypothesize that the Jahn-Teller distortion of the $^4T_1$ excited state, which splits the *d* orbital degeneracies, plays an important role in orienting the empty t_2 orbital for effective ferromagnetic superexchange. Figure 3.7B illustrates two of the possible Jahn-Teller distortions of the $^4T_1$ excited state.[67] In Fig. 3.7B(left), Mn^{2+} undergoes a C_{3v} distortion involving contraction along the Mn^{2+}-Se^{2-}(bridge) axis, orienting the empty a_1 orbital for effective superexchange. In Fig. 3.7B(right), Mn^{2+} undergoes a D_{2d} distortion involving dihedral compression and positioning the empty b_2 orbital for effective superexchange. These distortions would not only favor a single superexchange pathway, but would also increase the overlap integral for the one destabilized (empty) orbital, thereby increasing the magnitude of J_{dd}. A more detailed description of the Jahn-Teller effect in the luminescent Mn^{2+} $^4T_1$ excited state will be presented elsewhere.[68]

3.3.D. Density functional theory calculations.

Additional insight into the excited-state Mn^{2+}-Mn^{2+} exchange coupling is obtained from DFT calculations. The energies of $Zn_{84}Mn_2Se_{86}$ nanocrystals containing Mn^{2+}-Mn^{2+} dimers in their ground state and first electronic excited states were calculated for scenarios in which the dimer spins were forced to align either ferromagnetically or antiferromagnetically. The energy difference between these two cases was then used to calculate J_{dd} according to eqs 8a and 8b, which reflect the energies of the $S = 0 \rightarrow 5$ (GS) and $S = 0 \rightarrow 4$ (ES) Landé spin ladders.

$$J_{dd}^{GS} = \frac{E_{AFM}^{GS} - E_{FM}^{GS}}{30} \tag{8a}$$

$$J_{dd}^{ES} = \frac{E_{AFM}^{ES} - E_{FM}^{ES}}{18} \tag{8b}$$

All total-energy calculations were performed after complete geometry optimization, which accounts for changes in cation site symmetry, orbital overlap, and hence exchange

energies upon relaxation of the electronically excited Mn^{2+} ion. For the ground state, the value of J_{dd} calculated in this way is -0.68 meV, which agrees reasonably well with the experimental value (~-1.0 meV).[18, 33, 60] In the dimer excited state, the ferromagnetic configuration was found to be more stable than the antiferromagnetic configuration by 24.5 meV, corresponding to J_{dd} = +1.36 meV (eq 8b). DFT calculations thus predict net ferromagnetic exchange in the luminescent excited states of Mn^{2+}-Mn^{2+} dimers, in agreement with experiment.

Figure 3.8 shows density-of-states (DOS) diagrams calculated for the antiferromagnetically coupled Mn^{2+}-Mn^{2+} ground state ($|^6A_1,^6A_1\rangle$) and the ferromagnetically coupled Mn^{2+}-Mn^{2+} excited state ($|^4T_1,^6A_1\rangle$). In the ground state (Fig. 3.8A), antiferromagnetic coupling gives a symmetrical spin population with no net spin (S = 0). In the excited state (Fig. 3.8B), the spin projection of the dimer is no longer symmetrical. Specifically, new β spin density appears near the valence band edge (the spin-down e electron), and the empty spin-up t_2 orbital now resides within the ZnSe gap. Additionally, the d orbital manifolds are broadened relative to the ground state, reflecting splittings due to low-symmetry structural relaxation.

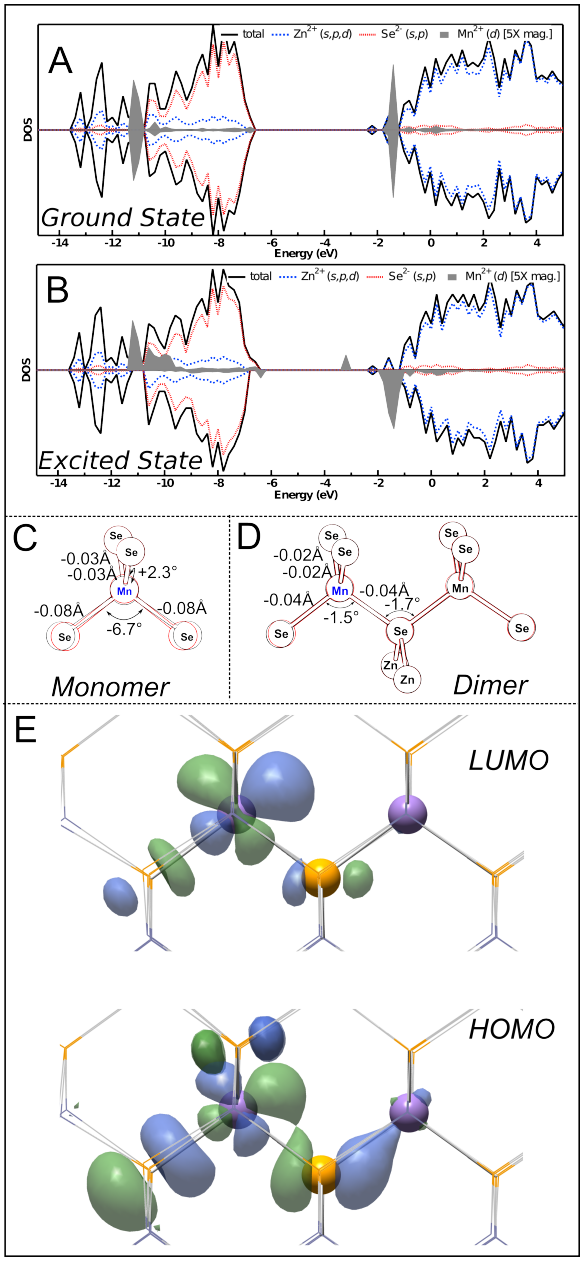

FIG 3.8. (color online) Results from DFT calculations on $Zn_{84}Mn_2Se_{86}$ nanocrystals. **(A, B)** Density-of-states diagrams for the antiferromagnetically coupled $|^6A_1,^6A_1\rangle$ ground state (A) and the ferromagnetically coupled $|^4T_1,^6A_1\rangle$ excited state (B). The top and bottom of each plot denote α and β spins, respectively. **(C, D)** Structural changes upon photoexcitation of Mn^{2+} monomer and Mn^{2+}-Mn^{2+} dimer. Ground-state (black) and excited-state (red) structures are illustrated, and the most significant changes in bond lengths and angles upon excitation are indicated. **(E)** Electron density contours of the Mn^{2+}-Mn^{2+} dimer LUMO and HOMO in the ferromagnetically coupled $|^4T_1,^6A_1\rangle$ excited state, which correspond primarily to the empty and doubly occupied orbitals of the photoexcited Mn^{2+} ion, respectively. Mn^{2+} ions are shown in purple, Zn^{2+} in blue, and Se^{2-} in yellow.

Figure 3.8C shows the calculated distortion upon excitation of an isolated Mn^{2+} ion to its $^4T_1$ state. All four Mn^{2+}-Se^{2-} bonds contract because of depopulation of a t_2 antibonding orbital, but two of the bonds contract more than the other two, breaking the T_d cation symmetry. This distortion resembles a partner function of the Jahn-Teller-active T_2 stretching coordinate, in which two bonds contract and two elongate. A similar distortion is calculated for the excited Mn^{2+} in the $|^4T_1,^6A_1\rangle$ dimer excited state (Fig. 3.8D), but the distortions appear smaller. Importantly, one of the shortened bonds is to the bridging Se^{2-}, indicating the depopulated t_2 orbital is directed toward this Se^{2-}, favoring ferromagnetic Mn^{2+}-Mn^{2+} superexchange coupling (Section C).

Figure 3.8E(LUMO) shows a contour plot depicting this empty orbital in the dimer excited state. This empty orbital indeed shows a substantial σ-type antibonding interaction with the bridging Se^{2-} p orbital, reflecting the primary ferromagnetic superexchange pathway of the luminescent $|^4T_1,^6A_1\rangle$ excited state. Details of the excited-state distortions, and contour plots for all 20 d-based dimer orbitals, are provided as Supplemental Materials.[69]

An interesting result from the DFT calculations is that the HOMO is also significantly hybridized with the bridging Se^{2-} in the $|^4T_1,^6A_1\rangle$ excited state (Fig. 3.8E(HOMO)). This covalency arises from the relatively high energy of this β-spin electron (Fig. 3.8B) because of the single-site Coulomb interaction, and it implies a significant contribution to excited-state magnetic exchange coupling involving this HOMO. This interaction was neglected in the perturbation treatment of Section C because of the smaller metal-ligand overlap of the cubic e orbitals. Importantly, superexchange involving this orbital also stabilizes the ferromagnetic configuration of Mn^{2+}-Mn^{2+} dimer spins.[65]

Overall, the DFT calculations predict ferromagnetic exchange coupling in the first electronic excited state of Mn^{2+}-Mn^{2+} dimers in ZnSe, in agreement with experiment. The DFT calculations illustrate symmetry-reducing Jahn-Teller distortions in the first excited states of Mn^{2+} monomers and Mn^{2+}-Mn^{2+} dimers in ZnSe, which in the latter promote overlap of the empty d orbital of t_2 parentage with the bridging Se^{2-}, in good agreement with expectations from perturbation analysis. The DFT calculations further suggest an additional effective ferromagnetic exchange pathway involving the excited-state HOMO.

3.4. Summary

The excited-state magnetism of photoexcited Mn^{2+}-Mn^{2+} dimers in $Zn_{1-x}Mn_xSe$ nanocrystals has been investigated using time-resolved MCPL spectroscopy. These experiments reveal *ferromagnetic* exchange coupling in the luminescent $|^4T_1,^6A_1\rangle$ electronic excited state of Mn^{2+}-Mn^{2+} dimers, in contrast with the antiferromagnetic exchange coupling universally observed in the $|^6A_1,^6A_1\rangle$ ground states of Mn^{2+}-Mn^{2+} dimers in ZnSe and related semiconductors. Perturbation theory and DFT calculations indicate that this change in the sign of J_{dd} derives primarily from a ferromagnetic superexchange pathway involving spin transfer into the empty t_2 orbital of the excited Mn^{2+} ion. Both perturbation and DFT analyses indicate that this empty t_2 orbital has a lobe oriented toward the bridging Se^{2-}, well situated for effective ferromagnetic superexchange. Ferromagnetic superexchange involving the doubly occupied *e* orbital in the dimer excited state is also suggested by DFT calculations. This new information about the magnetic properties of photoexcited Mn^{2+}-Mn^{2+} dimers in II-VI semiconductors appears to resolve a long-standing question in the literature, and may warrant revisiting the assignment of single crystal absorption and emission spectra for this class of materials.

The observation of ferromagnetic exchange coupling within the excited states of Mn^{2+}-Mn^{2+} dimers in ZnSe could potentially have interesting ramifications for optically switchable magnetism in semiconductors relevant to spin electronics. Although the materials investigated here are not immediately applicable for optical switching, the sensitized $S = 0 \rightarrow 4$ photoexcitation within a semiconductor, combined with the 100% circularly polarized luminescence of this excited state under a magnetic field, is highly attractive for further investigation in this regard. For example, future synthetic advances may open routes to materials containing only dimers or related small clusters.[70] In such materials, these photoinduced spin-state changes would manifest themselves as giant Zeeman splittings of the semiconductor band structure in ways that could be useful for optically triggered spin filtering or spin transduction applications.

3.5. References

1. Vlasenko, N. A.; Popkov, Y. A., *Opt. Spektrosk.* 1960, **8** (1), 81-88.
2. Beaulac, R.; Ochsenbein, S. T.; Gamelin, D. R., Colloidal Transition-Metal-Doped Quantum Dots. In Semiconductor Quantum Dots, 2nd ed.; Klimov, V. I., Ed. CRC Press: 2010; pp 397-453.

3. Shibata, K.; Nakayama, E.; Souma, I.; Murayama, A.; Oka, Y., *Phys. Status Solidi B* 2002, **229**, 473-476.
4. Ronda, C., Luminescence: From Theory to Applications. Wiley-VCH: Weinheim, Germany, 2008.
5. Chen, H.-Y.; Chen, T.-Y.; Son, D. H., *J. Phys. Chem. C* 2010, **114**, 4418–4423.
6. Toyama, T.; Adachi, D.; Fujii, M.; Nakano, Y.; Okamoto, H., *J. Non-Cryst. Sol.* 2002, **299-302**, 1111-1115.
7. Yang, H.; Holloway, P. H.; Ratna, B. B., *J. Appl. Phys.* 2003, **93** (1), 586-592.
8. Wood, V.; Halpert, J. E.; Panzer, M. J.; Bawendi, M. G.; Bulović, V., *Nano Lett.* 2009, **9**, 2367–2371.
9. Erickson, C. S.; Bradshaw, L. R.; McDowall, S.; Gilbertson, J. D.; Gamelin, D. R.; Patrick, D. L., 2013, submitted.
10. Irvine, S. E.; Staudt, T.; Rittweger, E.; Engelhardt, J.; Hell, S. W., *Angew. Chem.* 2008, **47**, 2685-2688.
11. Vlaskin, V. A.; Janßen, N.; van Rijssel, J.; Beaulac, R.; Gamelin, D. R., *Nano Lett.* 2010, **10**, 3670–3674.
12. Viswanatha, R.; Pietryga, J. M.; Klimov, V. I.; Crooker, S. A., *Phys. Rev. Lett.* 2011, **107** (6), 067402.
13. Beaulac, R.; Archer, P. I.; van Rijssel, J.; Meijerink, A.; Gamelin, D. R., *Nano Lett.* 2008, **8**, 2949-2953.
14. Furdyna, J. K.; Kossut, J., Diluted Magnetic Semiconductors. Academic: N.Y., 1988; Vol. 25.
15. Jonker, B. T.; Park, Y. D.; Bennett, B. R.; Cheong, H. D.; Kioseoglou, G.; Petrou, A., *Phys. Rev. B* 2000, **62**, 8180-8183.
16. Awschalom, D. D., Spin Electronics. Kluwer Academic Publishing: Boston, 2004.
17. Rüster, C., et al., *Phys. Rev. Lett.* 2003, **91**, 216602.
18. Brumage, W. H.; Yarger, C. R.; Lin, C. C., *Phys Rev* 1964, **133** (3A), A765-A767.
19. Ochsenbein, S. T.; Feng, Y.; Whitaker, K. M.; Badaeva, E.; Liu, W. K.; Li, X.; Gamelin, D. R., *Nat. Nanotechnol.* 2009, **4**, 681–687.
20. McClure, D. S., *J. Chem. Phys.* 1963, **39** (11), 2850.
21. Pohl, U. W.; Gumlich, H.-E., *J. Cryst. Growth* 1990, **101** (1-4), 521-524.
22. Pohl, U. W.; Gumlich, H.-E., *Phys. Rev. B* 1989, **40** (2), 1194-1201.
23. Benecke, C.; Busse, W.; Gumlich, H.-E.; Pohl, U. W., *Phys. Status Solidi B* 1985, **128** (2), 701-707.
24. Gumlich, H.-E., *J. Lumin.* 1981, **23**, 73-99.
25. Busse, W.; Gumlich, H.-E.; Meissner, B.; Theis, D., *J. Lumin.* 1976, **12**, 693-700.
26. Langer, D.; Ibuki, S., *Phys Rev* 1965, **138** (3A), A809-A815.
27. Dietl, T.; Peyla, P.; Grieshaber, W.; d'Aubigné, Y. M., *Phys. Rev. Lett.* 1995, **74** (3), 474-477.
28. Kreissl, J., *Phys. Status Solidi A* 1986, **97** (1), 191-198.
29. Kreissl, J.; Gehlhoff, W., *Phys. Status Solidi A* 1984, **81** (2), 701-707.
30. Nandagawe, J. K.; Patil, P. K.; Bote, P. R.; Lawangar-Pawar, R. D., *Solid State Commun.* 1991, **77** (7), 513-515.
31. Title, R. S., *Phys Rev* 1963, **131** (6), 2503-2504.
32. Abraham, G.; Nelkowski, H.; Pradella, H.; Sahm, J.; Zink, K., *Phys. Status Solidi B* 1985, **132** (2), K133-K138.
33. Roehrig, R. Elektronen-Spin-Resonanz (ESR) von Mangan-Paaren in Zinksulfid und Magnetische Eigenschaften von B-Mangansulfid. University of Freiburg, 1973.

34. Ferguson, J.; Guggenheim, H. J.; Tanabe, Y., *J. Appl. Phys.* 1965, **36** (3), 1046.
35. Wenger, O. S.; Valiente, R.; Güdel, H. U., *Phys. Rev. B* 2001, **64** (23), 235116.
36. Goede, O.; Heimbrodt, W.; Thong, D. D., *Phys. Status Solidi B* 1984, **126** (2), K159-K163.
37. Güdel, H. U., *Comments Inorg. Chem.* 1984, **5**, 189-204.
38. Archer, P. I.; Santangelo, S. A.; Gamelin, D. R., *J. Am. Chem. Soc.* 2007, **129**, 9808-9818.
39. McLaurin, E. J.; Vlaskin, V. A.; Gamelin, D. R., *J. Am. Chem. Soc.* 2011, **133**, 14978-14980.
40. Reiss, P.; Protière, M.; Li, L., *Small* 2009, **5** (2), 154-168.
41. See Supplemental Material at [URL will be inserted by publisher] for additional details on sythesis and characterization procedures.
42. Wyckoff, R. W. G., Crystal Structures. Interscience Publishers: New York, 1963; Vol. 1.
43. Badaeva, E.; Feng, Y.; Gamelin, D. R.; Li, X., *New J. Phys* 2008, **10**, 055013.
44. Wang, L.-W.; Li, J., *Phys. Rev. B* 2004, **69** (15), 153302.
45. Huang, X.; Lindgren, E.; Chelikowsky, J., *Phys. Rev. B* 2005, **71** (16), 165328.
46. Frisch, M. J., et al. Gaussian Development Version, H21+; Gaussian, Inc.: Wallingford, CT.
47. Perdew, J.; Burke, K.; Ernzerhof, M., *Phys. Rev. Lett.* 1996, **77** (18), 3865-3868.
48. Perdew, J. P.; Burke, K.; Ernzerhof, M., *Phys. Rev. Lett.* 1997, **78** (7), 1396-1396.
49. Adamo, C.; Barone, V., *J. Chem. Phys.* 1999, **110** (13), 6158-6170.
50. Wadt, W. R.; Hay, P. J., *J. Chem. Phys.* 1985, **82** (1), 284-298.
51. Hay, P. J.; Wadt, W. R., *J. Chem. Phys.* 1985, **82** (1), 270-283.
52. Badaeva, E.; May, J. W.; Ma, J.; Gamelin, D. R.; Li, X., *J. Phys. Chem. C* 2011, **115** (43), 20986.
53. Badaeva, E.; Isborn, C.; Feng, Y.; Ochsenbein, S.; Gamelin, D.; Li, X., *J. Phys. Chem. C* 2009, **113** (20), 8710.
54. Peng, B.; Liang, W.; White, M. A.; Gamelin, D. R.; Li, X., *J. Phys. Chem. C* 2012, **116**, 11223-11231.
55. Beaulac, R.; Feng, Y.; May, J.; Badaeva, E.; Gamelin, D.; Li, X., *Phys. Rev. B* 2011, **84** (19), 195324.
56. See Supplemental Material at [URL will be inserted by publisher] for comparison of polarization resolved spectra.
57. Fournier, D.; Boccara, A. C.; Rivoal, J. C., *J. Phys. C Solid State* 1977, **10** (1), 113-121.
58. Behringer, R. E., *J. Chem. Phys.* 1958, **29** (3), 537.
59. We note that the saturation magnetization of PTI appears to depend on Mn^{2+} concentration, progressing to larger apparent S values at higher Mn^{2+} concentrations (approaches S = 4 at 3.5%; See Supplemental Material). This behavior is tentatively attributed to the effects of higher-nuclearity Mn^{2+} clusters in the higher-concentration samples, but this trend has not been investigated in detail. For this reason, the analysis in Fig. 3.4 focuses on a low-concentration sample where only monomers and dimers are prominent.
60. Beaulac, R.; Gamelin, D. R., *Phys. Rev. B* 2010, **82**, 224401.
61. Larson, B. E.; Hass, K. C.; Ehrenreich, H.; Carlsson, A. E., *Phys. Rev. B* 1988, **37** (8), 4137-4154.
62. Blinowski, J.; Kacman, P.; Majewski, J. A., *Phys. Rev. B* 1996, **53** (15), 9524-9527.
63. Weihe, H.; Güdel, H. U., *J. Am. Chem. Soc.* 1998, **120** (12), 2870-2879.
64. Weihe, H.; Güdel, H. U., *Inorg. Chem.* 1997, **36** (17), 3632-3639.
65. Weihe, H.; Güdel, H. U.; Toftlund, H., *Inorg. Chem.* 2000, **39** (7), 1351-1362.
66. See Supplemental Material at [URL will be inserted by publisher] for details of pertubation theory calculations.

67. Bersuker, I. B.; Polinger, V. Z., Vibronic Interactions in Molecules and Crystals. Springer-Verlag: Berlin Heidelberg, 1989.
68. Bradshaw, L. R.; Dempsey, J. L.; Polinger, V. Z.; Beaulac, R.; Schimpf, A. M.; McLaurin, E. J.; Vlaskin, V. A.; Crooker, S. A.; Gamelin, D. R., unpublished results.
69. See Supplemental Material at [URL will be inserted by publisher] for excited state geometry and contour plots of relevant d-orbitals.
70. Jawaid, A. M.; Chattopadhyay, S.; Wink, D. J.; Page, L. E.; Snee, P. T., *ACS Nano* 2013, **7** (4), 3190-3197.

Chapter 4. Luminescence Saturation via Mn^{2+}-Exciton Cross Relaxation in Colloidal Doped Semiconductor Nanocrystals

Abstract. Colloidal Mn^{2+}-doped semiconductor nanocrystals such as Mn^{2+}:ZnSe have attracted broad attention for potential applications in phosphor and imaging technologies. Here, we report saturation of the sensitized Mn^{2+} photoluminescence intensity at very low continuous-wave (CW) and quasi-CW photoexcitation powers under conditions that are relevant to many of the proposed applications. Time-resolved photoluminescence measurements and kinetic modeling indicate that this saturation arises from an Auger-type nonradiative cross relaxation between an excited Mn^{2+} ion and an exciton within the same nanocrystal. A lower limit of $k = 2\times10^{10}$ s^{-1} is established for the fundamental rate constant of the $Mn^{2+}(^4T_1)$-exciton cross relaxation. Reprinted with permission from: Bradshaw, L. R.; Hauser, A.; McLaurin, E. J.; Gamelin, D. R., *Journal of Physical Chemistry C* 2012, **116** (16), 9300-9310.

4.1. Introduction

Mn^{2+} is an effective luminescence activator in many semiconductor matrices, and consequently Mn^{2+}-doped semiconductors have been employed as phosphors in photoluminescent and electroluminescent technologies for many years.[1-3] In photoluminescence (PL), photoexcitation of the semiconductor is followed by rapid (picosecond) non-radiative energy transfer to excite Mn^{2+} to its $^4T_1$ state (Mn*), which then relaxes back to the $^6A_1$ ground state radiatively with approximately millisecond lifetimes, depending on the lattice and temperature.[4-8] The long Mn^{2+} $^4T_1$ excited-state lifetime is a bottleneck at large excitation rates, however, causing luminescence saturation.[9-11] In bulk Mn^{2+}-doped semiconductors, a combination of Mn^{2+} concentration-dependence and PL time-dependence measurements has led to the conclusion that saturation is not only associated with depletion of ground-state Mn^{2+} but also depends on Mn* energy migration and non-radiative Mn*-Mn* cross relaxation.[11-15] In EL devices, Mn*-electron Auger-type de-excitation has also been identified as an important deactivation mechanism.[12,16-19]

Considerable recent effort has turned to doping semiconductor nanostructures with Mn^{2+}. Exploration of these classic phosphor materials on nanometer length scales has uncovered completely new physical properties,[8,20-22] the technological potential of which cannot be fully assessed until the properties themselves are understood at a fundamental level. For example, the ability to detect and manipulate individual spins has been demonstrated in epitaxial "self-

assembled" quantum dots doped with single Mn^{2+} ions,[23-27] making these materials potentially attractive for quantum information processing[28] and solitary dopant optoelectronics ("solotronics").[29] Colloidal Mn^{2+}-doped quantum dots with strong quantum confinement have shown spontaneous photomagnetization[30] and charge-controlled magnetization[31] at elevated temperatures, both involving orientation of localized Mn^{2+} spins by delocalized charge carriers via strong *sp-d* exchange coupling. Energy gap tuning using the quantum confinement effect has revealed intrinsic dual emission in colloidal Mn^{2+}-doped semiconductor nanocrystals,[7,32,33] and phase transfer into aqueous solution has opened doors for application of colloidal Mn^{2+}-doped semiconductor nanocrystals in bioimaging.[33-36]

Recently, three groups have reported PL saturation with increasing excitation power in colloidal Mn^{2+}-doped semiconductor nanocrystals.[37-39] One group has attributed Mn^{2+} PL saturation to complete depletion of ground-state Mn^{2+} in the nanocrystals.[37] Another has described saturation from Mn^{2+} photoionization via two sequential absorption/energy-transfer cycles, generating Mn^{3+} plus a hot electron.[38] The third describes saturation from exciton-exciton Auger recombination prior to energy transfer to Mn^{2+}.[39] These experiments were all performed using very large pulse energies (up to 20 mJ/cm^2) to achieve multiple photoexcitation events per nanocrystal within single laser pulses. Although the PL saturation in colloidal nanocrystals may at first appear similar to that in bulk, key experimental differences are evident: Whereas PL saturation in bulk becomes more facile with increasing Mn^{2+} concentration, in the nanocrystals it becomes less facile,[37] and whereas PL saturation in bulk is characterized by a reduction in Mn^{2+} PL decay time, the nanocrystals show no change in Mn^{2+} PL decay times in the saturation regime.[38] The dominant process underlying PL saturation in Mn^{2+}-doped semiconductor nanocrystals thus appears to be fundamentally different from the one that dominates in bulk semiconductors. Given the broad interest in Mn^{2+}-doped semiconductor nanocrystals for optical imaging, magneto-optics, and photophysics, as well as the general historical importance of Mn^{2+}-doped semiconductor phosphors, a thorough understanding of these PL nonlinearities in Mn^{2+}-doped semiconductor nanocrystals is needed.

Here, we describe the excitation power dependence of PL from colloidal Mn^{2+}-doped II-VI nanocrystals under continuous-wave (CW) and quasi-CW photoexcitation conditions. A sub-linear dependence of the time-integrated Mn^{2+} PL on excitation power is observed even at very low excitation powers, with complete saturation achieved using only modest excitation powers.

The nanocrystal PL quantum yields are reduced by over an order of magnitude traversing from the low-power limit to the saturation regime. Two-pulse photoexcitation measurements unambiguously demonstrate that the reduction in quantum yield is associated with the population of excited Mn^{2+} ions. Time-resolved PL measurements implicate a fast (picosecond) non-radiative Mn*-exciton Auger-type cross relaxation as the fundamental origin of the PL saturation. These results are simulated using a kinetic model that accounts for Mn*-exciton cross relaxation explicitly, from which a cross-relaxation rate constant of at least 2×10^{10} s^{-1} is determined. These results emphasize the importance of the very long Mn^{2+} $^4T_1$ excited-state lifetime in governing the photophysical properties of Mn^{2+}-doped semiconductor nanocrystals, and have implications for future applications of such nanophosphors involving high-power photoexcitation.

4.2. Experimental

4.2A. Synthesis and general characterization.

Mn^{2+}-doped CdS, and core-doped core/shell ZnSe/ZnS and core/multishell ZnSe/ZnS/CdS/ZnS nanocrystals were synthesized as described previously.[33,40] Mn^{2+}:ZnSe nanocrystals were made by thermal decomposition of the tetramer, $(Me_4N)_2[Zn_4(SePh)_{10}]$ in the presence of $MnCl_2$.[41] These nanocrystals were then coated with ZnS or CdS shells by successive slow additions of zinc- or cadmium oleate and trioctylphosphine sulfide.[42,43] Mn^{2+}:CdS nanocrystals were made by injecting a solution of S in octadecene into a hot (305°C) solution of CdO and $Mn(OAc)_2$ in oleic acid, oleyl amine, and octadecene.[44] Samples were characterized by electronic absorption spectroscopy, TEM, ICP-MS, EPR spectroscopy, and photoluminescence quantum yield measurements (Hamamatsu integrating sphere). Relevant results from these characterization experiments are included in Supporting Information. Unless otherwise stated, the results presented in this manuscript were collected using Mn^{2+}:ZnSe/ZnS/CdS/ZnS nanocrystals (= $Zn_{0.9955}Mn_{0.0045}Se$/ZnS/CdS/ZnS QDs), which showed the greatest photostability, but similar results were obtained for all systems studied. The results from parallel experiments performed on Mn^{2+}:ZnSe/ZnS nanocrystals are included in Supporting Information.

4.2.B. Photoluminescence measurements.

PL samples were prepared by sandwiching drop-coated films of quantum dots between two sapphire disks. Films were prepared to have optical densities below 0.1 at the excitation wavelength. A brass foil with a 500 μm pinhole was mounted on the outside of the disks, and the

samples were cooled to 7.5 K in a He flow cryostat. Illumination and PL collection were both performed through the pinhole to ensure a uniform excitation density and to reduce the effects of scattering. The experimental results were influenced by the excitation beam intensity profile, with Gaussian profiles yielding noticeably less defined saturation curvature than the top-hat profiles provided by use of the pinhole. Laser powers were measured with a Coherent Lab-max power meter using an LM-2 UV head. Powers measured before the cryostat were converted to power density by measuring the fraction of the beam that passed through the pinhole in the absence of sample, accounting for losses due to reflection off the cryostat windows. A shutter was inserted in front of the cryostat to minimize possible long-term radiation damage.

The UV lines of an Ar^+ ion laser (~357 nm) were used for CW photoexcitation. Quasi-CW PL measurements were performed using the frequency doubled output of a Ti:Sapphire laser (150 fs pulses, 76 MHz, ~385 nm). The excitation beam was collimated to a diameter of 3 mm and brought in to the sample at a steep angle (~10°).

Time-integrated PL spectra were collected by passing the collected light through a fiber to a monochromator (0.5 m, 150 g/mm grating blazed at 500 nm) equipped with a LN_2 cooled CCD detector. Each spectrum was collected over a 5 second integration window. All variable-power measurements were performed both by increasing and by decreasing the power across the full power range to ensure the absence of radiation damage. Time-resolved PL data were collected using a streak camera mounted on a 0.5 m monochromator (50 g/mm, 600 nm blaze). The single-pulse excitation experiments were performed using the 337 nm output of a N_2 laser operating at 18 Hz with a pulse duration of ~0.8 ns. Time-resolved PL was measured using a PMT and a multi-channel scalar. The two-pulse variable delay experiments were performed using the Ti:Sapphire output and a pulse picker triggered by a function generator. This configuration allowed photons to be delivered to the sample in pairs of pulses every 10 ms, with variable delay between the two pulses, and with constant time-integrated power. For these experiments only, the beam was focused to a spot size of ~50 μm on the sample, resulting in energy densities reaching ~16 $\mu J/cm^2$.

4.3. Results

4.3.A. Photoluminescence power dependence.

Figure .4.1 summarizes the excitation power dependence of the time integrated PL for a series of Mn^{2+}-doped II-VI semiconductor nanocrystals, measured at 7.5 K under CW and quasi-CW excitation conditions. Low temperatures were used in these measurements to eliminate potential contributions from laser heating on PL quantum yields and lifetimes (the PL quantum yield of the Mn^{2+}:ZnSe/ZnS/CdS/ZnS nanocrystals was temperature independent below ~200 K, see Supporting Information), but similar results were also obtained at room temperature.

Figure .4.1A shows PL spectra collected for Mn^{2+}:ZnSe/ZnS/CdS/ZnS nanocrystals at several CW excitation powers. The spectra are dominated by the intense Mn^{2+} $^4T_1 \rightarrow {}^6A_1$ luminescence band centered at 590 nm, and also show weak excitonic luminescence centered at 445 nm. The Mn^{2+} PL intensity increases with increasing excitation power over the experimental power range of 1 - 20 mW (<0.1 - 1.1 W/cm^2), but the increase is not linearly proportional to the excitation power. At high excitation powers, the Mn^{2+} PL becomes independent of excitation power. In contrast, the excitonic PL intensity increases linearly with increasing excitation power over the entire power range. In addition to these two PL features, a weak, broad PL band is evident near the Mn^{2+} PL peak. This broad band is attributed to surface-trap emission. This PL is readily separated from that of the Mn^{2+} because of its linear power dependence (see Supporting Information).

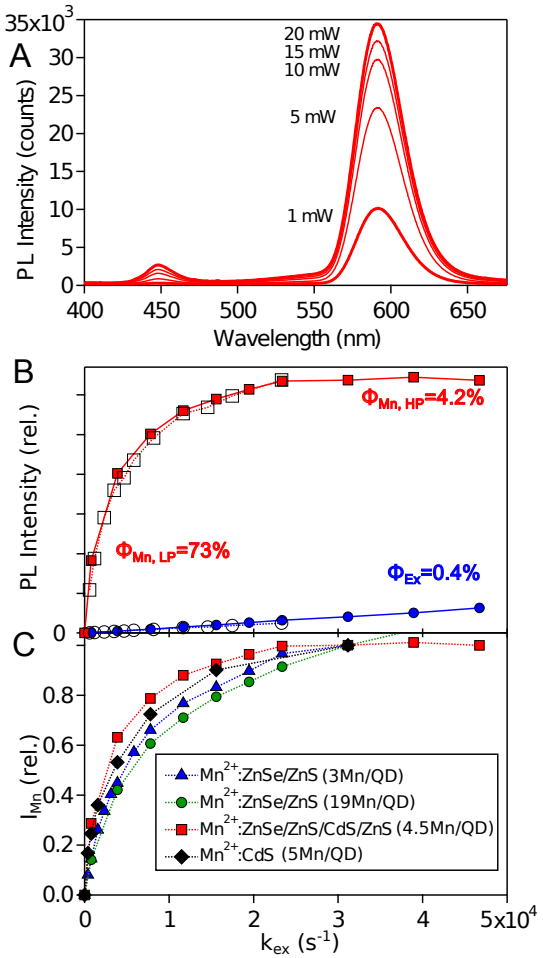

Figure 4.1. (A) Power dependence of the time-integrated, 7.5 K photoluminescence from Mn^{2+}:ZnSe/ZnS/CdS/ZnS QDs under CW excitation. 20 mW in this experiment corresponds to 1.1 W/cm^2 and $k_{ex} \approx 2.3\times10^4$ s^{-1} (see text). **(B)** The integrated Mn^{2+} (squares) and excitonic (circles) PL intensities of the same sample plotted vs k_{ex}, from both CW (open) and quasi-CW (filled) excitation. **(C)** Normalized Mn^{2+} PL intensities from several Mn^{2+}-doped nanocrystals plotted vs k_{ex}. Squares: $Zn_{0.9955}Mn_{0.0045}Se$/ZnS/CdS/ZnS QDs (avg. 4.5 Mn^{2+}/QD, d = 6.0 nm, E_g = 2.8 eV). Circles: $Zn_{0.984}Mn_{0.016}Se$/ZnS QDs (avg. 19 Mn^{2+}/QD, d = 6.0 nm, E_g = 3.0 eV). Triangles: $Zn_{0.995}Mn_{0.005}Se$/ZnS QDs (avg. 3 Mn^{2+}/QD, d = 3.5 nm, E_g = 3.1 eV). Diamonds: $Cd_{0.995}Mn_{0.005}S$ QDs (avg. 5 Mn^{2+}/QD, d = 4.5 nm, E_g = 2.8 eV). For comparison, the data are normalized at $k_{ex} = 3.1\times10^4$ s^{-1}.

Figure 4.1B plots the integrated Mn^{2+} and excitonic PL intensities from Fig. 4.1A vs nanocrystal excitation rate constant, along with similar data collected using quasi-CW excitation. The excitation rate constant is defined as $k_{ex} = \sigma q_p$, where σ is the nanocrystal absorption cross section at the excitation wavelength and q_p is the photon flux. For example, for the quasi-CW

data in Fig. 4.1B, careful measurement through a pinhole centered in the cryostat gave an irradiation intensity of I_{max} = 5 W/cm^2 at the maximum laser power of 60 mW (λ = 385 nm), corresponding to a photon flux $q_p = I/h\nu = 10^{19}$ s^{-1}cm^{-2}. A value of $\sigma \sim 5\times10^{-15}$ cm^2 was estimated at this wavelength from literature oscillator strengths.[45,46] Together, these values give an excitation rate constant of $k_{ex} \approx 5\times10^4$ s^{-1} at I_{max} for this particular measurement.

The CW and quasi-CW excitation modes yielded indistinguishable PL results. For both, sub-linear Mn^{2+} PL power dependence was observed at all excitation rate constants, even below ~5×10^3 s^{-1}. At an excitation rate constant of 5×10^4 s^{-1} the Mn^{2+} PL was completely saturated. Because of this strongly sub-linear power dependence, the Mn^{2+} PL quantum yield also changed with excitation power. In the low power limit, the quantum yield was 73%. At the highest power in Fig. 4.1B, the quantum yield had dropped to only 4.2%. Mn^{2+} PL in doped semiconductor nanocrystals is thus highly nonlinear even with modest CW excitation powers. In contrast to the Mn^{2+} PL saturation, the excitonic intensity increased linearly with excitation power over the entire power range examined here, having a constant quantum yield of ~0.4%.

Mn^{2+}-doped nanocrystals of several different compositions were examined, and all showed similar Mn^{2+} PL saturation. Figure 4.1C plots the data from four different samples including those of Figs. 1A and B as well as Mn^{2+}:CdS and Mn^{2+}:ZnSe/ZnS nanocrystals. Despite differences in PL decay times (both Mn^{2+} and excitonic), Mn^{2+} concentrations, and PL quantum yields, saturation was observed over a similar range of k_{ex} in all samples. These results indicate that facile Mn^{2+} PL saturation is a general property of Mn^{2+}-doped semiconductor nanocrystals.

4.3.B. Time-resolved photoluminescence.

Figure 4.2 plots the Mn^{2+} $^4T_1 \rightarrow {}^6A_1$ PL decay vs time, measured following pulsed excitation. This PL decay is characterized by a single exponential with τ_{Mn} = 379 μs, consistent with previous measurements on related samples.[8] On the same time axis, Fig. 4.2 also plots integrated Mn^{2+} PL intensities measured using pairs of excitation pulses with long delay times between pairs. The data are plotted as a function of the delay time between the two pulses in each pair (top, see Experimental). These experiments were performed with 16 μJ/cm^2 excitation power at 385 nm, with which ~10% of the nanocrystals were excited per pulse. Starting from delay times well beyond the Mn^{2+} $^4T_1$ lifetime (>3 ms), the points in Fig. 4.2 show that the integrated Mn^{2+} PL intensity decreased as the two pulses were brought closer together. The

change in integrated Mn^{2+} PL intensity plotted vs delay time between pulses is characterized by a single exponential with the same apparent time constant as the Mn^{2+} $^4T_1$ PL decay (~379 µs). This result identifies the reduction in Mn^{2+} PL intensity in Fig. 4.2 as arising from photoexcitation of nanocrystals by the second pulse within the Mn^{2+} $^4T_1$ excited-state lifetime of the first excitation pulse, *i.e.*, photoexcitation of nanocrystals *that already contain excited* Mn^{2+}. By extension, these results allow the conclusion that the PL saturation in Fig. 4.1 also arises from photoexcitation of nanocrystals that already contain excited Mn^{2+}. By correlating it with the Mn^{2+} excited-state population, other possible origins of the PL saturation such as laser heating[47] or photo-charging[48] are excluded.

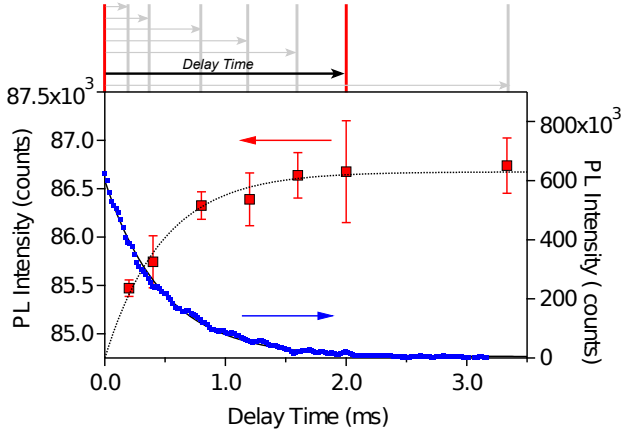

Figure 4.2. Right axis: Mn^{2+} PL decay in the Mn^{2+}:ZnSe/ZnS/CdS/ZnS nanocrystals of Fig. 4.1. The solid line shows a single exponential decay curve with τ = 379 µs. Left axis: Integrated Mn^{2+} PL intensity measured with pairs of excitation pulses, plotted as a function of the delay time between the two pulses. The top panel depicts this experiment schematically. Error bars represent standard deviations of four measurements. The grey dashed line shows the τ = 379 µs decay of the Mn^{2+} PL. Data measured at 7.5 K.

Figure 4.3 summarizes the influence of excitation power on the Mn^{2+}:ZnSe/ZnS/CdS/ZnS nanocrystal PL time dependence using quasi-CW excitation conditions (150 fs pulses, 76 MHz repetition rate). Fig. 4.3A shows a streak camera image collected following an excitation pulse at time = 0. The Mn^{2+} PL intensity is effectively constant over the entire dark time between excitation pulses (13 ns). On the other hand, the excitonic photoluminescence shows a burst of intensity, followed by decay.

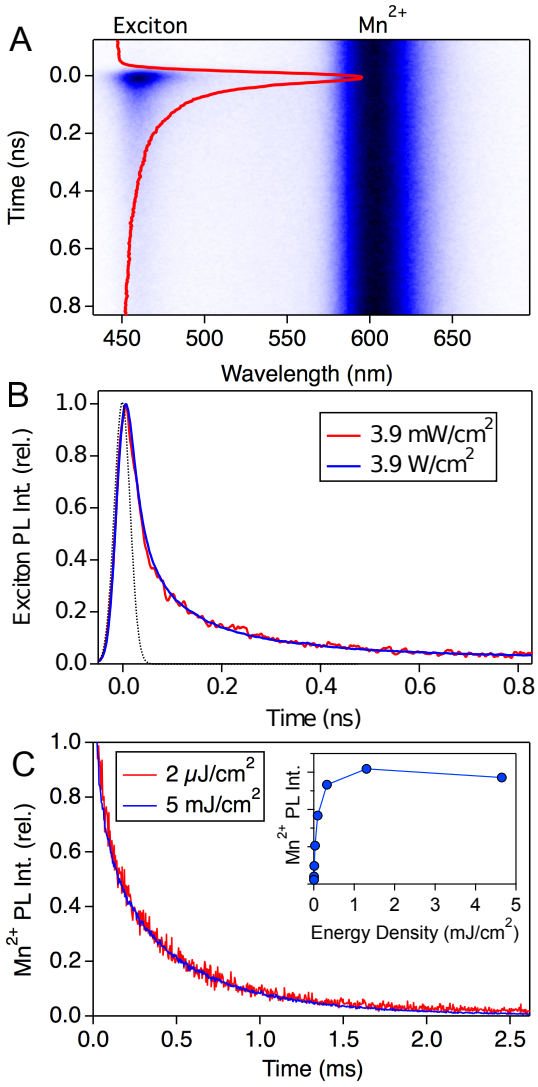

Figure 4.3. (A) Streak camera image (7.5 K, 0.4 W/cm^2) showing the time dependence of the excitonic and Mn^{2+} PL from the Mn^{2+}:ZnSe/ZnS/CdS/ZnS nanocrystals of Fig. 4.1. The red line plots the excitonic luminescence intensity (integrated between 439 and 481 nm) vs time. **(B)** Excitonic PL measured using low- and high-power excitation, both at 7.5 K. The dotted line represents the instrument response function. **(C)** Mn^{2+} PL decay traces collected with low- and high-power pulsed excitation at 7.5 K (18 Hz repetition rate, 337 nm). The inset shows saturation of the integrated Mn^{2+} PL with increasing pulse energy density under the same experimental conditions.

Figure 4.3B plots normalized excitonic PL decay traces collected at low and high excitation powers. These excitonic PL decay traces are fit well using a bi-exponential function with two distinct time constants, τ_1 = 29 ps and τ_2 = 308 ps. The fast and slow components account for 34% and 66% of the overall excitonic PL. Exciton-to-Mn^{2+} energy transfer takes place within a few tens of picoseconds.[4-7] The excitonic PL having τ_2 = 308 ps thus decays too slowly to come from doped QDs, and is attributed to undoped QDs. The excitonic PL decay time of τ_1 = 29 ps agrees well with those of other doped QDs, and this component is thus assigned to doped QDs. τ_1 = 29 ps is close to the instrument response function, and faster decay would not be resolved. This value is therefore considered a measure of the slowest energy transfer processes within the ensemble of doped QDs. These assignments are supported by analysis of Mn^{2+} distributions within the ensemble of nanocrystals (*vide infra*).

Figure 4.3B also demonstrates that the excitonic PL decay dynamics are unchanged over the excitation power range in which the Mn^{2+} PL saturates and its quantum yield decreases by an order of magnitude. As discussed in the Analysis section, this result implies that the non-radiative processes responsible for Mn^{2+} saturation occur on the same timescale as exciton-to-Mn^{2+} energy transfer.

Figure 4.3C plots the Mn^{2+} PL decay measured following pulsed excitation at low and high excitation powers (18 Hz repetition rate, 337 nm). The inset illustrates PL saturation at the high-power conditions used for this measurement. There is no discernable change in Mn^{2+} PL decay time upon traversing from low- to high-power excitation, indicating that PL saturation is not associated with a reduction in the intrinsic Mn^{2+} PL quantum yield.

4.4. Analysis

4.4.A. Staircase excitation model.

Figure 4.4A describes the well-established scheme by which a nanocrystal containing *m* Mn^{2+} dopants is photoexcited. After photoexcitation of the nanocrystal (with rate constant k_{ex}), the resulting exciton (QD*) can recombine (k_{QD}) or be quenched via nonradiative energy transfer to Mn^{2+} ($m \cdot k_{et}$). The excited Mn^{2+} (Mn*) decays with rate constant k_{Mn}. The rate constants k_{QD} and k_{Mn} described here represent the sum of radiative and non-radiative contributions. All four of the above rate constants (k_{ex}, k_{QD}, k_{et}, k_{Mn}) have been determined experimentally.

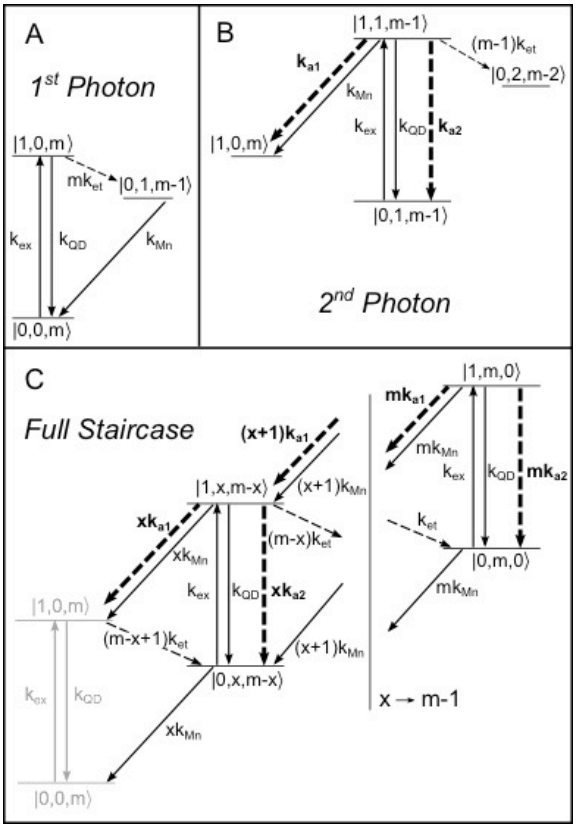

Figure 4.4. (A) Schematic description of low-power photoexcitation of a Mn^{2+}-doped nanocrystal containing m Mn^{2+} ions. QD $\rightarrow$ QD* photoexcitation proceeds with a rate constant of k_{ex}. The photoexcited QD can relax by recombination (k_{QD}) or by energy transfer to Mn^{2+} (k_{et}). The excited-state Mn^{2+} relaxes with k_{Mn}. States are denoted by the number of excitons, the number of excited-state Mn^{2+} ions, and the number of ground state Mn^{2+} ions, *i.e.*, |#QD*, #Mn*, #Mn⟩. **(B)** Schematic description of photoexcitation of a Mn^{2+}-doped QD that already contains an excited-state Mn^{2+} ion. In addition to recombination and energy transfer to Mn^{2+}, QD* may now relax via one of two Auger cross-relaxation processes (k_{a1} and k_{a2}), differentiated by their final states. **(C)** In a nanocrystal with m Mn^{2+} ions, multiple sequential photoexcitation events can yield $x \leq m$ excited Mn^{2+} ions, with corresponding changes in cross-relaxation and energy-transfer rates.

Figure 4.4B illustrates how the excited state dynamics may change when the excitation rate is large enough that the nanocrystal absorbs a second photon while one of the Mn^{2+} dopants is still in its excited state from a preceding photoexcitation event. This situation introduces new Auger-type cross-relaxation processes. Two types of cross relaxation can be distinguished on the basis of their final states (exciton or $Mn^{2+}(^4T_1)$), and these are indicated by the rate constants k_{a1} and k_{a2}, respectively. For example, the excited Mn^{2+} may transfer its energy to the exciton to

yield ground-state Mn^{2+} and a hot exciton, which may then relax nonradiatively to return to QD*. Similarly, the exciton may transfer its energy to Mn* to yield an upper Mn^{2+} excited state, which may then relax nonradiatively back to the $^4T_1$ state. The possibility of branching between the exciton and $Mn^{2+}(^4T_1)$ final states during relaxation is also accounted for in this model. In all processes, thermalization is assumed to be rapid relative to luminescence.

Figure 4.4C extends the scenario of Fig. 4.4B to account for any arbitrary number of sequential excitations per nanocrystal, including the possibility of exciting all Mn^{2+} ions to their $^4T_1$ excited states. This "staircase" excitation scheme forms the basis of the kinetic model employed here. For small k_{ex} relative to k_{et} and k_{QD}, eqs 1 and 2 describe the population dynamics implied by Fig. 4.4C in terms of a set of coupled differential equations for a nanocrystal containing m Mn^{2+} dopants, for x = 0, 1, 2, ..., m, where x is the number of excited Mn^{2+} ions in that nanocrystal. Equation 1a describes the Mn* population dynamics. In the special case of x = 0, eq. 1b applies.

$$\frac{d|\mathrm{QD},x\mathrm{Mn}^*,(m-x)\mathrm{Mn}\rangle}{dt} = -(k_{ex} + \mathrm{x}k_{Mn})|\mathrm{QD},x\mathrm{Mn}^*,(m-x)\mathrm{Mn}\rangle + (m-x+1)k_{et}|\mathrm{QD}^*,(x-1)\mathrm{Mn}^*,(m-x+1)\mathrm{Mn}\rangle + (k_{QD} + xk_{a2})|\mathrm{QD}^*,x\mathrm{Mn}^*,(m-x)\mathrm{Mn}\rangle + (x+1)k_{Mn}|\mathrm{QD},(x+1)\mathrm{Mn}^*,(m-x-1)\mathrm{Mn}\rangle \quad (4.1a)$$

$$\frac{d|\mathrm{QD},0\mathrm{Mn}^*,m\mathrm{Mn}\rangle}{dt} = -k_{ex}|\mathrm{QD},0\mathrm{Mn}^*,m\mathrm{Mn}\rangle + k_{QD}|\mathrm{QD}^*,0\mathrm{Mn}^*,m\mathrm{Mn}\rangle + k_{Mn}|\mathrm{QD},1\mathrm{Mn}^*,(m\text{-}1)\mathrm{Mn}\rangle \quad (4.1b)$$

Similarly, eq. 2 describes the excitonic (QD*) population dynamics implied by Fig. 4.4B.

$$\frac{d|\mathrm{QD}^*,x\mathrm{Mn}^*,(m-x)\mathrm{Mn}\rangle}{dt} = -\left(k_{QD} + xk_{Mn} + xk_{a1} + xk_{a2} + (m-x)k_{et}\right)|\mathrm{QD}^*,x\mathrm{Mn}^*,(m-x)\mathrm{Mn}\rangle + k_{ex}|\mathrm{QD},x\mathrm{Mn}^*,(m-x)\mathrm{Mn}\rangle + (x+1)(k_{Mn} + k_{a1})|\mathrm{QD}^*,(x+1)\mathrm{Mn}^*,(m-x-1)\mathrm{Mn}\rangle \quad (4.2a)$$

For the special case of $x = m$, eq. 2b applies.

$$\frac{d|\mathrm{QD}^*,m\mathrm{Mn}^*,0\mathrm{Mn}\rangle}{dt} = -\left(k_{QD} + mk_{Mn} + mk_{a1} + mk_{a2}\right)|\mathrm{QD}^*,m\mathrm{Mn}^*,0\mathrm{Mn}\rangle + k_{ex}|\mathrm{QD},m\mathrm{Mn}^*,0\mathrm{Mn}\rangle \quad (4.2b)$$

In formulating eqs 1 and 2, three assumptions have been made: (*i*) k_{ex} does not depend on the number of excited Mn^{2+} ions in the QD; (*ii*) the effective energy-transfer rate constant from the exciton to Mn^{2+} is proportional to the number of Mn^{2+} in the ground state and can be written

as $k_{eff} = (m\text{-}x)k_{et}$, where k_{et} is the rate constant for transfer in a nanocrystal with a single Mn^{2+}; (*iii*) because the upper excited states formed via both cross-relaxation processes relax very quickly to their respective lowest excited states by internal conversion, the rate constants k_{a1} and k_{a2} are rate limiting. Like k_{et}, k_{a1} and k_{a2} are assumed to be additive per excited Mn^{2+}. Finally, in using effective rate constants, distributions in energy transfer and cross-relaxation rate constants due to nanocrystal size or dopant-position distributions are neglected.

By solving eqs 1 and 2 for continuous irradiation, the steady state populations at each level in the staircase scheme of Fig. 4.4B can be calculated. Importantly, all of the necessary rate constants are known from independent experiments, except for k_{a1} and k_{a2}. k_{ex} is determined from the measured power density and the literature absorption cross section of ZnSe (5×10^{-15} cm^2).[45] The other rate constants were determined here: $k_{Mn} = 2640$ s^{-1} from Fig. 4.2, and $k_{QD} = 3\times10^9$ s^{-1} from the slow component of Fig. 4.3B. From the fast component of Fig. 4.3B, we estimate $k_{et} \geq$ ~3×10^{10} s^{-1}, and a value of $k_{et} = 5\times10^{10}$ s^{-1} is taken for the model calculations. This effective rate constant encompasses variations due to distributions in QD size or Mn^{2+} position. To convert excited state populations to PL intensities, the populations calculated from eqs 1 and 2 were scaled by the quantum yields and lifetimes of the two emissive excited states, which were either measured directly or determined from experimental data using the calculated dopant distribution (see below). In all model calculations reported here, the Auger cross-relaxation rate constants are therefore the only variable parameters. From the data in Fig. 4.3B, the cross-relaxation rate constant is estimated to be on the same order of magnitude as k_{et} for the following reasons: In the limit of slow cross relaxation, the apparent exciton decay time would increase upon Mn^{2+} PL saturation, but no increase is observed. Similarly, in the limit of fast cross relaxation, the apparent exciton decay time would decrease upon Mn^{2+} PL saturation, but this decrease is not observed. An initial trial value of 5×10^{10} s^{-1} ($\approx k_{et}$) was therefore taken for the model calculations. As described in Section C (below), simulations of the power dependence data using eqs 1 and 2 ultimately yield a cross-relaxation rate constant of $>2\times10^{10}$ s^{-1}.

Mn*-Mn* annihilation was purposefully omitted from this model. The data in Fig. 4.3C and those reported previously in ref. 38 for related CdS/Mn^{2+}:ZnS nanocrystals demonstrate that the Mn^{2+} PL decay time is unaltered in the saturation regime. This behavior contrasts with the reduced Mn^{2+} PL lifetimes observed with increased excitation densities in related bulk materials, which suggested Mn* energy migration followed by Mn*-Mn* cross relaxation.[11-15] Such

processes occur on the ten-microsecond timescale[14,15] and they become slower at lower Mn^{2+} concentrations.[49] Mn*-Mn* cross relaxation is therefore far too slow to be responsible for the PL saturation in Figs. 1-3.

Exciton-exciton Auger relaxation has also been deliberately omitted. Under the CW or quasi-CW excitation conditions used here, the excitation rate constants are too small to photoexcite a QD twice within the exciton lifetimes found in Fig. 4.3. Exciton-exciton Auger relaxation can therefore be ruled out as the origin of the Mn^{2+} PL saturation in Figs. 1-3.

4.4.B. Dopant distributions.

A realistic description of the distribution of Mn^{2+} within the experimental ensemble of nanocrystals is critical. Whereas analytical techniques provide the global average number of Mn^{2+} per average QD ($\bar{m}$), it is generally recognized that these Mn^{2+} are distributed among the QDs according to Poissonian statistics. Figure 4.5 plots the Poissonian distribution expected for $\bar{m}$ = 4.5. In any real sample, however, the QD size distribution is also an important aspect of the dopant distribution, because small changes in diameter correspond to large changes in nanocrystal volume. Figure 4.5 therefore also plots the distribution of Mn^{2+} ions ($\bar{m}$ = 4.5) within an ensemble of d_{avg} = 4.5 nm nanocrystals (core diameter of the QDs used for Figs. 1-3) with a Gaussian distribution in particle diameter described by a half-width of 2 nm (or σ = 0.85 nm, as estimated from the absorption spectrum), obtained by calculating a Poissonian distribution of dopants at each QD volume within the size distribution (see Appendix). This more realistic distribution is broader than the one obtained for uniform d = 4.5 nm nanocrystals. Specifically, more nanocrystals contain no Mn^{2+}, and more nanocrystals contain larger numbers of Mn^{2+}. For the kinetics calculations, differential equations were generated and solved for each value of m within this distribution.

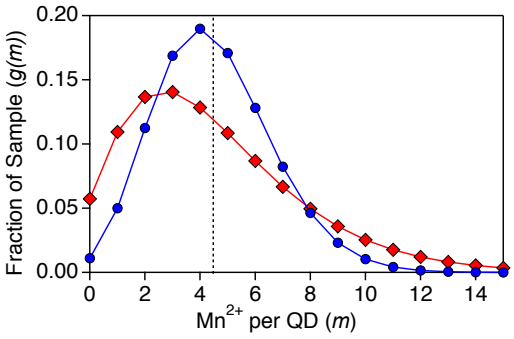

Figure.4.5: Distributions of Mn^{2+} ions over the ensemble of Mn^{2+}:ZnSe/ZnS/CdS/ZnS nanocrystals from the sample of Fig. 4.1, possessing Mn^{2+}:ZnSe cores with an average diameter of d_{avg} = 4.5 nm and an average number of Mn^{2+}/QD of $\bar{m}$ = 4.5. The dashed line indicates the average of $\bar{m}$ = 4.5 Mn^{2+}/QD. The circles indicate the Poissonian distribution calculated for uniform d = 4.5 nm nanocrystals. The diamonds indicate the distribution calculated by folding the Poissonian dopant distribution with a Gaussian nanocrystal size distribution for d_{avg} = 4.5 nm, σ = 0.85 nm. See Appendix for details.

4.4.C. Results of the model calculations.

Figure 4.6A shows the steady-state Mn^{2+} excited-state populations calculated from eqs 1 and 2 as a function of k_{ex} without any Auger quenching (k_{a1} = k_{a2} = 0), and with k_{a1} and k_{a2} independently set to 5×10^{10} s^{-1}, the value estimated from Fig. 4.3B. All three curves show population saturation in the same range of k_{ex}. Without any cross relaxation, the population distribution asymptotically approaches the limit in which all 4.5 Mn^{2+}/QD are in their $^4T_1$ excited state. This approach is slow because of the broad tailing distribution in Mn^{2+}/QD at large values (Fig. 4.5). When cross relaxation occurs with Mn^{2+} $^4T_1$ as its final state (k_{a2}), this same asymptote is approached, but more slowly. When the excitonic state is the final state of the cross-relaxation process (k_{a1}), saturation is reached with only about half of the total Mn^{2+}/QD in their excited state.

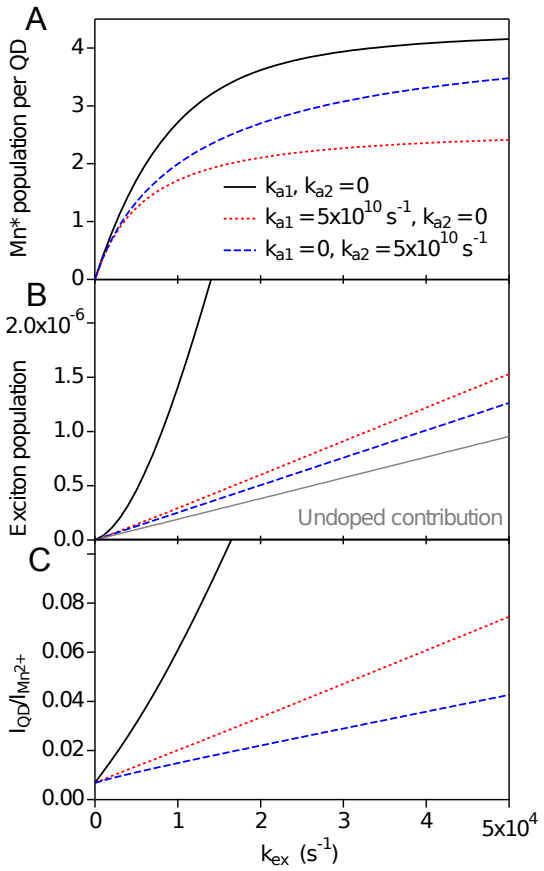

Figure 4.6. (A) Mn^{2+} excited-state population per QD as a function of the excitation rate constant k_{ex} for no Auger cross relaxation (—), for cross relaxation via k_{a1} = 5×10^{10} s^{-1} (···), and for cross relaxation via k_{a2} = 5×10^{10} s^{-1} (---). **(B)** Exciton population as a function of k_{ex} for the same values of k_{a1} and k_{a2}. The contribution from undoped QDs is shown in grey. **(C)** The ratio of exciton to Mn^{2+} steady-state photoluminescence intensities as a function of k_{ex} for the same values of k_{a1} and k_{a2}.

The exciton population is even more sensitive to the Auger processes, as shown in Fig. 4.6B. Without any cross relaxation, the exciton population rises rapidly and superlinearly as all of the Mn^{2+} become excited (solid curve). With Auger quenching, however, its dependence on k_{ex} becomes linear and is dominated by the undoped subset. The effects of k_{a1} and k_{a2} are very similar in this regard, but k_{a2} is slightly more effective at quenching the excitonic population.

Experimentally, it is easier to obtain accurate *relative* exciton and Mn^{2+} luminescence intensities than it is to obtain accurate absolute luminescence quantum yields of either independently. It is therefore valuable to explore how the ratio of these two intensities (I_{QD}/I_{Mn}) may reflect the proposed quenching processes. Figure 4.6C replots the calculated results from

Fig. 4.6B in this fashion and reveals important differences in I_{QD}/I_{Mn} for different Auger cross-relaxation rate constants. In the absence of cross relaxation, I_{QD}/I_{Mn} increases superlinearly to very large values over the experimental range of k_{ex}, reaching 0.38 at the right side of the plot. I_{QD}/I_{Mn} decreases substantially when Auger cross relaxation is introduced (either k_{a1} or $k_{a2} \neq 0$), and its dependence on k_{ex} becomes more linear. In addition, the value of the ratio at the maximum k_{ex} decreases with increasing cross relaxation rate constants. These changes reflect in part the greater relative contribution of the undoped QDs to the excitonic PL when cross relaxation is active. For illustration, setting $k_{a1} = k_{et}$ or $k_{a2} = k_{et}$ gives the two curves shown in Fig. 4.6C. These curves have values of $I_{QD}/I_{Mn} = 0.074$ and 0.043, respectively, at $k_{ex} = 5\times10^4$. Figure 4.6C thus illustrates that plotting I_{QD}/I_{Mn} vs k_{ex} allows assessment of the cross-relaxation rate constant. Additionally, the intercept at $k_{ex} = 0$ in Fig. 4.6C is independent of cross relaxation, being sensitive only to k_{et} and the relative contributions of doped and undoped nanocrystals to I_{QD}. The excitonic PL from undoped QDs can therefore be used as an internal reference in this analysis.

Figure 4.7 therefore re-plots the Mn^{2+} and excitonic PL intensities from Fig. 4.1B as I_{QD}/I_{Mn} vs k_{ex} for comparison with the model calculations. In addition to I_{QD}/I_{Mn}, the contributions from doped and undoped QDs to I_{QD}/I_{Mn} are plotted individually, as decomposed by the time-resolved PL data in Fig. 4.3. I_{QD}/I_{Mn} has an intercept of 0.0036 (0.0013 from doped QDs), and reaches a value of 0.10 (0.035 from doped QDs) at the right edge of the plot. Between these two values, the experimental power dependence of I_{QD}/I_{Mn} is essentially linear.

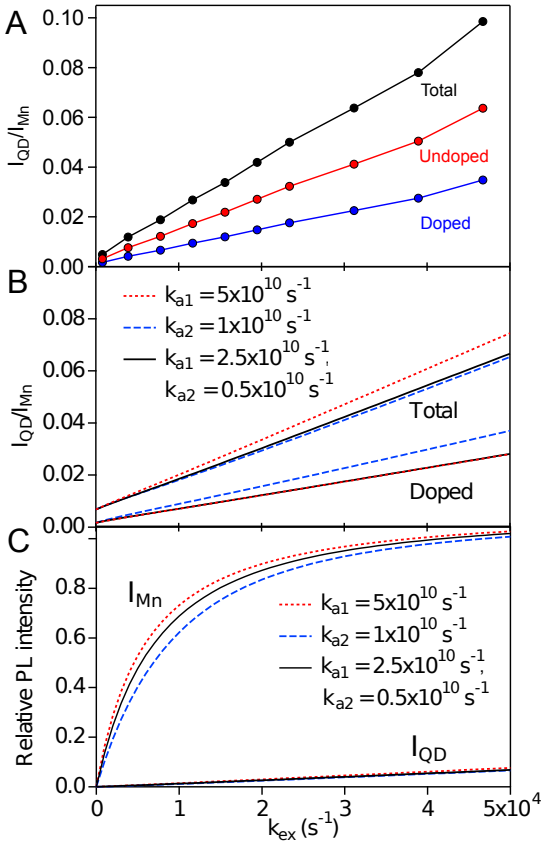

Figure 4.7. (A) Experimental PL ratios I_{QD}/I_{Mn} plotted as a function of excitation rate constant, from the PL intensities presented in Fig. 4.1B. The contributions from doped and undoped QDs to I_{QD} are also plotted independently. **(B)** I_{QD}/I_{Mn} calculated from eqs 1 and 2 using $k_{a1} \neq 0$, $k_{a2} \neq 0$, or a combination of the two. **(C)** I_{QD} and I_{Mn} calculated under the same conditions. At $k_{ex} = 5\times10^4\ s^{-1}$, Mn^{2+} excited-state populations were 2.4, 4.0, and 2.9 Mn*/QD for k_{a1}, k_{a2}, and the combination described in the inset.

As shown in Fig. 4.7B, the experimental results are reproduced well using either $k_{a1} = 5\times10^{10}\ s^{-1}$, $k_{a2} = 1\times10^{10}\ s^{-1}$, or both parameters at half of these values. The calculated curves reproduce the linearity, slopes, intercepts, and relative contributions of doped and undoped (= total - doped, not plotted) QDs seen in the experimental data. Decreasing the cross-relaxation rate constant by less than one order of magnitude yields substantially different slopes and intercepts that do not reproduce the experimental results (*vide infra*). We therefore conclude that the cross-relaxation rate constant is $\sim10^{10}\ s^{-1}$ or faster.

With the kinetic parameters from Fig. 4.7B, the individual PL intensities I_{Mn} and I_{QD} can now be calculated under the same conditions, and these results are presented in Fig. 4.7C for

comparison with Fig. 4.1. The calculations show 2.4, 4.0, or 2.9 excited Mn^{2+} per QD at k_{ex} = 5×10^{4} s^{-1} for k_{a1} = 5×10^{10} s^{-1}, k_{a2} = 1×10^{10} s^{-1}, or both parameters at half of these values, respectively. For the same rate constants, excitonic steady-state populations reach only ~10^{-6}/per QD, with approximately two thirds of this population originating from undoped particles.

The ability of the model calculations to determine the cross-relaxation rate constants quantitatively can be assessed by plotting I_{QD}/I_{Mn} vs these rate constants. Figure 4.8A plots the dependence of I_{QD}/I_{Mn} on k_{a1} for fixed k_{ex} = 4×10^{4} s^{-1} (high power regime). Initially, I_{QD}/I_{Mn} decreases sharply with increasing k_{a1}. At larger k_{a1}, however, I_{QD}/I_{Mn} increases again gradually. Examination of the doped and undoped QD contributions individually shows that I_{QD} at high powers is mostly due to undoped nanocrystals. For the doped subset, I_{QD}/I_{Mn} is large at small k_{a1} but decreases sharply with increasing k_{a1}, asymptotically approaching a value of 0.02. The most significant aspect of Fig. 4.8A is the crossing point around k_{a1} = 2×10^{10} s^{-1}, where the excitonic PL from undoped nanocrystals surpasses that from doped nanocrystals. From the experimental data in Fig. 4.3, the excitonic PL from undoped QDs is twice that of doped QDs, indicating that the cross-relaxation rate constant in the experimental samples must be to the right of this crossing point. Reasonable agreement with experiment in both absolute values and relative contributions from doped and undoped QDs is achieved for k_{a1} ~ 5×10^{10} s^{-1}. A similar conclusion is obtained from analysis of the dependence of I_{QD}/I_{Mn} on k_{a2} (see Supporting Information).

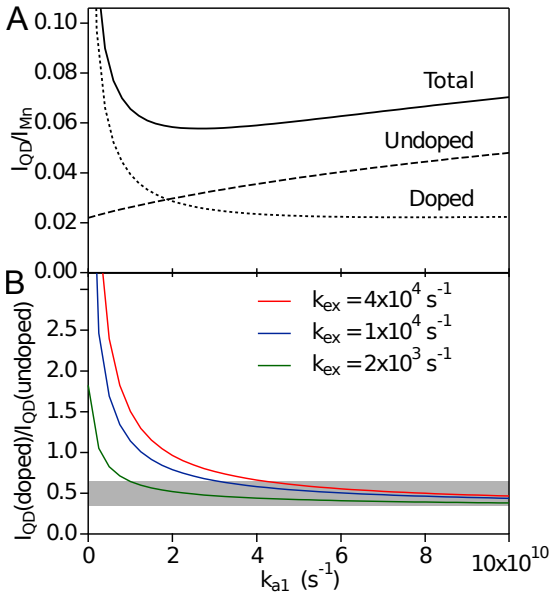

Figure 4.8. (A) I_{QD}/I_{Mn} calculated as a function of the cross-relaxation rate constant k_{a1} at fixed k_{ex} = 4×10^4 s^{-1}. The contributions from doped (···) and undoped (---) excitonic PL are plotted individually. **(B)** The ratio of doped to undoped excitonic PL as a function of cross-relaxation rate constant (k_{a1}), at several excitation rate constants. The shaded region indicates the ratio observed experimentally.

Figure 4.8B plots the ratio of doped to undoped excitonic PL (I_{QD}(doped)/I_{QD}(undoped)) vs k_{a1} for three excitation rates. For all three curves, the ratio decreases sharply with increasing k_{a1} and then levels out. At small k_{a1}, the ratio depends strongly on k_{ex}, but at larger k_{a1} the curves converge to a value close to the ratio measured experimentally (~0.5, Figs. 3B, 7A), indicated by the shaded region. To reproduce I_{QD}(doped)/I_{QD}(undoped) quantitatively, including its independence from k_{ex} (Fig. 4.3B), the cross relaxation must have a rate constant of at least 4×10^{10} s^{-1}. A similar analysis assuming only $k_{a2} \neq 0$ yields a lower limit of k_{a2} = 2×10^{10} s^{-1} (see Supporting Information).

4.5. Discussion

Mn^{2+} PL saturation has been observed at low CW and quasi-CW excitation powers for a variety of nanocrystals including Mn^{2+}-doped ZnSe, CdS, and core/multishell nanocrystals. Previous studies of Mn^{2+} PL power dependence in Mn^{2+}-doped semiconductor nanocrystals used high-power pulsed excitation to achieve saturation, and saturation was attributed to multi-exciton

Auger recombination prior to energy transfer to Mn^{2+},[39] excitation of all Mn^{2+},[37] or sequential energy transfer to Mn^{2+} causing $Mn^{2+/3+}$ ionization.[38] Because saturation occurs at low CW excitation rates (Fig. 4.1), multi-exciton Auger recombination can be ruled out. If Mn^{2+} PL saturation resulted from sequential excitation of all Mn^{2+} ions, excitonic PL intensities would increase superlinearly as Mn^{2+} PL saturates, and exciton PL decay times would approach those of the undoped QDs. The results in Figs. 1B and 3B demonstrate that this is not the case. PL saturation due to excitation of all Mn^{2+} ions is therefore also ruled out. Nevertheless, two-pulse measurements (Fig. 4.2) unambiguously link Mn^{2+} PL saturation with photoexcitation of QDs that already contain Mn^{2+} in its $^4T_1$ excited state.

From the rapid reduction in PL quantum yield, it is evident that Mn^{2+} PL saturation is accompanied by efficient nonradiative deactivation. The experimental results implicate exciton-Mn^{2+} cross relaxation as the primary process reducing Mn^{2+} PL quantum yield with increasing excitation power. The analysis above demonstrates that this cross relaxation process has an effective rate constant comparable to that of energy transfer ($k_{et} = 5\times10^{10}$ s^{-1}). With inclusion of cross relaxation, the staircase excitation model (Fig. 4, eqs 1, 2) reproduces the experimental observations using a cross-relaxation rate constant of at least 2×10^{10} s^{-1}, with all other input parameters fixed from experiment, capturing the essence of the PL saturation effect. We note that the curves shown in Fig. 4.7 were generated without iterative fitting, which would undoubtedly yield better quantitative reproduction of the experimental data but would not improve our qualitative understanding of the underlying physical processes.

The kinetic model reproduces the main experimental observations, but it cannot definitively differentiate between the two possible microscopic processes of QD* $\rightarrow$ Mn* or Mn* $\rightarrow$ QD* energy transfer (described by k_{a1} and k_{a2}, respectively). The microscopic mechanism behind the cross relaxation thus remains an open question. A previous report has suggested that cross relaxation involves donor-type ionization of Mn^{2+} to form Mn^{3+} and a "hot electron,"[38] which would be accounted for by k_{a2} in eqs 1 and 2 assuming return to the Mn^{2+} $^4T_1$ excited state upon cooling. For cross relaxation to cause $Mn^{2+/3+}$ ionization, however, the exciton must be sufficiently energetic to excite the Mn^* into a photoionization state. The commonly referenced positions of the $Mn^{2+/3+}$ ionization levels in II-VI semiconductors, derived from resonant photoelectron spectroscopy (RPES), place the $Mn^{2+/3+}$ level ~3.5 eV below the valence band edge for bulk Mn^{2+}:CdS, Mn^{2+}:ZnSe, and Mn^{2+}:ZnS.[50,51] As such, $Mn^{2+/3+}$ ionization to the

conduction band from the $^4T_1$ state should *always* occur outside the semiconductor energy gap, and could therefore not be achieved with one additional quantum of band-gap energy delivered via energy transfer. The similarity of the PL saturation across a variety of doped semiconductor nanocrystals with substantially different energy gaps (Fig. 4.1) also argues against formation of any specific excited state during cross relaxation. This reasoning leads us to suggest that hot *excitons* (rather than hot electrons from $Mn^{2+/3+}$ ionization) are formed by the cross-relaxation process described here.

Mn^{2+} ionization energies in semiconductors are not fully understood, however, and it is conceivable that the lowest-energy $Mn^{2+/3+}$ photoionization actually occurs below the position estimated from RPES data. RPES data do show a minor peak ~1 eV below the VB edge, for example, but this peak is generally assigned as a "shake-up" satellite.[51] Excited-state absorption (ESA) measurements on Mn^{2+}-doped ZnS and ZnSe crystals also clearly show mid-gap absorption from the $^4T_1$ state as low as ~1 eV,[36,52,53] but numerous spin-allowed *d-d* transitions are expected in this same energy region, and ESA is furthermore unable to distinguish between donor- and acceptor-type photoionization processes. Computational studies suggest that this ESA spectrum derives entirely from *d-d* transitions.[54] Overall, the interpretation of this mid-gap absorption remains too tentative to draw firm conclusions about its relationship to RPES data.

The difference in PL saturation between bulk and nanocrystalline Mn^{2+}-doped semiconductors is also an interesting issue. Given the numerous reports of PL saturation in related phosphors,[9-11] saturation of the slow Mn^{2+} PL is not unexpected, but the low excitation rates and low Mn^{2+} concentrations at which it occurs in these nanocrystals appear to differentiate this saturation from those described in closely related bulk materials.[11-15] The same Mn^{2+}-exciton cross relaxation is undoubtedly active in bulk Mn^{2+}-doped semiconductors, but it is apparently not the dominant cause of saturation. In the nanocrystals investigated here, the Mn^{2+} concentrations are too small for energy migration of the type observed in bulk, and time-resolved measurements reveal no slow contributions to the Mn^{2+} excited-state decay dynamics. The colloidal Mn^{2+}-doped semiconductor nanocrystals are certainly conducive to observation of Mn^{2+}-exciton cross relaxation because of the absence of other nonlinear processes. Moreover, the longer intrinsic lifetimes of excitons in strongly quantum confined nanocrystals may favor Mn^{2+}-exciton cross relaxation. Finally, the dominance of Auger cross relaxation may reflect enhancement of Mn^{2+}-exciton exchange coupling for Mn^{2+} near the centers of the nanocrystals.

Beyond the interesting fundamental issues related to electronic structure, the observation of PL saturation at low CW excitation powers has important practical implications. Many excitation sources can readily reach power densities where saturation effects are not negligible (> ~100 mW/cm^2, Fig. 4.1), raising the possibility that PL quantum yields or other PL properties of Mn^{2+}-doped semiconductors may be unknowingly measured under nonlinear conditions. Certain measurements may even be difficult to perform *without* encountering power saturation, for example optical microscopy or single-particle spectroscopy, which often use power densities of kW/cm^2,[36,55] well within the saturation regime seen in Fig. 4.1. The highly efficient cross relaxation may thus define the performance limits of these phosphors in various applications. On the positive side, the high efficiency of Mn^{2+}-exciton cross relaxation should provide an effective route to light-driven PL modulation, an attractive technique for improving spatial resolution in optical microscopies.[56] PL modulation via Mn^{2+}-exciton cross relaxation should be more effective than via mid-gap ESA[36] because of the much greater absorption cross section of the band-to-band transitions ($\sigma_{QD} \sim 10^{-15}$ cm^2 vs $\sigma_{ESA} \sim 10^{-20}$ cm^2).

4.6. Summary

Mn^{2+} photoluminescence saturation with increasing excitation power has been observed in several Mn^{2+}-doped semiconductor nanocrystals using low-power CW and quasi-CW photoexcitation. Two-pulse photoexcitation experiments unambiguously associate this saturation with photoexcitation of QDs that already contain Mn^{2+} in its $^4T_1$ excited state. In the saturation regime, the lack of power dependence in the time-resolved excitonic PL implicates a non-radiative quenching process with kinetics similar to the exciton-to-Mn^{2+} energy transfer step, which occurs with $k_{et} \sim 10^{10}$ s^{-1}. An Auger-type cross relaxation involving nonradiative energy transfer between an excited-state Mn^{2+} and an exciton is proposed to explain the observations. A kinetic model has been developed that reproduces the experimental results using a cross-relaxation rate constant of at least 2×10^{10} s^{-1}. This highly efficient cross relaxation leads to reduced PL quantum yields whenever photoexcitation rate constants are comparable to Mn^{2+} decay rate constants, which are typically in the range $k_{Mn} \sim 10^3$ - 10^4 s^{-1} ($\tau \sim 0.1$ - 1.0 ms). Because of the large absorption cross sections of semiconductor nanocrystals and the fast energy transfer to Mn^{2+}, such excitation rate constants are easily achieved. PL nonlinearities can thus be expected under many conditions, including those used for optical imaging and single-particle

spectroscopies.[57,58] This highly efficient Mn^{2+}-exciton cross relaxation should provide an attractive alternative to Mn^{2+}-centered excited-state absorption for improving spatial resolution in optical microscopies via light-driven PL modulation.[56]

4.7. Addendum.

The average diameter ($d_{avg} \equiv d_0$) of an ensemble of doped nanocrystals can be determined from the average energy of the first excitonic absorption feature. From the width and shape of this exciton absorption band, a Gaussian distribution with a standard distribution in core diameter (σ) can be estimated as given by eq A1.

$$g(d) = \frac{1}{\sqrt{2\pi}\sigma} e^{-\frac{(d-d_0)^2}{2\sigma^2}} \tag{4.A1}$$

The volume of a given particle is $V(d) = \frac{\pi}{6} d^3$ and the distribution in core volume is therefore given by eq A2, which corresponds to a skewed Gaussian.

$$g(V) = g(d)\left(\frac{\partial V}{\partial d}\right)^{-1} = g(d)\frac{2}{\pi d^2} \tag{4.A2}$$

The average number of dopants per QD of volume V ($\bar{m}_V$) is proportional to the global average number of dopants per QD of average volume V_{av} ($\bar{m}$) as given by eq A3.

$$\bar{m}_V = \bar{m}\frac{V}{V_{avg}} \tag{4.A3}$$

The size distribution can thus be rewritten in terms of a dopant distribution as in eq A4.

$$g(\bar{m}_V) = g(V)\left(\frac{\partial m}{\partial V}\right)^{-1} = g(V)\frac{V_{avg}}{\bar{m}} \tag{4.A4}$$

Within each set of particles in the volume interval [V, V+dV], the actual number of dopants (m) per QD is given by a Poisson distribution around $\bar{m}_V$, weighted by the overall number of QDs with that $\bar{m}_V$, as in eq A5.

$$g(\bar{m}_V, m) = \frac{\bar{m}_V{}^m \cdot e^{-\bar{m}_V}}{m!} \cdot g(\bar{m}_V) \tag{4.A5}$$

Figure A1 shows a two-dimensional plot with $\bar{m}_V$ in one dimension and m in the other, calculated using $\bar{m}$ = 4.5, d_0 = 4.5 nm, and σ = 0.85 nm, *i.e.*, the parameters used for the simulations described in the manuscript text. For this plot, a Poissonian distribution was

calculated for each value of $\bar{m}_V$, with an area equal to $g(\bar{m}_V)$. The distribution in Fig. 4.5 was then generated from these data by integrating over all particles with the same number of dopants (m). Simulations were performed for each point along the distribution of Fig. 4.5 with the assumption that the QD size dependence of all rate constants can be neglected.

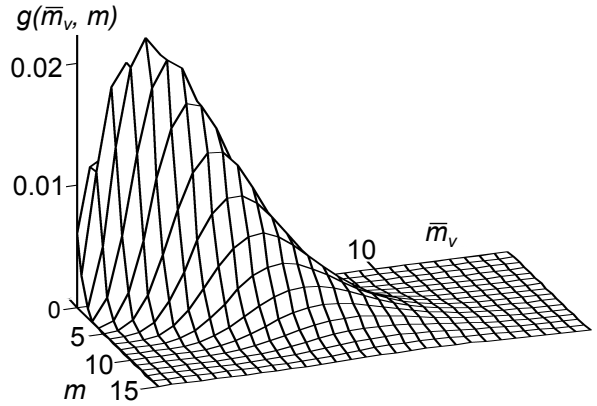

Figure 4.A1. Distribution function $g(\bar{m}_V, m)$, where $\bar{m}_V$ is the average number of dopants per QD of volume V and m is the actual number of Mn^{2+} per QD according to a Poissonian distribution around $\bar{m}_V$. This distribution function is calculated for $\bar{m} = 4.5$, $d_0 = 4.5$ nm, and $\sigma = 0.85$ nm.

4.8. References

(1) Yen, W. M.; Shionoya, S.; Yamamoto, H., (Eds.) *Fundamentals of Phosphors*. CRC Press: Boca Raton, 2006.

(2) Ronda, C.; (Ed.), *Luminescence: From Theory to Applications*. Wiley-VCH: Weinheim, 2008.

(3) Vlasenko, N. A.; Popkov, Y. A., Study of electroluminescence of a sublimated ZnS-Mn phosphor. *Optika I Spektroskopiya* **1960,** *8*, 81.

(4) Shibata, K.; Nakayama, E.; Souma, I.; Murayama, A.; Oka, Y., Exciton Recombination Processes in $Cd_{1-x}Mn_xSe$/ZnSe Quantum Dots under Magnetic Fields. *Phys. Stat. Sol. (b)* **2002,** *229*, 473.

(5) Seufert, J.; Bacher, G.; Scheibner, M.; Forchel, A.; Lee, S.; Dobrowolska, M.; Furdyna, J. K., Dynamical Spin Response in Semimagnetic Quantum Dots. *Phys. Rev. Lett.* **2002,** *88*, 027402.

(6) Chen, H.-Y.; Chen, T.-Y.; Son, D. H., Measurement of Energy Transfer Time in Colloidal Mn-Doped Semiconductor Nanocrystals. *J. Phys. Chem. C* **2010,** *114*, 4418.

(7) Vlaskin, V. A.; Janßen, N.; van Rijssel, J.; Beaulac, R.; Gamelin, D. R., Tunable Dual Emission in Doped Semiconductor Nanocrystals. *Nano Lett.* **2010,** *10*, 3670.

(8) Beaulac, R.; Ochsenbein, S. T.; Gamelin, D. R., Colloidal Transition-Metal-Doped Quantum Dots. In *Semiconductor Quantum Dots*, 2nd ed.; Klimov, V. I., Ed. CRC Press: 2010; pp 397.

(9) Mikoshiba, S.; Shirai, S.; Shinada, S.; Fukushima, M., Saturation of Zn_2SiO_4:Mn luminescence under intense VUV excitation. *J. Appl. Phys.* **1979,** *50*, 1088.

(10) de Leeuw, D. M.; 't Hooft, G. W., Method for the analysis of saturation effects of cathodoluminescence in phosphors; applied to Zn_2SiO_4:Mn and $Y_3Al_5O_{12}$:Tb. *J. Lumin.* **1983,** *28*, 275.
(11) Törnqvist, R., Manganese concentration dependent saturation in ZnS:Mn thin film electroluminescent devices. *J. Appl. Phys.* **1983,** *54*, 4110.
(12) Müller, G. O.; Neugebauer, J.; Mach, R.; Reinsperger, U., Excited state interaction in the dopant system in ZnS:Mn electroluminescence devices. *J. Cryst. Growth* **1990,** *86*, 890.
(13) Vereshchagin, I. K.; Kezik, V. I.; Pautkina, A. V., Quenching of the luminescence of ZnS:Mn at high excitation levels. *J. Appl. Spectroscopy* **1991,** *55*, 1175.
(14) Agekyan, V.; Vasil'ev, N.; Serov, A., Rapid luminescence saturation of the Mn^{2+} 3d shell in the $Cd_{1-x}Mn_xTe$ dilute magnetic semiconductor with a high manganese concentration. *Phys. Sol. State* **1999,** *41*, 41.
(15) Agekyan, V.; Vasil'ev, N.; Serov, A.; Filosofov, N., Intracenter Luminescence of Mn^{2+} in $Cd_{1-x}Mn_xTe$ and $Cd_{1-x-y}Mn_xMg_yTe$ under Intense Optical Pumping. *Phys. Sol. State* **2000,** *42*, 836.
(16) Gordon, N. T.; Allen, J. W., Auger quenching of luminescence in manganese-doped zinc sulfide. *Sol. St. Comm.* **1981,** *37*, 441.
(17) Gumlich, H.-E., Electro- and photoluminescence properties of Mn^{2+} in ZnS and ZnCdS. *J. Lumin.* **1981,** *23*, 73.
(18) Langer, J. M., Where the metal-semiconductor junction emits light. *J. Lumin.* **1981,** *23*, 141.
(19) Langer, J. M.; Lemanska-Bajorek, A.; Suchocki, A., A method of excitation profiling in high-field electroluminescence. *Appl. Phys. Lett* **1981,** *39*, 386.
(20) Bacher, G.; Schömig, H.; Scheibner, M.; Forchel, A.; Maksimov, A. A.; Chernenko, A. V.; Dorozhkin, P. S.; Kulakovskii, V. D.; Kennedy, T.; Reinecke, T. L., Spin–spin interaction in magnetic semiconductor quantum dots. *Physica E* **2005,** *26*, 37.
(21) Beaulac, R.; Archer, P. I.; Ochsenbein, S. T.; Gamelin, D. R., Mn^{2+}-Doped CdSe Quantum Dots: New Inorganic Materials for Spin-Electronics and Spin-Photonics. *Adv. Funct. Mater.* **2008,** *18*, 3873.
(22) Henneberger, F.; Puls, J., Diluted Magnetic Quantum Dots. In *Introduction to the Physics of Diluted Magnetic Semiconductors*, Kossut, J.; Gaj, J. A., Eds. Springer-Verlag Berlin: Berlin, 2010; Vol. 144, pp 161.
(23) Besombes, L.; Léger, Y.; Maingault, L.; Ferrand, D.; Mariette, H.; Cibert, J., Probing the Spin State of a Single Magnetic Ion in an Individual Quantum Dot. *Phys. Rev. Lett.* **2004,** *93*, 207403.
(24) Besombes, L.; Léger, Y.; Maingault, L.; Mariette, H., Spin properties of charged Mn-doped quantum dot. *J. Appl. Phys.* **2007,** *101*, 081713.
(25) Léger, Y.; Besombes, L.; Fernández-Rossier, J.; Maingault, L.; Mariette, H., Electrical Control of a Single Mn Atom in a Quantum Dot. *Phys. Rev. Lett.* **2006,** *97*, 107401.
(26) Léger, Y.; Besombes, L.; Maingault, L.; Ferrand, D.; Mariette, H., Geometrical Effects on the Optical Properties of Quantum Dots Doped with a Single Magnetic Atom. *Phys. Rev. Lett.* **2005,** *95*, 047403.
(27) Maingault, L.; Besombes, L.; Léger, Y.; Bougerol, C.; Mariette, H., Inserting one single Mn ion into a quantum dot. *Appl. Phys. Lett.* **2006,** *89*, 193109.
(28) Cerletti, V.; Coish, W. A.; Gywat, O.; Loss, D., Recipes for spin-based quantum computing. *Nanotechnology* **2005,** *16*, R27.
(29) Koenraad, P. M.; Flatte, M. E., Single dopants in semiconductors. *Nat. Mater.* **2011,** *10*, 91.

(30) Beaulac, R.; Schneider, L.; Archer, P. I.; Bacher, G.; Gamelin, D. R., Light-Induced Spontaneous Magnetization in Colloidal Doped Quantum Dots. *Science* **2009,** *325*, 973.
(31) Ochsenbein, S. T.; Feng, Y.; Whitaker, K. M.; Badaeva, E.; Liu, W. K.; Li, X.; Gamelin, D. R., Charge-Controlled Magnetism in Colloidal Doped Semiconductor Nanocrystals. *Nature Nanotechnology* **2009,** *4*, 681.
(32) Beaulac, R.; Archer, P. I.; van Rijssel, J.; Meijerink, A.; Gamelin, D. R., Exciton Storage by Mn^{2+} in Colloidal Mn^{2+}-Doped CdSe Quantum Dots. *Nano Lett.* **2008,** *8*, 2949.
(33) McLaurin, E. J.; Vlaskin, V. A.; Gamelin, D. R., Water-Soluble Dual-Emitting Nanocrystals for Ratiometric Optical Thermometry. *J. Am. Chem. Soc.* **2011,** *133*, 14978.
(34) Wang, S.; Jarrett, B. R.; Kauzlarich, S. M.; Louie, A. Y., Core/Shell Quantum Dots with High Relaxivity and Photoluminescence for Multimodality Imaging. *J. Am. Chem. Soc.* **2007,** *129*, 3848.
(35) Pradhan, N.; Battaglia, D. M.; Liu, Y.; Peng, X., Efficient, Stable, Small, and Water-Soluble Doped ZnSe Nanocrystal Emitters as Non-Cadmium Biomedical Labels. *Nano Lett.* **2007,** *7*, 312.
(36) Irvine, S. E.; Staudt, T.; Rittweger, E.; Engelhardt, J.; Hell, S. W., Direct light-driven modulation of luminescence from Mn-doped ZnSe quantum dots. *Angew. Chem.* **2008,** *47*, 2685.
(37) Chen, O.; Shelby, D. E.; Yang, Y.; Zhuang, J.; Wang, T.; Niu, C.; Omenetto, N.; Cao, Y. C., Excitation-Intensity-Dependent Color-Tunable Dual Emissions from Manganese-Doped CdS/ZnS Core/Shell Nanocrystals. *Angew. Chem.* **2010,** *49*, 10132.
(38) Chen, H.-Y.; Chen, T.-Y.; Berdugo, E.; Park, Y.; Lovering, K.; Son, D. H., Hot Electrons from Consecutive Exciton-Mn Energy Transfer in Mn-Doped Semiconductor Nanocrystals. *J. Phys. Chem. C.* **2011,** *115*, 11407.
(39) Taguchi, S.; Ishizumi, A.; Kanemitsu, Y., Multicarrier Recombination and Energy Transfer in Mn-Doped CdS Nanocrystals Studied by Femtosecond Pump–Probe Spectroscopy. *J. Phys. Soc. Jpn.* **2010,** *79*, 063710.
(40) White, M. A.; Weaver, A. L.; Beaulac, R.; Gamelin, D. R., Electrochemically Controlled Auger Quenching of Mn^{2+} Photoluminescence in Doped Semiconductor Nanocrystals. *ACS Nano* **2011,** *5*, 4158.
(41) Archer, P. I.; Santangelo, S. A.; Gamelin, D. R., Inorganic Cluster Syntheses of TM^{2+}-Doped Quantum Dots (CdSe, CdS, CdSe/CdS): Physical Property Dependence on Dopant Locale. *J. Am. Chem. Soc.* **2007,** *129*, 9808.
(42) Li, J. J.; Wang, A. Y.; Guo, W.; Keay, J. C.; Mishima, T. D.; Johnson, M. B.; Peng, X., Large-Scale Synthesis of Nearly Monodisperse CdSe/CdS Core/Shell Nanocrystals using Air-Stable Reagents via Successive Ion Layer Adsorption and Reaction. *J. Am. Chem. Soc.* **2003,** *125*, 12567.
(43) Chen, H.-S.; Lo, B.; Hwang, J.-Y.; Chang, G.-Y.; Chen, C.-M.; Tasi, S.-J.; Wang, S.-J. J., Colloidal ZnSe, ZnSe/ZnS, and ZnSe/ZnSeS Quantum Dots Synthesized from ZnO. *J. Phys. Chem. B* **2004,** *108*, 17119.
(44) Nag, A.; Chakraborty, S.; Sarma, D. D., To Dope Mn^{2+} in a Semiconducting Nanocrystal. *J. Am. Chem. Soc.* **2008,** *130*, 10605.
(45) Norberg, N. S.; Parks, G. L.; Salley, G. M.; Gamelin, D. R., Giant Excitonic Zeeman Splittings in Colloidal Co^{2+}-Doped ZnSe Quantum Dots. *J. Am. Chem. Soc.* **2006,** *128*, 13195.
(46) Reiss, P.; Protiere, M.; Li, L., Core/Shell Semiconductor Nanocrystals. *Small* **2009,** *5*, 154.

(47) Kurbanov, S. S.; Igamberdiev, K. T.; Kang, T. W., The UV-laser induced heating effect on photoluminescence from ZnO nanocrystals deposited on different substrates. *J. Phys. D* **2010,** *43*, 115401.
(48) McGuire, J. A.; Sykora, M.; Robel, I.; Padilha, L. A.; Joo, J.; Pietryga, J. M.; Klimov, V. I., Spectroscopic Signatures of Photocharging due to Hot-Carrier Transfer in Solutions of Semiconductor Nanocrystals under Low-Intensity Ultraviolet Excitation. *ACS Nano* **2010,** *4*, 6087.
(49) Benalloul, P.; Benoit, J.; Duran, J.; Evesque, P.; Geoffroy, A., Diffusion and trapping in ZnS:Mn electroluminescent thin films. *Sol. State Comm.* **1984,** *51*, 389.
(50) Taniguchi, M.; Fujimori, M.; Fujisawa, M.; Mori, T.; Souma, I.; Oka, Y., Mn 3d partial density-of-states and p-d hybridization in $Cd_{1-x}Mn_xY$ (Y = S, Se and Te). *Sol. State. Comm.* **1987,** *62*, 431.
(51) Weidemann, R.; Gumlich, H. E.; Kupsch, M.; Middelmann, H. U.; Becker, U., Partial density of Mn 3d states and exchange-splitting changes in $Zn_{1-x}Mn_xY$ (Y=S,Se,Te). *Phys. Rev. B* **1992,** *45*, 1172.
(52) Dreyhsig, J.; Allen, J. W., Absorption from the Excited State in ZnS:Mn. *J. Phys.: Condens. Matter* **1989,** *1*, 1087.
(53) Dreyhsig, J.; Stutenbäumer, U.; Gumlich, H. E.; Allen, J. W., Excited State Absorption (ESA) of Mn in ZnS and ZnSe. *J. Cryst. Growth* **1990,** *101*, 443.
(54) Stavrev, K. K.; Zerner, M. C., On the Jahn-Teller effect on Mn^{2+} in zinc-blende ZnS crystal. *J. Chem. Phys.* **1995,** *102*, 34.
(55) Ebenstein, Y.; Mokari, T.; Banin, U., Fluorescence quantum yield of CdSe/ZnS nanocrystals investigated by correlated atomic-force and single-particle fluorescence microscopy. *Appl. Phys. Lett.* **2002,** *80*, 4033.
(56) Gustafsson, M. G. L., Nonlinear structured-illumination microscopy: Wide-field fluorescence imaging with theoretically unlimited resolution. *Proc. Nat. Acad. Sci.* **2005,** *102*, 13081.
(57) Zhang, Y. P.; Gan, C. L.; Muhammad, J.; Battaglia, D.; Peng, X. G.; Xiao, M., Enhanced Fluorescence Intermittency in Mn-Doped Single ZnSe Quantum Dots. *J. Phys. Chem. C* **2008,** *112*, 20200.
(58) Ishizumi, A.; Kanemitsu, Y., Blinking Behavior of Surface-Defect and Impurity Luminescence in Nondoped and Mn^{2+}-Doped CdS Nanocrystals. *J. Phys. Soc. Jpn.* **2009,** *78*, 083705.

Chapter 5. Nanocrystals for Luminescent Solar Concentrators

Abstract. Luminescent solar concentrators (LSCs) harvest sunlight over large areas and concentrate this energy onto photovoltaics or for other uses by transporting photons through macroscopic waveguides. Although attractive for lowering solar energy costs, LSCs remain severely limited by luminophore reabsorption losses. Here, we report a quantitative comparison of four types of nanocrystal phosphors recently proposed to minimize reabsorption in large-scale LSCs: two nanocrystal heterostructures and two doped nanocrystals. Experimental and numerical analyses both show that even the small core absorption of the leading NC heterostructures causes major reabsorption losses at relatively short transport lengths. Doped NCs outperform the heterostructures substantially in this critical property. A new LSC phosphor is introduced, $Cd_{1-x}Cu_xSe$ nanocrystals, that outperforms all other leading NCs by a significant margin in both small- and large-scale LSCs under full-spectrum conditions.

5.1 Introduction

Luminescent solar concentrators (LSCs) are antenna systems that harvest sunlight and concentrate photons through the processes of photon absorption, luminescence, and waveguiding. One attractive LSC device comprises a planar waveguide containing embedded luminophores with photovoltaics (PVs) mounted at the waveguide edges, as depicted in Figure 5.1A. In this device, the concentrated photons are converted to electricity by the PVs, allowing large-area solar harvesting while requiring only small-area PVs. Such LSCs can possibly lower the cost of solar energy.[1-3] Specific LSC applications include solar collectors for integration into existing windows, electronic devices, or fiber optics,[3, 4] photon transport for passive daylighting,[5, 6] and active color filters (*e.g.*, in tandem PV cells[7] or greenhouse panels[8]). Regardless of their specific application, LSCs universally rely on photon transport over macroscopic distances, which makes them susceptible to a variety of loss mechanisms. For a waveguide as in Figure 5.1A made of glass or plastic ($n \sim 1.5$), approximately 75% of the emitted photons are successfully trapped in waveguide modes,[1] with the remainder lost to the "escape-cone" defined by Snell's law. Photons that are captured by total internal reflection can still be lost via scattering from the waveguide surface, internal defects, or even the luminophores themselves (such as with microcrystalline phosphors[9]), or via reabsorption by the luminophores followed by non-radiative decay or emission into the escape cone. Reabsorption losses have historically limited practical implementation of large-scale LSCs.[3, 10, 11]

Recent advances in the synthesis of luminescent nanocrystals (NCs) with high photoluminescence (PL) quantum yields, tunable solar absorption, and good photostability have stimulated interest in nanocrystals for LSC technologies.[12-14] Several reports have claimed that NCs can solve the reabsorption problem.[15-19] One strategy for eliminating self-absorption using NCs involves the growth of nanocrystal heterostructures that integrate wider-gap semiconductors with small cores having a narrower bandgap (*e.g.*, CdS on CdSe cores, Figure 5.1B-i,ii).[15, 18, 19] In such NCs, the wider-gap material dominates the absorption spectrum, and red-shifted luminescence occurs either from the core or from spatially indirect transitions across the heterointerface. Large shell:core volume ratios imply small relative absorption from the luminescent excited state. Doped semiconductor NCs have also been demonstrated to show small LSC reabsorption losses.[17] In Mn^{2+}-doped ZnSe NCs, for example, the NC efficiently sensitizes excitation of Mn^{2+} impurity ions to their $^4T_1$ ligand-field excited state, which emits with high quantum yield and a very large effective Stokes shift that results in little or no reabsorption losses in the corresponding LSCs.[17]

The vastly different device configurations used in previous studies of nanocrystal LSCs make direct comparison of nanocrystal performance difficult. For example, device thicknesses ranged from a few hundred microns[16, 17] to over 1 cm,[15, 18] and transverse optical densities at the NCs' first absorption features (OD_t) ranged from 0.1 to 0.6. Both of these parameters affect reabsorption, which is proportional to the concentration of luminophore and hence determined by the ratio of OD_t to waveguide thickness (t) according to Beer's law. For practical applications, both OD_t and t will undoubtedly require careful optimization in planar 2-D LSCs based on physical and economic criteria, and developments in microcell LSCs[20, 21]or other configurations may even lead to entirely new structural paradigms, but advances in the development of LSC luminophores need not be conflated with these device-level considerations.

Here, we report the quantitative assessment of four types of nanocrystals as potential LSC luminophores: the core/shell and dot-in-rod heterostructures of Figure 5.1B-i,ii, and two new doped-nanocrystal LSC phosphors. In one, we have modified our previously reported motif of Mn^{2+}-doped ZnSe NCs by incorporating Cd^{2+} to increase solar absorption (Figure 5.1B-iii). For capture of an even broader portion of the solar spectrum, we have also used narrower-gap CdSe NCs to sensitize Cu^+ luminescence (Figure 5.1B-iv). To date, there have been no reports of any copper-doped nanocrystal LSCs. We note additionally that the synthetic techniques employed to

make these doped NCs are novel and produce NCs with the highest reported PL quantum yields to date. Further, these materials allow facile tunability of the solar absorption edge, which is much more difficult in heterostructure materials that are constrained by the bulk bandgap of the sensitizing material. This tunability across the entire visible spectrum afforded by these two doped NCs broadens the potential applications of LSCs considerably.

Using a one-dimensional liquid waveguide with translatable excitation (Figure 5.1C) as a standard device geometry, we have quantified the reabsorption losses of these four types of nanocrystals by measuring their luminescence spectra as a function of photon transport distance, *L*, up to 1.2 m, encompassing the length scales considered relevant for practical solar windows, panels, or daylighting, for example. These measurements agree well with the reabsorption probabilities predicted from NC absorption and PL spectra. The results show that reabsorption losses remain a major problem for the two leading heterostructured NC phosphors, but are more effectively eliminated in both types of doped semiconductor NCs. In particular, the copper-doped NCs are found to be the "best-in-class" phosphors, outperforming the other nanocrystals in total solar concentration at both short and long LSC lengths. In addition to highlighting doped NCs as a promising new class of LSC luminophores, this work provides a benchmark for quantitative evaluation of new LSC luminophores developed in the future.

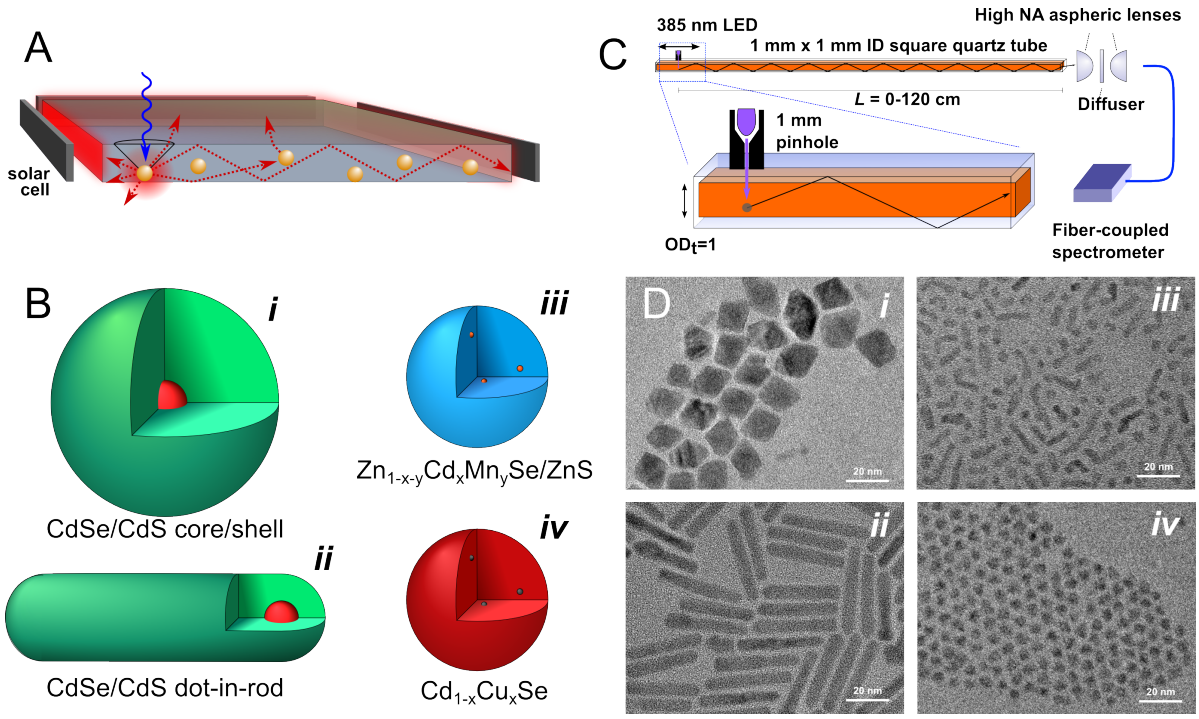

Figure 5.1. (A) A typical planar LSC configuration, in which a luminophore (yellow spheres) is incorporated into a waveguide material surrounded on all edges by solar cells. Sunlight (blue arrow) is absorbed by the luminophore, and the luminescence (red arrows) is waveguided to the solar cells at the edges. **(B)** Schematic depictions of four types of nanocrystals proposed for use in LSCs. **(C)** Schematic depiction of the apparatus used for measuring excitation distance dependent PL spectra. **(D)** TEM images of the NCs investigated here: (*i*) CdSe/CdS core/shell NCs, (*ii*) CdSe/CdS dot-in-rod NCs, (*iii*) $Zn_{0.87}Cd_{0.11}Mn_{0.02}Se/ZnS$ NCs, and (*iv*) representative $Cd_{0.999}Cu_{0.001}Se$ NCs.

5.2 Results

Nanocrystals of the types illustrated in Figure 5.1B were prepared by literature methods (see Methods). Figure 5.1D shows representative TEM images of the CdSe/CdS core/shell NCs, CdSe/CdS dot-in-rod NCs, $Zn_{0.87}Cd_{0.11}Mn_{0.02}Se/ZnS$ NCs, and $Cd_{0.999}Cu_{0.001}Se$ NCs used in this study. The core/shell NCs of Figure 5.1D-i and the dot-in-rod NCs of Figure 5.1D-ii were grown using the same d = 2.7 nm wurtzite CdSe cores. The CdSe/CdS core/shell NCs appear to be octahedrally faceted, with an average side length of 13.5 nm, implying a CdS:CdSe volume ratio of 114:1. The CdSe/CdS dot-in-rod NCs have an average overall dimension of 6.1 nm × 32.2 nm, and a CdS:CdSe volume ratio of 110:1. Figure 5.1D-iii shows $Zn_{0.87}Cd_{0.11}Mn_{0.02}Se/ZnS$ NCs with an average diameter of 3.8 nm, some of which appear to have undergone "oriented attachment"[22] to form short rods.[23] The $Zn_{0.87}Cd_{0.11}Mn_{0.02}Se$ cores showed an average diameter

of 3.2 nm and a similar distribution of shapes. The $Cd_{0.999}Cu_{0.001}Se$ NCs shown in Figure 5.1D-iv appear roughly spherical with an average diameter of 5.7 nm.

Figure 5.2A plots absorption and PL spectra of the same NCs, all with concentrations adjusted to reach OD ~ 1 at the first intense absorption feature in a 1 mm pathlength cuvette. The wavelengths of these first absorption features (λ_{thresh}) are listed in Table 5.1. These data confirm previously reported spectra of similar samples. From these spectra, all samples appear to have minimal overlap between absorption and luminescence, as desired for LSC applications. It is important to recognize, however, that the critical transport direction in LSCs is lateral, not normal to the surface, and that lateral device dimensions are typically orders of magnitude larger than the pathlengths used to collect these and other published NC absorption spectra. To illustrate, Figure 5.2B plots absorption spectra of the same NC solutions measured using a 1-cm pathlength cuvette and magnified tenfold for an effective 100x magnification. Absorption features from the CdSe cores of the CdSe/CdS heterostructures are now clearly visible, but the $Zn_{0.87}Cd_{0.11}Mn_{0.02}Se/ZnS$ and $Cd_{0.999}Cu_{0.001}Se$ NCs still show only weak, broad absorption in the vicinity of their PL. Based on Mn^{2+}-doped ZnS thin films,[24] the extinction coefficient associated with the luminescent $^6A_1 \rightarrow {}^4T_1$ transition is on the order of 1 $M^{-1}cm^{-1}$, corresponding to an OD of less than 7×10^{-5} in Figure 5.2B. We thus attribute the small tail in the $Zn_{0.87}Cd_{0.11}Mn_{0.02}Se/ZnS$ absorption spectrum to NC surface states, or possibly trace impurities in solution, but not to the luminescent center itself. Indeed, some of this absorption tail could be removed by addition of tri-butyl phosphine (TBP, see Figure S1), which suggests it may arise from NC surface oxidation. Overall, this feature has an absorbance of 0.01 at 600 nm over 1 cm, and the TBP also contributes small vibrational overtone absorption peaks at 850 and 925 nm. The $Cd_{0.999}Cu_{0.001}Se$ NCs have a small amount of strongly reabsorbed excitonic PL from a subset of undoped NCs, which accounts for roughly 3% of the overall PL. The magnified absorption spectrum of these NCs shows a broad absorption tail that overlaps the blue edge of the redshifted PL feature (700-850 nm). We attribute this absorption to the $ML_{CB}CT$ transition that is responsible for the PL.[25] Much of the $Cd_{0.999}Cu_{0.001}Se$ PL is shifted to even longer wavelengths (>850 nm), where the absorption spectrum shows only a very small tail that is again likely due to NC surface states.

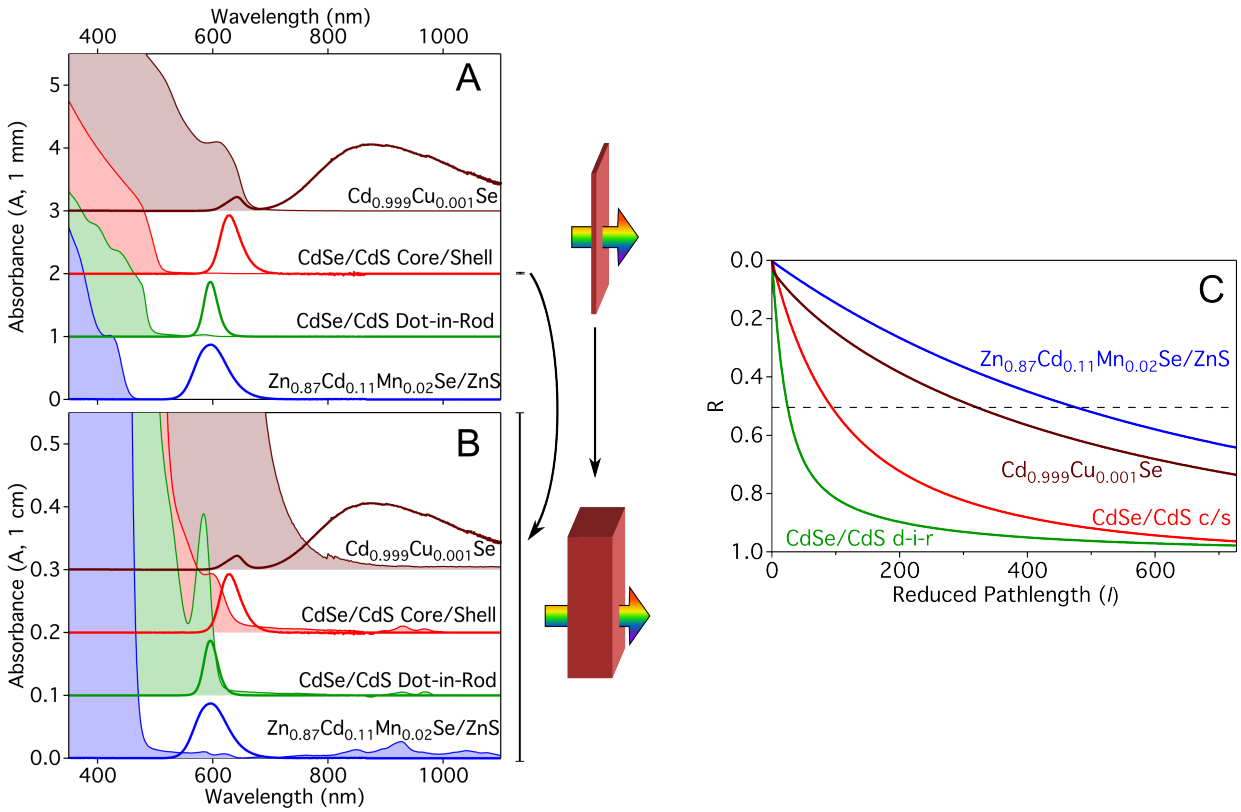

Figure 5.2. (A) Absorption spectra (solid lines with shading) over a 1 mm pathlength, and dilute photoluminescence spectra of $Cd_{0.999}Cu_{0.001}Se$ (maroon, d = 5.7 nm), CdSe/CdS core/shell NCs (red, core d = 2.7 nm), CdSe/CdS dot-in-rod NCs (green, core d = 2.7 nm) and $Zn_{0.87}Cd_{0.11}Mn_{0.02}Se/ZnS$ (blue, core d = 3.2 nm). **(B)** Absorption spectra of the same samples measured in a 1-cm pathlength cuvette illustrating the overlap between absorption and PL. Note the 10x magnified y axis. **(C)** Reabsorption probability, $R(l)$, calculated from the spectra in Figure 5.2B according to equation 5.1 and plotted versus l. The dashed line indicates $R_{0.5}$, which for a given sample represents the value of l corresponding to 50% probability of reabsorption.

Table 5.1. Characterization metrics for nanocrystalline LSC phosphors.

NC Sample	λ_{thresh} (nm)	$R_{0.5}$[a]	$L_{1/2}$ (cm)[b]	η_{PL}[c]	Abs. Solar Flux[f] ($A_{sol,NC}$) $\times 10^{20}$	Projected FG 120cm x 120cm 2-D LSC (G = 300)	Projected FG_{max} for 2-D LSC
$Zn_{0.87}Cd_{0.11}Mn_{0.02}Se/ZnS$	429	470	118	0.88[d]	1.5	8.6	32.9
$Cd_{0.999}Cu_{0.001}Se$	624	320	42	0.27[d] (0.40[d])	8.9	10.1 (16.0)[g]	15.6 (26.2)[g]
CdSe/CdS core/shell	480	92	12	0.68[d] (0.86[e])	3.3	5.7 (9.0)[g]	7.2 (12.3)[g]
CdSe/CdS dot-in-rod	476	24	4	0.86[d]	2.9	4.2	5.4

[a]Calculated using eq. 5.1. [b]For comparison, measurements with the benchmark organic dye perylene yield $L_{1/2}$ = 4 cm (Supplementary Information, Figure S2). [c]Where different from those measured for the samples in Fig. 5.2, the best-reported luminescence quantum yields are given in parentheses. [d]From this work, measured with 385 nm excitation. [e]From ref. 19. [f]In units of photons/(m^2 sec). For reference, the total solar flux absorbed by bulk Si is 24.8×10^{20} photons/(m^2 sec), and for bulk CdSe is 11.6×10^{20} photons/(m^2 sec). [g]Calculated using the best-reported luminescence quantum yield.

To assess LSC applicability, the absorption and PL spectra in Figure 5.2 can be used to estimate the probability of reabsorption of emitted photons by these NCs. One way to do so is to quantify the parameter S introduced in ref. 10, which represents the ratio of extinction coefficients at the absorption and emission maxima. S does not take into account the absorption or PL lineshapes, however, and it is difficult to interpret for some NCs that lack a well-defined absorption maximum. Instead, we analyze the probability that an emitted photon will be reabsorbed over a reduced pathlength l, as given by equation 5.1.[1, 26]

$$R(l) = \int PL_{norm}(\lambda)\left(1 - 10^{-A_{norm}(\lambda)\cdot l}\right)d\lambda \qquad [5.1a]$$

$$l = \frac{L \cdot OD_t}{t} \qquad [5.1b]$$

Here, $PL_{norm}(\lambda)$ and $A_{norm}(\lambda)$ represent the luminescence and absorption spectra, normalized by area and at λ_{thresh}, respectively. The reduced pathlength l is defined in equation 5.1b and accounts for device geometry tradeoffs between luminophore concentration and waveguide thickness (t) governed by Beer's law. For example, the device structure from ref. 18 (t = 5 mm, OD_t = 0.2, L = 21.5 cm) has a maximum l of ~8.6, which corresponds to L = 1.4 cm in the liquid waveguide of Figure 5.1C (t = 1.65 mm, OD_t = 1). Other recent NC LSC devices have had maximum l values of ~5.5,[19] ~8.6,[16] ~0.6,[15] and ~53,[17] although exact determination of these values is difficult due to the varying shapes and configurations of these devices. Using equation 5.1a, $R(l)$ was calculated from each set of spectra in Figure 5.2 for values of l up to 730 (Figure 5.2C). $R(l)$ drops most rapidly with increasing l for the two NC heterostructures and less rapidly for the two

doped NCs, illustrating smaller reabsorption losses in the latter. Because $R(l)$ is a complex function of l, it cannot be summarized using any single parameter, but we find that the distance at which there is a 50% probability of reabsorption ($R_{0.5}$) provides a useful device-independent luminophore figure of merit calculable from only absorption and PL spectra. Values of $R_{0.5}$ for the nanocrystals of Figure 5.1 are compiled in Table 5.1. As anticipated from the spectra of Figure 5.2B, $R_{0.5}$ is significantly larger for the doped NCs than for the heterostructure NCs, which suggests that LSCs made from the doped NCs should suffer less from reabsorption losses. Although $R(l)$ and $R_{0.5}$ provide useful metrics for estimating reabsorption probabilities, any quantitative prediction of LSC device performance must take into account numerous other factors including device geometry, PL quantum yields, solar absorption, waveguide modes and losses, and scattering losses. It is thus challenging to compare phosphors for large-scale LSC applications with confidence without further experimental input. Motivated by this challenge, we therefore performed a direct empirical comparison of these NCs in the large-scale LSC configuration depicted in Figure 5.1C.

Solutions of the four NC phosphors described above with $OD_t = 1$ (over 1 mm) were loaded into the liquid-waveguide device of Figure 5.1C. Figures 3A-D show their luminescence spectra collected at different values of L, where L is the distance between the excitation source and the end of the waveguide (see Methods). The two-dimensional plots show PL intensity as a function of wavelength and L. Figure 5.3A shows that much of the CdSe/CdS dot-in-rod NC PL is lost within the first few cm, and only some of the lowest-energy PL is detectable beyond ~20 cm. The observed PL redshift is due to greater reabsorption losses on the higher energy side of the PL spectrum, as anticipated from Figure 5.2B and illustrated schematically in Figure 5.3E. The CdSe/CdS core/shell NC data in Figure 5.3B also show a rapid loss of PL intensity accompanied by a PL red shift with increasing L. In contrast with the NC heterostructures, the two doped NCs show little or no PL redshift with increasing L. Figure 5.3C plots PL spectra of the $Zn_{0.87}Cd_{0.11}Mn_{0.02}Se/ZnS$ NCs, which decrease gradually in intensity with increasing L, accompanied by only minor spectral changes. These data are consistent with the absorption spectrum in Figure 5.2B, which shows nearly uniform, weak absorption across the PL energy range. At L > ~50 cm, small dips become evident in the Mn^{2+} PL spectra arising from absorption by C-H stretching harmonics of the surface ligands and solvent. Similar data are obtained for the $Cd_{0.999}Cu_{0.001}Se$ NCs (Figure 5.3D). As expected from Figure 5.2, the excitonic emission and the

blue edge of the $Cd_{0.999}Cu_{0.001}Se$ $ML_{CB}CT$ PL band is lost to reabsorption, but the red edge decreases only gradually with increasing L. The feature at ~930 nm arises from fiber transmission-loss effects.

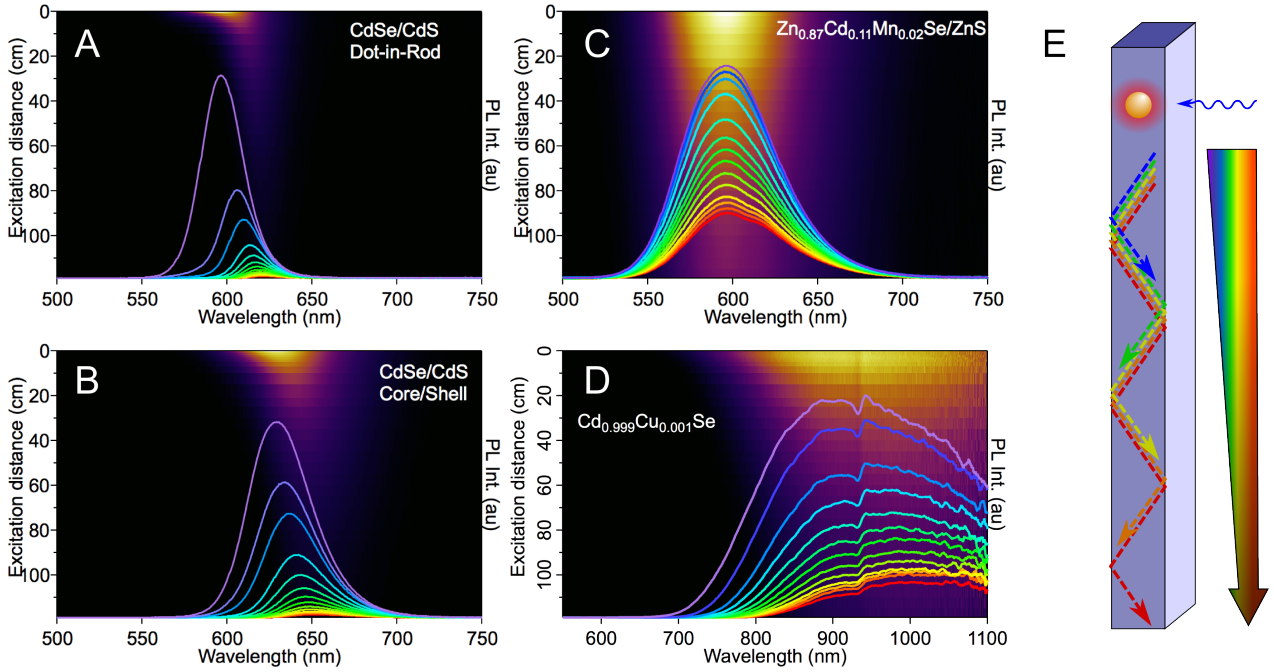

Figure 5.3. Graphical depictions of PL intensity measured as a function of excitation distance (L) and wavelength for **(A)** CdSe/CdS dot-in-rod NCs, **(B)** CdSe/CdS core/shell NCs, **(C)** $Zn_{0.87}Cd_{0.11}Mn_{0.02}Se/ZnS$ NCs, and **(D)** $Cd_{0.999}Cu_{0.001}Se$ NCs. Color scales are linear and normalized at L = 0.5 cm. Spectra are overlaid on these images to more precisely illustrate the spectral changes as excitation distance increases from 0.5 cm (purple) to 120 cm (red) **(E)** Schematic demonstration of distance dependent attenuation where reabsorption losses preferentially attenuate the blue edge of the spectrum.

Figure 5.4A summarizes the results of Figure 5.3 by plotting integrated PL intensities versus L for all four NC phosphors, normalized at L = 0. These traces were corrected for waveguide losses, obtained by measuring similar data from 100-fold diluted samples of $Zn_{0.87}Cd_{0.11}Mn_{0.02}Se/ZnS$ and $Cd_{0.999}Cu_{0.001}Se$ NCs, but the uncorrected data are qualitatively very similar (see Supplementary Information). Importantly, because these data were all collected under identical conditions, they allow a quantitative model-independent comparison of these four NCs for potential large-scale LSC applications. The dot-in-rod and core/shell NCs show distinctly non-exponential PL decay with L, whereas the PL from the two doped NCs appears to

drop more exponentially with L. The non-exponential decay with L stems from the existence of non-uniform absorption across the PL spectrum in the two heterostructure NCs. This curvature is predicted remarkably well by equation 5.1, as shown in Figure 5.2C, confirming this interpretation and the validity of $R(l)$ as a metric for assessing luminophore reabsorption losses in actual waveguides. For comparison with $R_{0.5}$, we parameterize the LSC half-length ($L_{1/2}$),[27] *i.e.*, the value of L at which the integrated PL intensity is 50% of its original value. Table 5.1 summarizes these results and shows that the doped NCs have $L_{1/2}$ values nearly an order of magnitude larger than the NC heterostructures (Table 5.1). The trend in $L_{1/2}$ values is very similar to that in $R_{0.5}$, with quantitative discrepancies likely due to a combination of photon recycling (not accounted for in $R_{0.5}$) and experimental uncertainties in the absorption spectra. Overall, these measurements emphasize that even small PL reabsorption probabilities can severely impair LSC performance on practical length scales, and highlight the critical need for improved luminophores with truly small reabsorption as in the doped NCs described here.

An important outcome of these measurements is the experimental validation of equation 5.1 as a powerful tool for screening potential LSC luminophores. The relatively simple calculation of $R(l)$ allows evaluation of reabsorption probabilities for any luminophore without the need for device fabrication, and it yields easily interpretable results. Standardization of the assessment of candidate LSC luminophores without preparing and measuring LSCs avoids convolution of luminophore and device performance. In this way, device and luminophore innovations may advance independently from one another.

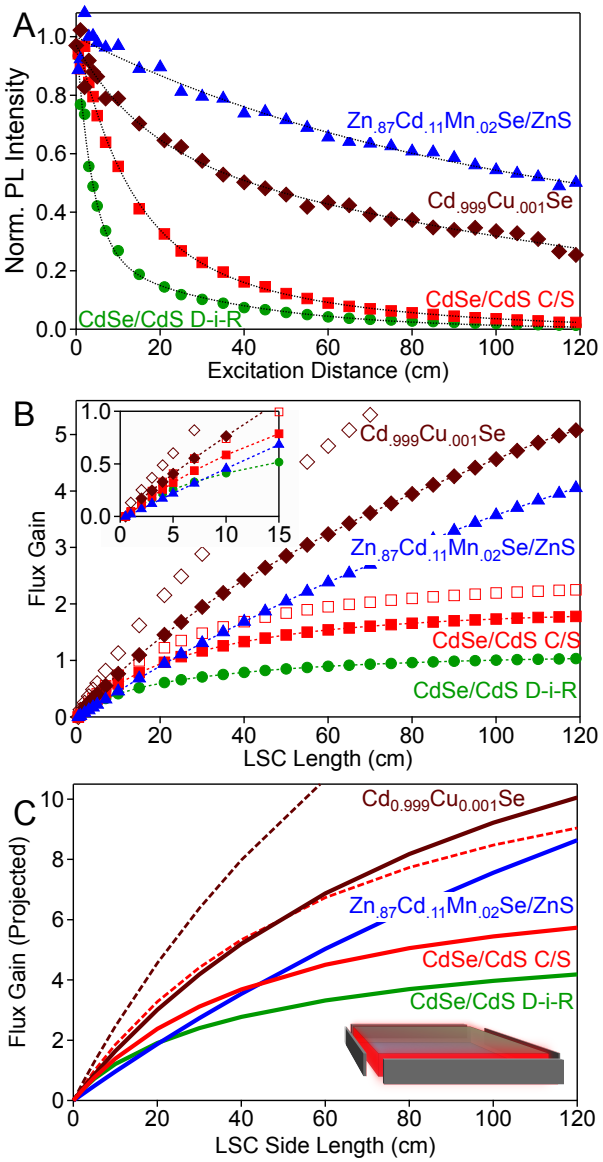

Figure 5.4. (A) Spectrally integrated PL intensity plotted as a function of excitation distance (L) for CdSe/CdS dot-in-rod NCs (green circles), CdSe/CdS core/shell NCs (red squares), $Cd_{0.999}Cu_{0.001}Se$ NCs (maroon diamonds) and $Zn_{0.87}Cd_{0.11}Mn_{0.02}Se/ZnS$ NCs (blue triangles). Intensities are corrected for waveguide losses. **(B)** Flux gains of the same four NC samples calculated by eq. 5.2 for the characterization device coupled to Si photovoltaics under AM1.5 solar irradiation plotted as a function of LSC length. Open symbols were calculated using best-reported η_{PL} (Table1). **(C)** Flux gains calculated for 2-D LSC devices coupled to Si photovoltaics under AM1.5 solar irradiation using the same four NC samples, plotted as a function of LSC side length. Solid lines use as-measured η_{PL} and dashed lines used best-reported η_{PL} (Table 5.1).

These experimental data can now be used to predict the solar LSC performance of these same NCs, *e.g.*, when the one-dimensional liquid waveguide device of Figure 5.1C is connected to Si photovoltaics at the waveguide ends and illuminated with the full solar spectrum. Although this linear LSC configuration would not be attractive for most practical applications, the results illustrate the LSC performance of the NCs well. Figure 5.4B plots projected flux gain (*FG*) values for the one-dimensional waveguide coupled to Si photovoltaics as function of LSC length for the same four NCs, calculated according to equation 5.2.[17]

$$FG = G_{geo} \cdot \eta_{EC} \cdot \frac{\eta_{PV}^{pl}}{\eta_{PV}^{AM1.5}} \cdot \eta_{PL} \cdot \frac{A_{Sol,NC}}{A_{Sol,PV}} \cdot \int_0^L I_{PL}(L)\,dL \qquad [5.2]$$

Here, $A_{\mathrm{Sol,NC}}$ and $A_{\mathrm{Sol,PV}}$ are the solar fluxes absorbed by the NCs and the Si PV, respectively, G_{geo} is the geometric gain of the device, η_{PL} is the NC PL quantum yield, η_{EC} is the escape cone loss factor, η_{PV} is the efficiency of the Si PV either at the PL wavelength or under AM 1.5 irradiation as indicated, and $I_{\mathrm{PL}}(L)$ is the experimental distance-dependent waveguided PL intensity reported in Figure 5.4A. The absorbed solar flux (A_{sol}) is calculated using equation 5.3, where $A(\lambda)$ represents the absorption spectrum of the PV or LSC, and $S(\lambda)$ represents the solar spectrum in units of photons/(nm m^2 sec).

$$A_{sol} = \int S(\lambda) \cdot (1 - 10^{-A(\lambda)})\,d\lambda \qquad [5.3]$$

In the case of the square quartz liquid waveguide used here (Figure 5.1C), $\eta_{\mathrm{EC}} \sim 0.5$ because there are two escape cones (vertical and horizontal), whereas a planar LSC would have $\eta_{\mathrm{EC}} \sim 0.75$. The ratio $\eta_{\mathrm{PL}}{}^{\mathrm{PL}}/\eta_{\mathrm{PL}}{}^{\mathrm{AM1.5}}$ was taken as 1 based on the Panasonic 25.6% efficiency crystalline Si solar cell reported in ref. 28, which shows ~100% EQE from 500-1000 nm. These calculations were performed using two sets of η_{PL} values, those measured experimentally for the samples of Figure 5.4A, and the largest reported values (see Table 5.1). Additionally, to highlight the effects of reabsorption, the *FG* values presented in Figure 5.4B were calculated using the PL intensities corrected for waveguide losses, but *FG*s calculated from raw PL intensities are very similar (Supplementary Information, Figure S3). Importantly, the *FG* analysis using equation 5.2 is validated by experimental measurement of the solar *FG* for the $Zn_{0.87}Cd_{0.11}Mn_{0.02}Se/ZnS$ NCs using the full-length device of Figure 5.1C, which yielded a value

of FG = 3.7 that is in reasonable agreement with the value predicted for this sample in Figure 5.4B (FG = 4.1).

For short LSCs (magnified in the inset of Figure 5.4B), reabsorption losses are not yet dominant and all four NCs show nearly linear increases in FG with L. The slope in this region is determined by the product $A_{Sol,NC} \times \eta_{PL}$. Even though the highest reported η_{PL} of $Cd_{1-x}Cu_xSe$ NCs is only 0.4, $A_{Sol,NC}$ for these NCs is over twice that of the other NCs (Figure 5.2A, Table 5.1). The $Cd_{0.999}Cu_{0.001}Se$ NCs are thus the top performer in short LSCs, followed by the CdSe/CdS core/shell NCs. The $Cd_{0.999}Cu_{0.001}Se$ NCs continue to excel as the LSC length increases because of their combination of large $A_{Sol,NC}$ and small reabsorption losses, and thus remain the clear top performer at all 1-D LSC lengths examined here. $Cd_{0.999}Cu_{0.001}Se$ NCs therefore outperform all other nanocrystal LSC phosphors reported to date by a significant margin. We note that the value of η_{PL} = 0.4 measured here is the highest yet reported for $Cd_{1-x}Cu_xSe$ NCs, but passivation of surface states (*e.g.*, *via* shell growth) may allow this value to be increased further, as reported for other copper-doped NCs.[29] We have also noticed variations in $L_{1/2}$ due to differences in the non-specific absorption attributed to surface traps or impurities discussed above (see Supplementary Information), *e.g.*, we measured $L_{1/2}$ = 51 cm for a different $Cd_{0.999}Cu_{0.001}Se$ NC sample.

It is instructive to compare the CdSe/CdS heterostructures and $Zn_{0.87}Cd_{0.11}Mn_{0.02}Se/ZnS$ NCs in Figure 5.4B. $A_{Sol,NC}$ is almost twice as large for both of the heterostructure NCs as for the $Zn_{0.87}Cd_{0.11}Mn_{0.02}Se/ZnS$ NCs, and all have comparable η_{PL}, so the heterostructures perform much better in small LSCs (Figure 5.4B, inset). As the LSC length increases, however, the heterostructure NCs suffer from major reabsorption losses and their FGs plateau (a characteristic of the one-dimensional architecture). In contrast, the $Zn_{0.87}Cd_{0.11}Mn_{0.02}Se/ZnS$ NCs show only minor losses with increasing LSC length. They surpass the dot-in-rod NCs at $L \sim 7$ cm, and surpass the core/shell NCs at $L \sim 37$ cm. The lack of a FG plateau up to L = 120 cm with both of the doped NCs highlights the substantially smaller reabsorption in these NCs than in the heterostructure NCs. For large-scale LSC applications, the $Zn_{0.87}Cd_{0.11}Mn_{0.02}Se/ZnS$ NCs are thus superior to the heterostructure NCs despite absorbing less of the solar spectrum. LSCs made with luminophores that do not absorb very much visible light, such as $Zn_{0.87}Cd_{0.11}Mn_{0.02}Se/ZnS$ or related Mn^{2+}-doped NCs, are particularly attractive when transparency is desired, for example in smart-window applications.

Finally, we extrapolated the performance of these NCs to large-area 2-D LSCs. *FG* was calculated as a function of side length for square LSC devices with t = 1 mm, OD_t = 1, and Si PVs attached to all four edges using the NC absorption and luminescence spectra from Figure 5.2B along with the η_{PL} values reported in Table 5.1 (see Supplementary Information). Figure 5.4C plots the calculated *FG* values versus 2-D LSC side length. The trends with increasing LSC size are similar to those found for the 1-D device (Figure 5.4B). In particular, the $Cd_{0.999}Cu_{0.001}Se$ NCs are again the top performer in both small- and reasonably large-area LSCs, despite their relatively low η_{PL}. As anticipated from the 1-D measurements and calculations, the $Zn_{0.87}Cd_{0.11}Mn_{0.02}Se$/ZnS NCs excel at extremely large dimensions, surpassing first the CdSe/CdS core/shell NCs (at an LSC size of ~1.3 m x 1.3 m) and then even the $Cd_{0.999}Cu_{0.001}Se$ NCs (at ~10 m x 10 m, see Supplementary Information). Table 5.1 summarizes the calculated *FG* values for a device area of 1.2 m x 1.2 m (the square equivalent of our laboratory 1-D liquid waveguide), as well as the projected maximum *FG* values. Overall, these calculations reaffirm the "best-in-class" performance of the new LSC phosphor, $Cd_{0.999}Cu_{0.001}Se$ NCs, on many length scales, and validate the use of the 1-D waveguide for experimentally assessing the performance of luminophores in large-scale 2-D LSCs. The similarity of the size-dependent *FG* curves for the $Cd_{0.999}Cu_{0.001}Se$ and CdSe/CdS core/shell NCs demonstrates that high PL quantum yields not only improve *FG* in small LSCs but also mitigate reabsorption losses in large LSCs through increased photon recycling. This principle is also evident from comparison of the curves calculated for the same sample using as-measured and best-reported η_{PL} values (Figure 5.4). .

5.3 Discussion

Semiconductor NCs have recently been proposed as attractive spectral conversion phosphors for next-generation LSCs. To date, a quantitative assessment of these materials for this purpose has been lacking. In this study, we performed a variety of spectroscopic and one-dimensional waveguide measurements aimed at comparing the leading NC candidates for potential large-scale LSC applications. The experimental results demonstrate that even seemingly small absorption features in the region of luminescence are detrimental to LSC performance on large length scales. CdSe/CdS heterostructure NCs perform well on small length scales, but on large length scales they suffer from major losses due to reabsorption of emitted photons. For the two doped NCs whose luminescent transitions are subject to very little

reabsorption, the performance at large length scales is in fact limited only by parasitic absorption from vibrational harmonics of the matrix, matrix impurities, or NC surface states. These limitations are not intrinsic to the phosphor and can be circumvented. Among the four types of NCs examined here, the "best-in-class" phosphors for full-spectrum concentration by a substantial margin are the $Cd_{1-x}Cu_xSe$ NCs, which absorb the greatest fraction of the solar spectrum and display relatively small reabsorption losses. LSC applications of copper-doped NCs have not been demonstrated previously. The $Zn_{0.87}Cd_{0.11}Mn_{0.02}Se/ZnS$ NCs excel at very large dimensions while retaining visible transparency, and are thus attractive for smart-window applications.

In addition to experimental measurements of luminescence in large-scale waveguides, this study presents, and validates with experimental data, a standardized methodology that allows facile *prediction* of the performance of new luminophores in LSCs from their absorption and PL spectra. The calculation of $R(l)$ using equation 5.1 allows evaluation of reabsorption for any luminophore without the need for elaborate device fabrication, and it yields easily interpretable results. The predicted reabsorption losses with LSC length agree with experimental results remarkably well, lending credence to flux gains projected from these same experimental parameters for large-scale 2-D LSCs.

Finally, we examine the potential for future improvement of NCs as LSC luminophores. For the CdSe/CdS heterostructure NCs, the PL quantum yields and solar absorption are both near their theoretical limits, meaning that any improvements must come from reduced reabsorption. Although larger shell volumes would reduce reabsorption, previous studies have pointed out that larger shell thicknesses may lead to reduced quantum yields.[30] Calculations also indicate that Rayleigh scattering from core/shell NCs becomes appreciable over meter-scale pathlengths for NCs with diameters > ~10 nm, and that the optimum balance between reabsorption and scattering still involves appreciable losses (see Supplementary Material). New heterostructures such as PbSe/CdSe NCs could increase $A_{sol,NC}$ and offset some of the major reabsorption and scattering losses in large-scale LSCs. For the doped NCs, tuning the bandgap (either by size or alloying) and increasing PL quantum yield could potentially increase performance by over a factor of two. In $Zn_{1-x-y}Cd_xMn_ySe/ZnS$ NCs, tuning λ_{thresh} to ~480 nm by changing size or alloy composition would more than double $A_{sol,NC}$ relative to the NCs reported here, without introducing new reabsorption losses. Narrower energy gaps (λ_{thresh} > 480 nm) lead to recovery of

excitonic emission via thermal repopulation[31] and would not be beneficial. Similarly, adjusting the energy gap of $Cd_{1-x}Cu_xSe$ NCs to the bulk limit would increase $A_{sol,NC}$ by over 35% relative to the NCs studied here. Even though the best $Cd_{1-x}Cu_xSe$ PL quantum yield achieved here (η_{PL} = 0.4) is the highest yet reported for $Cd_{1-x}Cu_xSe$ NCs, it may be possible to further increase η_{PL} by passivation of surface states, as reported for other copper-doped NCs,[29] which could improve performance of this "best-in-class" phosphor by more than a factor of two at all LSC length scales, and even more for large-pathlength devices due to greater photon recycling efficiency (see Supplementary Information). Switching from CdSe to other related copper-doped phosphors such as Cu^+:InP[32] or $CuInS_2/ZnS$[29] would yield similarly small PL reabsorption while eliminating Cd^{2+}. A challenge with all of the copper-doped NCs is their broad PL, which begins to extend past the absorption threshold of silicon when the energy gap becomes too narrow. Finally, the observation that weak, nonspecific absorption attributed to direct excitation of surface traps can be moderated chemically points to the possibility of further improvements in this direction for all of these NC phosphors. Overall, even with their relatively low η_{PL}, the $Cd_{1-x}Cu_xSe$ NCs reported here combine effective solar absorption with very low reabsorption to substantially outperform all other NCs tested here at all but the largest LSC lengths and areas, marking a significant advance in the development of nanocrystalline phosphors for LSC applications. More generally, these results highlight the attractiveness of doped nanocrystals as phosphors for LSCs.

5.4 Methods

5.4.A Synthesis. All chemicals were used as supplied from Aldrich with the exception of tri-*n*-octyl phosphine (TOP), which was purchased from Strem.

$Zn_{0.87}Cd_{0.11}Mn_{0.02}Se$ NCs. $Zn_{1-x-y}Cd_xMn_ySe$ NCs were grown with slight modifications to previously reported synthetic methods[23] based on the the thermal decomposition of the cluster NMe_4 Zn_4SePh_{10}. 10.8 g of hexadecyl amine with 12 mg $MnCl_2 \bullet 4H_2O$ and 15 mg of $CdCl_2$ were first degassed under vacuum at 130° C for 1hr, after which 400 mg of NMe_4 Zn_4SePh_{10} and 20 mg of Se were added anaerobically. The resulting mixture was again degassed at 130° C for 1 hr before ramping the temperature to 270° C, where it was held for 15 min before cooling slowly to 100° C. The resulting NCs were twice crashed out with ethanol, separated by centrifuging, and resuspended in toluene.

$Zn_{0.87}Cd_{0.11}Mn_{0.02}Se/ZnS$ NCs. ZnS shells were grown by transferring the toluene suspension of $Zn_{0.87}Cd_{0.11}Mn_{0.02}Se$ NCs to a flask containing 3g oleylamine and 3g octadecane, from which the toluene was removed and the resulting suspension degassed for 1 hr at 130° C. $Zn(Oleate)_2$ was prepared by reacting 440 mg $Zn(oAc)_2$ with 4.4 g of oleic acid and 4.4 ml of octadecene under vacuum at 110° C until all volatile components were removed. The flask was then put under a nitrogen atmosphere, 36 mg S dissolved in 3.6 mL of TOP was injected, and the resulting mixture cooled to room temperature. The temperature of the flask containing the NCs was raised to 225° C and the $Zn(Oleate)_2$-TOP-S mixture was injected via syringe pump at a rate of 0.5 ml/hr. The resulting NCs were again purified by flocculation with ethanol followed by resuspension in toluene.

CdSe (core) NCs. CdSe cores were synthesized by according to the standard hot-injection synthesis as reported in ref. 16 wherein 60 mg of Selenium dissolved in 360 mg of TOP is rapidly injected into a degassed solution of 60 mg CdO, 280 mg octadecylphosphonic acid, and 3 g trioctylphosphine oxide (TOPO) at 380°C. The heating mantle was removed immediately after injection and the cooled solution of nanocrystals was purified by flocculation with ethanol followed by resuspension in toluene. These NCs had $d = 2.7$ nm.

CdSe/CdS core/shell NCs. CdS shells were grown on the above cores according to ref. 19, wherein 20 ml of a 0.08 M $Cd(oleate)_2$ solution in octadecene (ODE) and 20 mL of 2 mM solution of octanethiol in ODE were separately injected at 2.5 ml/hr to a degassed solution containing 100 nmol of CdSe cores in 3 ml of ODE and 3 ml of oleylamine at 310°C. 2 ml of oleic acid was injected 2 hrs and 4 hrs after the beginning of the injection. After injection was complete, the solution was allowed to stir at 310°C for an additional 15 minutes before cooling and purification by flocculation with ethanol followed by resuspension in toluene.

CdSe/CdS dot-in-rod NCs. CdS rods were grown onto the above cores according to ref. 16, wherein 2 nmol of the CdSe cores dissolved in 1.5 g TOP with 120 mg sulfur was injected rapidly into a degassed solution containing 60 mg CdO, 80 mg hexylphosphonic acid, 0.29 g octadecylphosphonic acid, and 3 g TOPO at 360°C. After injection, the solution is stirred for 8 min with the temperature recovering to 360°C, after which it was cooled and purified by flocculation with ethanol followed by resuspension in toluene.

$Cd_{1-x}Cu_xSe$ NCs. $Cd_{1-x}Cu_xSe$ NCs were synthesized by adapting the "heat-up" method for the synthesis of CdSe NCs first reported by Chen, et al.[33] Briefly, cadmium myristate (113

mg), selenium dioxide (22 mg), and copper (I) chloride (4 mg) were degassed under vacuum in octadecene (10 g) at room temperature for 30 minutes. Heating this mixture to 230 °C under nitrogen for 5 minutes produced a dark brown solution. After dropwise addition of 0.2 mL of oleic acid, the mixture was cooled to room temperature. Addition of 1 volume equivalent of anhydrous ethanol followed by centrifugation produced dark brown pellets that were resuspended in toluene, sonicated, and centrifuged again to remove insoluble impurities. Any adventitious CuSe formed during the reaction was reduced and removed by adding ~0.5 mL of TOP followed by flocculation with ethanol and resuspension in toluene or tetrachloroethylene. Quantum yields as high as 0.4 were measured for these $Cd_{1-x}Cu_xSe$ NCs, but synthetic conditions were not optimized to reproduce this high quantum yield in batches large enough to fill the liquid waveguide. These quantum yields are higher than the previous best reported value for $Cd_{1-x}Cu_xSe$ NCs of 0.25.[34]

5.4.B Spectroscopy and characterization. Absorption measurements were taken using a Cary 500 spectrometer, and PL was measured using an Ocean Optics USB-2000+ spectrometer or a liquid-nitrogen-cooled CCD (Acton) coupled to a 0.5m monochromator (for $Cd_{0.999}Cu_{0.001}Se$ measurements), both corrected for spectral sensitivity. Quantum yields were measured using a Hamamatsu integrating sphere quantum yield measurement system with 385 nm excitation. TEM images were collected on an FEI Tecnai microscope, and NC compositions were determined by inductively coupled plasma-atomic emission spectrometry.

The liquid waveguide apparatus for measuring LSC reabsorption losses (Figure 5.1C) is based on a 120 cm long square quartz tube (supplied by Friederick and Dimmock Co.) with a 1 mm inner dimension (1.65 mm outer dimension) suspended over a black aluminum channel that was illuminated by a 1 mm spot from a 385 nm LED at variable distances from the end. Waveguided light was then collected through high numerical aperture (NA=0.79) lenses through a diffuser to ensure equivalent collection of all waveguide modes, and measured using a fiber-coupled spectrometer. Because one end of the tube was sealed and flattened to avoid effects of a meniscus on detection, the tube was filled with toluene solutions of luminophore through a removable capillary. Because the $Cd_{0.999}Cu_{0.001}Se$ NC PL overlaps with strong vibrational overtones of toluene (see Figure S4), these NCs were measured in tetrachloroethylene. Before measurement, each sample was filtered through a 200 nm pore-size PTFE syringe filter. Photographs of this device are provided in Appendix D.

5.5 References

1. Batchelder, J. S.; Zewai, A. H.; Cole, T., Luminescent solar concentrators. 1: Theory of operation and techniques for performance evaluation. *Appl. Opt.* 1979, **18**, 3090-3110.
2. Reisfeld, R.; Shamrakov, D.; Jorgensen, C., Photostable solar concentrators based on fluorescent glass films. *Sol. Energ. Mat. Sol. C.* 1994, **33**, 417-427.
3. Debije, M. G.; Verbunt, P. P. C., Thirty Years of Luminescent Solar Concentrator Research: Solar Energy for the Built Environment. *Adv. Energy Mat.* 2012, **2**, 12-35.
4. McIntosh, K. R.; Yamada, N.; Richards, B. S., Theoretical comparison of cylindrical and square-planar luminescent solar concentrators. *Appl. Phys. B* 2007, **88**, 285-290.
5. Bornstein, J. G. In Luminescent Solar Concentrator Daylighting, Proc. SPIE 0502, Optical Materials Technology for Energy Efficiency and Solar Energy Conversion III, 1984; pp 138-145.
6. Earp, A. A.; Smith, G. B.; Franklin, J.; Swift, P., Optimisation of a three-colour luminescent solar concentrator daylighting system. *Sol. Energ. Mat. Sol. C.* 2004, **84**, 411-426.
7. Fisher, B.; Biddle, J., Luminescent spectral splitting: Efficient spatial division of solar spectrum at low concentration. *Sol. Energ. Mat. Sol. C.* 2011, **95**, 1741-1755.
8. Hammam, M.; El-Mansy, M. K.; El-Bashir, S. M.; El-Shaarawy, M. G., Performance evaluation of thin-film solar concentrators for greenhouse applications. *Desalination* 2007, **209**, 244-250.
9. Boer, D. K. G. d.; Broer, D. J.; Debije, M. G.; Keur, W.; Meijerink, A.; Ronda, C. R.; Verbunt, P. P. C., Progress in phosphors and filters for luminescent solar concentrators. *Opt. Express* 2012, A395-A405.
10. Currie, M. J.; Mapel, J. K.; Heidel, T. D.; Goffri, S.; Baldo, M. A., High-Efficiency Organic Solar Concentrators for Photovoltaics. *Science* 2008, **321**, 226-228.
11. Wilson, L. R. Luminescent solar concentrators: a study of optical properties, re-absorption and device optimisation. Heriot-Watt University, Edinburgh, 2010.
12. Bomm, J.; Buchtemann, A.; Chatten, A. J.; Bose, R.; Farrell, D. J.; Chan, N. L. A.; Xiao, Y.; Slooff, L. H.; Meyer, T.; Meyer, A.; van Sark, W. G. J. H. M.; Koole, R., Fabrication and Full Characterization of State-of-the-Art Quantum Dot Luminescent Solar Concentrators. *Sol. Energ. Mat. Sol. C.* 2011, **95**, 2087-2094.
13. Inman, R. H.; Shcherbatyuk, G. V.; Medvedko, D.; Gopinathan, A.; Ghosh, S., Cylindrical luminescent solar concentrators with near-infrared quantum dots. *Opt. Express* 2011, **19**, 24308-24313.
14. Purcell-Milton, F.; Gun'ko, Y. K., Quantum dots for Luminescent Solar Concentrators. *J Mater Chem* 2012, **22**, 16687-16697.
15. Krumer, Z.; Pera, S. J.; van Dijk-Moes, R. J. A.; Zhao, Y.; de Brouwer, A. F. P.; Groeneveld, E.; van Sark, W. G. J. H. M.; Schropp, R. E. I.; de Mello Donega, C., Tackling self-absorption in luminescent solar concentrators with type-II colloidal quantum dots. *Sol. Energ. Mat. Sol. C.* 2013, **111**, 57-65.
16. Bronstein, N. D.; Li, L.; Xu, L.; Yao, Y.; Ferry, V. E.; Alivisatos, A. P.; Nuzzo, R. G., Luminescent Solar Concentration with Semiconductor Nanorods and Transfer-Printed Micro-Silicon Solar Cells. *ACS Nano* 2013, **8**, 44-53.
17. Erickson, C. S.; Bradshaw, L. R.; McDowall, S.; Gilbertson, J. D.; Gamelin, D. R.; Patrick, D. L., Zero-Reabsorption Doped-Nanocrystal Luminescent Solar Concentrators. *ACS Nano* 2014, **8**, 3461-3467.

18. Meinardi, F.; Colombo, A.; Velizhanin, K. A.; Simonutti, R.; Lorenzon, M.; Beverina, L.; Viswanatha, R.; Klimov, V. I.; Brovelli, S., Large-area luminescent solar concentrators based on "Stokes-shift-engineered" nanocrystals in a mass-polymerized PMMA matrix. *Nat Photon* 2014, **8**, 392-399.
19. Coropceanu, I.; Bawendi, M. G., Core/Shell Quantum Dot Based Luminescent Solar Concentrators with Reduced Reabsorption and Enhanced Efficiency. *Nano Lett.* 2014, **14**, 4097-4101.
20. Yoon, J.; Li, L.; Semichaevsky, A. V.; Ryu, J. H.; Johnson, H. T.; Nuzzo, R. G.; Rogers, J. A., Flexible concentrator photovoltaics based on microscale silicon solar cells embedded in luminescent waveguides. *Nature Commun* 2011, **2**, No. 343.
21. Shen, Y.; Jia, Y.; Sheng, X.; Shen, L.; Rogers, J. A.; Giebink, N. C., Nonimaging Optical Gain in Luminescent Concentration through Photonic Control of Emission Étendue. *ACS Photonics* 2014, **1**, 746-753.
22. Yin, Y.; Alivisatos, A. P., Colloidal nanocrystal synthesis and the organic-inorganic interface. *Nature* 2005, **437**, 664-670.
23. McLaurin, E. J.; Fataftah, M. S.; Gamelin, D. R., One-step synthesis of alloyed dual-emitting semiconductor nanocrystals. *Chem. Comm.* 2013, **49**, 39-41.
24. McClure, D. S., Optical Spectra of Exchange Coupled Mn++ Ion Pairs in ZnS:MnS. *J. Chem. Phys.* 1963, **39**, 2850-2855.
25. Suzuki, A.; Shionoya, S., Mechanism of the Green-Copper Luminescence in ZnS Crystals. I. Direct Evidence for the Pair Emission Mechanism. *J. Phys. Soc. Jpn.* 1971, **31**, 1455-1461.
26. Birks, J. B., Photophysics of Aromatic Molecules. Wiley-Interscience: London, 1970.
27. Earp, A. A.; Smith, G. B.; Swift, P. D.; Franklin, J., Maximising the light output of a Luminescent Solar Concentrator. *Solar Energy* 2004, **76**, 655-667.
28. Green, M. A.; Emery, K.; Hishikawa, Y.; Warta, W.; Dunlop, E. D., Solar cell efficiency tables (version 44). *Prog. Photovoltaics* 2014, **22**, 701-710.
29. Zhang, W.; Lou, Q.; Ji, W.; Zhao, J.; Zhong, X., Color-Tunable Highly Bright Photoluminescence of Cadmium-Free Cu-Doped Zn,ÄìIn,ÄìS Nanocrystals and Electroluminescence. *Chem. Mater.* 2013, **26**, 1204-1212.
30. Ghosh, Y.; Mangum, B. D.; Casson, J. L.; Williams, D. J.; Htoon, H.; Hollingsworth, J. A., New Insights into the Complexities of Shell Growth and the Strong Influence of Particle Volume in Nonblinking "Giant" Core/Shell Nanocrystal Quantum Dots. *J. Am. Chem. Soc.* 2012, **134**, 9634-9643.
31. Vlaskin, V. A.; Janßen, N.; van Rijssel, J.; Beaulac, R.; Gamelin, D. R., Tunable Dual Emission in Doped Semiconductor Nanocrystals. *Nano Lett.* 2010, **10**, 3670–3674.
32. Xie, R.; Peng, X., Synthesis of Cu-Doped InP Nanocrystals (d-dots) with ZnSe Diffusion Barrier as Efficient and Color-Tunable NIR Emitters. *J. Am. Chem. Soc* 2009, **131**, 10645-10651.
33. Chen, O.; Chen, X.; Yang, Y.; Lynch, J.; Wu, H.; Zhuang, J.; Cao, Y. C., Synthesis of Metal–Selenide Nanocrystals Using Selenium Dioxide as the Selenium Precursor. *Angew. Chem. Int. Edit.* 2008, **47**, 8638-8641.
34. Grandhi, G. K.; Tomar, R.; Viswanatha, R., Study of Surface and Bulk Electronic Structure of II-VI Semiconductor Nanocrystals Using Cu as a Nanosensor. *ACS Nano* 2012, **6**, 9751-9763.

Chapter 6. Zero-Reabsorption Doped-Nanocrystal Luminescent Solar Concentrators

Abstract. Optical concentration can lower the cost of solar energy conversion by reducing photovoltaic cell area and increasing photovoltaic efficiency. Luminescent solar concentrators offer an attractive approach to combined spectral and spatial concentration of both specular and diffuse light without tracking, but have been plagued by luminophore self-absorption losses when employed on practical size scales. Here, we introduce doped semiconductor nanocrystals as a new class of phosphors for use in luminescent solar concentrators. In proof-of-concept experiments, visibly transparent, ultraviolet-selective luminescent solar concentrators have been prepared based on colloidal Mn^{2+}-doped ZnSe nanocrystals that show no luminescence reabsorption. Optical quantum efficiencies of 37% are measured, yielding a maximum projected energy concentration of ~6× and flux gain for a-Si photovoltaics of 15.6 in the large-area limit, for the first time bounded not by luminophore self-absorption but by the transparency of the waveguide itself. Future directions in the use of colloidal doped nanocrystals as robust, processable spectrum-shifting phosphors for luminescent solar concentration on the large scales required for practical application of this technology are discussed.
Reprinted with permission from: Erickson, C. S.; Bradshaw, L. R.; McDowall, S.; Gilbertson, J. D.; Gamelin, D. R.; Patrick, D. L., Zero-Reabsorption Doped-Nanocrystal Luminescent Solar Concentrators. *ACS Nano* 2014, **8** (4), 3461-3467.

6.1. Introduction

Luminescent solar concentrators (LSCs) are dye-containing waveguides used to collect and concentrate sunlight for energy conversion.[1,2] Simultaneous spectral and spatial concentration is achieved without the use of focusing optics. Instead, sunlight absorbed by the dye is emitted into guided modes to travel by total internal reflection for collection at the perimeter (Figure 6.1). LSCs require no solar tracking, exhibit omnidirectional acceptance providing comparable performance under diffuse and specular illumination, and offer the potential for higher energy concentration ratios (CR) than designs based on mirrors or lenses.[3] Their ability to deliver high-irradiance, narrow-bandwidth light by active wavelength shifting makes LSCs particularly suitable for driving photovoltaics and semiconductor-based photochemical processes where wavelength-to-bandgap matching can be exploited to improve efficiency and mitigate thermal rejection.[4] Unlike lens- and mirror-based concentrators, LSCs selectively collect sunlight in a limited spectral band, established by the absorption range of the luminophore. Other wavelengths are transmitted for use in secondary applications such as

interior lighting, heat generation, or photovoltaic conversion, enabling high combined-cycle efficiencies. The LSC itself obeys the single-bandgap Shockley-Queisser efficiency limit,[5] with maximum energy efficiencies of $E_{lim} \approx 3$ - 5% for UV-selective collection, increasing up to ~30% if absorption extends into the near infrared. The thermodynamically limited energy concentration ratio depends on the effective luminescence Stokes shift, with values of $CR_{lim} \geq 100$ predicted at room temperature for a Stokes shift of ~0.1eV.[6] Attached photovoltaics receive high-irradiance, narrow-bandwidth light, resulting in a power density enhancement (referred to as the flux gain) up to several times larger than CR_{lim} when the photovoltaic's bandgap is matched to luminophore emission.[7]

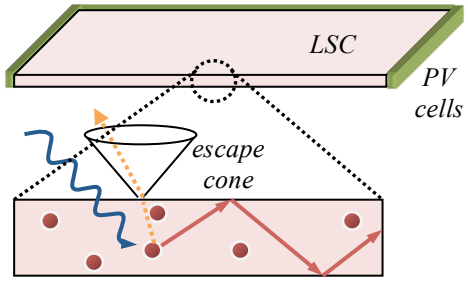

Figure 6.1. A luminescent solar concentrator. Sunlight (blue) is absorbed by luminophores and emitted into a planar waveguide (red), traveling to the edge of the collector to concentrate light for conversion by PV cells. A fraction of light is lost to non-unity LQY or out the escape cone (dashed orange) with each successive re-absorption/re-emission event.

Despite several decades of research,[8,9] actual LSC performance levels remain far below these thermodynamic limits, primarily due to three main factors: (1) only a fraction of incident sunlight is absorbed, determined by the integrated overlap of luminophore absorption and solar spectra; (2) only a fraction of absorbed light is re-emitted, depending on the luminophore's luminescence quantum yield (LQY); (3) only a fraction of this emitted light is captured in guided modes (~75% in an LSC waveguide with refractive index n ~ 1.5), with the remainder (~25%) lost out the top or bottom escape cone defined by Snell's Law.[10] Most problematic of all is that losses from mechanisms (2) and (3) occur repetitively, because photons travelling within the waveguide may be absorbed and re-emitted by other luminophores multiple times before reaching an edge. In practical LSC implementations, for example, optical path lengths may easily reach a meter or more, and even small overlap between absorption and emission spectra

results in catastrophic self-absorption losses. Concentrator efficiencies thus fall exponentially with the number of re-absorption / re-emission events, which is in turn determined by the overlap of luminophore absorption and emission spectra and by the device dimensions.

Efforts to improve LSC performance by reducing luminophore self-absorption or mitigating its effects have included the use of dichroic mirrors and other photonic structures to reduce escape-cone losses,[11] controlling luminophore orientation to capture a greater proportion of emitted photons in guided modes,[12] and use of large Stokes shift luminophores.[13] Regarding the latter, a wide range of materials and strategies have been investigated, including organometallic and sensitized lanthanide phosphors,[14] Stokes shift enhancement by solid-state solvation,[15] and other concepts.[16,17] Various types of semiconductor nanocrystals (quantum dots, or QDs) have also been investigated, including those with both Type I and Type II heterointerfaces.[18] Despite these efforts, it has proven difficult to identify phosphors that simultaneously absorb strongly, are photostable, are solution processable, and generate sufficiently large Stokes shifts without sacrificing LQYs.

Here, we demonstrate a new class of LSCs based on impurity-doped QDs as the active phosphor material. Incorporation of small amounts (0.1 ~ 1 atom %) of a luminescence activator ion within a QD introduces new localized excited states within the bandgap that can be efficiently excited via energy transfer from the photoexcited host semiconductor.[19] Emission from these states is downshifted substantially relative to the semiconductor absorption so that, by choosing an activator whose extinction coefficient is sufficiently small, self-absorption can be effectively eliminated. The same mechanism is employed by classic sensitized inorganic phosphors commonly used in lighting or display applications.[20] Importantly, the small dimensions of colloidal doped QDs eliminates scattering effects typical of classic inorganic phosphor microcrystal powders.

In addition to minimal self-absorption and scattering, doped QDs possess several other characteristics useful for LSC applications. The semiconductor host provides a large extinction coefficient along with broadband absorption that is in principle tunable over a wide spectral range through composition and size control. Doped QDs also exhibit minimal concentration quenching and higher resistance to photo-oxidation than most organic dyes or undoped nanocrystals.[21] Depending on the semiconductor, they can be made from low cost, nontoxic, Earth-abundant starting materials, and they are compatible with a variety of economical solution-

based synthesis and processing techniques advantageous for integration into polymer or glass waveguides. While doped QDs have been investigated extensively as phosphors[22] and for their unusual magneto-optical and magneto-electronic properties,[23] to our knowledge this class of materials has not previously been used in LSCs.

6.2. Results and Discussion

As proof of concept, we have prepared and studied LSCs based on Mn^{2+}-doped ZnSe/ZnS core-shell quantum dots. ZnSe is a direct bandgap semiconductor with a bulk bandgap of ~3.1 eV, meaning it selectively absorbs UV light. In the weak tetrahedral field provided by the ZnSe lattice, substitutional Mn^{2+} impurity ions possess a $^6A_1$ ground state and show luminescence associated with a $^4T_1 \rightarrow {}^6A_1$ d-d transition at an energy of ~2.1 eV (Figure 5.2A).[19] This Mn^{2+} luminescence is efficiently sensitized by the host ZnSe nanocrystal (Figure 5.2B). The luminescence sensitization scheme active in our colloidal Mn^{2+}-doped ZnSe nanocrystals is very similar to that of bulk Mn^{2+}-doped ZnSe, but the colloids show greater sensitization efficiencies because of longer excitonic lifetimes and faster energy transfer. At room temperature, the rate of energy transfer from the photoexcited nanocrystal to Mn^{2+} (~ps) greatly exceeds that of exciton recombination (~ns),[24,25] yielding effectively quantitative energy capture by Mn^{2+}. The excited Mn^{2+} then relaxes to its ground state with a high room-temperature LQY. The corresponding $^6A_1 \rightarrow {}^4T_1$ absorption transition is spin-forbidden, with a maximum extinction coefficient of only ~1 $M^{-1}cm^{-1}$, about five orders of magnitude smaller than that of the host nanocrystal. This difference in absorptivity yields a large *effective* Stokes shift of as much as ~1 eV, precluding self-absorption of Mn^{2+} emission and thereby overcoming a key challenge in LSC phosphor design. Although the long (~ms) lifetime of the $^4T_1$ excited state can lead to luminescence quenching via a multiphoton process,[25,26] the threshold photon flux for this effect greatly exceeds solar irradiance.[27]

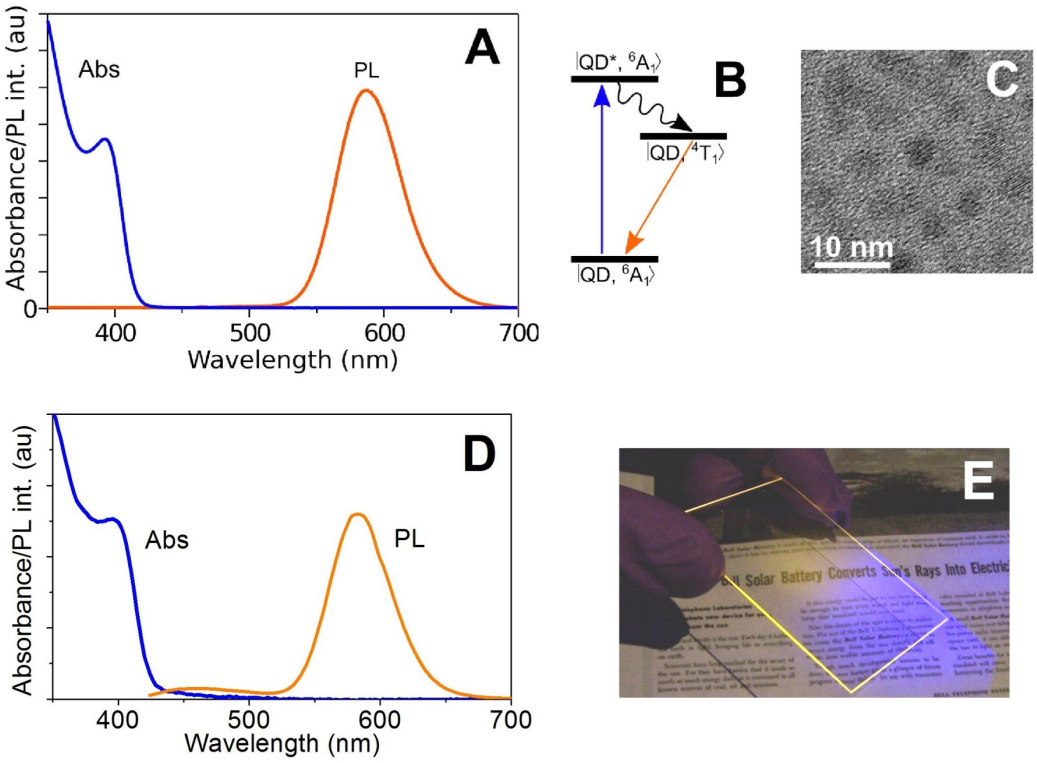

Figure 6.2. **(A)** Absorption and photoluminescence spectra of colloidal Mn^{2+}-doped ZnSe/ZnS QDs in toluene. **(B)** Schematic description of luminescence sensitization in Mn^{2+}-doped QDs. Photon absorption by the doped quantum dot in its ground state ($|QD,{}^6A_1\rangle$) gives the excited quantum dot ($|QD^*,{}^6A_1\rangle$). Energy rapidly localizes to excite Mn^{2+} within the QD ($|QD, {}^4T_1\rangle$), which then emits with a high quantum yield. Radiative processes are indicated as straight lines and nonradiative processes as wavy lines. **(C)** TEM image of representative Mn^{2+}-doped ZnSe/ZnS QDs. **(D)** Absorbance and photoluminescence spectra of Mn^{2+}:ZnSe/ZnS QDs in an LSC device. **(E)** A device seen under UV illumination.

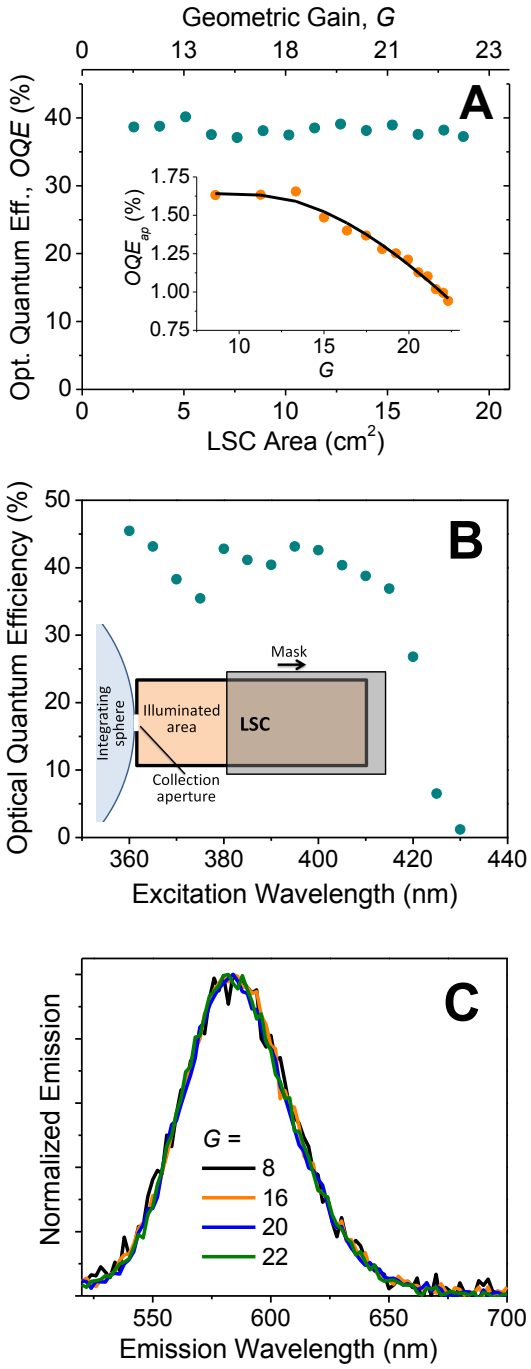

Figure 6.3. **(A)** The dependence of optical quantum efficiency on doped-nanocrystal LSC area and geometric gain for full perimeter, index-matched collection (OQE), and as measured through the collection aperture (OQE_{ap}, inset). Solid line results from fitting the model described in the text and SI. **(B)** Dependence of the OQE on excitation wavelength. OQE is independent of excitation wavelength above the bandgap. Inset: A monochromatic excitation source positioned above the device provides uniform light over the unmasked area, with edge-emitted light collected through an aperture into an integrating sphere. **(C)** Normalized edge emission spectra. **(A)** and **(C)** were obtained by excitation at 400 nm.

Mn^{2+}-doped ZnSe/ZnS nanocrystals (Figure 6.2C) were synthesized by methods adapted from those described previously[28,25] and incorporated into polymer films by dispersing a toluene suspension of nanocrystals into a mixture of laurylmethacrylate, tri-octyl phosphine, and ethylene glycol di-methacrylate, containing a photo-initiator (Methods). Devices were largely transparent to visible light (Figure 6.2E), with an optical density up to 0.30 at the first exciton absorption maximum, depending on the concentration of doped QDs used. Despite this transparency, waveguided luminescence is still clearly visible by eye when exposed to diffuse sunlight on a cloudy day (see SI). Overall concentrator dimensions were 25 x 75 x 0.42 mm, corresponding to a geometric gain, defined as the ratio of facial to edge area, $G = 22$.

LSC absorbance and facial emission spectra are shown in Figure 6.2D. The peak exciton absorption occurs at 396 nm and is size-tunable over the range 350 ~ 450 nm for this composition. The small absorption tail extending from the band edge is likely caused by scattering. With above-bandgap excitation (400 nm), luminescence is dominated by the Mn^{2+} $^4T_1 \rightarrow {}^6A_1$ transition centered at 582 nm. A second broad emission feature is observed at ~435 nm that can be attributed to weak fluorescence from the waveguide polymer. This feature was also present in control devices containing no doped QDs, and it was not present in the toluene suspension of doped QDs.

Unlike other concentrator designs, wavelengths not collected by an LSC are transmitted, and hence available for use by a secondary process, such as for interior lighting. Accordingly, LSC performance is expressed in terms of the fraction of solar photons harvested by the concentrator, or optical quantum efficiency (OQE), defined as the fraction of absorbed photons concentrated at device edges. OQE was measured as a function of geometric gain under uniform diffuse illumination by collecting edge-emitted light through an aperture into an integrating sphere connected to a fluorometer. The remaining device perimeter was blackened with ink to eliminate reflections. Successively larger illuminated areas were measured using a movable mask (inset, Figure 6.3B) and the full perimeter OQE was computed, correcting for the finite size of the edge collection aperture and reflection losses at the aperture arising from the use of a non-index matched detector (for details, see SI). Figure 6.3A shows the results of these measurements under illumination near the first excitonic absorption peak (400 nm). OQE_{ap}, shown in the inset, is the non-index matched collection efficiency through the small measurement aperture; the main figure shows the full perimeter OQE for an index-matched

detector. The difference in curvature between the two plots stems from the decreasing solid angle occupied by the aperture as G increases. At $G = 22$, corresponding to full area illumination, OQE = 37%, with efficiency being independent of excitation energy above the bandgap (Figure 6.3B). As shown in Figure 6.3C, the spectral distribution of edge-emitted light shows negligible variation with increasing G, contrasting with the behavior of previously studied LSC luminophores where self-absorption produces a strong bathochromic shift in edge-emitted light with increasing G.[29] This result highlights the lack of self-absorption in doped nanocrystal LSCs.

In the absence of self-absorption, the relationship between OQE, luminophore LQY, and waveguide propagation and escape cone losses, is:

$$OQE = LQY\epsilon_{ec}\epsilon_{wg}(G), \qquad (1)$$

where the escape cone loss term is given by Snell's Law: $\epsilon_{ec} = 1 - \sqrt{1 - 1/n^2} \approx 0.75$, based on isotropic emission and a waveguide refractive index $n = 1.5$. $\epsilon_{wg}(G)$ represents losses due to waveguide scattering and absorption, whose combined effects are expressed through a waveguide attenuation coefficient α_{dB}, defined such that the fraction of photons lost per unit distance l is $e^{-4.34 l \alpha_{dB}}$.[30] Given ϵ_{ec}, Equation (1) allows determination of the other two loss mechanisms in an LSC –LQY and waveguide losses– from measurements of OQE vs G. For a uniformly illuminated rectangular LSC measuring $L \times W$, the proportion of emitted light surviving to reach an edge, subject to waveguide losses, is

$$\epsilon_{wg}(G) = \frac{1}{4\pi WL}\int_0^W \int_0^L \int_0^{2\pi} 2 \int_{\theta_{ec}}^{\pi/2} e^{-4.34\alpha_{dB} l(x,y,\theta,\varphi)} \sin\theta d\theta d\varphi dy dx \qquad (2)$$

where $\theta_{ec} = \sin^{-1}(1/n)$ is the escape cone angle and $l(x, y, \theta, \varphi)$ is the distance a photon travels to the edge when emitted from (x, y) with directional spherical coordinates (θ, φ). Combining Equations 1 and 2 and solving numerically, we fit the measured $OQE_{ap}(G)$ (inset Figure 6.3A) to find LQY = 53% and α_{dB} = 0.085 dB/cm (see SI for details). For the sample in Figure 6.3, the doped QD LQY measured in toluene was 50%, close to the fitted value. This result indicates that the doped QD LQY is preserved upon incorporation into the polymer device.

The flux gain,

$$F \approx CR\left(\eta_{PV}^{e_{em}} / \eta_{PV}^{AM1.5}\right) \qquad (3)$$

is the power produced from edge-attached photovoltaic cells relative to that produced from the same photovoltaic cells under direct AM1.5 exposure. Here $\eta_{PV}^{e_{em}}$ and $\eta_{PV}^{AM1.5}$ are the

photovoltaic conversion efficiencies at the peak LSC emission energy and under broadband AM1.5 illumination, respectively, and the energy concentration ratio $CR = OQE \times GN_{abs}e_{em}$, where N_{abs} is the number of solar photons absorbed by the LSC per unit area per second, found by integrating the AM1.5 solar spectrum over the doped QD absorption range (300 – 420 nm, Figure 6.3B), and e_{em} = 2.12 eV is the energy per luminescent photon. Figure 5.4 shows the size-dependent energy concentration ratio for a square LSC based on the LQY and α_{dB} for the experimental device in Figure 3, as well as the flux gain predicted for attached a-Si photovoltaic cells (see SI for details). The maximum concentration ratio and power density enhancement are projected to reach $CR_{max} = 6\times$ and $F_{max} = 15.6\times$ in the large-G limit, among the highest yet reported.[15,31,32] Projected maximum flux gains for other benchmark photovoltaic technologies are given in Table S1; several exceed 10×. These findings demonstrate the potential to achieve substantial reductions in photovoltaic area through optical concentration using doped nanocrystal LSCs. CR_{max} and F_{max} in doped QD LSCs are limited by parasitic waveguide losses (α_{dB}), which become the dominant loss mechanism for large G (inset, Figure 6.4). Such losses affect all LSCs, but heretofore have generally been negligible compared to self-absorption related losses. This result suggests significant further improvements in large-area doped QD concentrator performance should be possible using more transparent polymer waveguide materials, for example optical polysiloxanes or cyclic perfluoropolymers, which have intrinsic attenuation coefficients 1 – 3 orders of magnitude lower than polyacrylates at visible and near-IR wavelengths.[33,34]

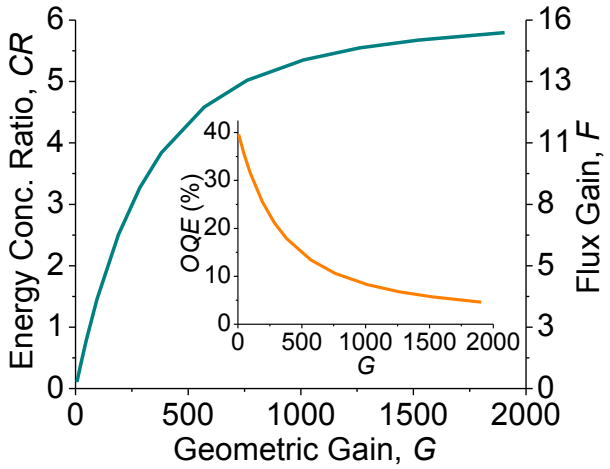

Figure. 4. Predicted energy concentration ratio and flux gain for a-Si PVs as a function of geometric gain for square Mn^{2+}-doped ZnSe/ZnS nanocrystal LSCs (α_{dB} = 0.085 dB/cm, LQY = 0.53). *F* and *CR* asymptotically approach 15.6× and 6× in the large area limit, respectively. Inset: optical quantum efficiency becomes limited by parasitic waveguide losses at large G. For our device thickness, G = 2000 corresponds to an LSC edge length of 3.36 m. See SI for details.

6.3. Conclusions

In summary, colloidal doped nanocrystals are demonstrated as a promising new class of zero-reabsorption luminophores for LSC applications. Using Mn^{2+}-doped ZnSe/ZnS nanocrystals as the active phosphor material, concentrating polymer films capable of selectively absorbing solar UV light and producing intensified emission with optical quantum efficiencies approaching 40% have been demonstrated. These concentrators are largely transparent to visible light, making them attractive for application as transparent window coatings or in multi-junction concentrator/PV configurations. As the first report of this approach, we anticipate further major improvements in LSC efficiencies using doped semiconductor nanocrystals. For the Mn^{2+}-doped ZnSe/ZnS-based LSCs described here, the nanocrystal LQYs can be increased by optimizing QD surface passivation, and the energy gap can be narrowed by alloying with a small amount of Cd^{2+}. Waveguide losses, currently the limiting factor in our devices, can be reduced by improved processing and use of more transparent polymers. As such, the Mn^{2+}-doped nanocrystal LSCs described here hold promise for practical window-layer applications where transparency is desired. More generally, even higher LSC limiting efficiencies, concentration ratios, and flux gains can be expected from the use of related doped nanocrystals that absorb and emit at lower energies. Such experiments are presently underway.

6.4. Methods

Doped QD synthesis. Mn^{2+}-doped ZnSe core nanocrystals were prepared by lyothermal degradation of $[Zn_4(SePh)_{10}](Me_4N)_2$ in the presence of $MnCl_2$. ZnS shells were grown by successive ionic layer adsorption and reaction (SILAR) deposition from $Zn(oleate)_2$ and tri-*n*-octyl phosphine sulfide (TOP-S). In a typical synthesis, 200 mg of $[Zn_4(SePh)_{10}](Me_4N)_2$ and 10 mg of Se were added anaerobically to a degassed mixture of 5.4 g of hexadecylamine and 5 mg of $MnCl_2$ in a three-necked round bottom flask, and the temperature was raised to 275 °C. After 20-60 min at 275 °C, the mixture was cooled and nanocrystals precipitated by addition of ethanol. The nanocrystals were then resuspended in toluene, where they were purified by repeated precipitation with ethanol, isolation by centrifuging, and resuspension in toluene. Following purification, ZnS shells were grown by alternating slow addition of approximately monolayer equivalents of $Zn(oleate)_2$ and TOP-S to a degassed mixture containing the isolated nanocrystals, 1.5 g of oleylamine, and 1.5 g of octadecene, held at 225 °C. Each addition was allowed to react for 30 minutes before the subsequent addition. After shell growth, the mixture was cooled and purified in the same manner as described above. Electronic absorption spectra of toluene suspensions were collected using a Cary 500 spectrometer. Photoluminescence spectra were collected using 405 nm excitation and an Ocean Optics USB2000 spectrometer for detection. Transmission electron microscopy (TEM) images were collected using a FEI Tecnai G2 F20.

Device Fabrication. Nanocrystals were incorporated into polymer films by dispersing a toluene suspension into a 5:1:1 by weight mixture of laurylmethacrylate, tri-octyl phosphine, and ethylene glycol di-methacrylate, containing <1% wt of Irgacure 651 photo-initiator (CIBA). Several droplets of the resulting mixture were placed onto a clean borosilicate glass coverslip, which was then covered by a second coverslip, and the resulting glass/solution/glass samples were photopolymerized with UV light under nitrogen for 1-3 hours to form a solid film with a thickness of approximately 100 μm. Except at the collection aperture, all device edges were blackened with a marker.

Device Characterization. Absorbance measurements were performed with a Jasco UV-VIS spectrophotometer. Edge emission measurements were performed using a Horiba Fluorolog model FL3-21 fluorometer connected via fiber optic cable to an integrating sphere. Further details are provided in the text and SI.

6.5. References and Notes

[1] (a) Weber WH, Lambe J, (1976) Luminescent greenhouse collector for solar radiation. *Appl. Opt.* 15(10): 2299-2300. (b) Goetzberger A, Greubel W, (1977) Solar energy conversion with fluorescent collectors. *Appl. Phys*. 14(2): 123-139.

[2] Swanson RM, (2000) The Promise of Concentrators. *Prog. Photo. Res. App*. 8: 93-111.

[3] Debije MG, Verbunt PPC, (2012) Thirty years of luminescent solar concentrator research: solar energy for the built environment. *Adv. Energy Mat*. 2(1): 12-35.

[4] Huang X, Han S, Huang W, Liu X, (2013) Enhancing solar cell efficiency: the search for luminescent materials as spectral converters. *Chem. Soc. Rev*. 42(1): 173-201.

[5] Rau U, Einsele F, Glaeser GC, (2005) Efficiency limits of photovoltaic fluorescent collectors. *Appl. Phys. Lett.* 87(17): 171101/1-171101/3.

[6] Smestad G, Ries H, Winston R, Yablonovitch E, (1990) The thermodynamic limits of light concentrators. *Sol. En. Mat.* 21(2-3): 99-111.

[7] Batcheldar JS, Zewail AH, Cole T, (1979) Luminescent solar concentrators. 1: Theory of operation and techniques for performance evaluation. *Appl. Opt*. 18(18): 3090-3110.

[8] Verbunt PPC, Debije MG, (2011) Progress in Luminescent Solar Concentrator Research: Solar Energy for the Built Environment. *Proc. World Renewable Energy Congress* Linköping, Sweden, 2751-2759.

[9] van Sark WGJHM, (2012) Luminescent Solar Concentrators - a low cost photovoltaics alternative. *2nd European Energy Conference, Maastricht, The Netherlands 2nd European Energy Conference*, Maastricht, The Netherlands, EPJ Web of Conferences 33, 02003.

[10] The critical angle of the escape cone is $\theta_c = \sin^{-1}(n_{clad}/n_{core})$, where n_{clad} and n_{core} are the refractive indices of the waveguide cladding and core. For a polymer or glass waveguide in air with $n_{clad} = 1.5 \sim 1.7$, this leads to θ_c =35° – 45°, and $\eta_{trap} = 0.7 \sim 0.8$. Thus 20% - 30% of photons are lost with each successive re-absorption / re-emission. For a detailed discussion see: 13c.

[11] (a) Goldschmidt, J. C.; Peters, M.; Prönneke, L.; Steidl, L.; Zentel, R.; Bläsi, B.; Gombert, A.; Glunz, S.; Willeke, G.; Rau, U., (2008) Theoretical and experimental analysis of photonic structures for fluorescent concentrators with increased efficiencies. *Phys. Stat. Sol*. 205(12): 2811-2821; (b) Debije, M. G.; Van, M-P,; Verbunt, P., P., C.; Kastelijn, M., J.; vander Blom, R., H., L.; Broer, D., J.; Bastiaansen, W., M., (2010) Effect on the output of a luminescent solar concentrator on application of organic wavelength-selective mirrors. *Appl. Opt*. 49(4): 745-751; (c) Giebink, N. C.; Wiederrecht, G. P; Wasielewski, M. R. (2011) Resonance-shifting to circumvent reabsorption loss in luminescent solar concentrators. *Nature Phot*. 5: 694-701; (e) Verbunt, P. P. C.; Broer, D. J.; Bastiaansen, C. W. M.; Debije, M. G. (2009) The effect of an organic selectively-reflecting mirror on the performance of a luminescent solar concentrator. *Proc. of the 24th European PV Solar Energy Conference* 381-384.

[12] (a) Mulder, C. L.; Reusswig, P,. D.; Velázquez, A., M.; Kim, H.; Rotschild, C.; Baldo, M., A., (2010) Dye alignment in luminescent solar concentrators: I. Vertical alignment for improved waveguide coupling. *Opt. Express* 18(S1): A79-A90; (b) Debije, M. G. (2010) Solar energy collectors with tunable transmission. *Adv. Funct. Mat*. 20(9): 1498-1502; (c) McDowall, S.; Butler, T.; Bain, E.; Scharnhorst, K.; Patrick, D. L. (2013) Comprehensive analysis of escape-cone losses from luminescent waveguides. *Appl. Opt*. 52(6): 1230-1239; (d) MacQueen, R. W.; Cheng, Y. Y.; Clady, R. G. C. R.; Schmidt, T. W. (2010) Towards an aligned luminophore solar concentrator. *Opt. Expr*. 18(S2):A161-A166.

[13] Krumer, Z.; G. J. H. M. W. van Sark; Donegá, C. Schropp, R. E. I.,(2013) Exploration of parameters influencing the self-absorption losses in luminescent solar concentrators with an experimentally validated combined ray-tracing/Monte-Carlo model. *Proc. SPIE 8821, High and Low Concentrator Systems for Solar Electric Applications VIII*, 882104.

[14] (a) De Boer, D. K. G.; Broer, D., J.; Debije, M., G.; Keur, W.; Meijerink, A.; Ronda, C., R.; Verbunt, P., P., C., (2012) Progress in phosphors and filters for luminescent solar concentrators. *Opt. Express.* 20(S3): A395-A405.

[15] Currie MJ, Mapel JK, Heidel TD, Goffri S, Baldo, MA, (2008) High-Efficiency Organic Solar Concentrators for Photovoltaics. *Science* 321(11): 226-228.

[16] (a) Sanguineti, A.; Sassi, M.; Turrisi, R.; Ruffo, R.; Vaccaro, G.; Meinardi, F.; Beverina, L., (2013) High Stokes shift perylene dyes for luminescent solar concentrators. *Chem. Comm.* 49(16): 1618-1620; (b) Saraidarov, T.; Levchenko, V.; Grabowska, A.; Borowicz, P.; Reisfeld, R. (2010) Non-self-absorbing materials for Luminescent Solar Concentrators (LSC). *Chem. Phys. Lett*. 492(1-3): 60-62.

[17] van Sark W. G. J. H. M.; Barnham, K., W., J.; Slooff, L., H,; Chatten, A., J.; Büchtemann, A.; Meyer, A.; McCormack, S., J.; Koole, R.; Farrell, D., J.; Bose, R.; Beude, E., E.; Burgers, A., R.; Budel, T.; Quilitz, J,; Kennedy, M.; Meyer, T.; De Mello Donegà, C.; Meijerink, A.; Vanmaekelbergh, D., (2008) Luminescent solar concentrators - a review of recent results. *Optics Express* 16(26): 21773-21792.

[18] (a) Purcell-Milton, F.; Gun'ko, Y. K. J. (2012) Quantum dots for Luminescent Solar Concentrators. *J. Mat. Chem.* 22(33): 16687-16697; (b) Tackling self-absorption in luminescent solar concentrators with Type-II colloidal quantum dots, Kumer, Z.; Pera, S. J.; van Dijk-Moes, R. J. A.; Zhao, Y.; de Brouwer, A. F. P.; Groeneveld, E.; van Sark, W. G. J. H. M.; Schropp, R. E. I.; Donega, D. dM., Sol. En. Mat. Sol. Cells 2013, 111, 57-65.

[19] Beaulac R, Archer PI, Gamelin DR, (2008) Luminescence in Colloidal Mn^{2+}-Doped Semiconductor Nanocrystals. *J. Solid State Chem.* 181(7): 1582-1589.

[20] Ronda, C.; (Ed.), Luminescence: From Theory to Applications. Wiley-VCH: Weinheim, 2008.

[21] Hyldahl MG, Bailey ST, Wittmershaus BP, (2009) Photostability and performance of CdSe/ZnS quantum dots in luminescent solar concentrators. *Sol. En.* 83(4): 566-573.

[22] (a) Bol AA, Meijerink A, (1998) Long-lived Mn^{2+} emission in nanocrystalline ZnS:Mn^{2+}. *Phys. Rev. B* 58(24): R15997-R16000. (b) Suyver JF, Wuister SF, Kelly JJ, Meijerink A, (2000) Luminescence of nanocrystalline ZnSe:Mn^{2+}. *Phys. Chem. Chem. Phys.* 2(23): 5445-5448. (c) Pradhan N, Battaglia DM, Liu Y, Peng X, (2007) Efficient, Stable, Small, and Water-Soluble Doped ZnSe Nanocrystal Emitters as Non-Cadmium Biomedical Labels. *Nano Lett.* 7(2): 312-317. (d) Sarkar S, Karan NS, Pradhan N, (2011) Ultra-small Color Tunable Cu doped Ternary Nanocrystal Emitters. *Angew. Chem., Int. Edit.* 50: 6065-6069.

[23] (a) Hoffman DM, et al. (2000) Giant internal magnetic fields in Mn doped nanocrystal quantum dots. *Sol. State Comm.* 114(10): 547-550. (b) Norris DJ, Yao N, Charnock FT, Kennedy TA, (2001) High-Quality Manganese-Doped ZnSe Nanocrystals. *Nano Lett.* 1(1): 3-7. (c) Beaulac R, et al. (2008) Spin-Polarizable Excitonic Luminescence in Colloidal Mn^{2+}-Doped CdSe Quantum Dots. *Nano Lett.* 8(4): 1197-1201. (d) Beaulac R, Schneider L, Archer PI, Bacher G, Gamelin DR, (2009) Light-Induced Spontaneous Magnetization in Doped Colloidal Quantum Dots. *Science* 325(5943): 973-976.

[24] Chen HY, Chen TY, Son DH, (2010) Measurement of Energy Transfer Time in Colloidal Mn-Doped Semiconductor Nanocrystals. *J. Phys. Chem. C* 114(10): 4418-4423.

[25] Bradshaw LR, Hauser A, McLaurin EJ, Gamelin DR, (2012) Luminescence Saturation via Mn^{2+}-Exciton Cross Relaxation in Colloidal Doped Semiconductor Nanocrystals. *J. Phys. Chem. C* 116(16): 9300-9310.

[26] Irvine SE, Staudt T, Rittweger E, Engelhardt J, Hell SW, (2008) Direct Light-Driven Modulation of Luminescence from Mn-Doped ZnSe Quantum Dots. *Angew. Chemie Int. Ed.* 47(14): 2516-2519.

[27] Under broadband solar illumination the threshold for two photon quenching is reached roughly when the arrival rate per nanocrystal of absorbable photons (i.e. those with energies exceeding ϵ_{abs}) approaches the turnover frequency (~10^4 s^{-1}). The integrated AM1.5G photon flux from 280 nm to 425 nm (corresponding approximately the doped QD absorption range) is 10^{16} photons cm^{-2} s^{-1}. Assuming a doped QD extinction coefficient 10^5 M^{-1} cm^{-1} and a concentration high enough to absorb

99% of incident sunlight up to ϵ_{abs} (10^{-7} mol cm^{-2}), the quenching onset threshold is approximately 10^3 Suns.

[28] (a) McLaurin EJ, Vlaskin VA, Gamelin DR, (2011) Water-soluble dual-emitting nanocrystals for ratiometric optical thermometry. *J. Am. Chem. Soc.* 133(38): 14978-14980. (b) Reiss P, Protière M, Li L, (2009) Core/shell semiconductor nanocrystals. *Small* 5(2): 154-168.

[29] Wilson LR, et al. (2010) Characterization and reduction of reabsorption losses in luminescent solar concentrators. *Appl. Opt.* 49(9): 1651-1661.

[30] *Optical Propagation in Linear Media: Atmospheric Gases and Particles, Solid-State Components, and Water*, Thomas, ME, (2006) Oxford University Press, New York, NY.

[31] (a) Mugnier J, Dordet Y, Pouget J, Valeur B, (1987) *Revue Phys. Appl*. A photometric approach of fluorescent solar concentrators. Role of diffuse reflectors and spectral sensitivity of solar cells. 22(1): 89-99. (b) Roncali J, Garnier F, (1984) Photon-transport properties of luminescent solar concentrators: analysis and optimization. *Appl. Opt*. 23(16): 2809-2817.

[32] Batcheldar JS, Zewail AH, Cole T, (1981) Luminescent solar concentrators. 2: Experimental and theoretical analysis of their possible efficiencies. *Appl. Opt*. 20(21): 3733-3754.

[33] Su, K.; DeGroot Jr., J. V.; Norris, A. W.; Lo, P. Y., Siloxane materials for optical applications, *Proc. SPIE* **2005**, *6029*, 60291C.

[34] *Modern Fluoroorganic Chemistry*, Kirsch, P. (**2013**, Wiley-VCH, Weinheim, Germany)

Chapter 7. Dual-Emitting Nanoscale Temperature Sensors

Abstract: Soluble luminescent temperature probes are promising candidates for optical thermometry and thermography applications requiring precise, passive, and spatially resolved temperature data. Dual-emitting temperature sensors overcome many of the obstacles encountered with absolute intensity-based luminescence sensors, including optical occlusion, concentration variation, or non-specificity, by providing internally referenced (ratiometric) signals. Here, we provide an overview of the key mechanisms underpinning the dual emission of various nanostructures from recent literature and discuss their relationship to optical thermometry. Reprinted with permission from: McLaurin, E. J.; Bradshaw, L. R.; Gamelin, D. R., Dual-Emitting Nanoscale Temperature Sensors. *Chemistry of Materials* 2013, **25** (8), 1283-1292.

7.1. Introduction

Sensors are needed for monitoring local temperatures in diverse heterogeneous environments.[1-2] High-resolution, real-time temperature mapping would facilitate the study of fundamental biological processes such as protein folding[3] and calcium signaling,[4] biotechnological applications including PCR[5] and thermotherapeutics,[6] and other phenomena of current interest including heat dissipation during optical trapping[7] and "hot spots" in micro- or nano-electronics.[8-9] To this end, research into the development of luminescent temperature sensors has attracted broad attention. Of particular interest are soluble molecular[10-13] or nanoparticulate (NP)[14-16] luminophores showing temperature-dependent photoluminescence (PL), because these can be used for high-resolution thermal mapping in the liquid or solid phase.[17-18]

Here, we give a brief overview of nanoscale dual-emitting temperature sensors. Our discussion focuses on soluble nanostructures including nanocrystals (NCs), NC conjugates, molecular conjugates, and related systems, with the aim of illustrating the various electronic structures responsible for dual emission. Examples from the NC, lanthanide, molecular beacon, polymer NP, and doped NC literature are highlighted. For more general discussions of nanothermometry, the reader is referred to the excellent recent reviews of Jaque & Vetrone, and Carlos & co-workers.[19-20]

7.2. General Considerations In Ratiometric Optical Thermometry

7.2.A Dual Emission Scenarios

Many optical temperature sensors rely on changes in luminescence intensity as the reporting mechanism, for example, an increase in the nonradiative decay rate with increasing temperature that leads to diminished luminescence.[17-18, 21-22] Intensity-based temperature sensors are often susceptible to errors due to changes in probe concentration, excitation or detection efficiency, or a lack of specificity for temperature, however. For instance, luminescence may also be quenched by oxygen, sensor aggregation, or changes in pH, in addition to temperature increase.[23] Changes in the sensor local environment are difficult to control in complicated systems such as cells or micro-devices, and can cause inaccurate temperature measurement.[1-2] Such obstacles can often be overcome using ratiometric detection schemes.

Dual-emitting sensors show resolvable luminescence from two different excited states. When temperature changes one or both of these PL intensities, its effect is measurable from relative instead of absolute PL intensities, reducing the impact of extrinsic factors like fluctuations in excitation rate, detection efficiency, probe concentration, optical occlusion, or other local inhomogeneities that alter absolute intensities. Figure 7.1 summarizes three general scenarios by which dual emission (in the broadest sense of the term) has been achieved, categorized by the extent of population transfer between the two luminescent excited states. Figure 7.1a shows the trivial scenario involving a mixture of two independent luminophores, each with its unique PL temperature dependence. In this scenario, light is absorbed and emitted by each luminophore, and one or both of their luminescence intensities is temperature dependent. This scenario describes any case involving two emitters that act independently, whether physically connected or not. Figure 7.1b shows a qualitatively different mechanism by which dual emission has been achieved, involving two emitters that are coupled electronically such that energy transfer (ET) occurs from one (the Donor) to the other (the Acceptor). When ET occurs on the same timescale as Donor luminescence, emission is observed from both the Donor and the Acceptor. Figure 7.1c shows a third qualitatively different dual emission mechanism where the populations of two luminescent excited states are in thermal equilibrium. In this scenario, temperature controls the population distribution, and therefore the relative luminescence intensities from the two excited states. This scenario is achieved in the limit of rapid population exchange between the emissive states relative to luminescence from either

excited state. These three scenarios are qualitatively different from one another, and may be loosely associated with the strength of the electronic coupling governing population transfer between the two emissive excited states, which ranges from "decoupled" (Figure 7.1a) through "moderately coupled" (Figure 7.1b) to "strongly coupled" (Figure 7.1c).

7.2.B Kinetic Descriptions

The three scenarios illustrated in Figure 7.1 can be defined more precisely in terms of kinetics. In the scenario of Figure 7.1a, the two luminescent excited states are electronically independent, and there is no ET between them on the timescale of their luminescence ($1/\tau_{lum} >> k_{ET}$). Temperature measurements in this scenario are usually based on the change in PL quantum yield (Φ_{PL}) of one or both luminophores arising from temperature-dependent non-radiative decay kinetics ($k_{nr}(T)$). For example, when only one luminescence feature is temperature dependent, the luminescence intensity ratio can be described as shown in eq 7.1, where $I_n(T)$ is the temperature-dependent luminescence intensity from $|n\rangle \rightarrow |0\rangle$, with $|n\rangle$ as defined in Figure 7.1a, $k_{r,n}$ and $k_{nr,n}$ are the radiative and non-radiative decay rate constants of the same excited state, and $A_n(\lambda_{ex})$ is the absorbance to populate $|n\rangle$ at the excitation wavelength.

$$\frac{I_1(T)}{I_1(T)+I_2(T)} \propto \frac{A_1(\lambda_{ex})\cdot\Phi_{PL1}(T)}{A_1(\lambda_{ex})\cdot\Phi_{PL1}(T)+A_2(\lambda_{ex})\cdot\Phi_{PL2}(T)} \qquad [7.1]$$

$$= \frac{A_1(\lambda_{ex})\cdot\frac{k_{r1}}{k_{r1}+k_{nr1}(T)}}{A_1(\lambda_{ex})\cdot\frac{k_{r1}}{k_{r1}+k_{nr1}(T)}+A_2(\lambda_{ex})\cdot\frac{k_{r2}}{k_{r2}+k_{nr2}(T)}}$$

Careful selection of chemically similar luminophores can limit sensitivity to environmental factors, and hence improve selectivity for temperature.[24]

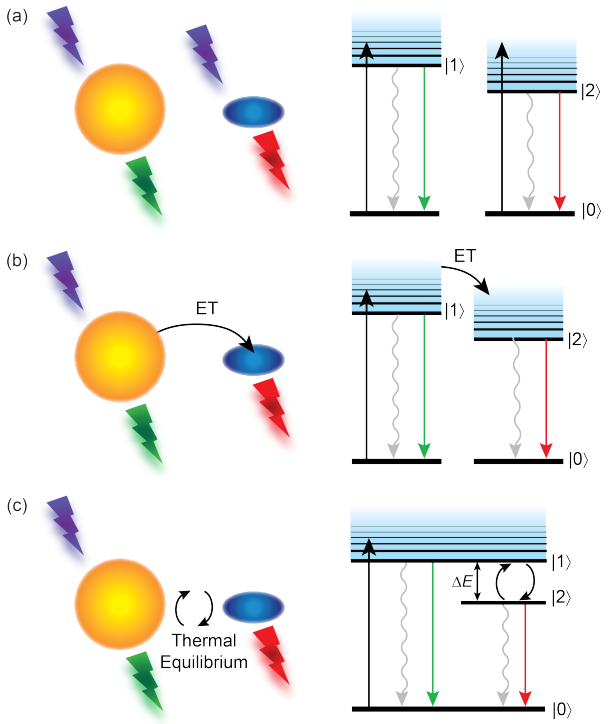

Figure 7.1. Schematic summaries of three different electronic structures leading to dual emission. (a) Two independent luminescent probes, $|1\rangle$ and $|2\rangle$. At least one shows a response to temperature. (b) Two luminophores interacting through energy transfer. (c) Two luminescent excited states in fast thermal equilibrium.

In the scenario of Figure 7.1b, photon absorption populates the Donor excited state, $|1\rangle$, from which Donor luminescence is competitive with energy transfer to the Acceptor, $|2\rangle$ ($1/\tau_{lum} \approx k_{ET}$, where τ_{lum} is the Donor luminescence lifetime in the absence of acceptor and k_{ET} is the rate constant for Donor-Acceptor energy transfer). The Donor luminescence at temperature T is then described by eq 7.2.

$$I_1(T) \propto A_1(\lambda_{ex}) \cdot \Phi_{PL1}(T) = A_1(\lambda_{ex}) \cdot \frac{k_{r1}}{k_{r1}+k_{nr1}(T)+k_{ET}(T)} \qquad [7.2]$$

In the limit of negligible direct excitation, the excited Acceptor population is determined by the quantum efficiency of the energy transfer process (Φ_{ET}). The Acceptor luminescence intensity is then described by eq 7.3.

$$I_2(T) \propto A_1(\lambda_{ex}) \cdot \Phi_{ET}(T) \cdot \Phi_{PL2}(T) = \frac{A_1(\lambda_{ex}) \cdot k_{ET}(T)}{k_{r1}+k_{nr1}(T)+k_{ET}(T)} \cdot \frac{k_{r2}}{k_{r2}+k_{nr2}(T)} \qquad [7.3]$$

Temperature can be assessed using changes in $I_1/(I_1+I_2)$ (or related ratios) resulting from temperature-dependent changes in Φ_{PL1}, Φ_{PL2}, or Φ_{ET}, as described by eq 7.4.

$$\frac{I_1(T)}{I_1(T)+I_2(T)} \propto \frac{\Phi_{PL1}(T)}{\Phi_{PL1}(T)+\Phi_{PL2}(T)\cdot\Phi_{ET}(T)} = \frac{k_{r1}}{k_{r1}+\frac{k_{r2}\cdot k_{ET}(T)}{k_{r2}+k_{nr2}(T)}} \quad [7.4]$$

Equation 7.4 demonstrates that, in contrast with decoupled excited states, the luminescence ratio measured in the scenario of Figure 7.1b is independent of both the excitation wavelength and non-radiative relaxation of the Donor.

For the scenario of strongly coupled excited states described by Figure 7.1c, population exchange between the two luminescent excited states is orders of magnitude faster than luminescence decay of either excited state ($1/\tau_{lum} << k_{ET}$), which establishes a thermal equilibrium between the two luminescent states. In this scenario, the luminescence intensity from each state depends on the product of its radiative decay rate constant and its Boltzmann population. Temperature is assessed by measuring the luminescence ratio described by eq 7.5, where ΔE is the energy difference between the two luminescent states (Figure 7.1c).[25]

$$\frac{I_1(T)}{I_1(T)+I_2(T)} = \frac{k_{r1}\cdot e^{-\Delta E/k_BT}}{k_{r1}\cdot e^{-\Delta E/k_BT}+k_{r2}\cdot\left(1-e^{-\Delta E/k_BT}\right)} \quad [7.5]$$

In this limit of excited-state thermal equilibrium, non-radiative processes decrease both emission intensities proportionally and therefore do not change the PL intensity ratio.

7.2.C Sensitivity Metrics

Definition of a sensitivity metric allows evaluation and comparison of optical temperature probes. In general terms, the internal (or intrinsic) sensitivity of any probe can be defined as in eq 7.6, where P is the measured temperature-sensitive parameter.

$$S_{int}(T) = \left|\frac{\partial P}{\partial T}\right| \quad [7.6]$$

Temperature sensors showing large absolute changes in P with small changes in temperature will be the most sensitive. In practice, however, quantitative comparison of temperature sensors that operate by different mechanisms has proven challenging. In an effort to compare broad categories of temperature sensors, Carlos & co-workers have advocated use of “relative sensitivity" (S_{rel}), defined as in eq 7.7.

$$S_{rel}(T) = \frac{\left|\frac{\partial P}{\partial T}\right|}{P} \quad [7.7]$$

For ratiometric optical thermometry, the sensitivity is determined by the change in PL ratio with change in temperature. We therefore define the internal sensitivity (S_{int}) as in eq 7.6, where $P = I_1/(I_1+I_2)$. Here, I_1 and I_2 are the two luminescence intensities of the dual emission. As defined here, this ratio is normalized and hence scales from zero to one. Note that defining P as I_1/I_2 instead may at first appear reasonable, but this ratio is not defined in the limit of $I_2 \rightarrow 0$. Using these definitions, eq 7.8 describes internal sensitivity for ratiometric sensors.

$$S_{int}(T) = \left| \frac{\partial\left(\frac{I_1}{I_1 + I_2}\right)}{\partial T} \right| \quad [7.8]$$

In practice, the sensitivity of any optical temperature probe must also depend on the probe's molar extinction coefficient at the excitation wavelength ($\varepsilon(\lambda_{ex})$) and its PL quantum yield (Φ_{PL}). We therefore define the external sensitivity (S_{ext}) as shown in eq 7.9.

$$S_{ext}(T) = S_{int}(T) \cdot \varepsilon(\lambda_{ex}) \cdot \Phi_{PL} \quad [7.9]$$

In addition to these parameters, how the measurement is physically performed also makes important contributions to the ability to detect temperature changes in the laboratory. For instance, the optical excitation and detection efficiencies, background luminescence, the windows of luminescence intensity integration, and other experimental factors will influence the signal-to-noise of any optical temperature measurement but are not intrinsic to the temperature sensing mechanism, and therefore cannot be defined uniquely. Finally, sensors with broad active temperature windows are sometimes desired, but this aspect of the sensor is not captured by the metrics outlined above. Indeed, the breadth of the temperature-sensing window is inversely related to $S_{int}(T)$. A good wide-range temperature sensor will therefore not have the highest $S_{int}(T)$, but must maintain a high $S_{ext}(T)$ over this broad window. Consequently, sensors with an appropriate balance of features must be identified for any particular application. With these caveats in mind, the metric of $S_{int}(T)$ still allows some degree of quantitative comparison among dual-emitting sensors, and we therefore report $S_{int}(T_{max})$ for the literature ratiometric temperature sensors discussed in this review. $S_{int}(T_{max})$ has been calculated from available experimental data, and where possible, linked to the mechanisms in section 2.2.

7.3. Experimental Examples

7.3.A Dual Emission from Two Decoupled Excited States

An early example of ratiometric luminescence nanothermometry involving decoupled luminescent excited states used Mn^{2+} and Eu^{3+} co-doped ZnS NCs (Mn^{2+}:Eu^{3+}:ZnS) as the probes.[26] Figure 7.2 summarizes luminescence data collected from these NCs at different temperatures and with different excitation wavelengths. Excitation at 394 nm yields primarily Eu^{3+} $^5D_0 \rightarrow {}^7F_2$ luminescence (Figure 7.2a), whereas excitation at 360 nm yields primarily Mn^{2+} $^4T_1 \rightarrow {}^6A_1$ luminescence (Figure 7.2b). Both luminescence intensities decrease with increasing temperature. The two luminescent excited states are electronically decoupled, and consequently their luminescence intensities vary independently. Nearly linear response curves are generated from each luminescence intensity when plotted vs temperature (Figure 7.2c). Figure 7.2d plots the ratio of Mn^{2+}:Eu^{3+} PL intensities (obtained with 360 and 394 nm excitation, respectively) vs temperature, and also yields a nearly linear response curve. The ratio of PL intensities in this system thus provides an internally referenced measurement of local temperature around the NC probes. Following section 2.3, these data correspond to a maximum internal sensitivity of $S_{int}(T_{max}) \approx 0.034\%\ °C^{-1}$ at ~80 °C.

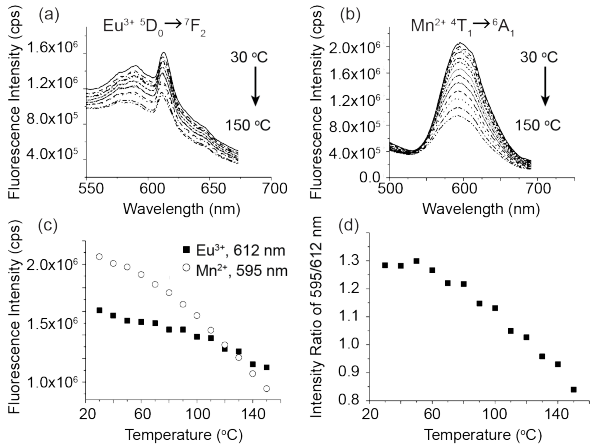

Figure 7.2. Luminescence data for Mn^{2+}:Eu^{3+}:ZnS NCs measured at different temperatures. (a) Eu^{3+} $^5D_0 \rightarrow {}^7F_2$ transition at 612 nm (394 nm excitation). (b) Mn^{2+} $^4T_1 \rightarrow {}^6A_1$ luminescence at 595 nm (360 nm excitation). (c) Eu^{3+} (squares) and Mn^{2+} (circles) PL intensities vs temperature. (d) Ratio of Mn^{2+} to Eu^{3+} PL intensities as a function of temperature. Adapted from ref. 26.

Related decoupled nanothermometers have used dyes with relatively temperature-independent PL such as Rhodamine 110 to generate internal reference signals for temperature-

dependent CdSe/ZnS NC PL.[27] Decoupled dual emission is a simple method for ratiometric optical thermometry, but the possibility of non-specific environmental factors changing the PL of the two luminophores differently (*i.e.*, $k_{nr,1}$ and $k_{nr,2}$ not solely dependent on temperature) may limit the accuracy and generality of this approach.

7.3.B. Dual Emission from Two Moderately Coupled Excited States

The second broad category of dual emitting temperature sensors is defined by two electronically coupled luminescent states in which one sensitizes the other via energy transfer. Here, dual emission is observed when radiative decay of the Donor is kinetically competitive with energy transfer between the two luminescent states (Figure 7.1b). This condition is frequently met when energy transfer proceeds via a Förster-type mechanism (Förster resonance energy transfer, FRET),[28] which is often relatively slow and hence allows Donor luminescence to compete. Examples of dual-emitting nanoscale temperature sensors in this category are described below.

7.3.B(a) Polymer Dots (Pdots).

Conducting polymers can be formed as NP micelles when combined with amphiphilic polymers in aqueous solution.[29] These NPs, known as “pdots", have many attractive properties for optical sensing, including large absorption cross-sections and high luminescence quantum yields. Pdot absorption and emission energies can be tuned by changing the identity of the conducting polymer. During micelle formation, pdots can also trap small molecules or NCs within their internal volumes, introducing new functionality including a second luminescent excited state. “Doped” pdots of this type have been used for a variety of biological applications including near-infrared imaging[30] and oxygen sensing.[31]

Figure 7.3a shows PL spectra measured at various temperatures for one such pdot composed of poly[(9,9-dioctylfluorenyl-2,7-diyl)-co-(1,4-benzo-(2,1’,3)-thiadiazole)] (PFBT, emits at 540 nm) doped with Rhodamine B (RhB, emits at 573 nm).[32] Photoexcitation of the polymer is followed by FRET to RhB, and dual emission is observed. Between 10 and 70 °C, a temperature independent FRET efficiency of up to 60% is observed. Using the pdot luminescence at 510 nm as an internal reference, temperatures were measured based on thermal quenching of the RhB luminescence. Figure 7.3b shows a plot of I_{573}/I_{510} vs temperature, which yields a linear relationship between 10 and 70 °C.[33] Following the definitions outlined in section 2.3, these data correspond to $S_{int}(T_{max}) \approx 0.23\%\ °C^{-1}$.

Figures 3c-f show red (RhB) and green (pdot) PL images of these sensors within HeLa cells, monitored at 13.5 and 36.5 °C (Figures 4c,e and 4d,f, respectively). The red channel (RhB) shows reduced emission at the lower temperature, while the green channel (pdot) remains nearly constant over this temperature range. The average cell temperatures reported by these PFBT-RhB optical sensors of 13.2 ± 0.9 and 35.7 ± 1.8 °C agree well with the external temperatures of 13.5 and 36.5 °C, respectively, indicating that these doped pdot sensors are suitable for probing temperature ratiometrically under biologically relevant conditions.

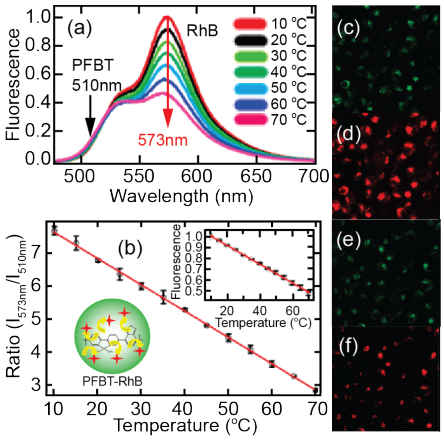

Figure 7.3. Pdot-RhB temperature sensor based on FRET. (a) The pdot Donor PL (510 nm) is temperature independent and provides an intensity reference. The RhB PL (573 nm) decreases with increasing temperature. (b) Ratio of 573 nm:510 nm PL intensities vs temperature, corresponding to $S_{int}(T_{max}) \approx 0.23\%\ °C^{-1}$. Insets: Normalized RhB PL intensities vs T, and illustration of RhB-encapsulated pdot. (c-f) Confocal microscopy images of HeLa cells labeled with PFBT-RhB using (c) 507-518 nm detection at 13.5 °C, (d) 507-518 nm detection at 36.5 °C, (e) 571-582 nm detection at 13.5 °C, and (f) 571-582 nm detection at 36.5 °C. At higher temperature, the cells show less red PL (571-582 nm). Adapted from ref. 32.

7.3.B(b) Semiconductor Nanocrystals.

Semiconductor NCs offer similar advantages to pdots: they are bright, can act as energy transfer donors, and can serve as scaffolds for building functionality.[34-38] Semiconductor NC bandgap energies can be tuned synthetically via quantum confinement or composition, providing a broad spectrum of accessible absorption and luminescence energies.[39-40]

Semiconductor nanocrystal/nanorods (NC/NRs) have attracted recent interest in various fields because of their unusual electronic structures and, for the purposes of optical sensing, their greater brightness relative to related spherical colloidal NCs.[41-42] Dual-emitting temperature sensors have been prepared by modification of such NC/NRs with FRET acceptor dyes.[43] Figure 7.4a depicts a CdSe/CdS NC/NR with the temperature sensitive dye Alexa-647 covalently attached to the surface. NC/NR photoexcitation is followed by partial energy transfer to the Alexa dyes, with FRET efficiencies ranging from 75-90%. Figure 7.4b shows PL spectra of these conjugates collected at various temperatures between 20 and 40 °C. The Alexa-647 luminescence, centered at ~670 nm, decreases with increasing temperature. The NC/NR luminescence, centered at ~615 nm, is also temperature dependent, decreasing in intensity and red-shifting with increasing temperature. Analysis of the PL data showed that the FRET efficiency was essentially constant over this temperature range. Plotting $I_{630\text{-}640}/I_{664\text{-}674}$ yields a linear temperature response from 20-26 °C (Figure 7.4c). Following section 2.3, these data correspond to $S_{int}(T_{max}) \approx 0.66\%\ °C^{-1}$.

The challenging process of delivering NCs to the cytosol of living cells is well documented.[44] The NC/NR-Alexa sensors were introduced into live cells using vector-mediated delivery by a cationic polymer colloid as previously described.[45] Figure 7.4d plots $I_{630\text{-}640}/I_{664\text{-}674}$ ratios measured in cells and in a cuvette for samples held at 20 and 25 °C. For both solution and intra-cellular measurements, the ratio $I_{630\text{-}640}/I_{664\text{-}674}$ increases with increasing temperature, but for any given temperature the luminescence ratio was larger when the probes were within the cells than when they were in aqueous buffer. This discrepancy is likely due to different local environments affecting the Alexa PL quantum yield. For quantitative measurements in diverse environments, such FRET-based dual-emitting temperature probes must therefore be calibrated within the target environment to ensure accurate reporting.

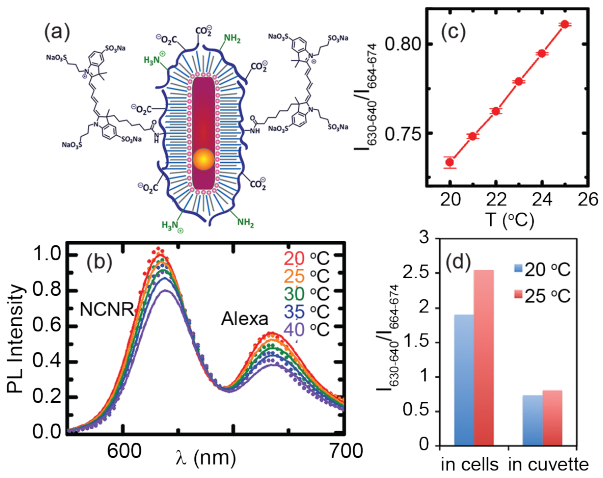

Figure 7.4. FRET-based NC/NR-Alexa-647 temperature sensor. (a) CdSe/CdS nanocrystal-nanorods (NC/NRs) modified by the temperature-sensitive dye Alexa-647, with Donor-Acceptor distances of ~7.5 nm. (b) The Alexa-647 PL decreases as temperature increases. The NC/NR PL decreases and redshifts with increasing temperature. (c) $I_{630\text{-}640}/I_{664\text{-}674}$ vs temperature, corresponding to $S_{int}(T_{max}) \approx 0.66\%$ $°C^{-1}$. (d) $I_{630\text{-}640}/I_{664\text{-}674}$ ratios measured in cells and in cuvette, showing different ratios in the cell measurements. Adapted from ref. 43.

7.3.B(c) Molecular Beacons.

In addition to generating dual emission, FRET may also be used as the temperature sensing mechanism itself in some cases.[46] When the luminophores Fluorescein (Donor) and Texas Red (Acceptor) are linked by a hairpin DNA strand, for example, the resulting molecular beacon (MB) shows strongly temperature-dependent FRET efficiencies that translate into changes in relative luminescence intensities from the two fluorophores with temperature. Figure 7.5a illustrates the major conformational change in the DNA hairpin linker of this system induced by temperature. Attaching the FRET Donor and Acceptor fluorophores to the two ends of this linker thus yields strongly temperature-dependent FRET efficiencies: k_{ET} decreases as the temperature increases because of hairpin unfolding.

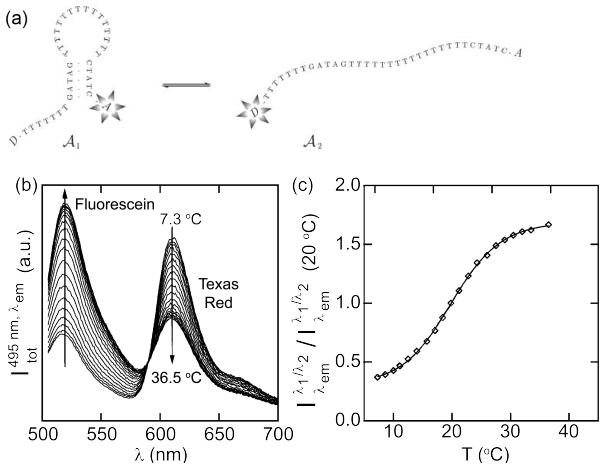

Figure 7.5. Molecular-beacon (MB) temperature sensor based on nucleic acid folding. (a) As temperature increases, the DNA hairpin unfolds and Donor/Acceptor FRET becomes less efficient. (b) PL spectra with Fluorescein as the Donor and Texas Red as the Acceptor, measured from 7.3 to 36.5°C. With increasing temperature, the Fluorescein PL (518 nm) increases and the Texas Red PL (610 nm) decreases. These data correspond to $S_{int}(T_{max}) \approx 2.1\%$ °C^{-1}. (c) I_{518}/I_{610} vs temperature, normalized at room temperature. Adapted from ref. 46.

Figure 7.5b shows PL spectra of this construct collected at various temperatures. The Fluorescein luminescence at 518 nm increases as the Texas Red Acceptor moves farther away, and the Texas Red luminescence at 610 nm shows a concominant decrease. Figure 7.5c plots the ratio of the two luminescence intensities (I_{518}/I_{610}) vs temperature, normalized to this intensity ratio at room temperature. This complex has a high maximum internal sensitivity of $S_{int}(T_{max}) \approx 2.1\%$ °C^{-1}, but over only a small temperature window, illustrating the inverse relationship between these two parameters.

The equilibrium between the closed and open states of the MB (Figure 7.5a) is sensitive to environmental parameters such as pH and the ionic strength of the solution in addition to temperature. At 296 K in 0.1 M NaCl Hepes pH 7.5, the DNA linker opens and closes with rate constants of $3.8 \pm 0.8 \times 10^4$ and $9 \pm 1 \times 10^3$ s^{-1}, respectively, which limit the temperature sensing timescale. Nevertheless, this approach is very flexible. The fluorescent dyes used as the energy transfer Donor and Acceptor in this type of construct may be varied based on the desired excitation and emission wavelengths, for example, and the oligonucleotide may also be varied to provide temperature sensitivity in different biologically relevant ranges. This strategy may

therefore be attractive for a variety of optical thermometry applications, although degredation of the MBs caused by nucleases may limit *in vivo* applications.[47]

7.3.3. Dual Emission from Two Excited States in Thermal Equilibrium

On the extreme end of the dual-emitting scenarios outlined in Figure 7.1 are the strongly coupled systems possessing two luminescent states whose populations can interconvert rapidly relative to the timescales of luminescence from either state (Figure 7.1c). If the energy gap between the emissive states is small enough to be bridged by the available thermal free energy, the luminescence intensity from each state is determined by its radiative rate constant and Boltzmann population, as described in section 2.2.

For optical thermometry, dual emitters operating by this mechanism have the attractive feature of being highly selective for temperature: Environmental factors may reduce the overall quantum yield by increasing nonradiative decay from either excited state, but fast population renormalization ensures that the same Boltzmann-derived PL intensity distribution is retained, *i.e.*, the temperature-sensitive parameter in eq 5 is independent of $k_{nr,1}$ and $k_{nr,2}$. Two illustrative examples are described below.

7.3.3(a) Lanthanides. Many of the physical properties of lanthanide ions derive from their strongly shielded valence-shell *f* electrons, which interact only weakly with their environment. A characteristic manifestation of such shielding is the existence of multiple *f-f* excited states showing negligible electron-nuclear coupling strengths, small crystal-field splittings, and small nonradiative decay rates. Lanthanides thus frequently show luminescence from multiple excited states that could be used for ratiometric temperature sensing.[48] Lanthanide-doped NCs provide an attractive crystalline form of these materials with excellent luminescence and processability properties.[16, 49]

Another attractive aspect of lanthanide-doped NCs for optical sensing is that in some cases, their luminescence can be generated by sensitized sequential multi-photon upconversion excitation by multiple pathways,[49-50]allowing NIR excitation that is ideal for biological applications due to reduced tissue absorption, background autofluorescence, and photodamage.[51] For example, the $^4S_{3/2}$ and $^2H_{11/2}$ excited-states of Er^{3+}/Yb^{3+} co-doped $NaYF_4$ NCs can be populated by sequential photoexcitation of Yb^{3+} (the Sensitizer), each followed by energy transfer to Er^{3+} (the Activator), to reach the $^4F_{7/2}$ excited state of Er^{3+}.[49, 52] Regardless of whether

excitation of the $^4F_{7/2}$ excited state is direct or via upconversion, it is followed by population thermalization. After thermalization, Er^{3+} ions in crystals frequently emit from both the $^2H_{11/2}$ and $^4S_{3/2}$ states, which are in thermal equilibrium with one another (Figure 7.6a).[50] Figure 7.6b shows PL spectra of Er^{3+}:Yb^{3+}:$NaYF_4$ NCs collected at two temperatures. At the higher temperature, the $^2H_{11/2}$ population is increased, resulting in increased 525 nm PL relative to 545 nm $^4S_{3/2}$ PL (Figure 7.6b). Figure 7.6c plots the PL data from these NCs measured at various temperatures as $\ln(I_{525}/I_{545})$ vs $1/T$, yielding a nearly linear response. Using this calibration curve, Yb^{3+}/Er^{3+} co-doped $NaYF_4$ NCs were used to image temperatures within cells under an applied voltage that induced apoptosis. Following section 2.3, the internal sensitivity of this system is estimated from the data to be $S_{int}(T_{max}) \approx 0.21\%\ °C^{-1}$.

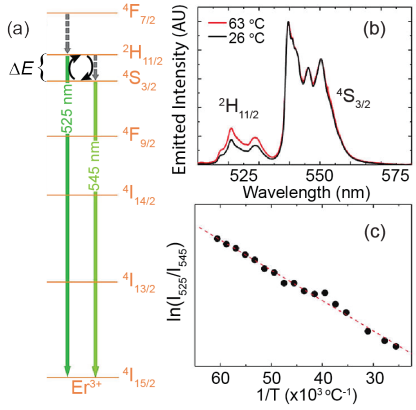

Figure 7.6. Er^{3+}:Yb^{3+}:$NaYF_4$ NC temperature sensor. (a) Schematic energy-level diagram illustrating luminescence transitions originating from the $^2H_{11/2}$ and $^4S_{3/2}$ excited states of Er^{3+}, centered at 525 and 545 nm, respectively. The populations of these two excited states are in thermal equilibrium. (b) PL spectra collected at 63 and 26 °C. More $^2H_{11/2}$ PL is observed at higher temperature. (c) $\ln(I_{525}/I_{545})$ vs $1/T$. These data correspond to $S_{int}(T_{max}) \approx 0.21\%\ °C^{-1}$. Adapted from ref. 52.

Many lanthanide ions show luminescence from multiple excited states and are therefore candidates for temperature sensing.[19] Because *f-f* transitions are parity forbidden to first order, however, widespread use of lanthanides as temperature sensors may be hindered by their low molar extinction coefficients (usually ~10 $M^{-1}cm^{-1}$), which lead to poor brightness and hence small $S_{ext}(T)$. For example, typical maximum molar extinction coefficients for the Er^{3+} $^4I_{15/2} \rightarrow {}^4S_{3/2}$ and $^4I_{15/2} \rightarrow {}^2H_{11/2}$ transitions are $\varepsilon_{max} \sim 2$ and ~7 $M^{-1}cm^{-1}$,[53] respectively, compared with

$\varepsilon_{max} \sim 8 \times 10^5$ $M^{-1}cm^{-1}$ for the visible absorption maximum of Fluorescein,[51] or $\varepsilon_{max} \sim 10^5$-$10^6$ $M^{-1}cm^{-1}$ for the first absorption maxima of CdSe NCs.[54]

7.3.3(b) Dual-Emitting Mn^{2+}-Doped Semiconductor Nanocrystals. Mn^{2+} has long been used as a luminescence activator in wide-gap semiconductors such as ZnS, ZnSe, and CdS.[55-56] Photoexcitation of these semiconductors is followed by picosecond energy localization at Mn^{2+}, which is promoted to its $^4T_1$ excited state and luminesces with a high quantum yield. Efficient sensitization of Mn^{2+} luminescence by wide-gap semiconductors underpins applications of this class of materials as phosphors and as the active materials of electroluminescent displays.[56-57]

Colloidal ZnS, ZnSe, and CdS NCs doped with Mn^{2+} show photophysical properties similar to those of their bulk counterparts.[58] This is not true for CdSe, the next member in the II-VI series of semiconductors. In contrast with Mn^{2+}-doped ZnS, ZnSe, and CdS quantum dots, strongly confined NCs of CdSe doped with Mn^{2+} show qualitatively different photophysical properties from bulk Mn^{2+}:CdSe. In bulk, the energy gap of CdSe (~1.7 eV) is smaller than the energy of the $Mn^{2+}(^4T_1)$ excited state, and only CdSe-based band-to-band luminescence is observed. Quantum confinement broadens the CdSe energy gap beyond the energy of the $Mn^{2+}(^4T_1)$ excited state, and Mn^{2+}-centered PL is recovered that behaves much as in Mn^{2+}-doped ZnS, ZnSe, and CdS.[59]

In addition, a new photophysical effect is observed when quantum confinement is used to bring the first excitonic excited state close in energy to the $Mn^{2+}(^4T_1)$ excited state.[25] As illustrated in Figure 7.7a, proximity of these two excited states results in thermally assisted repopulation of the emissive excitonic excited state from the emissive $Mn^{2+}(^4T_1)$ excited state, and consequently dual emission is observed. Figure 7.7b shows the first observation of this effect,[25] where gated PL spectra of 2.2 nm Mn^{2+}:CdSe NCs (Figure 7.7ci) were collected at various temperatures. Excitonic luminescence becomes increasingly apparent as the sample is warmed from -248 to -88 °C.

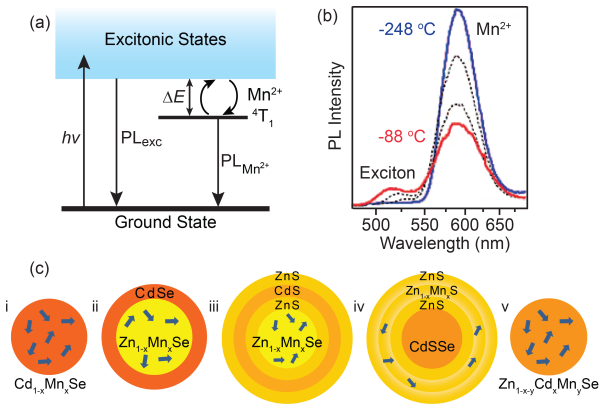

Figure 7.7. Mn^{2+}/exciton thermal equilibrium. (a) Energy diagram summarizing dual emission in Mn^{2+}-doped semiconductors. Semiconductor photoexcitation is followed by picosecond energy localization at Mn^{2+} to populate its luminescent $^4T_1$ excited state. At elevated temperature, the excitonic states may be thermally repopulated and excitonic luminescence recovered. Population interconversion is fast relative to either luminescence process. (b) Gated PL spectra of $d \approx 2.2$ nm Mn^{2+}-doped CdSe NCs at -248, -173, -130, and -88 °C. Adapted from ref. 25. (c) Dual-emitting Mn^{2+}-doped NCs have now been prepared with several related structures. From left to right: (i) Mn^{2+}:CdSe, (ii) $Zn_{1-x}Mn_xSe$/CdSe, (iii) $Zn_{1-x}Mn_xSe$/ZnS/CdS/ZnS, (iv) CdSSe/ZnS/$Zn_{1-x}Mn_xS$/ZnS, and (v) $Zn_{1-x-y}Cd_xMn_ySe$.

Several challenges inhibited implementation of the Mn^{2+}:CdSe (Figure 7.7ci) dual emitters as temperature sensors. Most significantly, the small NC size needed to recover Mn^{2+} emission ($d < \sim 3$ nm for room temperature[59]) made uniform doping difficult, and many of the NCs contained no Mn^{2+}. Time-gated luminescence spectroscopy was necessary to observe the exciton storage effect over the background luminescence from these undoped NCs.[25] Since this original observation of exciton storage by Mn^{2+}, the effect has been cultivated through development of new Mn^{2+}-doped semiconductor nanostructures such that it is now the dominant photophysical property at room temperature.[60] Separating the tasks of NC doping and energy-gap tuning overcame many of these challenges: Large, uniformly doped $Zn_{1-x}Mn_xSe$ NCs were prepared, and CdSe shells were used to reduce their band gap energies into the range where dual emission is observed.[60] The resulting $Zn_{1-x}Mn_xSe$/CdSe NCs are illustrated schematically in Figure 7.7cii. By varying only the temperature, the luminescence from these NCs can be converted from entirely Mn^{2+} emission at low temperature to entirely excitonic emission at high temperature, demonstrating pronounced intrinsic dual emission around room temperature in semiconductors for the first time.

The magnitude of luminescence intensity transfer provides a qualitative distinction between this dual emission mechanism and that of the Er^{3+} $^2H_{11/2}/^4S_{3/2}$ lanthanides described above. The similar radiative rate constants for the two emissive Er^{3+} states result in approximately equal emission intensities in the high limit. The two luminescent excited states of these dual-emitting NCs have a ~10^4 difference in their radiative rate constants, such that small excitonic populations derived from the tail of the Boltzmann distribution give rise to substantial excitonic luminescence. Specifically, a thermal exciton population of only one part in ~10^4 results in equal exciton and $Mn^{2+}(^4T_1)$ luminescence intensities. Because of the ca. millisecond Mn^{2+} lifetime and ca. picosecond exciton $\leftrightarrow$ $Mn^{2+}(^4T_1)$ population exchange times, the photoexcited NCs cycle between these two excited states many times prior to luminescence from either. A distinctive feature of this unusual electronic structure is thus a lengthening of the excitonic PL decay time by several orders of magnitude beyond its radiative lifetime: The exciton's energy is "stored" in the $Mn^{2+}(^4T_1)$ excited state.[25] Sufficient probability of thermal repopulation allows for excitonic luminescence. Another hallmark of this electronic structure is an acute sensitivity of the luminescence spectrum to temperature.

Although suitable for optical thermometry in inert atmosphere at ambient temperatures, $Zn_{1-x}Mn_xSe$/CdSe NCs are not sufficiently stable for applications in aqueous solution or at elevated temperatures. This instability is associated with the extreme sensitivity of the dual emission to the energy gap, which depends on very small amounts of Cd^{2+} ions on the $Zn_{1-x}Mn_xSe$ surfaces. Therefore, small changes in surface chemistry change ΔE and cause significant changes in the dual emission spectrum. Improved robustness was achieved by growing the core/multi-shell structures illustrated schematically in Figure 7.7ciii.[61] Here, $Zn_{1-x}Mn_xSe$ core NCs were coated with ZnS buffer layers, CdS band-gap tuning layers, and ZnS shell layers. The resulting NCs have increased quantum yields and improved stability. Moreover, this structure facilitates synthetic precision by reducing the sensitivity of ΔE to Cd^{2+} ions. Extremely robust NCs of this type were prepared with PL quantum yields up to 40% at room temperature, and with excellent stability up to 270 °C under inert atmosphere. Figure 7.8a shows PL spectra of these core/multi-shell NCs measured from -140 to 90 °C, corrected for instrument response and normalized to the total integrated PL intensity at each temperature. At low temperatures, the NCs show only the orange Mn^{2+} luminescence centered at ~590 nm. As the temperature increases, green excitonic emission centered at ~525 nm grows in, reflecting thermal exciton

repopulation. As with $Zn_{1-x}Mn_xSe/ZnCdSe$ NCs, luminescence intensity can be converted almost quantitatively from Mn^{2+} at low temperature to excitonic at high temperature.

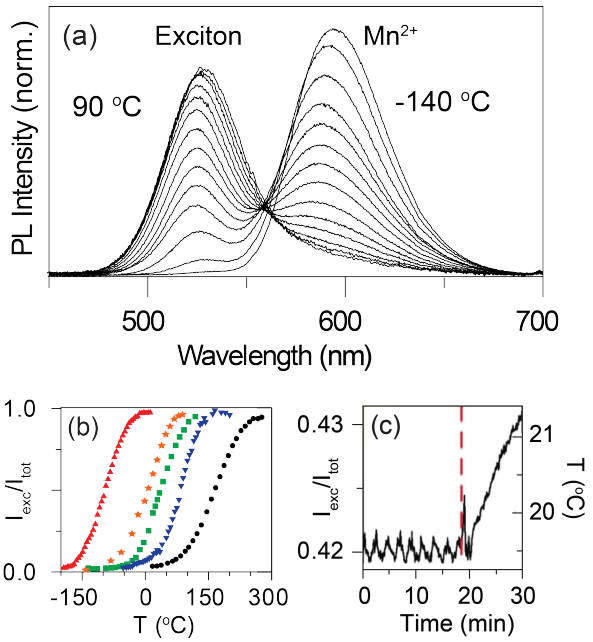

Figure 7.8. Dual-emitting Mn^{2+}-doped semiconductor NCs. (a) Variable-temperature PL spectra of colloidal $Zn_{1-x}Mn_xSe/ZnS/CdS/ZnS$ NCs, normalized by total integrated intensity. Adapted from ref. 61. (b) Thermometric response curves (I_{exc}/I_{tot} vs temperature) for various samples covering >400°C, corresponding to: $Zn_{1-x}Mn_xSe/CdSe$ (▲, ▼), $Zn_{1-x}Mn_xSe/ZnS/CdS/ZnS$ (★, ●), and $Zn_{1-x-y}Cd_xMn_ySe$ (■) NCs. The NCs with the largest ΔE are sensitive at highest temperatures. Adapted from refs. 60, 61, and 64. (c) I_{exc}/I_{tot} vs time in a temperature-controlled cuvette, showing oscillations of ±0.2 °C. The chiller was turned off at ~20 min (dashed line). Adapted from ref. 60.

Plotting the fractional excitonic PL intensity (I_{exc}/I_{tot}) from the spectra in Figure 7.8 vs temperature yields a thermometric calibration plot that transitions from 0 to 1 going from the low-temperature limit to the high-temperature limit. The slope of this plot gives $S_{int}(T)$ at each temperature. Figure 7.8b plots I_{exc}/I_{tot} vs temperature for five different dual-emitting NCs, prepared to have five different values of ΔE (Figure 7.7). These data illustrate: (1) for a given NC sample, the active temperature window is broad, spanning ~100 °C, and (ii) the active temperature window can be tuned across hundreds of degrees centigrade by tuning ΔE using simple synthetic modifications. The nearly parallel curves demonstrate that $S_{int}(T_{max})$ values are approximately equal for all of these samples with an average $S_{int}(T_{max})$ of ~1% $°C^{-1}$ and

individual values ranging from 0.74 to 1.42% $°C^{-1}$. The small variations in response curvature are predominantly caused by distributions in ΔE within the ensemble of NCs of any given sample, and by the existence of small amounts of trap PL.

Because of their large spectral changes with temperature and high brightness, these Mn^{2+}-based optical temperature sensors have sizeable external sensitivities (S_{ext}) that translate to an ability to measure small temperature changes with high precision. To illustrate, Figure 7.8c shows a time trace of the temperature of a colloidal NC suspension cooled by a recirculating chiller. Temperature was measured ratiometrically using lamp excitation and a simple fiber-coupled hand-held detector. Here, ±0.2 °C oscillations around the chiller setpoint are detected in real time with a signal-to-noise ratio of ~10:1, demonstrating the high laboratory sensitivities achievable with these dual-emitting NCs.

The successful synthesis of other Mn^{2+}-doped semiconductor NCs showing similar dual emission confirms the generality of the mechanism described in Figure 7.7a. Using similar synthetic techniques, a recent report showed thermally activated dual emission from core/multi-shell NCs in which Mn^{2+} was doped into thick ZnS shells grown around CdSSe cores (Figure 7.7civ).[62] Even though energy transfer to Mn^{2+} is slower when Mn^{2+} is located in large-bandgap shells,[63] it remains sufficiently fast to allow excited-state thermal equilibrium.

Most recently, dual-emitting NCs were prepared using NC alloying, rather than core/shell growth, to achieve Mn^{2+} doping and ΔE tuning.[64] Alloyed $Zn_{1-x-y}Cd_xMn_ySe$ NCs were synthesized by a one-step lyothermal degradation reaction. These NCs contain fewer Cd^{2+} ions per particle than any other dual-emitting NCs in this class. Moreover, the use of homogenous alloy composition to tune ΔE largely decouples the electronic structures of these NCs from their physical structures, offering more structural flexibility and simultaneously making the temperature sensing more robust against physical degradation. The demonstration of dual emission in $Zn_{0.64}Cd_{0.35}Mn_{0.01}Se$ nanorods shown in Figure 7.9 illustrates effective decoupling of NC physical structure from ΔE. Nanorods are generally brighter than their smaller NC counterparts because of increased molar extinction coefficients,[41] making dual-emitting nanorods attractive for some applications.

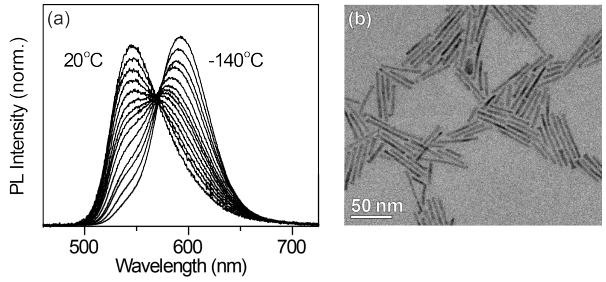

Figure 7.9. Dual-emitting Mn^{2+}-doped nanorods. (a) Variable-temperature PL spectra of colloidal $Zn_{0.64}Cd_{0.35}Mn_{0.01}Se$ nanorods, normalized by the total integrated PL intensity. (b) Transmission electron microscopy image of ~41 nm rods with $d \sim 4$ nm. Adapted from ref. 64.

As mentioned above, a hallmark of the exciton storage phenomenon is that the excitonic PL decays with a timescale determined by the Mn^{2+} population decay, which can be several orders of magnitude longer than the intrinsic radiative lifetime of the exciton. When I_{exc}/I_{tot} increases, the exciton and Mn^{2+} PL decay times both shorten and approach that of the exciton in the high-temperature limit. Figure 7.10 illustrates this strong temperature dependence, showing the time-resolved PL of alloyed dual-emitting NCs at two temperatures. The time-integrated PL is mostly Mn^{2+} (-30 °C) or excitonic (19 °C). Because the excitonic PL decay time at a given temperature is a function of ΔE, the distribution of ΔE present in any ensemble of NCs results in a time-dependent blueshift of the excitonic PL peak maximum (traced in Figure 7.10b). Equivalent results were obtained from core/shell NCs,[60] indicating the decays are characteristic of this dual-emission mechanism.

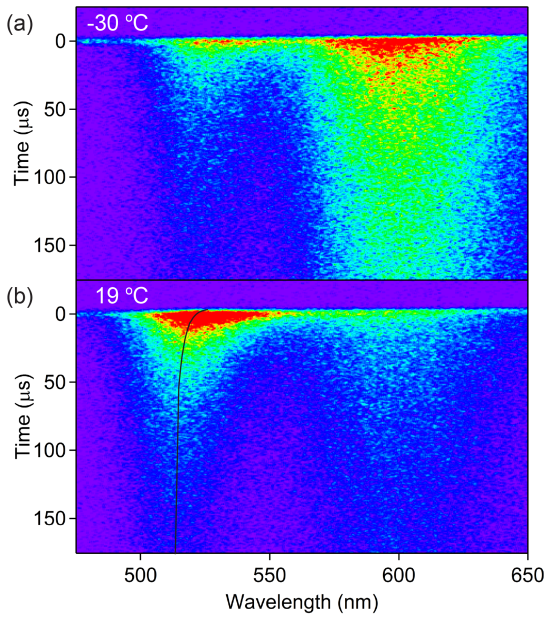

Figure 7.10. Time-resolved dual emission. PL of $Zn_{0.784}Cd_{0.209}Mn_{0.007}Se$ NCs measured at two temperatures, plotted vs time (vertical) and wavelength (horizontal). (a) At -30 °C, the spectrum is dominated by long-lived Mn^{2+} PL (~600 nm) with a decay time of ~435 μs. Excitonic PL is evident at ~525 nm. (b) At 19 °C, the spectrum shows strong excitonic PL (~510 nm) and reduced Mn^{2+} PL, both with decay times of ~70 μs. The black line traces the excitonic PL intensity maximum with time, emphasizing its blushift. Adapted from ref. 64.

Finally, for many applications, water solubility is required. Phase transfer usually decreases NC quantum yields and stabilities,[36] and such issues may be exacerbated in dual-emitting NCs because of their extreme sensitivity to changes in ΔE. Successful phase transfer of core/multi-shell dual-emitting NCs has been achieved using small-molecule ligands such as citrate[61] and *d*-penicillamine.[62] Figure 7.11a shows a photograph of the same dual-emitting $Zn_{1-x}Mn_xSe/ZnS/CdS/ZnS$ NCs in toluene and in water, along with a cartoon illustrating formation of a hydrophilic surface by citrate surface ligation. Although successful, the long-term photo- and thermal instabilities of such small-molecule-ligated NCs in water may pose challenges for many uses. More stable water-soluble dual-emitting NCs can be obtained using an encapsulating amphiphilic polymer that maintains the native surface-passivating ligands of the NC (hydrophobic), but makes the external surface hydrophilic. Figure 7.11b shows a photograph of another dual-emitting $Zn_{1-x}Mn_xSe/ZnS/CdS/ZnS$ NC sample in toluene and in water, along with a cartoon illustrating a possible mechanism by which the polymer *n*-octylamine-modified

poly(acrylic acid) solubilizes the NCs. These polymer-encapsulated dual-emitting NCs are stable in aqueous solution indefinitely, and are therefore well suited for certain aqueous applications.[36, 61]

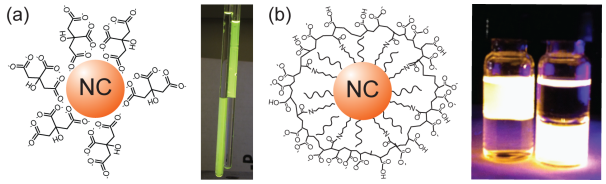

Figure 7.11. Phase transfer of dual-emitting Mn^{2+}-doped semiconductor NCs from toluene to water. (a) Exchange of the organic NC surface ligands with citrate yields aqueous NC suspensions. (b) Encapsulation of the NCs with an amphiphilic polymer (*n*-octylamine-modified poly(acrylic acid)) allows phase transfer and long-term stability. Adapted from ref. 61.

7.4. Summary

The wide variety of applications for which nanoscale temperature sensors are desired necessitates development of a broad portfolio of temperature sensors that excel in many complementary ways. Rather than focusing on specific applications, this review has attempted to clarify the photophysical mechanisms underpinning the dual emission reported for various optical temperature sensors that allow ratiometric detection. Examples from recent literature have been provided to illustrate the various mechanisms. A sensitivity metric has been defined specifically for dual-emitting sensors that enables quantitative comparison among them, and the limitations of such metrics have also been discussed. The recent discovery of a fundamentally new dual-emission phenomenon in Mn^{2+}-doped semiconductor NCs has been highlighted. This discovery has generated a new class of nanothermometers that excel in their tunability, sensitivity, brightness, and specificity for temperature, features that poise them well for many challenging applications in optical nanothermometry. Ongoing experiments with the various dual emitters discussed here will undoubtedly extend into the time domain, where fluorescence lifetime imaging microscopy (FLIM) would offer interesting opportunities, down to the single-fluorophore detection level, and into specific technological and biotechnological application areas.

7.5 References

(1) Gosse, C.; Bergaud, C.; Low, P. Molecular Probes for Thermometry in Microfluidic Devices. In *Thermal Nanosystems and Nanomaterials*, Springer-Verlag Berlin: Berlin, 2009; Vol. 118, pp 301-341.

(2) McCabe, K. M.; Hernandez, M. *Pediatr. Res.* **2010,** *67*, 469-475.

(3) Murphy, K. P.; Freire, E. *Adv. Protein Chem.* **1992,** *43*, 313-361.

(4) Clausen, T.; Vanhardeveld, C.; Everts, M. E. *Physiol. Rev.* **1991,** *71*, 733-774.

(5) Zhang, C. S.; Xing, D. *Nucleic Acids Res.* **2007,** *35*, 4223-4237.

(6) Sapareto, S. A.; Dewey, W. C. *Int. J. Radiat. Oncol. Biol. Phys.* **1984,** *10*, 787-800.

(7) Ashkin, A.; Dziedzic, J. M.; Yamane, T. *Nature* **1987,** *330*, 769-771.

(8) Colvin, J. *Microelectron. Reliab.* **1998,** *38*, 1705-1714.

(9) Shakouri, A. *Proc. IEEE* **2006,** *94*, 1613-1638.

(10) Schrum, K. F.; Williams, A. M.; Haerther, S. A.; Benamotz, D. *Anal. Chem.* **1994,** *66*, 2788-2790.

(11) Lou, J. F.; Hatton, T. A.; Laibinis, P. E. *Anal. Chem.* **1997,** *69*, 1262-1264.

(12) Ross, D.; Gaitan, M.; Locascio, L. E. *Anal. Chem.* **2001,** *73*, 4117-4123.

(13) Uchiyama, S.; de Silva, A. P.; Iwai, K. *J. Chem. Ed.* **2006,** *83*, 720-727.

(14) Lee, J.; Kotov, N. A. *Nano Today* **2007,** *2*, 48-51.

(15) Jorge, P.; Martins, M.; Trindade, T.; Santos, J.; Farahi, F. *Sensors* **2007,** *7*, 3489-3534.

(16) Fischer, L. H.; Harms, G. S.; Wolfbeis, O. S. *Angew. Chem. Int. Ed.* **2011,** *50*, 4546-4551.

(17) Allison, S. W.; Gillies, G. T. *Rev. Sci. Instrum.* **1997,** *68*, 2615-2650.

(18) Löw, P.; Kim, B.; Takama, N.; Bergaud, C. *Small* **2008,** *4*, 908-914.

(19) Brites, C. D. S.; Lima, P. P.; Silva, N. J. O.; Millan, A.; Amaral, V. S.; Palacio, F.; Carlos, L. D. *Nanoscale* **2012,** *4*, 4799-4829.

(20) Jaque, D.; Vetrone, F. *Nanoscale* **2012,** *4*, 4301-4326.

(21) Walker, G.; Sundar, V.; Rudzinski, C.; Wun, A.; Bawendi, M.; Nocera, D. *App. Phys. Lett.* **2003,** *83*, 3555-3557.

(22) Han, B.; Hanson, W. L.; Bensalah, K.; Tuncel, A.; Stern, J. M.; Cadeddu, J. A. *Ann. Biomed. Eng.* **2009,** *37*, 1230-1239.

(23) Stich, M. I. J.; Fischer, L. H.; Wolfbeis, O. S. *Chem. Soc. Rev.* **2010,** *39*, 3102-3114.

(24) Sakakibara, J.; Adrian, R. J. *Exp. Fluids* **1999,** *26*, 7-15.

(25) Beaulac, R.; Archer, P. I.; van Rijssel, J.; Meijerink, A.; Gamelin, D. R. *Nano Lett.* **2008,** *8*, 2949-2953.

(26) Wang, S.; Westcott, S.; Chen, W. *J. Phys. Chem. B* **2002,** *106*, 11203-11209.

(27) Guasto, J.; Breuer, K. *Exp Fluids* **2008,** *45*, 157-166.

(28) Förster, T. *Annal. Phys.* **1948,** *437*, 55-75.

(29) Tian, Z.; Yu, J.; Wu, C.; Szymanski, C.; McNeill, J. *Nanoscale* **2010,** *2*, 1999-2011.

(30) Jin, Y. H.; Ye, F. M.; Zeigler, M.; Wu, C. F.; Chiu, D. T. *ACS Nano* **2011,** *5*, 1468-1475.

(31) Wu, C.; Bull, B.; Christensen, K.; McNeill, J. *Angew. Chem. Int. Ed.* **2009,** *48*, 2741-2745.

(32) Ye, F.; Wu, C.; Jin, Y.; Chan, Y.-H.; Zhang, X.; Chiu, D. T. *J. Am. Chem. Soc.* **2011,** *133*, 8146-8149.

(33) Feller, G. *J. Phys.: Condens. Matter* **2010,** *22*, 323101.

(34) Medintz, I. L.; Mattoussi, H. *Phys. Chem. Chem. Phys.* **2009,** *11*, 17-45.

(35) Michalet, X.; Pinaud, F. F.; Bentolila, L. A.; Tsay, J. M.; Doose, S.; Li, J. J.; Sundaresan, G.; Wu, A. M.; Gambhir, S. S.; Weiss, S. *Science* **2005,** *307*, 538-544.

(36) Medintz, I. L.; Uyeda, H. T.; Goldman, E. R.; Mattoussi, H. *Nat. Mater.* **2005,** *4*, 435-446.

(37) Willard, D. M.; Carillo, L. L.; Jung, J.; Van Orden, A. *Nano Lett.* **2001,** *1*, 469-474.
(38) Somers, R. C.; Bawendi, M. G.; Nocera, D. G. *Chem. Soc. Rev.* **2007,** *36*, 579-591.
(39) Murray, C. B.; Norris, D. J.; Bawendi, M. G. *J. Am. Chem. Soc.* **1993,** *115*, 8706-8715.
(40) Smith, A. M.; Nie, S. M. *Accounts Chem. Res.* **2010,** *43*, 190-200.
(41) Talapin, D. V.; Koeppe, R.; Götzinger, S.; Kornowski, A.; Lupton, J. M.; Rogach, A. L.; Benson, O.; Feldmann, J.; Weller, H. *Nano Lett.* **2003,** *3*, 1677-1681.
(42) Carbone, L.; Nobile, C.; De Giorgi, M.; Sala, F. D.; Morello, G.; Pompa, P.; Hytch, M.; Snoeck, E.; Fiore, A.; Franchini, I. R.; Nadasan, M.; Silvestre, A. F.; Chiodo, L.; Kudera, S.; Cingolani, R.; Krahne, R.; Manna, L. *Nano Lett.* **2007,** *7*, 2942-2950.
(43) Albers, A. E.; Chan, E. M.; McBride, P. M.; Ajo-Franklin, C. M.; Cohen, B. E.; Helms, B. A. *J. Am. Chem. Soc.* 2012, *134*, 9565-9568.
(44) Delehanty, J. B.; Bradburne, C. E.; Boeneman, K.; Susumu, K.; Farrell, D.; Mei, B. C.; Blanco-Canosa, J. B.; Dawson, G.; Dawson, P. E.; Mattoussi, H.; Medintz, I. L. *Integr. Biol.* 2010, *2*, 265-277.
(45) Bayles, A. R.; Chahal, H. S.; Chahal, D. S.; Goldbeck, C. P.; Cohen, B. E.; Helms, B. A. *Nano Lett.* 2010, *10*, 4086-4092.
(46) Barilero, T.; Le Saux, T.; Gosse, C.; Jullien, L. *Anal. Chem.* 2009, *81*, 7988-8000.
(47) Li, J. J.; Geyer, R.; Tan, W. *Nucl. Acids Res.* 2000, *28*, e52.
(48) Wade, S. A.; Collins, S. F.; Baxter, G. W. *J. Appl. Phys.* 2003, *94*, 4743-4756.
(49) Heer, S.; Kömpe, K.; Güdel, H. U.; Haase, M. *Adv. Mater.* 2004, *16*, 2102-2105.
(50) Chan, E. M.; Gargas, D. J.; Schuck, P. J.; Milliron, D. J. *J. Phys. Chem. B* 2012, *116*, 10561-10570.
(51) Lakowicz, J. R. *Principles of Fluorescence Spectroscopy*. 3rd ed.; Springer: New York, 2006.
(52) Vetrone, F.; Naccache, R.; Zamarrón, A.; Juarranz de la Fuente, A.; Sanz-Rodríguez, F.; Martinez Maestro, L.; Martín Rodriguez, E.; Jaque, D.; García Solé, J.; Capobianco, J. A. *ACS Nano* 2010, *4*, 3254-3258.
(53) Hoogschagen, J.; Gorter, C. J. *Physica* 1948, *14*, 197-206.
(54) Yu, W. W.; Qu, L.; Guo, W.; Peng, X. *Chem. Mater.* 2003, *15*, 2854-2860.
(55) Yen, W. M. *Fundamentals of Phosphors*. CRC Press: Boca Raton, 2006.
(56) Ronda, C. *Luminescence: From Theory to Applications*. Wiley-VCH: Weinheim, Germany, 2008.
(57) Vlasenko, N. A.; Popkov, Y. A. *Opt. Spektrosk.* 1960, *8*, 81-88.
(58) Beaulac, R.; Ochsenbein, S. T.; Gamelin, D. R. Colloidal Transition-Metal-Doped Quantum Dots. In *Nanocrystal Quantum Dots, Second Edition*, Klimov, V. I., Ed. CRC Press: Boca Raton, 2010; pp 397-453.
(59) Beaulac, R.; Archer, P. I.; Liu, X. Y.; Lee, S.; Salley, G. M.; Dobrowolska, M.; Furdyna, J. K.; Gamelin, D. R. *Nano Lett.* 2008, *8*, 1197-1201.
(60) Vlaskin, V. A.; Janssen, N.; van Rijssel, J.; Beaulac, R.; Gamelin, D. R. *Nano Lett.* 2010, *10*, 3670-3674.
(61) McLaurin, E. J.; Vlaskin, V. A.; Gamelin, D. R. *J. Am. Chem. Soc.* 2011, *133*, 14978-14980.
(62) Hsia, C.-H.; Wuttig, A.; Yang, H. *ACS Nano* 2011, *5*, 9511-9522.
(63) Chen, H.-Y.; Maiti, S.; Son, D. H. *ACS Nano* 2011, *6*, 583-591.
(64) McLaurin, E. J.; Fataftah, M. S.; Gamelin, D. R. *Chem. Commun.* 2013, *49*, 39-41.

Appendix A. Supplementary Information for Chapter 2.

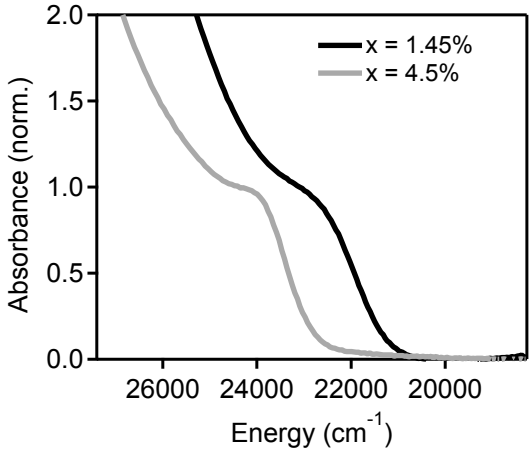

Figure A1. Room-temperature electronic absorption spectra of the two $Zn_{1-x}Mn_xSe$/ZnS/CdS/ZnS quantum dot samples used in this study.

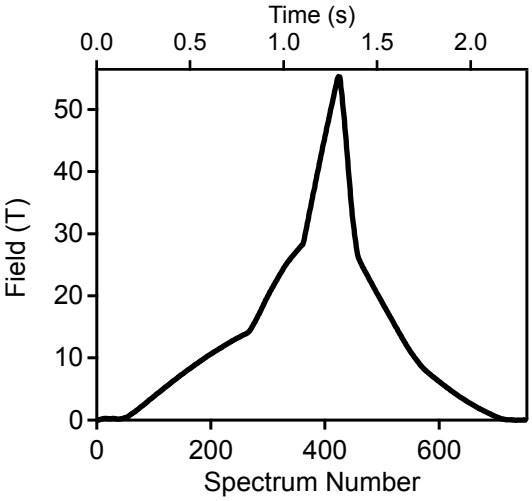

Figure A2. Typical field profile of the magnet pulse. Complete PL spectra were continuously acquired every 3.1 ms throughout the 2.3 second duration of the pulse.

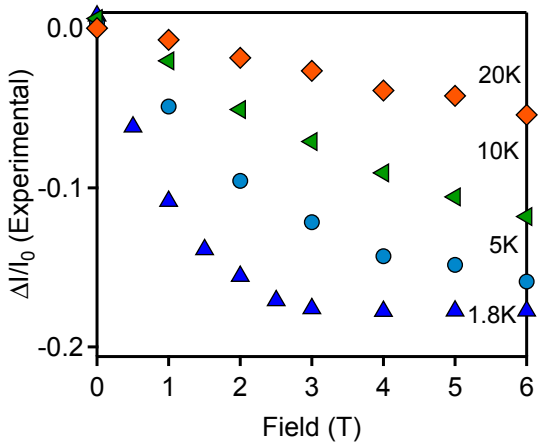

Figure A3. MCPL polarization ratios (symbols, left axis) for colloidal $Zn_{0.955}Mn_{0.045}Se/ZnS/CdS/ZnS$ quantum dots, measured as a function of magnetic field and temperature.

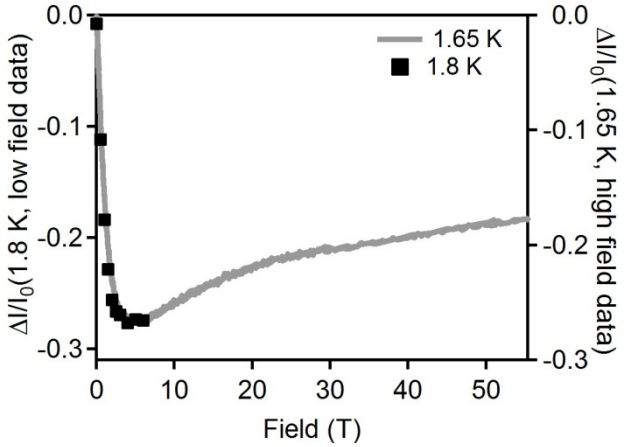

Figure A4. MCPL polarization ratios measured for the same colloidal $Zn_{1-x}Mn_xSe/ZnS/CdS/ZnS$ quantum dots (left axis, symbols) at 1.8 K in fields up to 6 T and (right axis, lines) at 1.65 K in fields up to 55 T. Small differences in absolute polarization ratio are observed that are attributable to depolarization effects. Independent measurements of depolarization in the former experiment indicated <10% depolarization. ($Zn_{0.9855}Mn_{0.0145}Se/ZnS/CdS/ZnS$ QDs, avg. 4.5 Mn^{2+}/QD, d = 6 nm, E_g = 2.8 eV)

Detailed description of model calculations.

Matrices to describe the spin and spin orbit portions of the Hamiltonian in equation A1,

$$H = D\left(S^2 - \frac{S(S+1)}{3}\right) + g \cdot \mu_B \cdot B\left(S_x \sin(\theta)\cos(\phi) + S_y \sin(\theta)\sin(\phi) + S_z \cos(\theta)\right) \qquad [A1]$$

are generated for the $^4A_2$ spin basis set:

$$S=\begin{pmatrix} -\frac{3}{2} \\ -\frac{1}{2} \\ \frac{1}{2} \\ \frac{3}{2} \end{pmatrix}$$

where S_x, S_y, and S_z are the spin matrices, given below for $S = 3/2$:

$$S_x = \begin{pmatrix} 0 & \frac{\sqrt{3}}{2} & 0 & 0 \\ \frac{\sqrt{3}}{2} & 0 & 1 & 0 \\ 0 & 1 & 0 & \frac{\sqrt{3}}{2} \\ 0 & 0 & \frac{\sqrt{3}}{2} & 0 \end{pmatrix}, S_y = \begin{pmatrix} 0 & \frac{i\sqrt{3}}{2} & 0 & 0 \\ -\frac{i\sqrt{3}}{2} & 0 & i & 0 \\ 0 & -i & 0 & \frac{i\sqrt{3}}{2} \\ 0 & 0 & -\frac{i\sqrt{3}}{2} & 0 \end{pmatrix}, S_z = \begin{pmatrix} -\frac{3}{2} & 0 & 0 & 0 \\ 0 & -\frac{1}{2} & 0 & 0 \\ 0 & 0 & \frac{1}{2} & 0 \\ 0 & 0 & 0 & \frac{3}{2} \end{pmatrix} \quad \text{[A2]}$$

Eigenvalues and eigenvectors, Ψ, of this Hamiltonian are then generated as a function of B, θ and ϕ. In order to account for rotations of the observation frame and the basis set, the $j = 3/2$ Wigner D matrix in equation A3 was applied to the resulting eigenvectors ($\Psi' = W_D \Psi$).

$$W_D = \begin{pmatrix} e^{-\frac{3i\gamma}{2}-\frac{3i\phi}{2}}\mathrm{Cos}\left[\frac{\theta}{2}\right]^3 & -\sqrt{3}e^{-\frac{3i\gamma}{2}-\frac{i\phi}{2}}\mathrm{Cos}\left[\frac{\theta}{2}\right]^2\mathrm{Sin}\left[\frac{\theta}{2}\right] & \sqrt{3}e^{-\frac{3i\gamma}{2}+\frac{i\phi}{2}}\mathrm{Cos}\left[\frac{\theta}{2}\right]\mathrm{Sin}\left[\frac{\theta}{2}\right]^2 & -e^{-\frac{3i\gamma}{2}+\frac{3i\phi}{2}}\mathrm{Sin}\left[\frac{\theta}{2}\right]^3 \\ \sqrt{3}e^{-\frac{i\gamma}{2}-\frac{3i\phi}{2}}\mathrm{Cos}\left[\frac{\theta}{2}\right]^2\mathrm{Sin}\left[\frac{\theta}{2}\right] & \frac{1}{2}e^{-\frac{i\gamma}{2}-\frac{i\phi}{2}}\mathrm{Cos}\left[\frac{\theta}{2}\right](-1+3\mathrm{Cos}[\theta]) & -\frac{1}{2}e^{-\frac{i\gamma}{2}+\frac{i\phi}{2}}(1+3\mathrm{Cos}[\theta])\mathrm{Sin}\left[\frac{\theta}{2}\right] & \sqrt{3}e^{-\frac{i\gamma}{2}+\frac{3i\phi}{2}}\mathrm{Cos}\left[\frac{\theta}{2}\right]\mathrm{Sin}\left[\frac{\theta}{2}\right]^2 \\ \sqrt{3}e^{\frac{i\gamma}{2}-\frac{3i\phi}{2}}\mathrm{Cos}\left[\frac{\theta}{2}\right]\mathrm{Sin}\left[\frac{\theta}{2}\right]^2 & \frac{1}{2}e^{\frac{i\gamma}{2}-\frac{i\phi}{2}}(1+3\mathrm{Cos}[\theta])\mathrm{Sin}\left[\frac{\theta}{2}\right] & \frac{1}{2}e^{\frac{i\gamma}{2}+\frac{i\phi}{2}}\mathrm{Cos}\left[\frac{\theta}{2}\right](-1+3\mathrm{Cos}[\theta]) & -\sqrt{3}e^{\frac{i\gamma}{2}+\frac{3i\phi}{2}}\mathrm{Cos}\left[\frac{\theta}{2}\right]^2\mathrm{Sin}\left[\frac{\theta}{2}\right] \\ e^{\frac{3i\gamma}{2}-\frac{3i\phi}{2}}\mathrm{Sin}\left[\frac{\theta}{2}\right]^3 & \sqrt{3}e^{\frac{3i\gamma}{2}-\frac{i\phi}{2}}\mathrm{Cos}\left[\frac{\theta}{2}\right]\mathrm{Sin}\left[\frac{\theta}{2}\right]^2 & \sqrt{3}e^{\frac{3i\gamma}{2}+\frac{i\phi}{2}}\mathrm{Cos}\left[\frac{\theta}{2}\right]^2\mathrm{Sin}\left[\frac{\theta}{2}\right] & e^{\frac{3i\gamma}{2}+\frac{3i\phi}{2}}\mathrm{Cos}\left[\frac{\theta}{2}\right]^3 \end{pmatrix}$$

[A3]

where γ is the Euler angle describing rotation around the z axis of the rotated reference frame. The probabilities, P, for emission of left and right circularly polarized light were then calculated using matrices, p, from Table 2.1:

$$p_- = \begin{pmatrix} \sqrt{\frac{1}{3}} \\ \sqrt{\frac{1}{5}} \\ \sqrt{\frac{1}{10}} \\ \sqrt{\frac{1}{30}} \end{pmatrix}, p_+ = \begin{pmatrix} \sqrt{\frac{1}{30}} \\ \sqrt{\frac{1}{10}} \\ \sqrt{\frac{1}{5}} \\ \sqrt{\frac{1}{3}} \end{pmatrix} \quad \text{[A4a]}$$

$$P_\pm = \Psi'^* \cdot \Psi' \cdot p_\pm^2 \quad \text{[A4b]}$$

For a given temperature, the Boltzmann population of each state was calculated based on the eigenvalues, and emission probability from each eigenstate weighted accordingly. To account for

the random NC orientation, $P_{\pm}$ was calculated and averaged over the unit sphere for values of θ, ϕ, and γ in steps of $\pi/20$, $\pi/10$, and $\pi/10$, respectively, for a total of 8000 points.

To calculate the average energy for right and left circularly polarized emission, an identical treatment to find eigenvalues and eigenvectors was applied to the ground state, using $D_{GS} = 0.0001$ cm^{-1}, and S ranging from -5/2 to 5/2, and the $j = 5/2$ Wigner D-matrix. The energy differences between the $^4A_2$ eigenstates and each of the $^6A_1$ eigenstates were multiplied by the Boltzmann population of the $^4A_2$ state, and the relative transition probability for that transition, and then averaged for each polarization. These emission energies were again orientation-averaged over 8000 points on the unit sphere for each magnetic field.

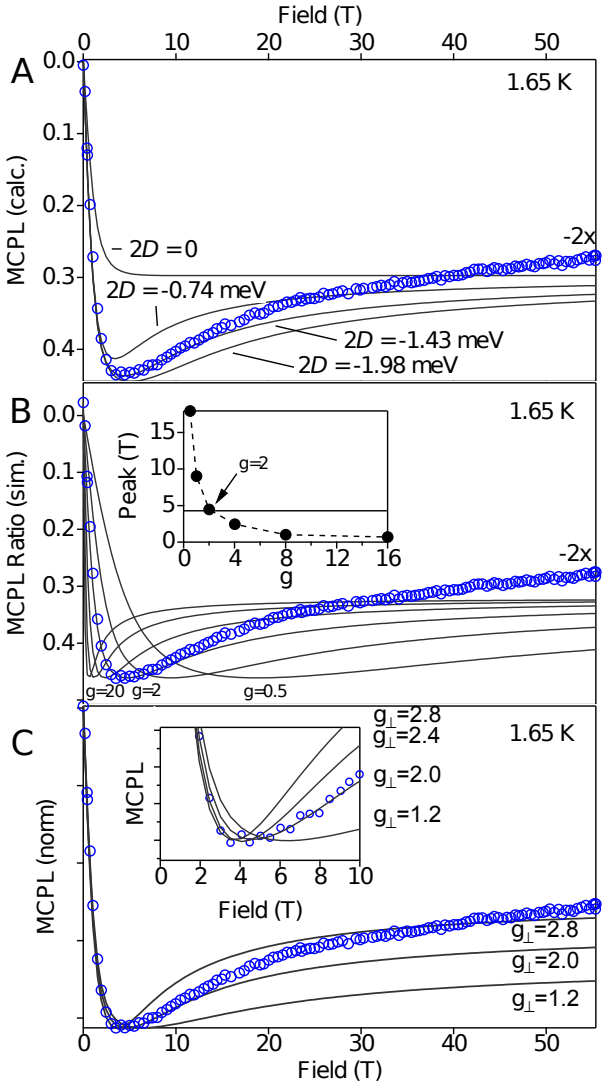

Figure A5. Calculated 1.65 K MCPL ratios (solid lines) for different values of **(A)** D and **(B)** isotropic g from equation 1, overlaid with the experimental data from $Zn_{0.9855}Mn_{0.0145}Se/ZnS/CdS/ZnS$ QDs, avg. 4.5 Mn^{2+}/QD, d = 6 nm, E_g = 2.8 eV (scaled -2x, circles). The inset to (B) plots the field at which $\Delta I/I$ is maximized vs g value, and the horizontal line indicates the experimental result. **(C)** Calculated 1.65 K MCPL ratios (solid lines) overlaid with experimental data (circles), for different values of $g_\perp = g_x = g_y$, with $g_{||} = g_z = 2.0$, calculated by distributing g across the second term of equation S1. All curves in (C) were scaled to their maximum polarization to emphasize differences in curvature. The inset is a magnified view of the low-field region.

Appendix B. Supplementary Information for Chapter 3.

Nanocrystal synthesis and characterization. $Zn_{1-x}Mn_xSe$ nanocrystals were synthesized by lyothermal degradation of the tetramer $[Zn_4(SePh)_{10}](Me_4N)_2$ in the presence of $MnCl_2$ and Se similar to previously published methods.[1] Unless otherwise specified, all chemicals were used as purchased from Aldrich. In a typical synthesis, 5.4 g of hexadecylamine (HDA) and 0 to 15 mg $MnCl_2$ were refluxed under vacuum at 130 °C for one hour. This amount of amine is half of that reported previously,[1] and was used because it was found to more reproducibly give spherical particles. After one hour, the temperature was lowered to 100 °C and 200 mg of $[Zn_4(SePh)_{10}](Me_4N)_2$ and 10 mg of Se were added anaerobically. The resulting solution was again refluxed under vacuum at 130 °C for one hour to remove volatile components. After degassing, the temperature was ramped to 275 °C over 5 min and held for 20 min, after which the heating mantle was removed to quench the reaction. Once the solution had cooled to below 80 °C, flocculation was induced with a 9:1 EtOH:MeOH mixture and the particles were separated by centrifugation. The NCs were subsequently purified by re-suspension in toluene and flocculation with EtOH.

Following previously reported procedures,[2,3] ZnS shells were grown on the above cores by successive additions of zinc oleate and trioctylphosphine sulfide (TOPS). Zinc oleate was prepared by reacting $Zn(OAc)_2$ (660 mg, 3 mmol) with excess oleic acid (5.7 g, 20 mmol) in 19.6 g of octadecene under vacuum at 100 °C. Because the zinc oleate is only soluble above 80 °C, a syringe heater was used to prevent precipitation during growth. TOPS was prepared by sonicating 32 mg sulfur in 4.3 g neat trioctyl phosphine (Strem) until it dissolved. To grow the shells, the toluene suspension of core NCs was added to a flask containing 1.5 g of oleylamine and 1.5 g of octadecene. The resulting mixture was heated to 130 °C under vacuum for one hour to remove the toluene and dry/degas the solvent. The temperature was then ramped to 225 °C, where 500 μL of the zinc oleate solution was added over 5 min. After 30 min, 250 μL of the TOPS solution was added over 5 min and the solution allowed to react for 30 min more. After three more identical additions of each precursor, the temperature was lowered to 130 °C and the NCs were allowed to anneal overnight. The resulting NCs were purified by suspension in toluene

and flocculation with ethanol. All $Zn_{1-x}Mn_xSe$ core NCs had diameters of d = 2.9 - 3.1 nm, and the $Zn_{1-x}Mn_xSe$/ZnS core/shell NCs had d = 3.7 - 4.0 nm. Final Mn^{2+} concentrations within the NC cores were determined by ICP-AES of the core/shell NCs scaled by the relative volume of the core and shell, as determined from XRD linewidths of the core and core/shell samples.[4] NCs were further characterized by EPR spectroscopy, which did not show any evidence of surface Mn^{2+}.[5] All of the core/shell nanocrystals made following these procedures showed similar absorption and PL spectra to those reported here, and all had room-temperature PL quantum yields of ~40%.

Details of computational methods. Density functional theory (DFT) calculations were performed with the development version of the Gaussian program.[6] Full geometry optimizations of the doped QDs were performed in the ground and excited states for both the antiferromagnetic (AFM) and ferromagnetic (FM) dimer configurations. Energies and electronic structures were obtained by solving the Kohn-Sham equations self-consistently using the PBE1PBE hybrid functional potential[7-9] with the LANL2DZ basis set,[10-12] in which core electrons are replaced by an effective core and only Zn^{2+} (4*s*, 3*d*, 4*p*), Se^{2-} (4*s*, 4*p*), Mn^{2+} (3*s*, 3*p*, 4*s*, 3*d*), and H (1*s*) atomic obitals are described with explicit basis functions. This computational scheme has been successful in describing the electronic structures of $Zn_{1-x}TM_xO$ (where TM = Co^{2+}, Mn^{2+}),[13-15] $Cd_{1-x}Mn_xS$,[16] and $Cd_{1-x}Mn_xSe$[17] nanocrystals. Convergence to the correct spin configuration was determined by analysis of the Mulliken spin density on each of the Mn^{2+} dopants. All molecular orbital plots were generated with an isosurface value of 0.035.

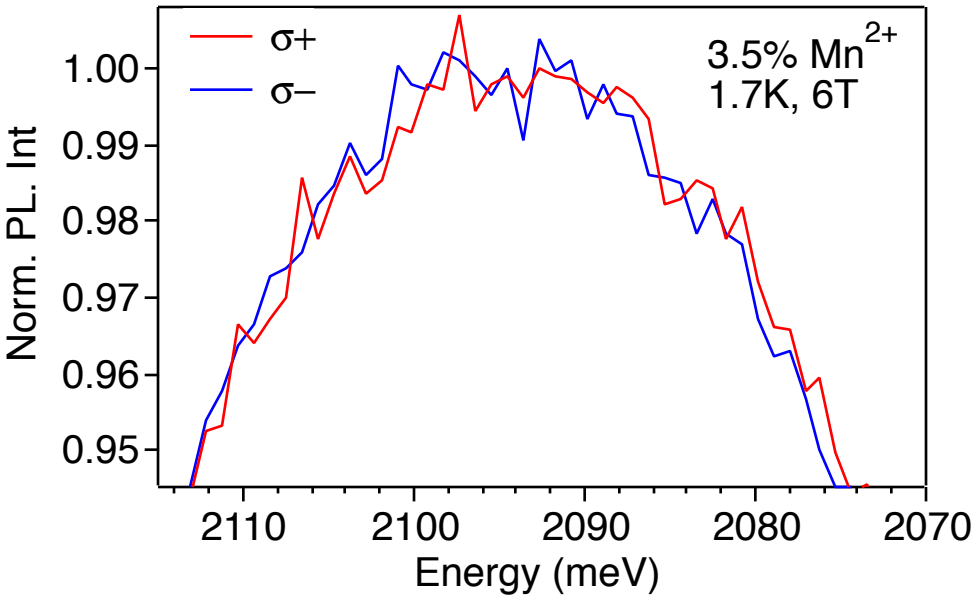

FIG B1. Normalized 1.7 K, 6 T MCPL spectra of 3.5% (x = 0.035) $Zn_{1-x}Mn_xSe$ nanocrystyals, demonstrating lack of a resolvable Zeeman splitting. An upper limit of < 1meV is estimated for the magnitude of this Zeeman splitting.

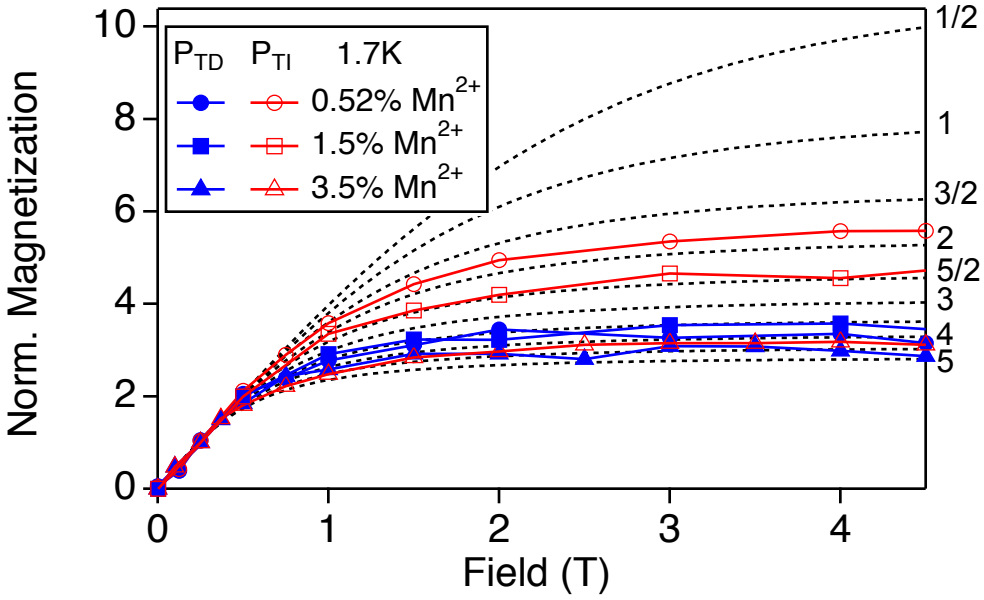

FIG B2. Magnetic field dependence of P_{TI} and P_{TD} for 0.52%, 1.5%, and 3.5% $Zn_{1-x}Mn_xSe$ nanocrystals. At all Mn^{2+} concentrations, P_{TD} saturates following roughly S = 7/2 – 4 behavior. Conversely, P_{TI} saturates faster at higher concentration, reaching $S \sim 4$ at 3.5% Mn^{2+}.

Calculation of J_{dd} from perturbation theory

Although derivation of a new band-structure-based superexchange calculation method is out of the scope of this paper, we can treat the Mn^{2+}-Mn^{2+} dimer with a simpler three-center model used for both semiconductor[18] and molecular systems.[19] The general derivation of *d-d* exchange in the three-center model is given in ref. [19], which concludes that exchange coupling involving spin transfer (*i*) between two half-filled orbitals (*ii*) from one half-filled to one empty orbital, or (*iii*) from one full to one half-empty orbital can be described in fourth-order perturbation theory by eqs S1, S2, and S3, respectively.

$$J_i = -\frac{2V_A^2V_B^2}{n_An_B}\left[\frac{1}{\Delta_B^2U_B}+\frac{1}{\Delta_A^2U_A}+\frac{1}{\Delta_B^2\Delta_{AB}}+\frac{2}{\Delta_A\Delta_B\Delta_{AB}}\right] \tag{S1}$$

$$J_{ii} = \frac{V_A^2V_B^2}{n_A(n_B+1)}\left[\frac{1}{\Delta_B^2U}-\frac{1}{\left(\Delta_B+I_{n_B+1}\right)^2\left(U+I_{n_B+1}\right)}+\frac{2}{\Delta_B\Delta_{AB}\Delta_A}-\frac{2}{\left(\Delta_B+I_{n_B+1}\right)\left(\Delta_{AB}+I_{n_B+1}\right)\Delta_A}+\frac{1}{\Delta_B^2\Delta_{AB}}-\frac{1}{\left(\Delta_B+I_{n_B+1}\right)^2\left(\Delta_{AB}+I_{n_B+1}\right)}+\frac{1}{\Delta_A^2\Delta_{AB}}-\frac{1}{\Delta_A^2\left(\Delta_{AB}+I_{n_B+1}\right)}\right] \tag{S2}$$

$$J_{iii} = \frac{1}{n_B(n_A+1)}\frac{V_A^2}{\Delta_B}\frac{V_B^2}{\Delta_B}\frac{I_{n_A+1}}{U^2} \tag{S3}$$

Here, n_A and n_B indicate the number of unpaired electrons on ions A and B, V is the transfer integral, U is the metal-to-metal charge transfer (MMCT) energy, Δ_A is the ligand to metal charge transfer (LMCT) energy for A, Δ_{AB} is the energy of the double LMCT state, and I_{nB+1} is the intra-atomic exchange integral. Since the charge transfer energies to $|^4T_1\rangle$ or $|^6A_1\rangle$ Mn^{2+} differ by 2.5 eV, it is necessary to use the full fourth order expressions.

To calculate J_{dd} for the one-orbital limit, it was assumed that $V_A = V_B$, $\Delta_A = \Delta_B = 6.1$ eV for the ground state, based on photoemission data in CdSe and relative band alignments,[20] U = 8.41 eV from ref [21], and $\Delta_{AB} = \Delta_A + \Delta_B$. The exchange integral ($V_{A,B}$) is the only unknown in equation S1, and can therefore be estimated from eq S1 and the experimental value of the ground state ($n_A = n_B = 5$) J_{dd} (~1 meV) to be 1 eV.[22] In the excited state, this same value of $V_{A,B}$ is used for both Mn^{2+} ions, but charge transfer energies (Δ and U) involving the excited Mn^{2+} are reduced by 2.5 eV to reflect the energy of the $^4T_1$ excited state. The intra-atomic exchange energy for the excited state (I_{nB+1}) is estimated using the approximation that $I_{nB+1} = (n_B + 1)I$ and

the value based on the ground state free ion of I_6 = 0.84 eV used in ref [20]. Equation S2 now gives the ferromagnetic coupling constant $J_{dd,ES}$ = +0.41 meV.

If exchange were dominated instead by the interaction of two half-filled orbitals, the reduced charge transfer energies of the excited state would strengthen the antiferromagnetic exchange coupling (by eq. S1) to J_{dd} =-3.6 meV. On the other extreme, if superexchange uses all three t_2 orbitals equally (such as is possible for pure T_d geometry), $V_{A,B}$ can be calculated for the ground state as above (except now over nine pathways) to be 0.58 eV. In the excited state, using only the t_2 orbitals, there are six remaining antiferromagnetic pathways each worth -0.44 meV (eq. S1) and three ferromagnetic worth +0.05 meV (eq. S2), the sum over which gives a coupling constant equal to -2.5 meV. This neglects participation from the *e* orbitals in the assumption that their overlaps are weaker, and interactions based on eq. S3 are inherently much weaker.[19]

All of these calculations assume the same exchange integral between the ground and excited states, which is likely incorrect under the influence of Jahn-Teller distortions. Jahn-Teller distortions that destabilize the empty orbital would potentially increase its overlap with bridging ligands, significantly changing V for that orbital. This greater overlap with the Jahn-Teller destabilized (empty) orbital would lead to stronger ferromagnetic interactions whether in the molecular description where the pertinent overlap is with a single bridging atom, or if the valence band acts as the bridging "ligand". Such a strong dependence of the superexchange sign and strength on Jahn-Teller distortions is commensurate with the observations in Cr^{2+} dimers made by Blinowski *et al.*[23] A realistic picture therefore would likely have both ferromagnetic and antiferromagnetic interactions active in the excited state, their relative strengths determined by the shifts in the coordinate frame and changes in overlap integrals caused by excited state Jahn-Teller distortion.

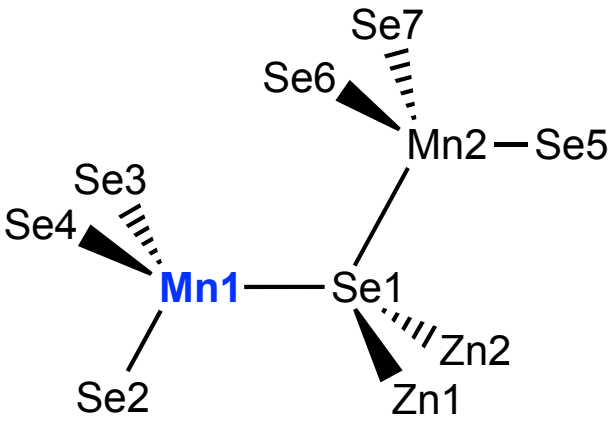

Dimer

Angle	Difference
Se1–Mn2–Se5	-0.189
Se5–Mn2–Se6	0.763
Se5–Mn2–Se7	-0.757
Se1–Mn2–Se6	0.900
Se1–Mn2–Se7	0.892
Se6–Mn2–Se7	-0.077
Mn2–Se1–Mn1	-1.693
Mn2–Se1–Zn2	-0.382
Mn2–Se1–Zn1	-0.412
Mn1–Se1–Zn2	1.013
Mn1–Se1–Zn1	0.946
Zn2–Se1–Zn1	0.423
Se4–Mn1–Se1	1.312
Se4–Mn1–Se3	-0.062
Se4–Mn1–Se2	-0.514
Se3–Mn1–Se1	1.234
Se3–Mn1–Se2	-0.509
Se2–Mn1–Se1	-1.497

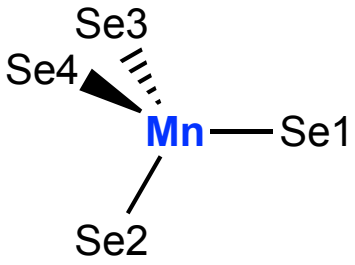

Monomer

Angle	Difference
Se1–Mn–Se2	1.011
Se1–Mn–Se3	1.051
Se1–Mn–Se4	2.267
Se2–Mn–Se3	-6.689
Se2–Mn–Se4	0.996
Se3–Mn–Se4	0.955

FIG B3. Bond-angle changes between $^6A_1$ and $^4T_1$ states of Mn^{2+} in the ZnSe lattice (excited state - ground state). The excited-state Mn^{2+} is depicted in blue. All bond angles are given in degrees. All changes in bond length over 0.1 Å are reported in the main text.

$Mn_2Zn_{84}Se_{86}$ Ferromagnetic *Fully Optimized* Excited State Molecular Orbitals			
ALPHA		**BETA**	
MO 575 -11.251 eV 0.787 Mn-d (0.778, 0.009)	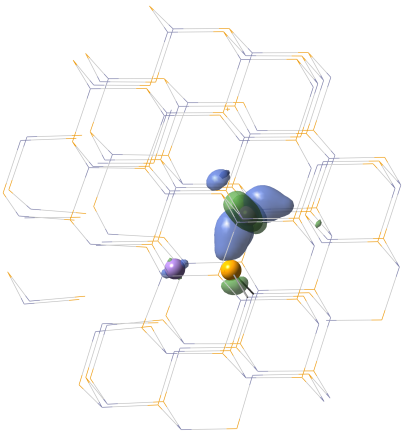	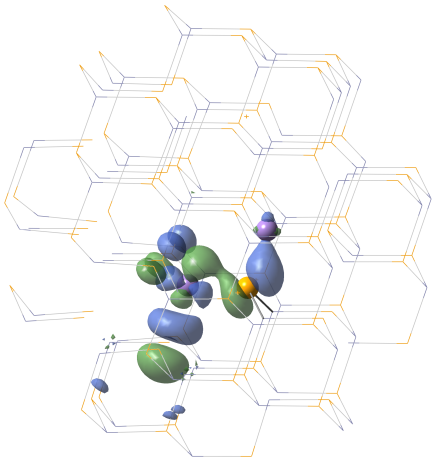	**HOMO MO 833 -6.480 eV 0.373 Mn-d (0.020, 0.353)**
MO 576 -11.250 eV 0.777 Mn-d (0.770, 0.007)	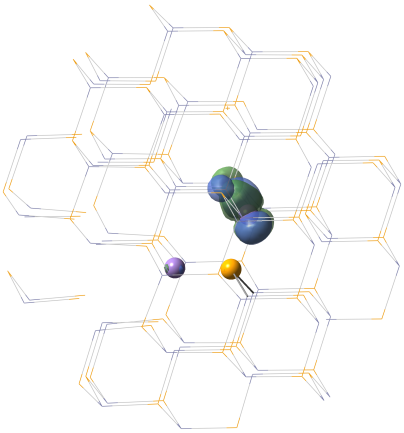	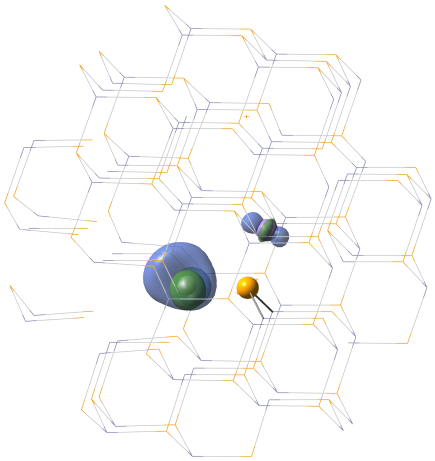	**MO 835 -1.817 eV 0.567 Mn-d (0.040, 0.528)**
MO 577 -11.226 eV 0.796 Mn-d (0.791, 0.006)	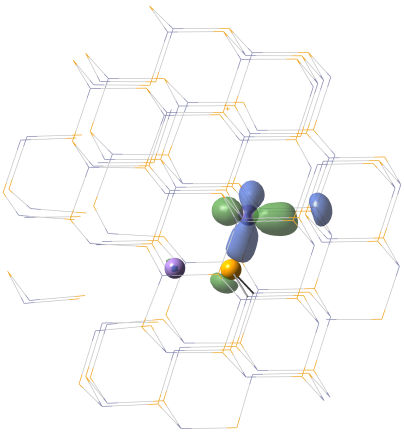	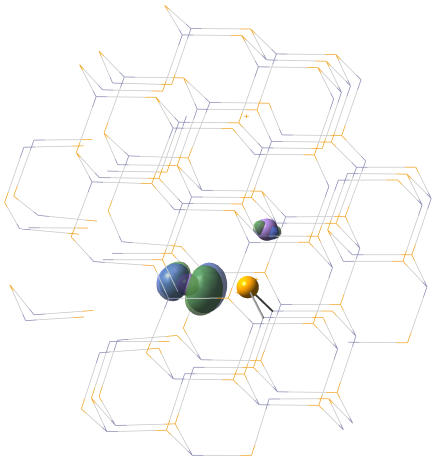	**MO 836 -1.743 eV 0.533 Mn-d (0.013, 0.520)**

MO 578 -11.153 eV 0.723 Mn-d (0.706, 0.017)	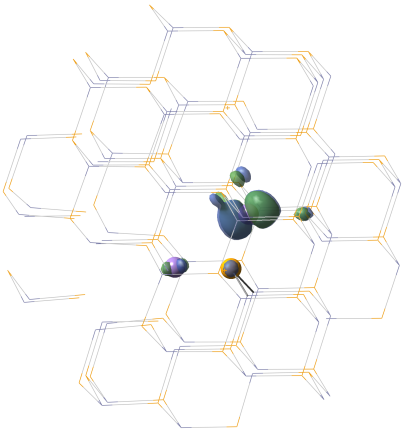	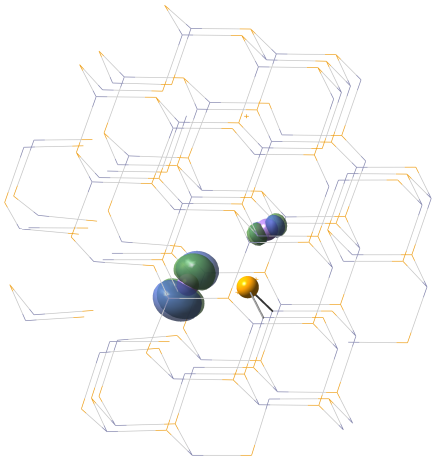	**MO 837 -1.717 eV 0.716 Mn-d (0.050, 0.666)**
MO 579 -11.136 eV 0.751 Mn-d (0.734, 0.017)	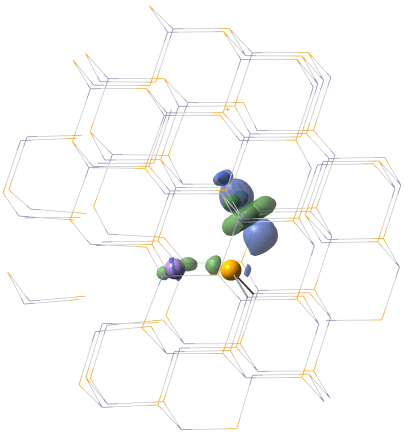	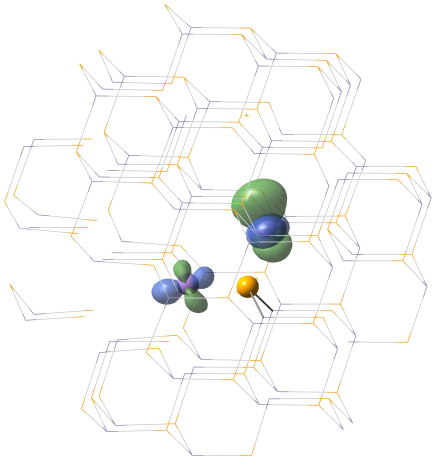	**MO 841 -1.489 eV 0.613 Mn-d (0.505, 0.108)**
MO 583 -10.738 eV 0.210 Mn-d (0.032, 0.178)	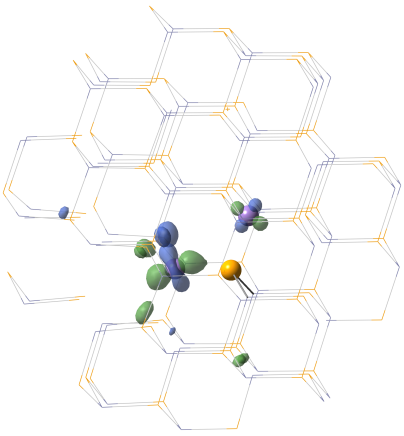	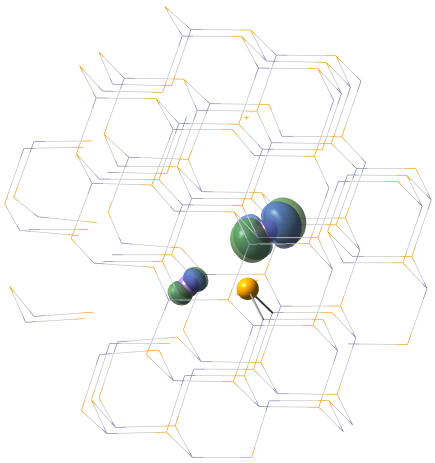	**MO 842 -1.484 eV 0.803 Mn-d (0.738, 0.065)**

MO 586 -10.706 eV 0.270 Mn-d (0.023, 0.247)	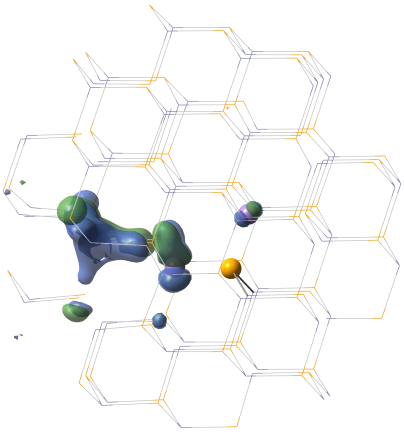	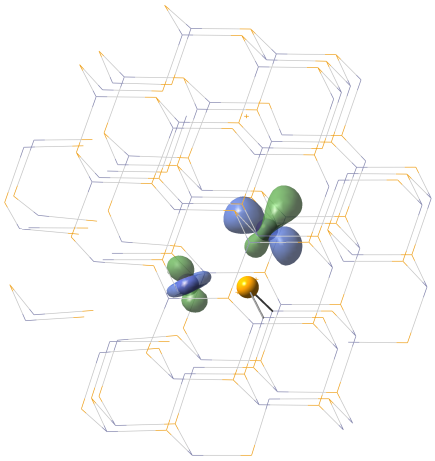	**MO 843 -1.456 eV 0.705 Mn-d (0.581, 0.124)**
MO 608 -10.246 eV 0.209 Mn-d (0.004, 0.204)	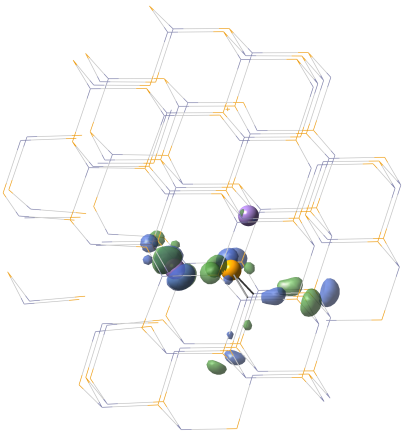	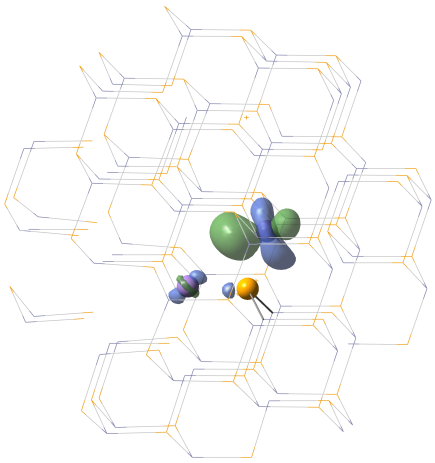	**MO 844 -1.414 eV 0.669 Mn-d (0.653, 0.015)**
MO 611 -10.088 eV 0.373 Mn-d (0.007, 0.366)	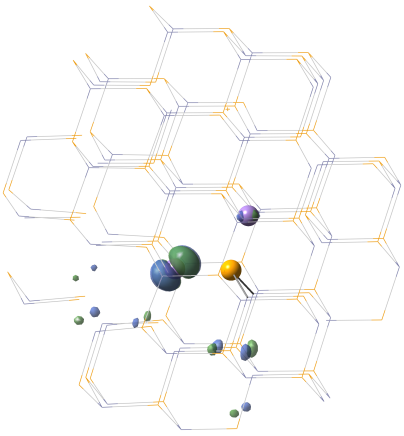	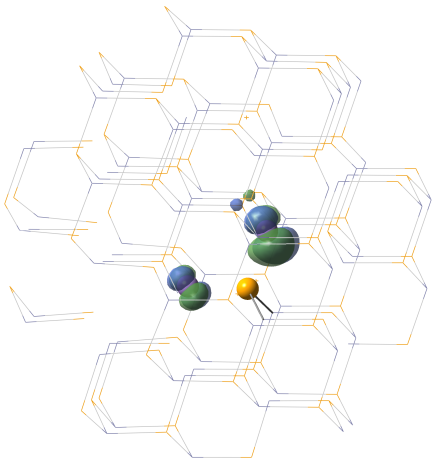	**MO 845 -1.388 eV 0.477 Mn-d (0.359, 0.118)**

LUMO MO 842 -3.260 eV 0.727 Mn-d (0.002, 0.725)	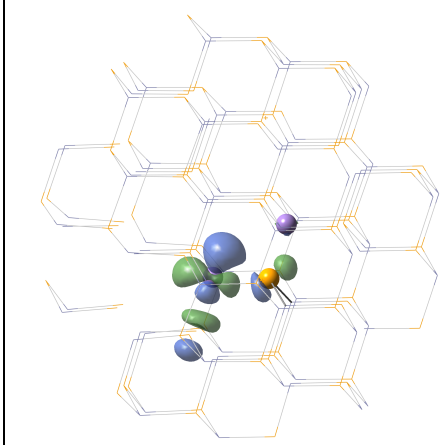	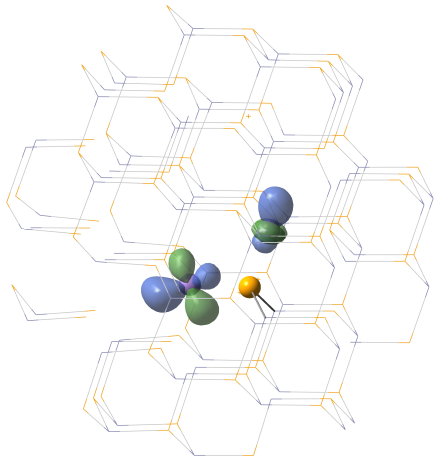	**MO 846 -1.342 eV 0.546 Mn-d (0.115, 0.431)**

FIG B4. The 20 molecular orbitals with the most Mn^{2+} *d*-orbital parentage, obtained from DFT calculations of $Zn_{84}Mn_2Se_{86}$. Mn^{2+} ions are purple, Se^{2-} as yellow, and Zn^{2+} as blue. The excited-state Mn^{2+} ion (Mn_{ES}) appears on the bottom left, and the ground-state Mn^{2+} (Mn_{GS}) on the top right. Molecular orbital energies, Mn^{2+} *d*-orbital contribution, and the relative contributions of each Mn^{2+} given as (Mn_{GS}, Mn_{ES}) are listed in the margins for each MO.

References

(1) Archer, P. I.; Santangelo, S. A.; Gamelin, D. R. *J. Am. Chem. Soc.* **2007**, *129*, 9808.
(2) McLaurin, E. J.; Vlaskin, V. A.; Gamelin, D. R. *J. Am. Chem. Soc.* **2011**, *133*, 14978.
(3) Reiss, P.; Protière, M.; Li, L. *Small* **2009**, *5*, 154.
(4) Borchert, H.; Shevchenko, E. V.; Robert, A.; Mekis, I.; Kornowski, A.; Grübel, G.; Weller, H. *Langmuir* **2005**, *21*, 1931.
(5) Beaulac, R.; Ochsenbein, S. T.; Gamelin, D. R. In *Semiconductor Quantum Dots*; 2nd ed.; Klimov, V. I., Ed.; CRC Press: 2010, p 397.
(6) Frisch, M. J.; Trucks, G. W.; Schlegel, H. B.; Scuseria, G. E.; Robb, M. A.; Cheeseman, J. R.; Scalmani, G.; Barone, V.; Mennucci, B.; Petersson, G. A.; Nakatsuji, H.; Caricato, M.; Li, X.; Hratchian, H. P.; Izmaylov, A. F.; Bloino, J.; Zheng, G.; Sonnenberg, J. L.; Hada, M.; Ehara, M.; Toyota, K.; Fukuda, R.; Hasegawa, J.; Ishida, M.; Nakajima, T.; Honda, Y.; Kitao, O.; Nakai, H.; Vreven, T.; Montgomery, J. A.; Jr; Peralta, J. E.; Ogliaro, F.; Bearpark, M.; Heyd, J. J.; Brothers, E.; Kudin, K. N.; Staroverov, V. N.; Kobayashi, R.; Normand, J.; Raghavachari, K.; Rendell, A.; Burant, J. C.; Iyengar, S. S.; Tomasi, J.; Cossi, M.; Rega, N.; Millam, J. M.; Klene, M.; Knox, J. E.; Cross, J. B.; Bakken, V.; Adamo, C.; Jaramillo, J.; Gomperts, R.; Stratmann, R. E.; Yazyev, O.; Austin, A. J.; Cammi, R.; Pomelli, C.; Ochterski, J. W.; Martin, R. L.; Morokuma, K.; Zakrzewski, V. G.; Voth, G. A.; Salvador, P.; Dannenberg, J. J.; Dapprich, S.; Daniels, A. D.; Farkas, Ö.; Foresman, J. B.; Ortiz, J. V.; Cioslowski, J.; Fox, D. J.; H21+ ed.; Gaussian, Inc.: Wallingford, CT.
(7) Perdew, J.; Burke, K.; Ernzerhof, M. *Phys. Rev. Lett.* **1996**, *77*, 3865.
(8) Perdew, J. P.; Burke, K.; Ernzerhof, M. *Phys. Rev. Lett.* **1997**, *78*, 1396.
(9) Adamo, C.; Barone, V. *J. Chem. Phys.* **1999**, *110*, 6158.
(10) Hay, P. J.; Wadt, W. R. *J. Chem. Phys.* **1985**, *82*, 299.

(11) Hay, P. J.; Wadt, W. R. *J. Chem. Phys.* **1985**, *82*, 270.
(12) Wadt, W. R.; Hay, P. J. *J. Chem. Phys.* **1985**, *82*, 284.
(13) Badaeva, E.; Feng, Y.; Gamelin, D. R.; Li, X. *New J. Phys* **2008**, *10*, 055013.
(14) Badaeva, E.; May, J. W.; Ma, J.; Gamelin, D. R.; Li, X. *J. Phys. Chem. C* **2011**, *115*, 20986.
(15) Badaeva, E.; Isborn, C.; Feng, Y.; Ochsenbein, S.; Gamelin, D.; Li, X. *J. Phys. Chem. C* **2009**, *113*, 8710.
(16) Peng, B.; Liang, W.; White, M. A.; Gamelin, D. R.; Li, X. *J. Phys. Chem. C* **2012**, *116*, 11223.
(17) Beaulac, R.; Feng, Y.; May, J.; Badaeva, E.; Gamelin, D.; Li, X. *Phys. Rev. B* **2011**, *84*, 195324.
(18) Larson, B. E.; Hass, K. C.; Ehrenreich, H.; Carlsson, A. E. *Phys. Rev. B* **1988**, *37*, 4137.
(19) Weihe, H. g.; Güdel, H. U.; Toftlund, H. *Inorg. Chem.* **2000**, *39*, 1351.
(20) Beaulac, R.; Gamelin, D. R. *Phys. Rev. B* **2010**, *82*, 224401.
(21) Chanier, T.; Virot, F.; Hayn, R. *Physical Review B* **2009**, *79*, 205204.
(22) This value of V is approximately the same as the Mn2+-valence band transfer integrals used by Larson (ref 1) and Beaulac (ref 3).
(23) Blinowski, J.; Kacman, P.; Majewski, J. A. *Phys. Rev. B* **1996**, *53*, 9524.

Appendix C. Supplementary Information for Chapter 4.

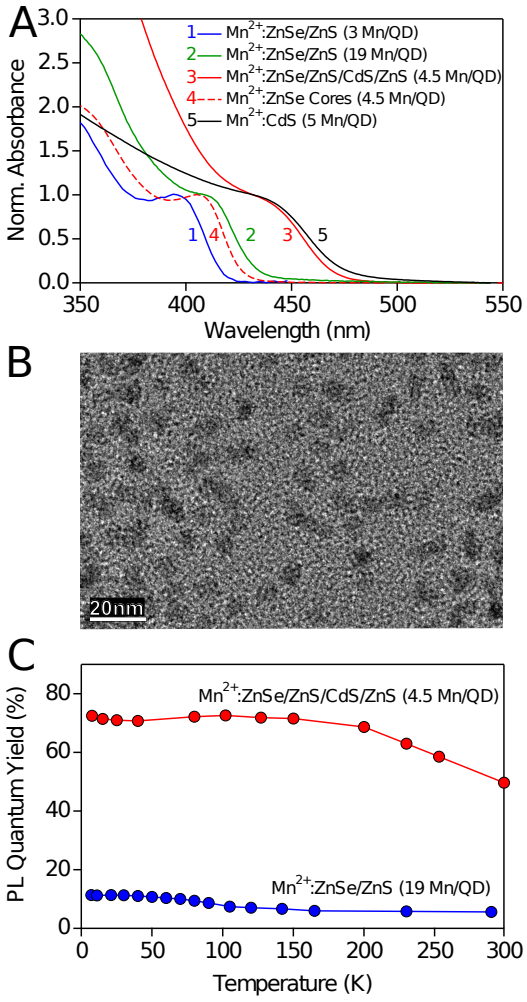

Figure C1. (A) Electronic absorption spectra of the four QD samples whose saturation behavior is demonstrated in Fig. 4.1 of the main text: $Zn_{0.995}Mn_{0.005}Se/ZnS$ (3 Mn^{2+}/QD), $Zn_{0.984}Mn_{0.016}Se/ZnS$ (19 Mn^{2+}/QD), $Zn_{0.9955}Mn_{0.0045}Se/ZnS/CdS/ZnS$ (4.5 Mn^{2+}/QD) as well as their $Zn_{0.9955}Mn_{0.0045}Se$ cores (4.5 Mn^{2+}/QD), and $Cd_{0.995}Mn_{0.005}S$ (5 Mn^{2+}/QD). Measurements were taken at room temperature. **(B)** A representative TEM image of the $Zn_{0.9955}Mn_{0.0045}Se/ZnS/CdS/ZnS$ QDs showing quasi-spherical crystals with ~6 nm diameters. The scale bar denotes 20 nm. **(C)** Temperature dependence of the PL quantum yields for the $Zn_{0.9955}Mn_{0.0045}Se/ZnS/CdS/ZnS$ and $Zn_{0.984}Mn_{0.016}Se/ZnS$ QDs. Room-temperature PL quantum yields were measured on colloidal suspensions using an integrating sphere.

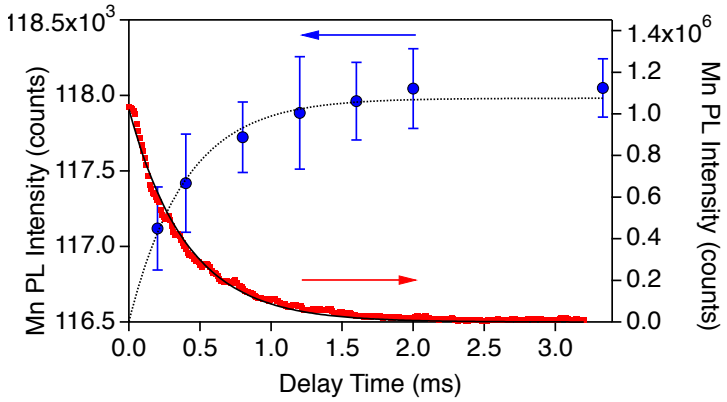

Figure C2. Right axis: Mn^{2+} PL decay in the Mn^{2+}:ZnSe/ZnS nanocrystals of Fig. 4.1C, fit with a single exponential with $\tau = 396$ µs. Left axis: Integrated Mn^{2+} PL intensity measured with pairs of excitation pulses, plotted vs the delay time between the two pulses. Error bars represent standard deviations of 5 measurements. The grey dashed line shows the $\tau = 396$ µs decay of the Mn^{2+} PL. Data measured at 7.5 K.

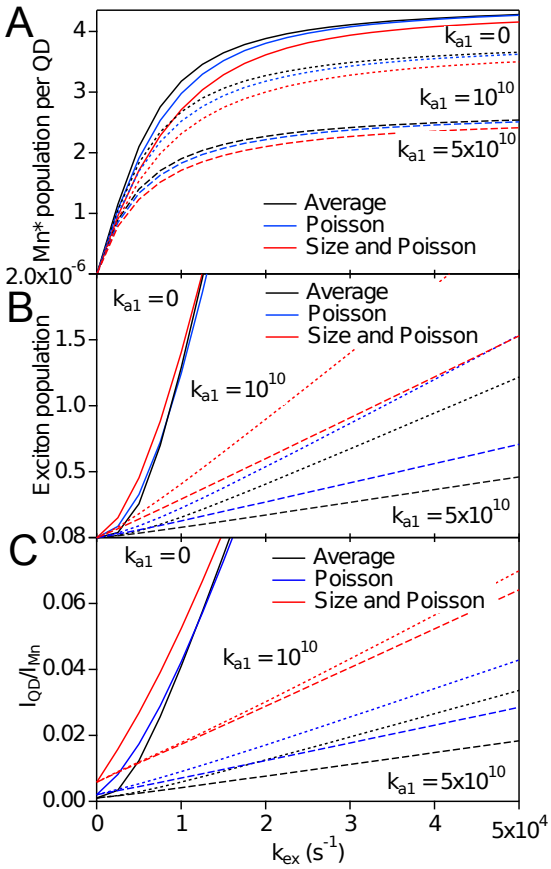

Figure C3. The effect on calculated populations of $^4T_1$ Mn^{2+} **(A)**, excitons **(B)**, and the PL ratio **(C)** of using only the average number of dopants (black), a Poissonian distribution (blue), and the model that folds the Poissonian distribution with the size distribution (red). Populations were calculated for Auger rate constants of k_{a1}=0 (—), 10^{10} s^{-1} (···), and 5×10^{10} (---).

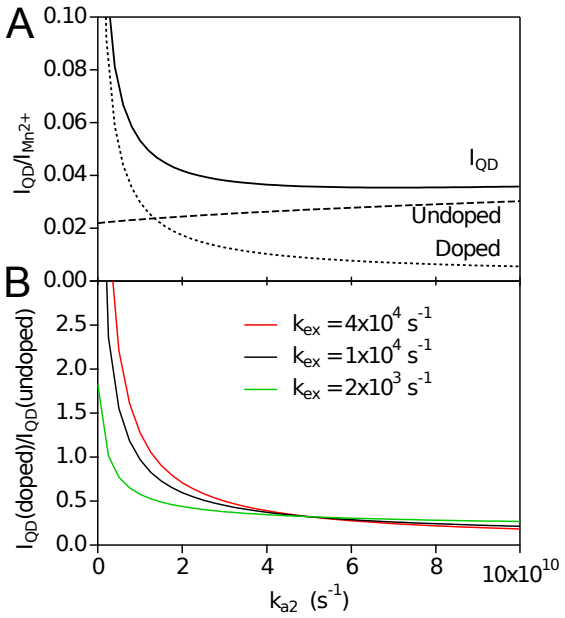

Figure C4. (A) I_{QD}/I_{Mn} calculated as a function of the cross-relaxation rate constant k_{a2} at fixed k_{ex} = 4×10^4 s^{-1}. The contributions from doped (···) and undoped (---) excitonic PL are plotted individually. **(B)** The ratio of doped to undoped excitonic PL as a function of cross-relaxation rate constant (k_{a2}), at several excitation rate constants.

Appendix D. Supplementary Information for Chapter 5.

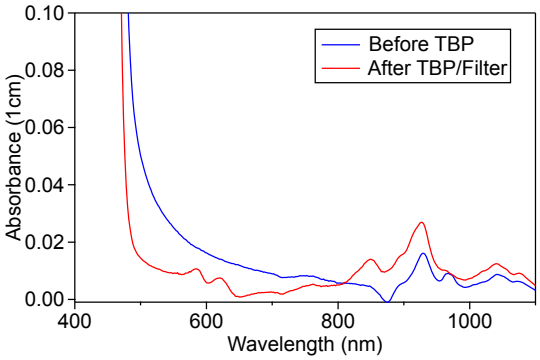

Figure D1. Absorption spectra measured over 1 cm pathlength of $Zn_{0.87}Cd_{0.11}Mn_{0.02}Se/ZnS$ NCs with OD_t = 1 (over 1 mm) as synthesized (blue) and after reduction with tri-butyl phosphine and filtration (red).

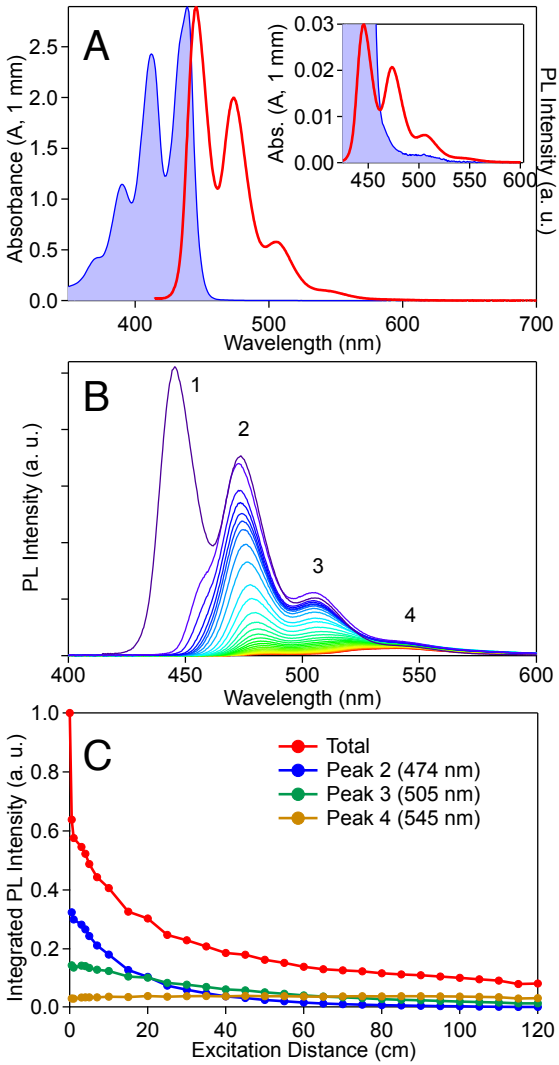

Figure D2. (A) Absorption (blue shaded) and dilute PL (red) spectra of perylene. The absorption spectrum was taken from the solution used for distance-dependent excitation experiments, in a 1 mm cuvette. The inset shows the same spectra, with the absorption spectrum magnified 100x. **(B)** Excitation-distance dependent PL spectra from L = 0 - 120 cm. The L = 0 cm spectrum was calculated by fitting the plot of the intensity of peak "2" versus L to a single exponential, and scaling the dilute PL spectrum to match this fit at L = 0 cm. **(C)** Plot of integrated PL intensity versus L for the total spectrum (red), and the individual peaks following the labeling in panel (B). Note that peak 4 actually increases with increasing L because of photon recycling.

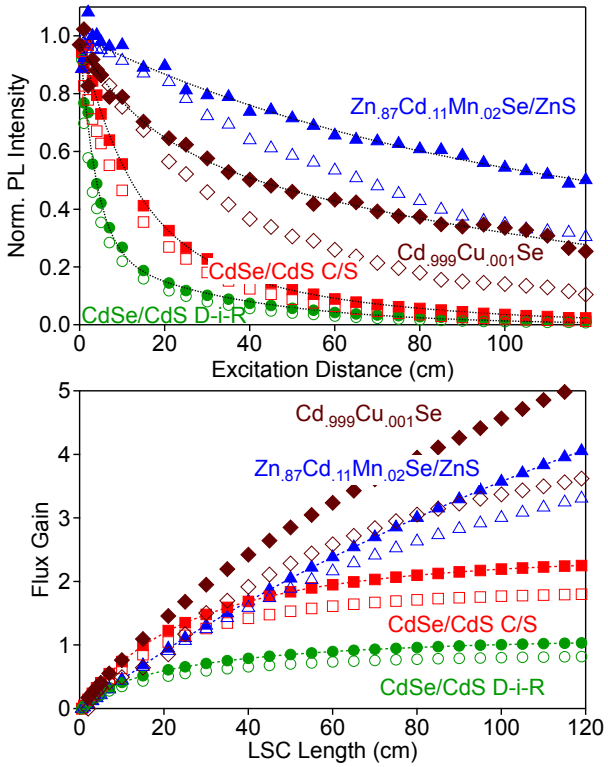

Figure D3. Plots of **(A)** measured PL intensity versus excitation distance *L* and **(B)** calculations of flux gain as a function of LSC length (as in Figure 4 of the main text), shown for raw PL intensities (open symbols) and PL intensities corrected for waveguide losses (closed symbols).

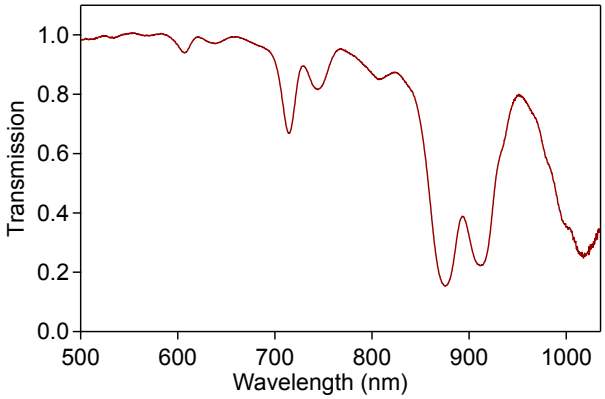

Figure D4. Transmission spectrum of toluene over 120 cm collected by coupling the light from a halogen lamp into the back end of the quartz waveguide from Figure 1C and comparing spectra from the empty and toluene-filled waveguide.

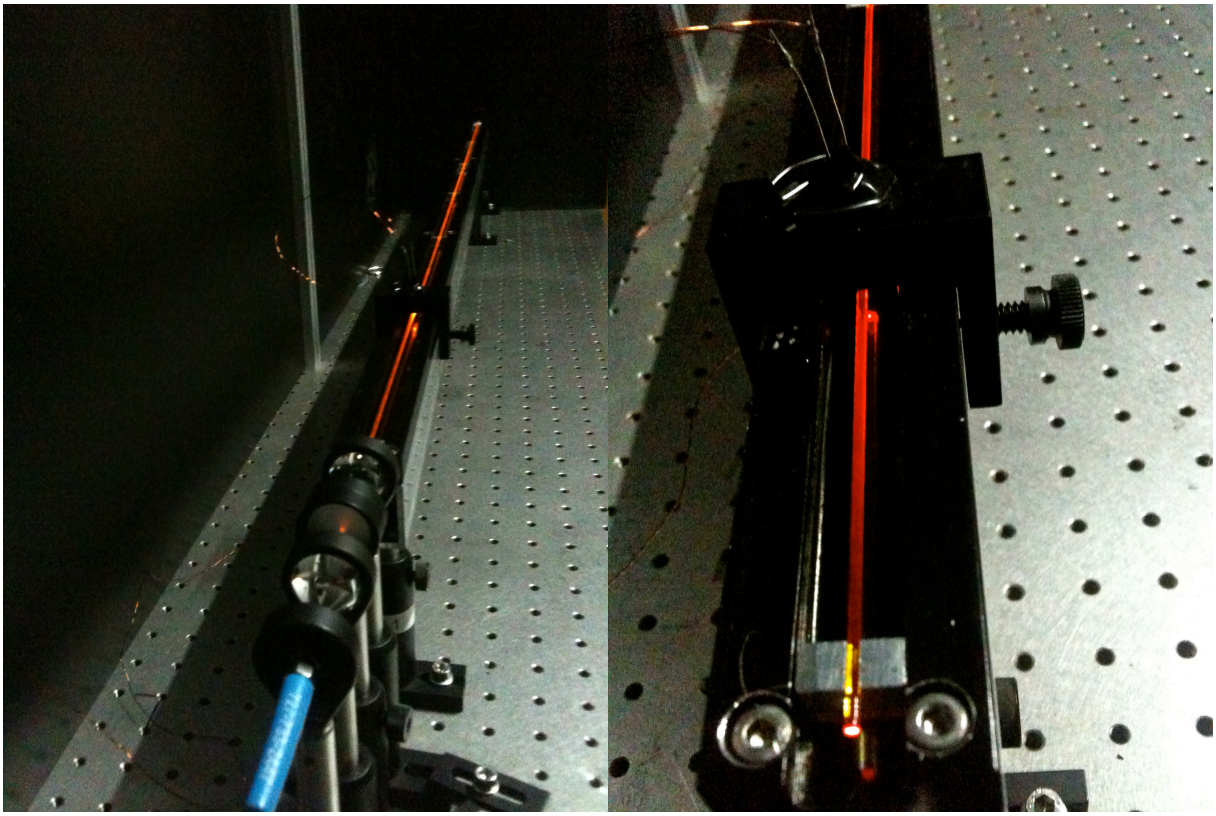

Figure D5. Photographs of the liquid waveguide showing the entire device and collection optics (left), and a close-up of the end of the tube and the movable excitation source (right).

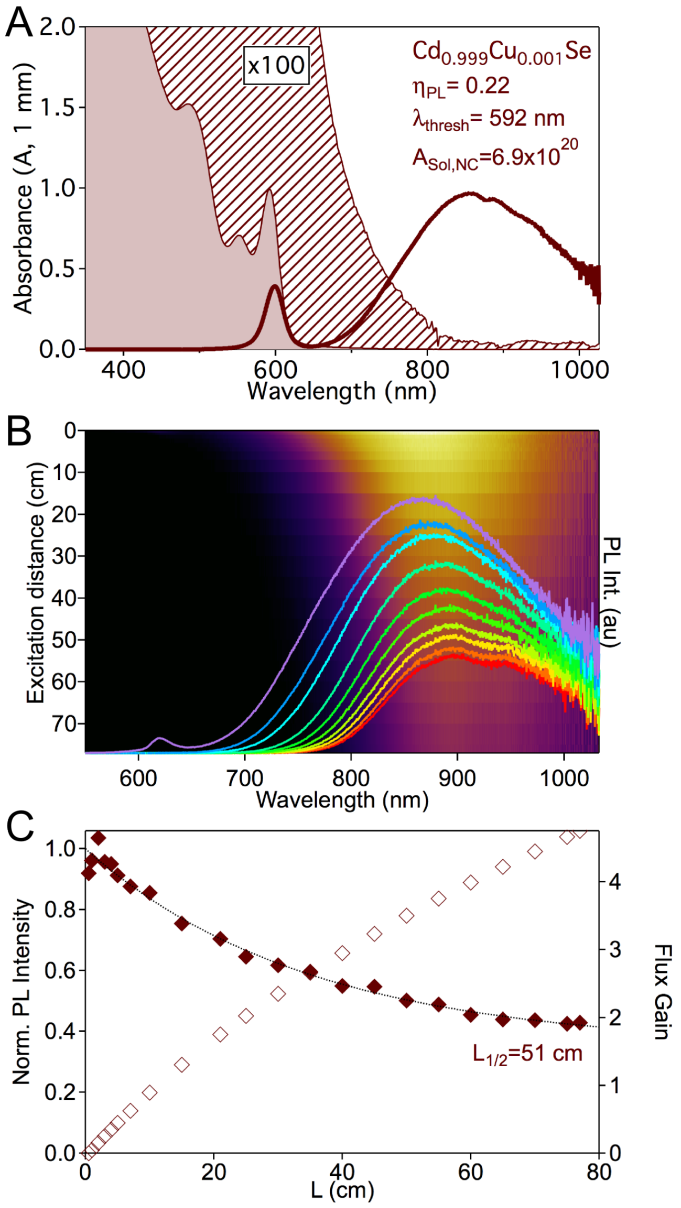

Figure D6. (A) Absorbance (shaded and diagonally patterned) and PL spectra (curve), **(B)** PL excitation distance dependence, and **(C)** L dependence of integrated PL intensity (left axis, closed symbols) and calculated FG (open symbols, right axis) for a different sample of $Cd_{0.999}Cu_{0.001}Se$ NCs than was used in the main text. Solar absorption is stated in units of photons/(m^2 sec). $L_{1/2}$ is significantly greater with these NCs than those in the main text. These NCs were not used in the main text because of the limited sample volume and their smaller solar absorption.

Calculation of 2-D LSC Flux Gain

In terms of OQE (the proportion of absorbed photons that reach the PV-covered edge of the LSC), the flux gain for a square $L \times L$ LSC is given by equation D1:

$$FG = G_{geo}(L) \cdot \frac{\eta_{PV}^{pl}}{\eta_{PV}^{AM\,1.5}} \cdot OQE(L). \quad [D1]$$

Here, $G_{geo}(L) = L^2/4Lt = L/4t$ where t is the LSC thickness. To compute OQE, under the assumption that there is no scattering, we first compute what proportion of emitted photons reach an edge of the LSC *without* being re-absorbed by a NC. This is governed by $PL(\lambda)$ and $A(\lambda)$ and is given by equation D2:

$$\rho(L) = \frac{1}{4\pi L^2} \iint_{L\times L} \int_0^{2\pi} \int_{\theta_{esc}}^{\pi-\theta_{esc}} PL(\lambda) 10^{-A(\lambda)\, l(x,y,\theta,\phi)} \sin\theta \; d\lambda \, d\theta \, d\phi \, dx \, dy \quad [D2]$$

Here, $l(x, y, \theta, \phi)$ is the distance a photon will travel from position (x, y) in the LSC, in direction (θ, ϕ) (in spherical coordinates) before reaching the edge of the LSC; $PL(\lambda)$ is the probability that an emitted photon has wavelength λ, and $10^{-A(\lambda)\, l(x,y,\theta,\phi)}$ is the probability that the photon will travel distance l given it has wavelength λ; θ_{esc} is the angle of the escape-cone.

From knowledge of $\rho(L)$ we compute $OQE(L)$ as follows: we make the assumption that the distribution of absorbed photons is uniform over the area of the LSC, and furthermore, that subsequent absorption events of recycled photons are also uniform over the LSC. From the initial absorption of photons, η_{PL} are emitted, $(1 - \eta_{PL}) + (1 - \eta_{EC})\eta_{PL} = 2 - \eta_{PL} - \eta_{EC}\eta_{PL}$ are lost due to less than unity quantum efficiency and due to escape-cone loss, and the proportion of photons which will reach the edge is $\rho\, \eta_{PL}$. The proportion that remains in the LSC is thus $1 - (2 - \eta_{PL} - \eta_{EC}\eta_{PL}) - \rho\, \eta_{PL} = \eta_{PL}(\eta_{EC} - \rho)$. Under the assumption that these remaining photons are absorbed uniformly over the LSC, second emission photons experience the same mechanism, and so $(2 - \eta_{PL} - \eta_{EC}\eta_{PL})(\eta_{PL}(\eta_{EC} - \rho))$ are lost, and $\rho\, \eta_{PL}(\eta_{PL}(\eta_{EC} - \rho))$ reach the edge of the LSC. What remains in the LSC is given by equation D3:

$$\eta_{PL}(\eta_{EC} - \rho) - (2 - \eta_{PL} - \eta_{EC}\eta_{PL})\big(\eta_{PL}(\eta_{EC} - \rho)\big) - \rho\, \eta_{PL}\big(\eta_{PL}(\eta_{EC} - \rho)\big) = \eta_{PL}^2(\eta_{EC} - \rho)^2 \quad [D3]$$

Repeating this process and summing over all absorption/re-emission events we arrive at the proportion of captured photons expressed in equation D4:

$$OQE(L) = \rho(L)\eta_{PL} \sum_{n=0}^{\infty} [\eta_{PL}(\eta_{EC} - \rho(L))]^n \; = \frac{\rho(L)\eta_{PL}}{1 - \eta_{PL}(\eta_{EC} - \rho(L))} \quad [D4]$$

Flux gain is then calculated by application the result of equation D4 to equation D1 for any side length, *L*. Results calculated for the four nanocrystals of the main manuscript are plotted in Figure D7.

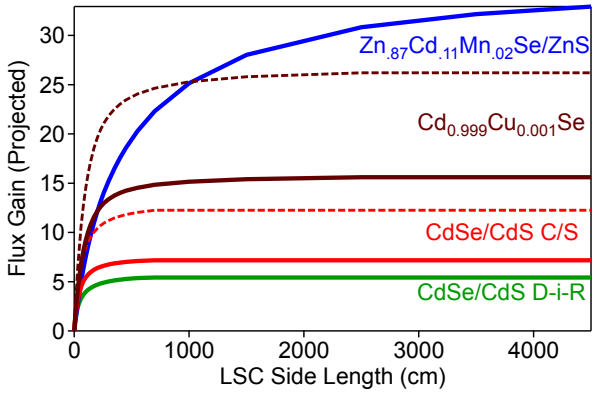

Figure D7. Projected flux gains for 1 mm thick, OD_t = 1 square-planar nanocrystal LSCs coupled to Si photovoltaics, under AM 1.5 solar irradiation, plotted as a function of side length. Dashed lines were calculated using best-reported quantum yields from Table 1.

Scattering by Nanocrystals

Figure D8 shows calculations of the contributions of Rayleigh scattering to losses over a 1 m pathlength in a nanocrystal LSC device. Effective absorbance was calculated according to equation D1,

$$A_R = \frac{2\pi^5}{3}\frac{d^6}{\lambda^4}\left(\frac{n_{dot}^2 - n_{sol}^2}{n_{dot}^2 + 2n_{sol}^2}\right)^2 \frac{C \cdot 100cm}{3.8 \cdot 10^{-17}} P_{EC} \qquad [D5]$$

where d is the diameter of the nanocrystal, n_{dot} is the index of refraction of the semiconductor (~2.5), n_{sol} is the index of refraction of the solvent (~1.5), and P_{EC} is the probability of escape cone loss from a scattering event, approximated as 20% based on the 1 + $\cos^2(\theta)$ angular anisotropy of Rayleigh scattering. The concentration of nanocrystals, C, was chosen to maintain an OD_t = 1 over 1 mm based on literature values for size dependent extinction coefficients.[1, 2] This qualitative model neglects effects of size distributions and changes in the size dependence of the extinction coefficient beyond the range measured in refs. 1 and 2. The wavelength, λ, is taken as the emission maximum for systems similar to those reported herein: ZnSe/ZnS, λ = 600 nm where Mn^{2+} emits; CdS NCs are assumed to emit as CdSe/CdS core shells at 625 nm; CdSe NCs are assumed to emit at 1000 nm either from $Cu^{+/2+}$ charge transfer or from sensitization of a PbSe core (for example).

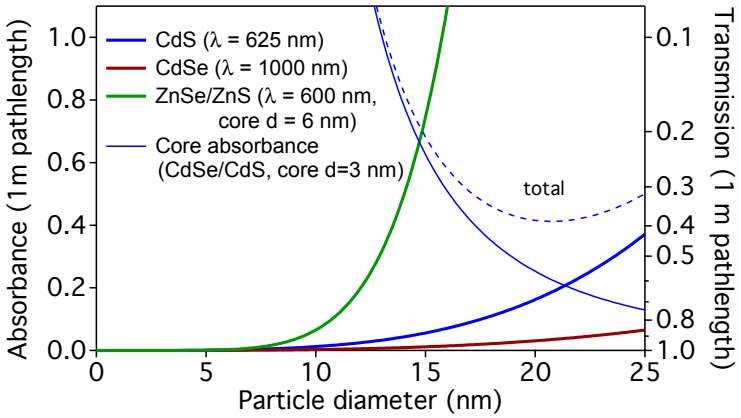

Figure D8. Calculated effective absorbance (left axis) and transmission (right axis) over 1 m due to Rayleigh scattering from CdS (blue), CdSe (red) and ZnSe/ZnS (green) NCs as a function of nanocrystal diameter. Scattering for CdS and CdSe nanocrystals was calculated at 625 nm and 1000 nm, respectively, and their concentration decreases as they get larger to maintain an $OD_t = 1$. Scattering for ZnSe/ZnS nanocrystals was calculated at 600 nm, with a constant concentration based on a core diameter of 6 nm and increasing the total diameter by only changing the shell thickness. The waveguide index of refraction was 1.5, and escape cone losses from a scattering event were taken to be 20%. Also shown is the effective absorbance (assuming unity QY and 25% escape cone loss) from reabsorption by the core for a CdSe/CdS nanocrystal with a 3 nm core (fine blue line), and total losses (dashed blue) for such a nanocrystal.

Also shown in Figure D8 is the calculated reabsorption at 625 nm from the core in a CdSe/CdS core/shell nanocrystal as a function of nanocrystal diameter. Still working at the 625 nm emission maximum, this curve is calibrated using our 13.5 nm nanocrystals, which have a 1 m OD (measured from Figure 5.2B) of 3.6. Assuming 100% PL quantum yield, a 25% escape cone loss per reabsorption leads to an effective 1 m OD of 0.9. Addition of the scattering and core absorption curves yields the dashed curve in Figure D8, which indicates that particles with $d \sim 20$ nm minimize total losses. Although these calculations may not be quantitatively accurate, they illustrate the existence of an optimal size for core/shell NCs to balance scattering and reabsorption losses, and even at this size these losses are substantial.

References

1. Yu, W. W.; Qu, L.; Guo, W.; Peng, X., Experimental Determination of the Extinction Coefficient of CdTe, CdSe, and CdS Nanocrystals. *Chem. Mater.* 2003, **15**, 2854-2860.

2. Norberg, N. S.; Parks, G. L.; Salley, G. M.; Gamelin, D. R., Giant Excitonic Zeeman Splittings in Colloidal Co2+-Doped ZnSe Quantum Dots. *J. Am. Chem. Soc.* 2006, **128**, 13195-13203.

Appendix E. Supplementary Information for Chapter 6.

Determination of the optical quantum efficiency. The measured experimental data, $OQE_{ap}(L)$, consist of non-index-matched collection of light over an aperture of width A centered on the $W = 2.5\,cm$ edge of an LSC with lateral dimensions $L{\times}W\ cm^2$; the LSC is illuminated uniformly over the full top face. From these measurements, we wish to estimate what would be the $OQE_{full}(L)$ of an LSC with lateral dimensions $L{\times}W\ cm^2$ if photons were collected on all four edges by an index-matched collection device. Computation of this estimate is based on the assumption that a photon which has been absorbed and emitted by a QD will not undergo a second absorption. We do, however, wish to include the possibility of loss of photons due to scattering and extinction by the matrix itself. Assuming that the probability of such loss is independent of location within the LSC, this loss is described by an extinction coefficient α. In what follows, we describe how we determine both LQY and α from the measured data.

Let $OQE^*_{ap}(L\,;\alpha,Q)$ be the theoretical measurement we will calculate, taking into account the Fresnel relations at the measurement aperture and assuming a matrix extinction of α and LQY of Q. By fitting $OQE^*_{ap}(L_j\,;\alpha,Q)$ to $OQE_{ap}(L_j)$ for the lengths L_j for which we have measurements, we determine α^* and Q^*, the best-fit parameters. Both $OQE_{ap}(L)$ and $OQE^*_{ap}(L\,;\alpha,Q)$ assume non-index-matched measurements. From knowledge of α^* and Q^* we can then compute $OQE^*_{full}(L)$, the predicted measurement when collection is made on all edges of the LSC and measurement is index-matched.

We introduce lateral coordinates (x,y) so that the LSC is $-W/2 \le x \le W/2$, $0 \le y \le L$, and the aperture is $-A/2 \le x \le A/2$, $y = 0$. (The thickness of the LSC plays no role in these computations.) To obtain OQE^*_{ap}, let $p(x,y\,;\alpha,Q)$ be the probability that a photon emitted from position (x,y) in the LSC: (i) reaches the side $y = 0$ within the aperture, at any z-value; (ii) lies within the side escape cone of the aperture; and (iii) refracts out of the LSC. Allowing z to be unconstrained corresponds to allowing total internal reflection between the top and bottom faces. The third requirement takes into account the transmission coefficient for unpolarized light, determined from the Fresnel relations. Given $p(x,y\,;\alpha,Q)$ (which is derived below), we have

$$OQE_{ap}^{*}(L\,;\alpha,Q)=\frac{1}{LW}\int_{-W/2}^{W/2}\int_{0}^{L}p(x,y\,;\alpha,Q)\,dx\,dy.$$

To obtain $p(x,y\,;\alpha,Q)$, first let $-\pi<\phi_1(x,y)<\phi_2(x,y)<0$ be such that the directions $(\cos\phi_i,\sin\phi_i)$ from (x,y) meet $(-W/2,0)$ and $(W/2,0)$, respectively. For each $\phi_1(x,y)<\phi<\phi_2(x,y)$, we define $0\le\theta\big(\phi(x,y)\big)\le\pi/2$ by

$$\theta\big(\phi(x,y)\big)=\begin{cases}\sin^{-1}\left(\dfrac{-1}{\sin\phi(x,y)}\sqrt{1-\dfrac{1}{n^2}}\right), & 1-\dfrac{1}{n^2}<\sin^2\phi(x,y)\\ 1, & \text{otherwise.}\end{cases}$$

This definition is such that either the vector $\vec{v}(\theta,\phi)=(\sin\theta\cos\phi,\sin\theta\sin\phi\,,\cos\theta)$ lies within the side escape cone (centered on the normal vector $\vec{\nu}=(0,-1,0)$ to the aperture) precisely for $\theta\big(\phi(x,y)\big)\le\theta\le\pi/2$, or $\theta\big(\phi(x,y)\big)=\pi/2$ if there is no θ for which the direction with that ϕ lies within the side escape cone. We define the transmission coefficient $T=1-\frac{1}{2}(R_s+R_p)$ where

$$R_s^2=\begin{cases}\dfrac{n\,\vec{v}\cdot\vec{\nu}-\sqrt{1-n^2(\vec{v}\cdot\vec{\nu})^2}}{n\,\vec{v}\cdot\vec{\nu}+\sqrt{1-n^2(\vec{v}\cdot\vec{\nu})^2}}, & \vec{v}\cdot\vec{\nu}>\sin^{-1}\dfrac{1}{n},\\ 1, & \text{otherwise,}\end{cases}$$

$$R_p^2=\begin{cases}\dfrac{n\sqrt{1-n^2(\vec{v}\cdot\vec{\nu})^2}-\,\vec{v}\cdot\vec{\nu}}{n\sqrt{1-n^2(\vec{v}\cdot\vec{\nu})^2}+\,\vec{v}\cdot\vec{\nu}}, & \vec{v}\cdot\vec{\nu}>\sin^{-1}\dfrac{1}{n},\\ 1, & \text{otherwise.}\end{cases}$$

Define T as a function of (θ,ϕ) by way of $\vec{v}(\theta,\phi)$ given in spherical coordinates. With these definitions,

$$p(x,y\,;\alpha,Q)=\frac{Q}{4\pi}\int_{\phi_1(x,y)}^{\phi_2(x,y)}2\int_{\theta(\phi(x,y))}^{\pi/2}T(\theta,\phi)\exp(-\alpha l(x,y,\theta,\phi))\sin\theta\,d\theta\,d\phi,$$

where $l(x, y, \theta, \phi)$ is the distance from the point (x, y) to the edge $y = 0$ in the direction with spherical coordinates (θ, ϕ). Specifically, $l(x, y, \theta, \phi) = \frac{-y}{\sin\theta \sin\phi}$.

Because α is unknown, we cannot compute $OQE^*_{ap}(L\,; \alpha, Q)$ directly. However, for values of $\alpha\, l \ll 1$, $\exp(-\alpha l) = 1 - \alpha l + \frac{1}{2}(\alpha l)^2 - \frac{1}{6}(\alpha l)^3 + \cdots \approx \sum_{j=0}^{N} \frac{\alpha^j l^j}{j!}$. As we shall see below, the requirement that $\alpha\, l \ll 1$ does indeed hold and the approximation is accurate with N as low as 3 or 4. We define the α-independent and Q-independent functions, $i \geq 0$,

$$f_i(L) = \frac{1}{2\pi LW} \int_{-W/2}^{W/2} \int_0^L \int_{\phi_1(x,y)}^{\phi_2(x,y)} \int_{\theta(\phi(x,y))}^{\pi/2} T(\theta, \phi) l(x, y, \theta, \phi)^i \sin\theta \; d\theta \; d\phi \; dx \; dy$$

which we can numerically compute for the measurement lengths $L_1, \ldots, L_{14}$ ($W = 2.5$). We then have

$$OQE^*_{ap}(L_k\,; \alpha, Q) \approx Q\left(f_0 - \alpha f_1(L_k) + \frac{1}{2}\alpha^2 f_2(L_k) - \cdots + \frac{(-1)^N}{N!}\alpha^N f_N(L_k)\right).$$

For a given N, we can now minimize the mean squared error (MSE) between this vector of values and the measured values:

$$\{\alpha^*, Q^*\} = \text{argmin}\left\{\sum_{k=0}^{14} \left(OQE^*_{ap}(L_k; \alpha, Q) - OQE_{ap}(L_k)\right)^2\right\}.$$

We find that MSE is 1.6×10^{-6} even for $N = 0$, but drops to 1.1×10^{-6} for $N = 3$ and remains so for $N = 4, 5$; the values of $\alpha^* = 0.0195$ and $Q^* = 0.530$ also remain unchanged beyond $N = 3$. In the paper we report the attenuation coefficient in units of dB / cm, computed from α^* using $\alpha_{dB} = 10\alpha^* \log_{10} e = 0.085$, where e is Euler's number.

Using α^*, Q^*, we can now calculate $OQE^*_{full}(L, W)$. Extend the definition of $l(x, y, \theta, \phi)$ to be the distance from (x, y) to the appropriate edge met by the vector with spherical coordinates (θ, ϕ). Then

$$OQE^*_{full}(L,W) = \frac{Q^*}{2\pi LW}\int_{-W/2}^{W/2}\int_0^L\int_0^{2\pi}\int_{\theta(\phi(x,y))}^{\pi/2} \exp(-\alpha^*\, l(x,y,\theta,\phi))\sin\theta\; d\theta\; d\phi\; dx\; dy.$$

In particular, we compute $OQE^*_{full}(L_k, 2.5)$ to obtain the predicted full perimeter, index-matched OQE measurements. In the main part of Figure 6.2A we plot $OQE_{ap}(L)\frac{OQE^*_{full}(L)}{OQE^*_{ap}(L)}$. We can further compute $OQE^*_{full}(L,L)$ for increasingly large values of L to predict performance of larger square LSCs (Figure 5.4).

Table E1. Projected maximum flux gains for Mn^{2+}-doped ZnSe/ZnS nanocrystal LSCs coupled to benchmark photovoltaic technologies, based on the experimental LSC parameters.

PV technology	Ref.	$\eta_{PV}^{AM1.5}$ (%)	$\eta_{PV}^{e_{em}}$ (%)	F_{max}
CIGS[(a)]	[1]	19.6	25.8	7.9
GaAs[(b)]	[2]	28.8	44.4	9.3
CdTe[(c)]	[3]	18.3	28.9	9.5
DSSC[(d)]	[4]	11.0	21.8	11.9
a-Si[(e)]	[5]	10.1	26.0	15.6
polymer[(f)]	11	9.9	26.2	15.9

[(a)]$CuInGaSe_2$ (National Renewable Energy Laboratory), *EQE* = 0.97, V_{OC} = 0.71 V, *FF* = 0.79. [(b)]Thin film GaAs (Alta Inc.), *EQE* = 0.97, V_{OC} = 1.12 V, *FF* = 0.87. [(c)]CdTe (General Electric, Inc.) *EQE* = 0.93, V_{OC} = 0.86 V, *FF* = 0.77. [(d)]Dye sensitized solar cell (Sharp Inc.) *EQE* = 0.92, V_{OC} = 0.71 V, *FF* = 0.70. [(e)]Amorphous silicon (Oerliken Solar), *EQE* = 0.93, V_{OC} = 0.89 V, *FF* = 0.67. [(f)]Polymer (Konarka Inc.), *EQE* = 0.97, V_{OC} = 0.82 V, *FF* = 0.70. Neglecting coupling losses and based on CR_{lim} = 6. V_{OC} does not include enhancements resulting from concentration, and hence may underestimate the maximum flux gain. *EQE* = photovoltaic external quantum efficiency at 2.12 eV; V_{OC} = open circuit voltage; *FF* = fill factor. Reported values at 25° C under AM1.5 conditions. $\eta_{PV}^{e_{em}} = (EQE \times V_{OC} \times FF)/(Ce_{em})$, C is the electronic charge.

Figure E1. A Mn^{2+}-doped ZnSe/ZnS nanocrystal luminescent solar concentrator device under diffuse solar excitation (cloudy day). Although largely transparent to visible light, the orange wave-guided luminescence of Mn^{2+} is clearly seen at the device edges.

References

[1] Green MA, Emery K, Hishikawa Y, Warta W, (2011) Solar cell efficiency tables (version 37). *Prog. Photovolt: Res. Appl*. 19(1): 84-92.

[2] Green MA, Emery K, Hishikawa Y, Warta W, Dunlop ED, (2012) Solar cell efficiency tables (version 40). *Prog. Photovolt: Res. Appl*. 20(5): 606-614.

[3] Green MA, Emery K, Hishikawa Y, Warta W, Dunlop ED, (2013) Solar cell efficiency tables (version 41). *Prog. Photovolt: Res. Appl*. 21(1): 1-11.

[4] Green MA, Emery K, Hishikawa Y, Warta W, Dunlop ED, (2011) Solar cell efficiency tables (version 39). *Prog. Photovolt: Res. Appl*. 20(1): 12-20.

[5] Green MA, Emery K, Hishikawa Y, Warta W, (2010) Solar cell efficiency tables (version 36). *Prog. Photovolt: Res. Appl*. 18(5): 346-352.